Characterisation of the mechanical properties of thin-film mirror coating materials for use in future interferometric gravitational wave detectors

Raymond Robie

School of Physics and Astronomy
University of Glasgow

Presented as a thesis for the degree of Ph.D. in the University of Glasgow, University Avenue, Glasgow G12 8QQ

June 2018

Table of contents

List of figures

List of tables

Acknowledgements

I would like to first thank my supervisor, Dr. Iain Martin, for his advice and tutelage over the course of my time at the Institute for Gravitational Research (IGR). It has been a privilege to learn the ins and outs of Academia and the LIGO-Virgo Collaboration (LVC) from him, as well as spend long nights in the lab and/or office vaguely on topic while working on a pressing experiment. I have enjoyed my time as a PhD student immensely, in no small part due to his supervision. I am further grateful for his extending the opportunity to work at the University of Glasgow, as the work presented in this thesis was carried out under a studentship granted from Dr. Martin's University of Glasgow Leadership Fellowship.

I would next like to thank my second supervisor Professor Sheila Rowan, as well as Professor Jim Hough, for their sound wisdom and eagerness to help whenever asked, no matter the query. They have set a premier example of enthusiasm, dedication, and pride in their management and operation of a large research group.

I am grateful for time spent with all the members of IGR and would like to thank Dr. Peter Murray for his help in the lab, for all the fun while travelling to conferences, and for the extensive editing help that was provided without being required of him. Thanks to Kieran Craig for showing me the ropes, to Richard Middlemiss for the endless procrastination and his unfailing ability to remain positive despite having never managed to beat me at squash in three years of playing, and to him and his better half Aliyssa Glen for being consummate hosts both during and after the PhD. Thanks to Jan Hennig for being a good sport about getting snookered, to him and Margot Phelps for all of the movies, and to him and Sean Leavey for the FIFA competition. Thanks to all of my officemates: Chris Bell, Becky Douglas, Valentina Mangino, Simon Tait, Mark Feltcher, Martin Hart, Hafizah Isa, Steven Bramsiepe and Sheena Barclay for making 427 great (except maybe Mark). I would also like to thank Dr. Liam Cunningham and Dr. Alan Cumming for their help in and around the labs and Prof. Stuart Reid for providing tantala coatings for this thesis and periodically popping his head in the

lab to say hello. I'll pour one out for Ally Houston, my fellow partner in professional degeneracy.

Others outwith IGR I would like to thank include Dr. Eric Yao for the masochistic task of managing Wednesday night football and the joyous task of managing the best Canadian demonstrator. Thanks to the whole of the aforementioned Wednesday night footballers, I'll be back to score an overhead goal someday, and to Gail Penny for the weekend hill walks and ruthless football tactics. I am grateful towards Professor Jodie Bradby and the rest of The Department of Electronic Materials Engineering at the Australia National University for hosting me in Canberra.

I would also like to thank those outside the science world who have been bedrocks of support throughout my time in Glasgow. Thanks to the Brentwood six and my AU brothers and sisters, all of whom I ghosted for four years. Thanks to my mom, Edith Matthai, for the trips home and the unfailing love, as well as for setting a strong example of how to carry oneself in the world, both professionally and away from work, and to Shawn and Paul Orme for the truly unmatched support during the final stages of the PhD. Finally, I am eternally grateful to my biggest cheerleader Mallory Orme, a lesser known saint who deserves more credit than I could possible give within this one document or a hundred more.

Preface

This thesis is an account of work carried out in the Institute for Gravitational Research (IGR) at the University of Glasgow between October 2013 and January 2018, focusing on the mechanical characterisation of dielectric thin-film coatings for use in future interferometric ground-based gravitational wave detectors.

Chapter 1 contains an introduction to gravitational waves and their astrophysical sources of origin. The current status of gravitational wave detectors is described, with a discussion of the primary noise sources limiting detector sensitivity. A summary of all detected gravitational wave signals is given as well.

Chapter 2 presents a more thorough look into coating thermal noise, focusing on the connection between mechanical dissipation within optical coatings and Brownian thermal noise in the detectors.

Chapter 3 describes coating deposition methods and the procedures used for characterising temperature-dependent coating mechanical loss, as well as the method for measuring the stress within a coating applied to a cantilever. Improvements to the mechanical loss data acquisition software used are also detailed, where the original program was created by Dr R. Nawrodt. Ellipsometry measurements of thermal oxide thicknesses presented in this chapter were performed by Mr. S. Tait.

Chapter 4 contains mechanical loss measurements of ion-beam sputtered SiO_2 after a number of post-deposition heat treatment temperatures and the loss of reactive low voltage ion-plated SiO_2 as deposited. Measurements of the coating as deposited and after 800 °C were carried out by the author with additional measurements made by Dr. I. Martin. All other heat treatments, uncoated control losses, and reactive low voltage ion-plated silica losses were measured by the author. Coating stress measurements were performed by the author, with assistance from Dr. K. Craig for the ion-beam sputtered silica sample deposited by the Commonwealth Scientific and Industrial Research Organisation. Characterisation of measurement uncertainties was performed with the help of Dr. C. Messenger, Dr. I. Martin, and Prof. J. Hough. Finite element modelling analysis of the connection between thermoelastic loss and

cantilever curvature was performed by Mr. M. Fletcher. All measurements within this chapter were made at the suggestion and under the guidance of Dr. I. Martin and Prof. S Rowan.

Chapter 5 presents the loss of two different thicknesses of ion-beam sputtered Al_2O_3. Measurements of the 505 nm coating as deposited were carried out by the author with assistance from Dr. I. Martin (as-deposited) and Dr. P. Murray (600 °C and 800 °C). Loss measurements of 2.02 µm alumina as deposited and after heat treatment at 300 °C, 600 °C, and 800 °C were performed by the author with assistance from Dr. P. Murray (600 °C and 800 °C). The 400 °C heat-treated 2.02 µm alumina data was acquired by Drs. I. Martin and P. Murray. All measurements within this chapter were made at the suggestion and under the guidance of Dr. I. Martin and Prof. S Rowan.

Chapter 6 contains mechanical loss measurements from a number of high refractive index coating materials. All coating loss measurements and analysis were performed by the author unless stated otherwise or specifically referenced in the text. The losses of 68% Ti:Ta_2O_5 as deposited and after the first 600 °C heat treatment were measured by Dr. P. Murray. The loss of 14% Ti:Ta_2O_5 was measured by Drs. K. Craig and M. Abernathy. Titania was measured as-deposited by Dr. P. Murray. Room temperature loss measurements of heat-treated 34.5% Zr:Ta_2O_5 were performed with assistance from Ms. A. Turner. Control samples used for loss analysis of the high index materials were measured with assistance from Drs. I. Martin, P. Murray, and K. Craig. Both the direct current magnetron sputtered Ta_2O_5 and 300 °C deposition temperature ion-beam sputtered Ta_2O_5 were provided by Prof. S. Reid and Dr. R. Birney. All measurements within this chapter were made at the suggestion and under the guidance of Dr. I. Martin and Prof. S Rowan.

Chapter 7 compares the estimated thermal noise of a number of multilayer coating designs based on the loss measurements from previous chapters and material properties from the literature. Quoted absorption measurements were performed by Dr. J. Steinlechner. All analysis was done by the author under the suggestion and guidance of Dr. I. Martin.

Appendix A shows the mechanical loss of silicon cantilevers manufactured through hydroxide catalysis bonding. The experiment was devised after conversations with Drs. K. Haughian, K. Craig, and P. Murray. Cantilever bonding was performed with Dr. M. Veggel and mechanical loss measurements were performed by the author with assistance from Dr. P. Murray. Optical profile measurements were performed with guidance from Dr. C. Bell, Dr. A. Cumming, and Prof. G. Hammond.

All coating mechanical loss analysis in Chapters 4 through 6 was conducted by the author (unless specifically referenced within the text), with characteristic times at

each temperature found through the use of ringdown fitting software written by Dr M. Abernathy.

Summary

Predicted by Einstein's General Theory of Relativity, gravitational waves are periodic fluctuations in the curvature of space-time that propagate at the speed of light and are caused by acceleration of asymmetric mass distributions. The first ever direct detection of gravitational waves was a signal originating from the final moments of a binary black hole inspiral and the subsequent merger. Four more black hole inspiral and mergers have been observed since the first detection, as well as the inspiral and merger of a binary neutron star system. These detections have provided a wealth of information about the black holes/binary stars from which the signals originate, and further detections will continue to both test General Relativity and provide ground-breaking insights into previously poorly characterised astrophysical systems.

The signals were detected by ground-based interferometric gravitational wave detectors. These instruments are comprised of two kilometre-scale arms arranged in an L-shape. A laser beam is split and travels the length of both arms and back before recombining. Under normal operation the recombined light has travelled an equal distance down each arm and destructively interferes. A passing gravitational wave will change the length of one arm relative to the other, resulting in an output signal. This change in interferometer arm length is in the order of $\sim 10 \times 10^{-20}$ m over a 4 km detector arm. The sensitivity of interferometric detectors is dependent on reducing numerous sources of noise.

A primary limiting noise source is the motion of the front face of test mass mirrors (which reflect the laser light within the detector arms) due to vibration from latent thermal energy in the highly reflective, multilayer coating materials. The power spectral density of this noise source is proportional to operation temperature and coating mechanical loss, which is a property describing energy dissipation within a material. Upgrades to current detectors, as well as proposed next-generation detectors, include operation at cryogenic temperatures to lower this thermally-induced noise. It is therefore crucial to know the low temperature mechanical loss of coating materials of interest for improving thermal noise within gravitational wave detectors. The

research presented focuses on mechanical loss and structural characterisation of coating materials with the goal of increasing the observational range of future gravitational wave detectors through reduction of coating thermal noise.

An introduction to gravitational waves, overview of astronomical sources, and discussion of the current, worldwide network of detectors and the sources of noise limiting their sensitivities is given in Chapter 1, which also contains a summary of all the detected signals up to this point. A more detailed discussion of coating thermal noise is given in Chapter 2, with a breakdown of the multiple forms of thermally-induced noise within test mass mirror coatings given, along with an explanation of the direct relation between mechanical loss and thermal noise.

Accurately characterising coating mechanical loss over a wide range of temperatures is valuable for both estimating thermal noise in next generation detectors and better understanding the links between coating structure and loss. The methods used for characterising coatings are discussed in Chapter 3 in addition to an overview of coating technologies. This chapter provides an explanation for the procedures behind the measurements presented throughout this thesis.

The mirror coatings used in current detectors are deposited via ion-beam sputtering and are comprised of alternating layers of high refractive index titania-doped tantalum pentoxide (Ti:Ta_2O_5) and low refractive index amorphous SiO_2. Chapter 4 contains a comprehensive study of the changes in mechanical loss of ion-beam sputtered silica with respect to post-deposition heat treatment, providing updated loss values for thermal noise estimation of current coatings and potential coating designs for future detectors. A peak in dissipation is observed at low temperatures and found to change location and shape with heat treatment, but the activation energy of this thermally activated peak remained constant. The minimum loss at low temperatures is found to occur after heat treatment at 600 °C, which is in contrast to the minimum loss at room temperature after 950 °C. The loss of a silica deposited by a new coating technique, reactive low voltage ion-plating, was found to be lower as-deposited than the 600 °C ion-beam sputtered silica. This technique involves deposition at over twice the temperature, so this loss result could be further evidence of high energy deposition techniques producing coatings with minimal distributions of two-level systems.

Chapter 5 contains measurements of Al_2O_3, a potential replacement for SiO_2 as the low refractive index coating material in multilayer coatings. The loss is found to be lower than 600 °C heat-treated SiO_2 by almost 50% at the low temperature peak but about four times higher at temperatures above 100 K. The loss of Al_2O_3 deposited at two different thicknesses (505 nm and 2.02 μm) exhibits minimal change in magnitude at temperatures below 40 K with heat treatment up to 800 °C. Heat treatment at 300 °C

reduces the loss above 40 K, but further heat treatment fails to produce significant reduction. In contrast, the coating stress for both thickness went from ∼475 GPa compressive stress to over 140 GPa tensile stress. This could suggest that there is no strong connection between low temperature mechanical loss and coating stress within Al_2O_3.

The high refractive index coating layers (Ti:Ta_2O_5) used in the advanced detectors are the dominant source of thermal noise within the highly reflective multilayer mirror coating at room temperature and has been shown to exhibit a peak in mechanical loss at cryogenic temperatures. Chapter 6 contains the mechanical loss characterisation of a number of alternate high refractive index coating materials. Increasing the titania doping percentage to 68% results in over an order of magnitude decrease in mechanical loss at temperatures below ∼100 °C after heat treatment, but the optical and structural properties require further study. Doping Ta_2O_5 with zirconium instead (34.5%) produces room temperature loss similar to Ti:Ta_2O_5 with heat treatments up to 600 °C with the added benefit of increased resistance to crystallisation. A decrease in loss with further heat treatment is expected with continued measurement. Measurements of pure TiO_2 show loss that decreases with heat treatment up to 300 °C, which is unexpected given evidence of crystallisation in titania coatings after annealing at 200 °C. The loss of reactive low voltage ion-plated silicon was measured and found to be lower than any previously measured ion-beam sputtered amorphous silicon (aSi) coating. Ta_2O_5 deposited by this same coating method did not display the same reduction compared to ion-beam sputtering seen with SiO_2 or aSi, with loss about 25% greater than ion-beam sputtered. Ta_2O_5 deposited through direct current magnetron sputtered did exhibit lower loss across all measured temperatures, but, with a measured absorption of ∼85 ppm, it is not competitive from an optical standpoint. All measured Ta_2O_5 coatings show a low temperature loss peak, but the peaks are not aligned with each other, ranging about 25 to 55 K. Calculations of the activation energies associated with each coating's peak are valuable for possible correlations between structural properties, mechanical loss, and deposition technique.

The mechanical loss characterisation from Chapters 3 through 5 are then summarised in Chapter 7, in which the coating Brownian noise is calculated for dual and multi-material coating stacks. All proposed coating combinations are compared to the estimated thermal noise of the mirror coatings in aLIGO and Advanced Virgo. Dual-material multilayer coating thermal noise estimates confirmed the value of Al_2O_3 as a low index material for detectors operating at temperatures within the silica loss peak, with a 20% and 25% reduction in Brownian noise at 10 and 20 K, respectively. The greatest reductions were seen with coatings where the high index material is amor-

phous silicon, which currently has absorption too high to use in a dual-material coating stack. Multi-material coatings have been proposed as a way to take advantage of these mechanical loss gains in light of the high absorption of aSi. The thermal noise estimate for the initial proposed coating design is updated based on new measurements of SiO_2 after heat treatment at 450 °C (the ideal annealing temperature for aSi absorption) and found to have significantly increased thermal noise. Replacing the SiO_2 with Al_2O_3 reduces the Brownian coating noise by 35% and 39% at 10 and 20 K, respectively, and is an immediately viable option as a low noise coating for future detectors. Continued research of reactive low voltage ion-plated coating materials is important; a speculative multi-material coating deposited by this method and assumed to have loss reductions through doping and heat treatment shows great promise, with estimated Brownian noise reductions of 31%, 33%, and 21% at 10, 20, and 123 K, respectively, compared to the current advanced detector multilayer coating.

Chapter 1

Gravitational wave detection

1.1 Introduction

First postulated by Albert Einstein in 1915 in his General Theory of Relativity, gravitational waves are periodically oscillating distortions in spacetime originating from acceleration of asymmetric mass distributions [1]. Einstein dismissed the possibility of direct measurement due to their extremely small physical effect in relation to measurement technology at the time, but on September 14th 2015 the Advanced Laser Interferometric Gravitational Wave Observatory (aLIGO) directly observed gravitational waves produced by the inspiral and merger of two black holes (a signal denoted GW150914), thus ushering in a new era of gravitational wave astronomy [2].

Gravitational radiation has an extremely weak interaction with matter, so large masses and accelerations, such as found in certain astrophysical events, are required to produce waves with amplitudes large enough to measure on Earth. In addition to the back hole inspirals and mergers already detected, possible sources of gravitational waves detectable by current instruments include supernovae, pulsars, binary neutron star systems, and the primordial gravitational wave background [3]. The weak nature of gravitation leads to advantages compared to observation techniques using electromagnetic radiation because gravitational waves are not as susceptible to scattering or absorption while propagating through the universe. Many cosmological and astronomical theories can be tested via gravitational wave observation, from the nature of the Universe a factor of $\sim 10^{49}$ earlier than that seen in the cosmic microwave background [3–5] to a significant increase in the knowledge of black hole formation and distribution [6, 7]. Furthermore, gravitational waves offer a completely new way to probe the Universe, so it is possible that brand new phenomena will be observed through regular observations.

Compelling evidence for the existence of gravitational waves was found through observations of the Hulse-Taylor binary pulsar system (PSR1913+16) whose orbital inspiral decay rate could not be fully explained through electromagnetic energy loss alone, and, instead, models for the orbital decay that included energy dissipation through gravitational wave emission were found to fit the observed inspiral pattern of the binary system [8, 9]. However, it was not until the direct detection of GW150914, and the subsequent detections of GW151226, GW170104, GW170608, GW170814, and GW170817 [10–14], that gravitational waves were unequivocally proven to exist.

The multiple direct observations came after approximately 50 years of gravitational wave detection research. Joseph Weber constructed the first detector in the 1960s, which consisted of a large aluminium bar with piezoelectric sensors in place to measure strains induced by passing gravitational waves [15]. There has since been significant advancements in detector technology, with resonant bar detectors being replaced by a worldwide network of Michelson interferometers with kilometre scale Fabry-Perot cavities as interferometer arms and broadband sensitivity [16–18]. For example, the aLIGO interferometric detector is designed to measure a change in arm length of $\sim 2 \times 10^{-20}$ m over a total length of 4 km within its most sensitive frequency range of $\sim$30-3000 Hz.

Current and future gravitational wave detectors are limited in their observational reach by a number of noise sources within and outwith the interferometers. The dominant noise sources include a fundamental limit stemming from quantum noise effects; gravitational coupling of the interferometer mirrors (test masses) with large masses in motion nearby; ground motion and anthropologically induced vibrations around the detector sites; and thermally induced motion in the interferometer optical components [16]. Technological and theoretical advancements in materials and interferometry have been implemented through several generations of detectors and have reduced the effects of the dominant noise sources to a level low enough for gravitational wave detection. Further improvements to detectors' sensitivity will increase the regularity with which gravitational waves are observed and thus significantly increase the science-scope of the detectors.

1.2 Gravitational wave radiation and its origin

1.2.1 The nature of gravitational waves

Gravitational radiation is comprised of transverse waves of strains in spacetime travelling at the speed of light and can be thought of as being analogous to electromagnetic

radiation in terms of their production; just as the acceleration of charge creates electromagnetic waves, the acceleration of mass produces gravitational waves. However, while electromagnetic radiation has complimentary positive and negative charges that can produce electric and magnetic dipoles, mass has no equivalent negative charge, which prohibits a dipole for gravitational radiation as a result of momentum conservation. While nothing prohibits higher order moments of mass distribution, gravitational waves are generally assumed to be quadrupolar, as this is the simplest polarity allowable by conservation constraints [19, 20]. The quadrupolar nature of gravitational waves results in emission only from acceleration of an asymmetric mass distribution, such as orbital bodies of differing mass in a binary system or the rotation of non-spherical bodies. Gravitational waves are typically emitted at twice the frequency of the system of origin.

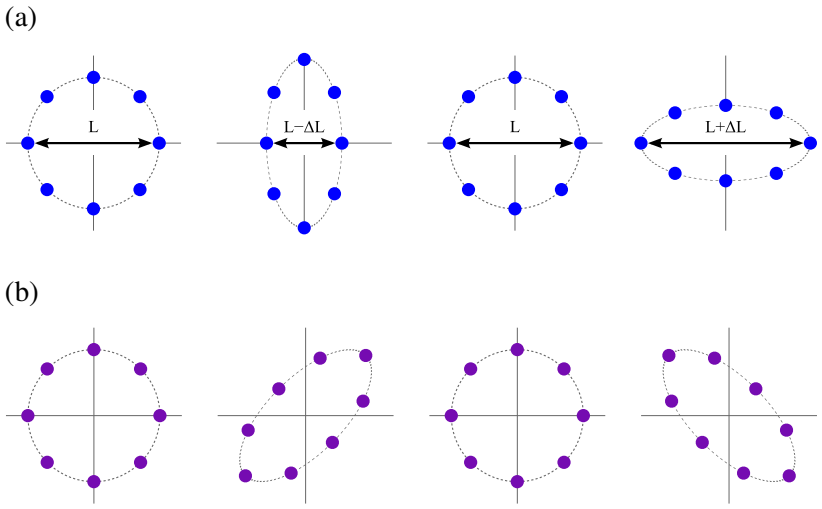

Fig. 1.1 Effect of an (a) h_+ and (b) $h_\times$ polarised gravitational wave passing perpendicularly through a ring of free-falling masses.

Gravitational radiation propagating through space-time produces differential strains in space corresponding to the specific polarisation of the quadrupolar moment, which can occur in either an $\times$ or + orientation. These strains can be visualised by considering a circular formation of free masses, as displayed in figure 1.1. The rings of masses, with diameter L in their original orientation, are subject to gravitational waves travelling perpendicular to the page and experience compression and extension, changing the diameter by ΔL as the wave passes. The amplitude, h, of the incident wave is given by

$$h = \frac{2\Delta L}{L}. \tag{1.1}$$

Producing a strain amplitude, h, large enough to measure is not feasible with man-made experiments* so potential sources of measurable gravitational wave radiation are astrophysical in nature, with masses and accelerations far exceeding anything possible on Earth. A number of astrophysical objects and systems are thought to produce gravitational waves, and are explained below.

1.2.2 Compact binary systems

The majority of stars exist in binary systems, which are deemed compact binary systems if there is one or more stellar remnant in the pair [22, 23]. A compact binary system will spiral inwards as a result of energy loss through emission of gravitational waves. This was observed over thirty years ago in the Hulse-Taylor binary pulsar system, which was found to have inspiral orbit characteristics matching a model of orbital energy loss corresponding to the emission of gravitational radiation [8, 9]. The orbital decay due to gravitational wave emission results in an increased orbital frequency, $f(t)$, characterised by [21]:

$$f(t) \approx 2.1\,\mathrm{Hz} \times M_{\mathrm{b}}^{\frac{5}{8}} \left(\frac{1\,\mathrm{day}}{\tau}\right)^{\frac{3}{8}}, \tag{1.2}$$

where τ is the time until the objects merge, and M_{b} is a parameter determined by the masses of the individual objects in the binary system, M_1 and M_2:

$$M_{\mathrm{b}} = \frac{(M_1 M_2)^{\frac{3}{5}}}{(M_1 + M_2)^{\frac{1}{5}}}\,. \tag{1.3}$$

The characteristic frequency change becomes important when estimating the strain amplitude measured on Earth from gravitational waves emitted by a compact binary inspiral at a distance d [24]:

$$h_{\mathrm{binary}} \approx 10^{23} \left(\frac{100\,\mathrm{Mpc}}{d}\right) \left(\frac{M_{\mathrm{b}}}{1.2\,\mathrm{M}_{\odot}}\right)^{\frac{5}{3}} \left(\frac{f}{200\,\mathrm{Hz}}\right)^{\frac{2}{3}}, \tag{1.4}$$

where $\mathrm{M}_{\odot}$ denotes solar mass. This continued orbital shrinkage and frequency increase creates a characteristic 'chirp' amplitude signal, where there is a long period of slowly rising amplitude and frequency followed by a sharp rise in both, corresponding to the moments just before the objects collide and merge. Compact binary systems are

*Sathyaprakash and Schutz have shown that a 10 m long beam with 1000 kg masses at each end rotating non-spherically at 10 Hz produces 20 Hz gravitational waves with an estimated amplitude of $\sim 10^{-43}$, which is $\sim$20 orders of magnitude smaller than the sources detectable by the most advanced gravitational wave detectors in operation [20, 21].

well-modelled, and the nature of the objects (whether neutron stars, black holes, or a black hole neutron star pair) can be determined from the change in amplitude and frequency during inspiral and coalescence.

Compact binary signals provide a wealth of astrophysical information. Determining the masses of the objects in the binary system will allow for updated population statistics for both black hole and neutron star systems. Coordination with electromagnetic observations can determine if binary mergers produce other forms of radiation, such as gamma ray bursts [25], and the near simultaneous detection of gravitational waves from a binary neutron star coalescence (denoted GW170817*) and a gamma ray burst (denoted GRB 170817A) from the same locality confirms that binary neutron star mergers can, in fact, create gamma ray bursts [26]. Measurements of a black hole binary system's final merger–occurring at highly relativistic speeds and in strongly warped spacetime–provides information on General Relativity and the nature of gravity, and measurements of a binary neutron system could provide information on the equation of state of nuclear matter [27, 28].

Inspiral sources serve as 'standard candles,' where distance can be determined accurately without a calibration or reference signal†, and known distances from many observed systems can provide density maps and, therefore, galaxy localisation. When combined with optical redshift measurements, this provides a method for determining the Hubble constant [3, 24]. This was successfully performed with the joint gravitational and electromagnetic wave observation of GW170817, which resulted in a measured value of roughly $70\,\mathrm{km\,s^{-1}\,Mpc^{-1}}$ for the mean expansion rate of the Universe [29].

1.2.3 Burst sources

Burst signals originate from singular acts of large acceleration and typically last less than one second. For example, supernovae resulting from gravitational collapse of highly evolved star cores have the potential to create bursts of gravitational waves if the events are asymmetric in mass distribution [30]. Most of the energy released during these events is released in the form of neutrinos, but a gravitational wave burst amounting to less than 1% of the total energy in these systems would produce strains large enough for measurement by ground based interferometric detectors [3]. Similarly, if the mass of a white dwarf surpasses the Chandrasekhar limit through disc accretion

*See section 1.7 for more information on GW170817 and other gravitational wave detections.

†If the time dependence of both the frequency and amplitude of the signal are measured, then the distance of the system can be calculated from the intensity of the detected gravitational waves [3].

it will collapse into a black hole, emitting a burst of gravitational waves due to the high rate of rotation during collapse [31].

Due to the complexity of the physics involved in core collapse, there are no robust theoretical models for their emission of gravitational wave signals [20]. The detectors, therefore, operate in an 'ears wide open' analysis configuration, which entails broadband searches for transient events in the data differing from known baseline interferometer sensitivities and data glitches. Operating multiple detectors simultaneously provides further, more robust confirmation of coherent signals without any prior knowledge of a specific waveform or predetermined area of the sky over which to search [27, 32].

The all-sky search algorithms optimised for finding un-modelled sources in the detector data were the first to trigger a signal alert for GW150914 [33]. While the observed event was two inspiralling black holes, the final merger of any compact binary system results in a burst signal. As expressed in equations 1.2 and 1.4, the coalescence 'chirp' is created by a sharp increase in frequency and amplitude, which appears as a transient/burst signal in the detector data. The well-modelled inspiral characteristics can then be found in the seconds prior to the flagged burst signal.

The burst signal created by both single astronomical objects collapsing/exploding and multiple objects coalescing is expected to create a secondary signal in the form of gravitational wave memory, which is the permanent distortion of spacetime following the peak in strain accompanying a burst of gravitational waves [34–36]. In the case of an inspiral this can be seen as a gradual increase in test mass displacement within the interferometer while the bodies' orbital period decreases, followed by a peak in strain energy and test mass movement, and then a return to an equilibrium distance different from the initial test mass separation. Interferometric detector test masses have elastic components that return the mirrors to their initial position, thus hindering direct observation at a signal to noise ratio acceptable for confirmation. However, increased population statistics for black hole mergers due to recent observations opens the opportunity to sum subthreshold signals and confirm detection [37, 38], and successful operation of a space-based gravitational wave detector, which would have truly free-floating test masses, would circumvent this issue and directly display the permanent test mass displacement [39].

1.2.4 Neutron stars

The rotation of neutron stars, whether isolated or in a binary pair, can result in the emission of long-lived, nearly sinusoidal, and consistent gravitational radiation [27,

40]. These signals are typically much weaker than theorised burst signals and transient events already observed, but the long term consistency inherent in the emitted gravitational radiation allows for integration over very long time scales and, therefore, an observable signal within the baseline noise of interferometric detectors [41].

Neutron stars emit gravitational waves if there is axial-asymmetry, which is likely to originate from either the formation of the neutron star or its interaction with other objects. Irregularities in the neutron star crust caused by the freezing and densification of a parent star could provide enough axial asymmetry to radiate a significant amount of gravitational waves [3]. Similarly, precession of the neutron star caused by a mismatch between the rotational axis and the axis of symmetry will result in gravitational wave emission [42]. The 'sloshing' of the fluid interior of neutron stars in the high spin rate of their early formation produces rotational instability with characteristic oscillations (r-modes), resulting in gravitational wave emission [43]. Neutron stars in low mass x-ray binary systems may accrete enough matter from their partner star to reach a spin rate high enough to excite these r-modes [44, 45]. Added mass through accretion in x-ray binary systems may also lead to axial asymmetry of the neutron star, which would lead to gravitational wave emission [3]. Finally, a strong magnetic field can cause bulging at the poles, causing the neutron star to lose energy via gravitational wave radiation during rotation [46]. The gravitational wave frequency varies according to the type of emission. For example, detection of waves at a frequency (f_{GW}) four thirds that of the rotational frequency (f_{rot}) indicates r-mode contribution, $f_{\mathrm{GW}} \approx f_{\mathrm{rot}}$ points towards precession as a significant contributor, and $f_{\mathrm{GW}} = 2f_{\mathrm{rot}}$ corresponds to triaxial ellipsoid neutron star, such as one distorted by a strong magnetic field [47].

The long-term integration* required to extract continuous wave signals from interferometric detector data requires a targeted frequency approach; computational priority is assigned to pulsars and x-ray binary systems with known emission frequencies. The rotational frequency of a pulsar is determined through electromagnetic observation, which can also supply the distance and sky location. The upper limit of observable gravitational wave strain from a given pulsar, called the spin-down limit, is calculated from the values attained through electromagnetic observation via:

$$h_0^{sd} = \left(\frac{5}{2} \frac{G I_{zz} |\dot{f}_{\mathrm{rot}}|}{c^3 d^2 f_{\mathrm{rot}}} \right)^{\frac{1}{2}}, \tag{1.5}$$

*During LIGO science run S6 and Virgo runs VSR2 and VSR4, the interferometric ground-based detectors Enhanced LIGO and Virgo produced a combined total of 410 days of data over which to integrate [48].

where G and c are the gravitational constant and speed of light, respectively, I_{zz} is the principle moment of inertia (canonically assumed to be $10^{38}\,\mathrm{kg\,m^2}$), d is the pulsar distance, f_{rot} and $|\dot{f}_{\mathrm{rot}}|$ are the pulsar frequency and the first derivative of the pulsar frequency with respect to time [41, 48]. Equation 1.5 assumes all rotational kinetic energy loss of a specified pulsar is converted into gravitational wave emission.

The 144 days of strain data from aLIGO's first observational run (O1) was searched at twice the rotational frequency of possible gravitational wave signals from 200 different pulsars known to fall within the sensitive frequency band of the detectors. No pulsar signals were detected, but a non-detection at the frequency of a known pulsar gives a measured upper limit of expected gravitational radiation emission amplitude by that pulsar at its characteristic frequency. For eight known pulsars, including Crab and Vela, the measured upper limit from O1 was below the calculated spin-down limit [41]. The increased strain sensitivity of future aLIGO observation runs will add pulsars to the eight already found to have constrained maximum gravitational wave amplitudes.

1.2.5 Stochastic background

A large number of weak, unresolved, uncorrelated astrophysical events combine to form the stochastic gravitational wave background (SGWB), which can be detected by correlating the outputs of multiple detectors [49–51]. Analogous to the Cosmic Microwave Background (CMB) for electromagnetic radiation, the SGWB is comprised of remnant gravitational waves from the early universe. Whereas the CMB is a view of the universe from roughly 10^5 years after the Big Bang, the primordial portion of the SGWB is comprised of gravitational wave signals as far back as 10^{-35} seconds after the Big Bang [3].

The SGWB is comprised of a multitude of possible sources: redshifted signals from the rapid expansion of quantised gravitational fields in the moments after the Big Bang [52], unresolved coalescences of binary black hole or neutron star systems [53], cosmic strings [54], rotating neutron stars [55], cosmological phase transitions in the early universe [56], and supernovae [57]. Detecting the stochastic background requires multiple detectors, as the signal is extremely difficult to separate from a single detector's baseline noise. Cross-correlating multiple detector data streams eliminates independent detector noise and allows searching for characteristic SGWB sources. Each theoretical source is predicted to have unique power spectral contributions to an overall background signal. The strain amplitude is thought to be [58]:

$$h_{\mathrm{GW}} = 4 \times 10^{-22} \sqrt{\Omega_{\mathrm{GW}}} \left(\frac{100\,\mathrm{Hz}}{f} \right)^{\frac{3}{2}} \frac{1}{\sqrt{\mathrm{Hz}}}\,, \tag{1.6}$$

where Ω_{GW} is the dimensionless, frequency independent gravitational wave energy density in a closed universe. The frequency independence of Ω_{GW} is due to the predicted flatness of the signal across the sensitive frequency band of ground-based interferometric detectors. Any concurrent observational runs will produce data pertaining to the stochastic background [59]. Advanced LIGO's first observational run resulted in significant improvements to the measured upper limit of energy density for both an isotropic and anisotropic picture of the SGWB [60, 61].

1.3 Gravitational wave detection

1.3.1 Resonance-based detectors

Joseph Weber proposed the first gravitational wave detectors in the late 1950s and operated two of them in the late 1960s [15, 62, 63] The detectors operated on the principle that a passing gravitational wave would excite the vibrational modes of a large bar [15, 64]. Any vibrations in the detector mass are converted to an electric signal through piezoelectric transducers. The bars have a very narrow frequency range for detection based on the resonant frequencies of the detector mass, so they are only able to detect signals from local supernovae or pulsars with rotational periods in the milliseconds [65]. Weber claimed a number of coincident events as signals, but around a dozen different research groups across the world* operated room temperature resonant bar detectors in the decades following Weber's original experiment and none succeeded in detecting gravitational waves, leading to Weber's results to be determined unverifiable and, thus, invalidated [66, 67].

The next generation of resonant bar detectors sought to improve strain sensitivity by cooling the bars in order to reduce noise caused by thermal vibrations [68]. Most cryogenic bar detectors were very similar, consisting of a ~ 2 tonne, $\sim$3 m long aluminium bar cooled to temperatures on the order of mK [69]. At the peak of cryogenic resonant bar sensitivity, five detectors combined to reach a collective strain sensitivity varying from 10^{-21} to 10^{-20} for frequencies between 850 Hz and 960 Hz but did not detect any gravitational waves [70, 71]. The narrow sensitive frequency band and insufficient sensitivity improvement have led to decommissioning of all resonant bar detectors [70, 72–74]. There are, however, two cryogenic spherical

*The Institute for Gravitational Research at the University of Glasgow was one of these groups.

resonant detectors still funded, named Mario Schendberg (Brazil) and MiniGRAIL (Netherlands) [75, 76].

1.3.2 Interferometric detectors

Shortly after Weber published his resonance-based detector design Gertsenshtein and Pustovoit [77] proposed an alternate gravitational wave detector in the form of an optical interferometer. Arguing that the sensitivity of the electromechanical readout was far worse than Weber claimed, they postulated that a Michelson interferometer using the new 'laser' would provide significant improvements to sensitivity [77]. An independent realisation of the advantages of an interferometric design came from Weiss, following the theoretical work of Pirani [78, 79].

A basic Michelson interferometer, as shown in figure 1.2, consists of a light source, beam splitter, end mirrors, and photodetector. Light passes through the beam splitter and is sent down each interferometer arm. The light reflects back towards the beam splitter, where it recombines and is sent to the photodetector. The interference pattern of the recombined light carries information about the relative change in length of the interferometer arms. The arms of the interferometer will expand and contract with displacement ΔL when a gravitational wave passes perpendicular to the plane of the interferometer, as was shown in figure 1.1, and the resulting change in length is registered as a characteristic interference pattern by the photodetector along the output path. Current interferometric detectors use techniques improving upon this basic Michelson design (discussed in section 1.5), but even the simple design shown in figure 1.2 gives the advantage of broadband operation, something not possible with single resonance bar detectors.

The first working prototype interferometric detector was built in Malibu, California at the Hughes Research Lab in the early 1970s; it had a folded beam path with an effective arm length of 8.5 m and was shot noise limited with a ∼45 mW helium neon input laser [80, 81]*. Improved prototypes were constructed in the years following, all utilising argon lasers: a 3 m prototype was built in Germany at the Max Planck Institute for Astrophysics in Garching, followed in the early 1980s by a 30 m instrument [82, 83], and a 1 m prototype was built in the late 1970s in Scotland at the University of Glasgow and upgraded to a 10 m interferometer in the early 1980s [84, 85]. This was followed shortly by the construction of a 40 m interferometer at Caltech [86]. Prototypes were also built in Japan and at MIT in the 1990s [87–89]. The successful

*see section 1.5.1 for an explanation of beam path folding and section 1.4.1.1 for information regarding shot noise

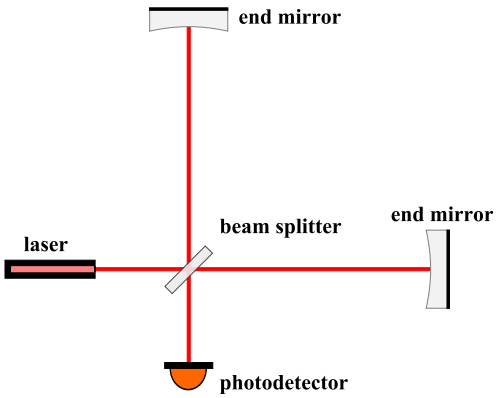

Fig. 1.2 A basic Michelson interferometer, where a laser beam is split and then recombined by a beam splitter after reflection from end mirrors. A photodetector measures the recombined light.

operation and technological advances of these multi-generation, small scale prototype interferometers led to construction in the early 1990s of the first full scale (600 m - 4 km) interferometric gravitational wave detectors, discussed further in section 1.6.

1.4 Limiting noise sources in interferometric detectors

Interferometric gravitational wave detectors are limited in their strain sensitivity by a number of sources deriving from both fundamental physical limits and technological road blocks. Over the past ~ 45 years of interferometer prototyping, operation, and refinement, detector strain sensitivity has increased by over six orders of magnitude*. The sources discussed in this section are the current limiting factors in pushing that sensitivity even further.

Figure 1.3 is the predicted noise performance for aLIGO at design sensitivity. It is a good representation of these dominant noise sources in all interferometric detectors, but hardware and configuration differences between detectors will alter the relative effects of each source. A number of interferometric techniques have been developed to mitigate some of the noise sources, as will be discussed in section 1.5.

*Forward's HRL prototype reached a strain noise level of $\sim 3 \times 10^{-16}\,\mathrm{Hz}^{-\frac{1}{2}}$. Advanced LIGO's noise curve reached $\sim 1 \times 10^{-23}\,\mathrm{Hz}^{-\frac{1}{2}}$ during O1

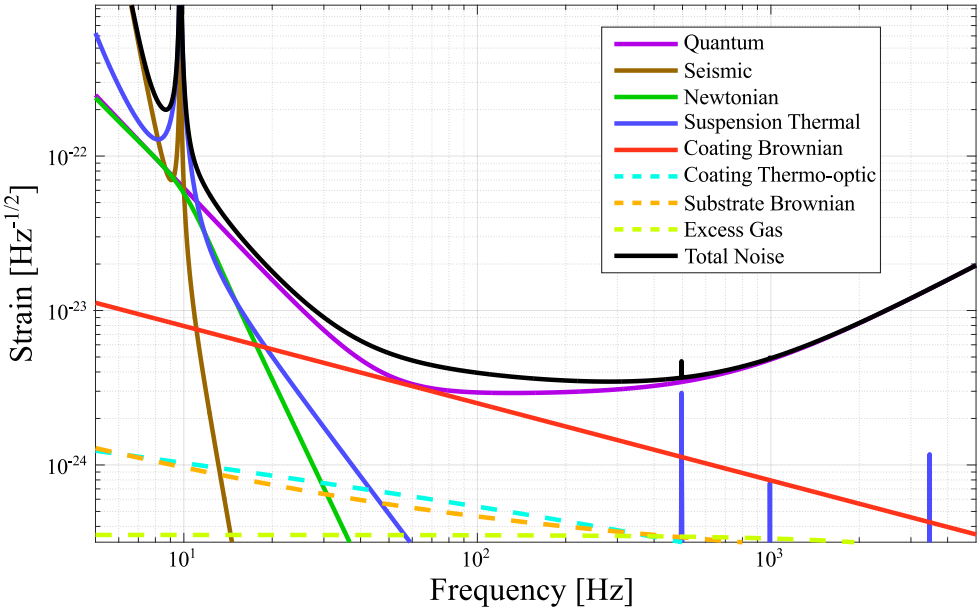

Fig. 1.3 Advanced LIGO noise at design sensitivity in strain per $\sqrt{\text{Hz}}$ for the most sensitive frequency band of the detector and an input laser power of 125 W. 'Coating Brownian', 'Substrate Brownian', and 'Coating Thermo-optic' noise sources are all sub-categories of thermal noise.

1.4.1 Quantum noise

Quantum noise describes the fundamental sensitivity limit created by trade-off between photon shot noise and radiation pressure noise, two independent noise sources that combine to form a standard quantum limit based on the Heisenberg uncertainty principle [90]. Quantum noise is a primary limiting noise source above $\sim$10 Hz for ground-based interferometric gravitational wave detectors (purple line in figure 1.3).

1.4.1.1 Photon shot noise

Photon shot noise arises from the fluctuation in photoelectric current created at the interferometer output port due to the statistical variation in the number of incident photons. Interferometric detectors are operated near a 'dark' interference fringe, which means that the photodetector receives very little light during operation. The number of photons (N) that result in a detected photocurrent over given measurement time are assumed to follow a Poisson distribution, which leads to a $\sqrt{N}$ uncertainty. This uncertainty can be shown to place a displacement sensitivity limit, δx_{shot}, on Michelson interferometers that is defined by [91]:

$$\delta x_{\text{shot}} = \left(\frac{hc\lambda\Delta f}{8\pi^2 P \cos^2(\theta/2)} \right)^{\frac{1}{2}} \tag{1.7}$$

where h is Planck's constant, c is the speed of light, λ is the laser wavelength, P is the laser power, θ is the phase difference between the light beams in each interferometer arm, and Δf is the bandwidth defined as $\frac{1}{2t}$, where t is the observational time. It can be seen that the displacement limit from photon shot noise can be lowered by increasing the laser power, or increasing the observation time, both of which effectively decrease the $\sqrt{N}$ uncertainty.

1.4.1.2 Radiation pressure noise

Radiation pressure noise is the error in test mass position sensing due to the transfer of momentum from the light in the interferometer to the test mass upon reflection. Radiation pressure within a Michelson interferometer causes a differential displacement sensitivity limit, δx_{rad}, that can be shown to be [91]:

$$\delta x_{\text{rad}} = \left(\frac{8Ph\Delta f}{m^2 \omega^4 c \lambda} \right)^{\frac{1}{2}} \tag{1.8}$$

where m is the mirror mass and ω is angular frequency. The displacement effects of radiation pressure can be seen to reduce with increased operation frequency, mirror mass, and, laser wavelength.

Unlike shot noise, it is not immediately apparent from where the statistical uncertainty arises with regards to radiation pressure noise. Radiation pressure in a simple Michelson can be thought of as originating from anti-correlated intensity changes in the interferometer arms, which results in differential forces on the test masses and an ensuing uncertainty regarding their positions. One possible reason for differential arm intensity is the statistical uncertainty in the photon distribution at the beamsplitter; photons are independently redirected to either interferometer arm and thus create a necessarily anti-correlated binomial distribution of N, which results in a varying radiation pressure proportional to $\sqrt{N}$ [92].

1.4.1.3 Standard quantum limit

The Standard Quantum Limit (SQL) is a limit in interferometer sensitivity stemming from the Heisenberg uncertainty principle and created by tuning input power such that radiation pressure and shot noise are minimised ($h_{\text{shot}} = h_{\text{rad}}$) at a certain frequency [93, 94]. Equations 1.7 and 1.8 are relatively simple derivations of shot and radiation pressure noise that assume the two effects are uncorrelated. A more rigorous, quantum look into radiation pressure and photoelectron shot noise in an interferometer shows the origin of the two to be the unintended injection of zero-point fluctuations in the

vacuum field via the interferometer output port; if the entering vacuum fluctuations are in-phase with one of the detector arms, then they will necessarily be out of phase with the other arm and create an anti-correlated fluctuation in arm intensity [95]. In this case the laser light is in a coherent state upon reaching the beamsplitter and radiation pressure noise comes from uncertainty in the amplitude quadrature, or real component of the laser light due to the incoherence injected via vacuum fluctuations. Shot noise would then arise from the uncertainty in the phase quadrature, or imaginary part of the interferometer light, which is displayed as quantum fluctuations in the number of photons at the output port.

The SQL is a fundamental sensitivity limit in current interferometric detectors, but it can be lowered by altering the relative noise quadratures in an injected vacuum. This is known as squeezing, and is discussed in more detail in section 1.5.3. Alternatively, if correlations can be introduced between the two quadratures then the SQL ceases to be a fundamental limit. Optical springs are an example of such forced correlations, where the optical cavity and mechanical systems are coupled [93, 96].

Measurement sensitivities well below the SQL at low frequencies can also be reached by creating an interferometer that produces a signal proportional to the speed of the test masses rather than their position [97]. These quantum nondemolition interferometers, also known as speed meters, are an alternative to the current Michelson interferometric gravitational wave detector design and are under development. For more information see [98–102].

1.4.2 Gravitational gradient noise

Gravitational gradient noise arises from direct gravitational coupling between test mass mirrors and mass density fluctuations in the surrounding area [103–105]. Also known as Newtonian noise, this fundamental noise source is a limiting noise source at low frequencies ($\leq$10 Hz) and is shown in figure 1.3 as a green line. Ambient seismic Rayleigh waves are the primary source of fluctuating gravitational fields causing mirror perturbations, but Newtonian noise is also created by human activity in the area surrounding the detector, transient atmospheric mass density changes, clouds passing over the detector, ocean and ground water dynamics, and wind-born objects striking the interferometer buildings [106–108].

The mirrors cannot be shielded or isolated from fluctuating gravitational fields, so the only solution for minimising Newtonian noise are to choose a low noise detector location and actively measure the gravitational field changes in the area surrounding the detector. The Japanese Kamioka Gravitational wave detector (KAGRA) and the

proposed European Einstein Telescope (ET) both use underground locations as a way to minimise the effects of gravitational gradients as seen on the surface. Operating the interferometers underground allows for far greater control and isolation from human-induced gravitational fluctuations, leaving seismic waves as the dominant source. The effect of seismic waves is expected to reduce exponentially with depth by $\sim e^{-4d/\lambda}$, where d is the depth and λ is the wavelength of the seismic wave. Operating a detector at 600 m underground reduces the seismic gravitational gradient noise by about a factor of ten at 1 Hz [106]. Another option is to operate the detector in space, entirely absent from the effects of earth-based gravitational field fluctuations, as is the plan for LISA, a European Space Agency run mission scheduled for launch in 2030* [110].

Another option for suppressing gravitational gradient noise, and the only one available to above-ground detectors already in operation, is to subtract measured fluctuations in the local gravitational field around the detectors in real time [106, 111]. This requires a network of seismometers placed around the detector to measure the seismic motion. The coupling effects of the gravitational gradients on the test masses are then modelled and subtracted from the detector output signal. It should be noted that this has yet to be tested on a detector but is under active research and development [112].

1.4.3 Seismic noise

Seismic noise is the primary sensitivity limitation below 10 Hz for ground-based detectors and originates from mechanical coupling between ground motion at the detector site and the test masses within the interferometer; it is represented in figure 1.3 as a brown line. Below 1 Hz seismic noise is dominated by a 'micro-seismic background' stemming from oceanic weather systems, where energy is transferred from the atmosphere to the ocean floor and then to the detector through surface waves in the ground; the increase in off-shore winter storms results in a strong seasonal dependence and locations near coastlines see an increase in the micro-seismic background due to their proximity to ocean waves crashing on the shore, with peaks at 80 mHz and 160 mHz [107, 113]. Wind and human activity are responsible for seismic noise at frequencies between 1 Hz and 10 Hz. Ideal detector sites are those isolated from major population centres due to anthropological seismic noise. The LIGO Livingston detector, for example, can lose ∼40 min of data acquisition time due to logging freight-trains passing roughly every day along a railroad track 7 km south of the detector [114].

*There is also a proposed space-based Japanese detector, DECIGO, which is currently still in the early stages of proof-of-concept [109].

A location on Earth deemed to have relatively low seismic noise still has an omnidirectional noise spectrum of $\sim 10^{-7} f^{-2}\,\mathrm{m/Hz^{\frac{1}{2}}}$ [21]. This means that, in order to detect GW150914, which displaced the aLIGO test masses by $\sim 4 \times 10^{-18}$ m, the seismic noise required reduction by at least eight orders of magnitude for the start of the waveform at 35 Hz and at least seven orders of magnitude for the merger signal at 150 Hz. Active and passive vibration isolation systems are implemented within the detectors to achieve the required suppression of seismic noise.

Isolation from horizontal motion is achieved through suspension of the test masses at each end of the interferometer arms. The horizontal displacement of a hanging mass in a single stage pendulum is proportional to $1/f^2$ for frequencies above the resonant frequency of the pendulum (f_0), thus providing significant decoupling between horizontal seismic and test mass motion at high frequencies. This effect can be augmented by adding further pendulum stages above the suspended mass, as it can be shown that a stacked pendulum system of N stages has a transfer function of [21]

$$\frac{x}{x_\mathrm{g}} \approx \left(\frac{f_0}{f}\right)^{2N}, \tag{1.9}$$

where x is the displacement of the mass at the end of the N stage pendulum and x_g is the horizontal ground motion. Similarly, vertical motion coupling is reduced by suspending the pendulum system from a multi-stage system of springs [115]. Each ground-based interferometric detector has a unique suspension design, but they all employ this pendulum-spring combination to provide significant isolation from seismic motion [16, 18, 40, 116, 117].

Passive damping reduces seismic noise above $\sim$10 Hz, but active, feedback-driven systems are needed to attenuate pendulum/mechanical resonances within the test mass suspensions and mitigate mirror motion at frequencies near the microseismic peak. For example, Virgo utilises an extremely effective multi-stage passive isolation suspension system (also known as the 'superattenuator') to suppress seismic noise at frequencies above 4 Hz, but below this threshold the mechanical resonant frequencies within the components of the superattenuator prohibit detector lock acquisition [118]. Active inertial damping prevents the ring-up of these resonances and minimises other, very low frequency motion. Advanced LIGO's suspension is not as robust at very low frequencies, and thus relies solely on active seismic isolation in this range [119]. This active isolation is often in the form of a feedforward control system using low-noise inertial sensors to register movement in the suspension stages and activate actuators to counteract the detected motion.

1.4.4 Thermal noise

Thermally driven motion at the molecular level within the test masses, suspensions, and mirror coatings combine to form a dominant source of noise in the most sensitive frequency band of interferometric detectors (shown as red, blue, cyan and orange in figure 1.3). Similar in nature to Brownian or Johnson noise, thermal noise originates from the $\frac{3}{2}k_{\mathrm{B}}T$ of thermal energy in each atom of a solid in thermal equilibrium*. This intrinsic thermal motion has the potential to excite resonant modes of the test mass coatings and suspensions, as well as the bulk of the test masses themselves. The magnitude of thermal noise contributions from each source is determined by the intrinsic mechanical energy dissipation of the material, as well as the heat-flow damping, or thermoelastic loss, of the components [120].

Mechanical loss†, ϕ, is a material property that, among other things, determines energy storage characteristics around resonant frequencies. Lowering the mechanical loss of an otherwise identical system results in broadband reduction in thermal displacement noise at the cost of increasing the energy storage, and thermal noise, at the resonant frequencies of the material. Therefore, it is advantageous for interferometric detectors to use materials with extremely low mechanical loss as test masses, suspensions, and mirror coatings. Fused silica has been shown to have intrinsically low mechanical loss, which is one of the reasons it is the test mass material used in all room-temperature interferometric detectors [87, 121].

Fused silica is also an ideal material for suspension fibres, as it can be heated and pulled to create ultra-thin, low-loss fibres, which can then be welded to the test mass, creating an extremely low loss monolithic silica test mass and suspension as the final pendulum stage [122, 123]. Previous suspension designs, such as those for the initial LIGO detectors, consisted of metal wire loops cradling the test mass and were designated from the start to be redesigned due to their high thermal noise [124]. Silica fibres have the added benefit of negating suspension thermoelastic noise when under an optimum magnitude of stress‡ [125, 126].

A more thorough explanation of thermoelastic loss and mechanical dissipation, specifically with regards to the highly reflective optical coatings used on the test masses, is given in Chapter 2.

*$\frac{1}{2}k_{\mathrm{B}}T$ in each degree of freedom

†Mechanical loss is equivalent to the inverse of the dimensionless quality factor, Q.

‡A stress of 175 ± 13 MPa was found by Bell et. al. to be optimum for cancelling thermal expansion and, therefore, thermoelastic noise within a silica fibre. The 40kg aLIGO test masses are suspended by four, predominantly 800 µm diameter fibres, corresponding to ∼195 MPa.

1.5 Interferometric techniques

A number of improvements to the basic Michelson interferometer shown in figure 1.2 have been developed in order to improve detector sensitivities. As mentioned in section 1.3.2, increasing the beam path directly magnifies the observed change in length from a passing gravitational wave. This extension can come in the form of lengthening the interferometer arms, but the Earth's curvature, along with geological and anthropological obstacles, prevent the practical construction of interferometric detector arms longer than a few kilometres. Folded and delay line interferometer configurations are two techniques to extend the effective beam path length and increase the exposure to gravitational waves without physically lengthening the arms. As discussed in section 1.4.1.3, increasing the power stored in the arms also improves detector sensitivity but only up to the standard quantum limit, which can be altered with the injection of squeezed light into the signal.

1.5.1 Optical path folding and Fabry-Perot cavities

Extending the interferometer arms is the simplest manner by which light-storage time is increased, but lengthening the travel time of the beam through manipulation of the optical path achieves the same outcome without the pitfalls of beam tube extension. The optical path can be folded by having the mirror at the end of each arm angled to reflect the laser light back through the length of the beam tube towards an end mirror near the beam splitter, thus doubling the round-trip length of the arms. This configuration is utilised by the German English Observatory (GEO) 600 to create a round-trip arm length of 2400 m within 600 m beam tubes [127]. Figure 1.4a shows this mechanical folding technique.

Another way to fold the beam path is to create an optical delay line, as displayed in figure 1.4b. Optical delay lines, which were first proposed by Herriott *et al* in 1964 and suggested for use in gravitational wave detectors by Weiss in 1972, are created by using curved mirrors to reflect the laser light a number of times between input and end mirrors before reading the signal [78, 82, 128]. The light enters and exits the arms through small holes in the input mirror, and hits different parts of the mirrors with each trip up and down the beam tube. A number of prototype interferometric detectors utilised optical delay lines, but scattering of the laser light hampered the sensitivity [82–84].

An alternative method is to use resonant optical cavities as interferometer arms. One suitable optical cavity configuration is the Fabry-Perot cavity, which creates

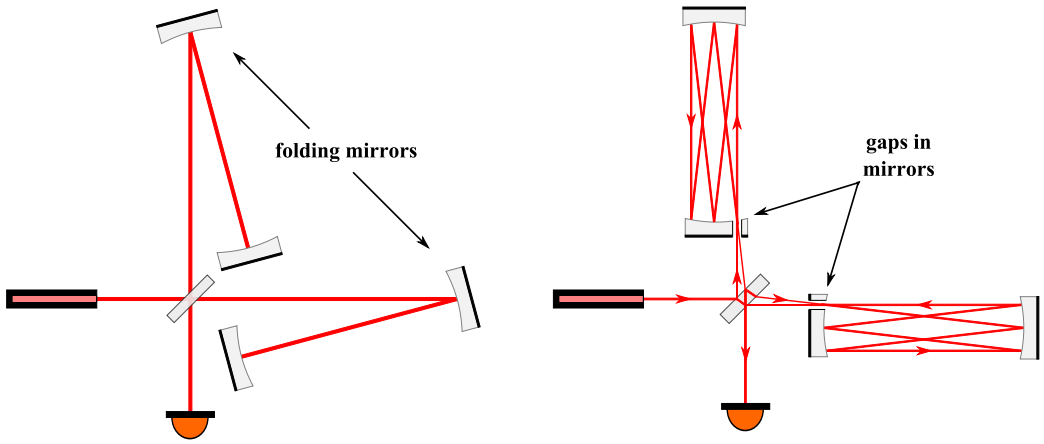

(a) Folded interferometer arms (b) Herriott multi-pass optical delay line

Fig. 1.4 Simplified schematic diagrams of two variants of folded Michelson interferometer.

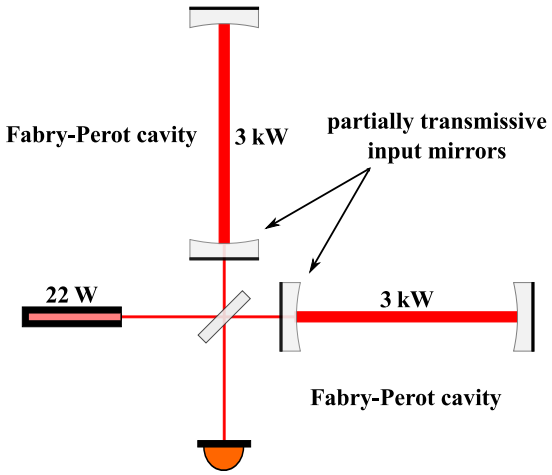

Fig. 1.5 Michelson interferometer with Fabry-Perot resonant cavities as the interferometer arms. The cavity power shown is based on aLIGO's arm cavity power buildup of a factor of ∼270 [129].

resonance through continuous reflection between parallel mirrors [130]. Fabry-Perot interferometers were used as highly sensitive long-line strain meters as early as 1972, and a number of the second generation prototype interferometers utilised Fabry-Perot cavities as detector arms [85, 86, 88, 130, 131]. All current ground-based detectors–except for GEO 600–are configured with Fabry-Perot resonant optical cavities spanning the full arm length, as shown in figure 1.5. Partially transmissive input mirrors allow the input laser beam to enter the beam tube, where it reflects continuously back and forth upon itself between the input and end mirrors before leaking out through the input mirror. This optical cavity is held on resonance to create a significant power buildup, the magnitude of which is dependent on the number of 'bounces' the light makes in the arm, which is dependent on optical properties of the input and end mirrors.

Fabry-Perot Michelson interferometers require additional control systems to remain locked on resonance. They are susceptible to parametric instability–a positive feedback loop of energy transfer between optical modes of resonant cavities and elastic modes of interferometer test masses–which leads to an upper limit for power storage in the arm cavities without attenuating measures* [133]. Even with these issues, Fabry-Perot optical cavities are the preferred design for current and future ground-based detector arms due to the strain sensitivity benefits of both increased light storage time in the arms and greater optical power.

1.5.2 Power and signal recycling

It can be shown that operating a Michelson interferometer so that the output is very close to a dark fringe results in the optimum signal-to-noise ratio [91]. In this configuration the interferometer acts as a mirror, with nearly all of the input light returning† to the laser. Placing a mirror with the correct transmission in front of the laser creates a resonant cavity between that mirror and the input test masses. If controlled properly, this results in no light returning to the laser; the beam exiting the arm cavities builds power in the power recycling cavity, which then pumps up the optical power within the detector arms [134]. A power-recycled Michelson interferometer is shown in figure 1.6a, with example power amplification for the resonant cavities.

*Parametric instabilities were observed for the first time in kilometre scale interferometric detectors during aLIGO's first observational run. Those instabilities observed were quelled by thermally tuning the optical cavity resonance, and the extra modes occurring at higher operating power are thought to be controllable through application of this method in combination with other mitigation techniques [132].

†Some of the input light is lost to scatter and absorption within the optical layout, as well as a small amount of transmission through the end test mass.

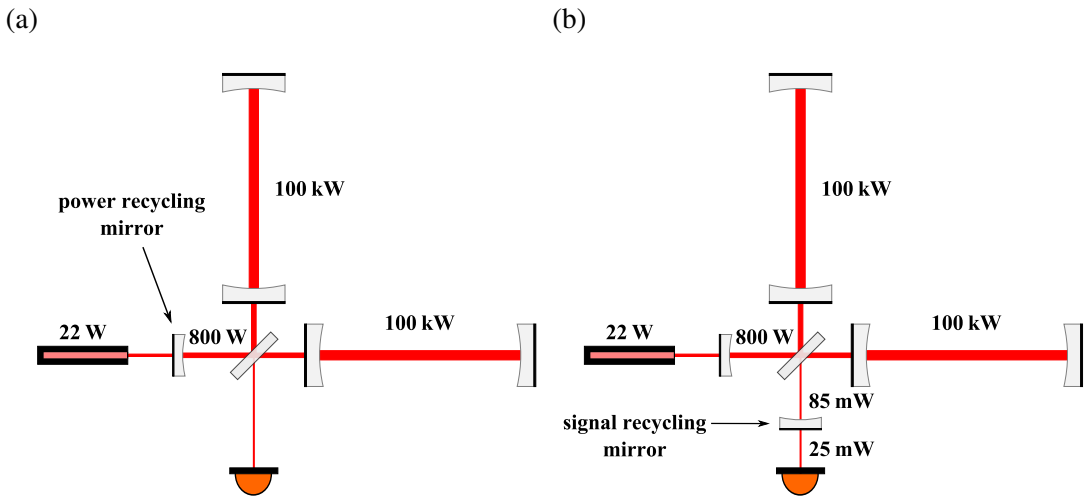

Fig. 1.6 Simplified schematic diagrams of Michelson interferometers with Fabry-Perot arm cavities and (a) power recycling and (b) both power and signal recycling (dual recycling). Beam power levels in each section of the interferometer are shown to highlight the gains from power recycling. Power levels match those in aLIGO for O1 ($\sim$ 8 times lower than designed power) [129].

Adding a partially transmissive mirror to the output signal, as shown in figure 1.6b, will create a resonant cavity between this 'signal recycling' mirror and the interferometer and boost output signal strength in a similar manner to how the power recycling mirror increases laser power with a resonant cavity between the input port and the interferometer [135–137]. As previously noted, the output port should receive no light when the interferometer is operating and there is no change in detector arm length. In the event of a signal incident upon the detector the primary, carrier wave remains resonant within the Fabry-Perot arms and it is the sidebands created by the gravitational wave that exit towards the photodetector. The addition of a signal recycling mirror returns these sidebands to the cavity arms where they resonate, increasing in size before returning to the photodetector.

The bandwidth over which a signal will be recycled back into the interferometer is determined by the reflectivity of the recycling mirror, and the centre of the frequency band is set by the length of the cavity formed between the recycling mirror and the interferometer [92]. The performance of the detector can therefore be optimised via signal recycling to create a very narrow peak sensitivity (detuned) or operate with broadband recycling (tuned) to increase sensitivity over a large bandwidth [138]. Improvement over a narrow bandwidth is advantageous for targeted searches of continuous gravitational wave sources, and gains in broadband sensitivity are beneficial for transient, 'chirp' signals. Dual recycling was first demonstrated successfully on a

large scale in GEO 600 [137], and all current ground-based interferometric detectors are designed to operate with dual recycling.

1.5.3 Squeezing

Squeezed states of light are nonclassical light fields with reduced uncertainty in a particular quadrature of the light's complex amplitude at the expense of increased uncertainty in the other quadrature. For a light field in either a coherent or a vacuum state, with complex amplitude $a = \hat{X} + i\hat{Y}$, where $[\hat{X}, \hat{Y}] = \frac{i}{2}$, the variance of the amplitude and phase quadratures ($\Delta^2\hat{X}$ and $\Delta^2\hat{Y}$) is at a minimum when $\Delta^2\hat{X} = \Delta^2\hat{Y} = \frac{1}{4}$ because the Heisenberg uncertainty principle limits the variants in the form $\Delta^2\hat{X}\Delta^2\hat{Y} \geq \frac{1}{16}$ [139, 140]. A squeezed state describes a class of uncertainty states where the minimum quantum noise is preserved without equal variance in phase or amplitude, eg $\Delta^2\hat{X} < \frac{1}{4}$ and $\Delta^2\hat{Y} > \frac{1}{4}$ or $\Delta^2\hat{X} > \frac{1}{4}$ and $\Delta^2\hat{Y} < \frac{1}{4}$. Figure 1.7b shows a squeezed vacuum state where the uncertainty in the amplitude has been lowered below the minimum of the ground state at the expense of a larger phase uncertainty; the ground state can be seen in figure 1.7a.

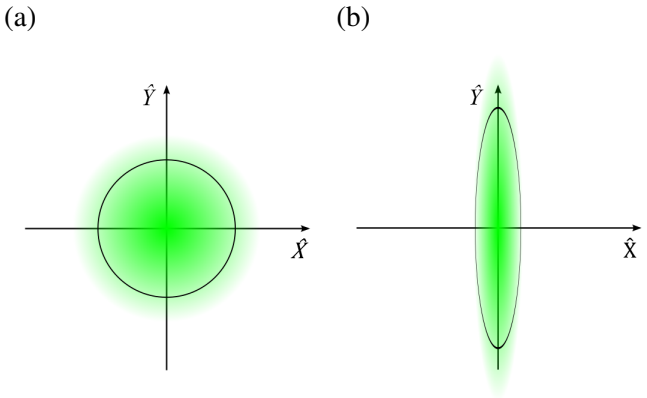

Fig. 1.7 Time independent Wigner probability functions for dark port modulation states. The green gradient represents quasi-probability, where a darker shade corresponds to a higher probability. (a) is the zero-point vacuum state. (b) is a squeezed vacuum state. Coherent laser light would match the shape and probability distribution of the vaccuum state in (a), but offset from centre in relation to the complex amplitude of the source.

As mentioned in section 1.4.1.3, radiation pressure noise and photoelectron shot noise in a Michelson interferometer correspond to amplitude and phase fluctuations in the vacuum electromagnetic field entering the dark port, ie $\Delta^2\hat{X}$ and $\Delta^2\hat{Y}$. It has been proved that injecting a squeezed vacuum state into a interferometer dark port reduces

either the shot noise or radiation pressure noise depending on the angle of the squeezed state [96, 141–145]. Furthermore, successful detector operation with injected squeezed light over an extended period of time has been demonstrated in GEO 600, where ~ 200 days of operation utilising squeezed vacuum occurred over the course of 11 months of data-taking [146, 147]. In addition to being the first application of non-classical, quantum states in an operational measurement device, the successful implementation of squeezed light in GEO 600 shows the sensitivity limitations determined by the SQL can be lowered and future interferometric detectors can tune their most sensitive regions based on the angle of the injected, squeezed vacuum.

1.6 Current state of gravitational wave detectors

A worldwide network of second generation, kilometre scale interferometric detectors will shortly be in a state of concurrent operation. The second generation detectors are based on almost fifty years of research and development in smaller scale interferometers and around twenty years of experience with full scale detectors. A greater spread in instruments across the Earth results in much better sky localisation for a source wave[148], so the detectors are built around the world, with two kilometre scale detectors in the USA, one each in Italy and Japan, and a slightly smaller detector in Germany. There are also multiple detectors designed for future construction, which when completed will push sensitivity limits even further. Figure 1.8 shows the target strain sensitivity for current and future interferometric detectors, which will be discussed in detail in the following sections.

1.6.1 GEO

GEO 600 is a British-German collaborative laser-interferometric gravitational wave detector located $\sim$20 km south of Hannover. Construction of GEO 600 began in 1995 based on experience with prototype interferometers at the University of Glasgow and the Max Planck Institute for Quantum Optics in Garching, with the first science runs taking place in 2002 [127]. The interferometer arms are 600 m, with mirrors suspended via monolithic silica fibres and configured to fold the beam path within each arm so there is a 2400 m round-trip interferometer length. The short length of the arms compared to other interferometric detectors necessitated implementation of advanced techniques in order to reach similar sensitivity levels. The successful operation of first generation GEO 600 proved the validity of a number of novel interferometer components and techniques now used in other, advanced detectors: triple pendulum

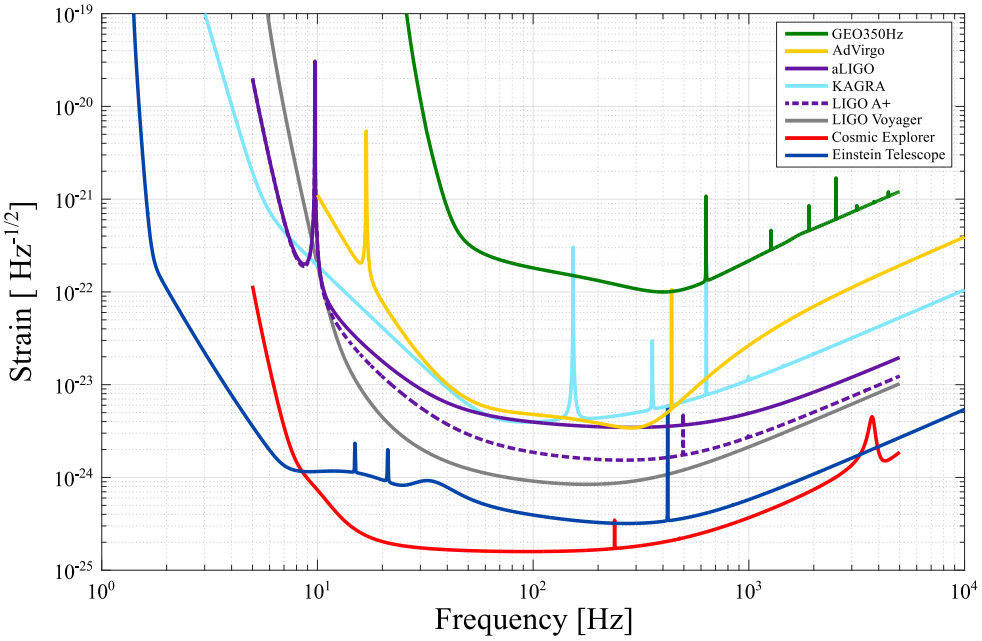

Fig. 1.8 Characteristic strain sensitivity for current and future ground-based gravitational wave detectors. Curve data for aLIGO, A+, Voyager, CE, and ET is from [149]; GEO 600 and KAGRA curve data is from [150] and [151], respectively. The space-based LISA has been left out for clarity, as it is most sensitive in the millihertz range.

mirror suspensions with the final, silica test mass stage monolithically suspended with welded silica fibres (attached to the test mass via hydroxide catalysis bonding) reduced low frequency noise and thermal noise [122, 127]; electrostatic drives suspended behind test masses provided cavity length control for rapid interferometer locking and stable operation; ring heaters behind the folding mirrors corrected aberration stemming from differing mirror radii of curvature [152]; and signal recycling increased the power within the arms and provided frequency specific tuning of the interferometer [135].

GEO-HF is the name given to a multi-stage set of upgrades that began in 2009 with the goal of increasing detector sensitivity above 500 Hz [153]. The most significant of these upgrades is the addition of a squeezed light source to the signal output port [146]. GEO 600 now uses squeezed light in its normal operational mode and has proven the effectiveness of squeezing by doubling the volume of the universe observable to GEO 600 without an increase in detector glitches [147]. Squeezing is an area of continued research and improvement, but its success in GEO 600 will result in its inclusion in future upgrades for other, advanced detectors.

GEO 600 contributed to a number of joint observational runs in the first generation gravitational wave detector network, and it remained in operation on 'Astrowatch' mode while the other detectors were offline for commissioning second generation

upgrades [154]. However, GEO 600 cannot match the broadband sensitivity of aLIGO and the other second generation detectors as they come online. The future of GEO 600 could include operational validation of future, novel interferometer technologies or operation under targeted frequency tuning to sacrifice broadband effectiveness in order to greatly increase sensitivity over very narrow bandwidth [155].

1.6.2 Advanced LIGO

The Laser Interferometer Gravitational-Wave Observatory (LIGO) is comprised of two interferometric detectors built in the late 1990s ∼3000 km apart in the USA [58]. The LIGO Hanford Observatory (LHO) is located in Washington state and was built with a 4 km and a 2 km interferometer (H1 and H2) housed within the same ultra-high vacuum beam tube. The LIGO Livingston Observatory is in Louisiana and has one, 4 km interferometer (L1). Both sites are shown in figure 1.9. The detectors were intended from the start to undergo multiple generations of upgrades, with detection thought likely to occur only after improvements to initial design sensitivity (iLIGO) [124]. Initial LIGO began operation in the early 2000s, reached design sensitivity in 2005, and operated in a data taking capacity until 2007. The detectors then underwent an intermediate upgrade known as Enhanced LIGO (eLIGO) and operated for a one year science run prior to the major upgrades associated with Advanced LIGO [156].

Fig. 1.9 Aerial views of the 4 km arm-length LIGO observatory sites in Hanford, Washington (left) and Livingston, Louisiana (right) [157].

The iLIGO configuration consisted of power recycled Fabry-Perot Michelson interferometers, with 1064 nm, 10 W Nd:YAG lasers providing 20 kW arm cavity power in H1, 15 kW in L1, and 10 kW in H2 [58]. The detectors used 10.7 kg, 25 cm diameter fused silica test masses suspended by a single loop of metal piano wire and reached a peak sensitivity of $\sim 2 \times 10^{-23}\, 1/\mathrm{Hz}^{1/2}$ around 110 Hz [156]. The

mirrors were coated with alternating layers of silica (SiO_2) and tantala (Ta_2O_5), which were chosen due to their low absorption and scatter when combined in a highly reflective stack optimised in thickness for the 1064 nm wavelength laser light in the cavities [158].

The eLIGO upgrades were installed from 2007 to 2009 and aimed to both double the sensitivity of the LIGO detectors and prove the effectiveness of subsystems essential for the aLIGO upgrade. A number of optical systems needed upgrading due to a tripling in laser power from iLIGO to eLIGO; the increase in power required a redesign of the thermal compensation system to mitigate the rise in thermal lensing and replacement of the input optics to handle ∼30 W [159]. The output port of the detectors saw a major upgrade, with the addition of an output mode cleaning cavity and a switch from a radio-frequency heterodyne detection system to a DC homodyne readout [160]. eLIGO successfully operated in a data-taking capacity for about a year (science run S6) before shutting down for comprehensive upgrades at both detector sites [156].

The switch to the second generation detector aLIGO began in 2011 and was completed with the start of O1 in the second half of 2015. aLIGO keeps the same facilities shown in figure 1.9, but replaces all of the interferometer components. LHO* and LLO have identical 4 km dual recycled Fabry-Perot interferometers with up to 750 kW cavity arm power from 125 W of input laser power [16]. The test masses are now 34 cm in diameter with a mass of 40 kg, monolithically suspended via welded, fused silica suspension fibres, and suspended from an improved vibration isolation system. Coating thermal noise was found to be a limiting source of noise in initial LIGO, with the high refractive index Ta_2O_5 layer dominating the noise contribution of coating stack [158, 161–163]. A lower mechanical loss high index material, 25% titania doped Ta_2O_5 (25% Ti:Ta_2O_5), replaced the pure tantalum pentoxide coating layer in the multilayer stack in order to reduce coating thermal noise for aLIGO[164, 165].

Advanced LIGO has yet to fully reach its designed strained sensitivity (as seen in figure 1.3), which is a factor of 10 greater than iLIGO at 100 Hz, which corresponds to a factor of1000 increase in the observable universe and includes a shift in the low frequency sensitivity limit from ∼40 Hz to ∼10 Hz [16]. Even at partial design sensitivity, aLIGO has already provided the first ever direct measurements of gravitational

*H2 was initially planned to be upgraded and remain in Hanford, but the components are now allocated for installation in India (see section 1.6.5.1 for information on LIGO India).

waves [2], as well as five other confirmed gravitational wave signals discussed in greater detail in section 1.7*.

1.6.3 Advanced Virgo

Advanced Virgo is the second generation upgrade to the 3 km long Virgo detector located in Cascina, Italy and run by a consortium that includes Italy, France, Holland, Poland, and Hungary. The new detector is designed to have a factor of ten improvement in sensitivity compared to the first generation Virgo detector [17, 166, 167]. Primary upgrades included welded silica suspension fibres for thermal noise reduction, an increase in laser power and Fabry-Perot arm cavity finesse, thermal compensation heaters to correct lens/mirror aberrations, an improved vacuum system to reduce residual gas noise, 25% Ti:Ta_2O_5/SiO_2 test mass mirror coatings, and signal recycling (now a dual recycled Michelson) [17]. The upgraded infrastructure will also allow for squeezing to be added as a possible later improvement [168]. As mentioned in section 1.4.3, Advanced Virgo has greater low frequency sensitivity than other second generation detectors due to its unique superattenuator seismic isolation and suspension system, which is comprised of five clusters of maraging steel suspension springs prior to the penultimate suspended test mass [118]. While it was not operational during advanced LIGO's first observational run (O1) or the beginning of O2, the advanced Virgo detector joined in data taking operations from August 1st, 2017 until the end of the second observation run on August 25th, 2017 and successfully detected two gravitational wave signals, GW170814 and GW170817† [169].

1.6.4 KAGRA

Japanese interferometric gravitational wave detection efforts began in the 1990s with the construction of TAMA 300, a 300 m Fabry-Perot Michelson interferometer that incorporated power recycling shortly after its initial, successful operation [170]. Upgrades to the seismic isolation system were carried out in 2005 (TAMA-SAS), but TAMA 300 was decommissioned shortly afterwards in order to focus efforts on the next generation Japanese prototype detector, the Cryogenic Laser Interferometer Observatory (CLIO) [171]. CLIO was completed in 2006 after four years of excavation and construction in the Kamioka Mine and is a non-recycled Fabry-Perot Michelson

*Subsequent rounds of detector upgrades are planned for the aLIGO sites as well as the construction of a new, third generation detector, both of which will be discussed in section 1.6.5.1.

†See section 1.7 for discussion of detected signals

interferometer with 100 m cavity arms and sapphire test masses suspended with aluminium fibres [171, 172]. CLIO demonstrated partial cryogenic detector operation and the corresponding reduction in thermal noise, but is currently not operational, with hardware and manpower shifted to the construction of Japan's first kilometre scale interferometric detector [173].

Previously referred to as the Large-scale Cryogenic Gravitational wave Telescope (LCGT), the KAmioka GRavitational wave detector (KAGRA) will be the culmination of years of tests and innovations at TAMA300 and CLIO. KAGRA is to be an underground, dual recycled Michelson interferometer with 3 km Fabry-Perot arm cavities and sapphire test masses cooled for operation at 20 K [18]. The detector is currently in the baseline KAGRA (bKAGRA) stage, after successful room temperature locking of a simplified version of the final interferometer design, dubbed initial KAGRA (iKAGRA). The goal of bKAGRA is to reach design sensitivity by upgrading in a number of phases, the first of which is to keep simplified output and input optics but demonstrate operation with cryogenic end test mass mirrors [174, 175].

1.6.5 Future detectors

1.6.5.1 LIGO-based detectors

As mentioned in 1.6.2, the components earmarked originally for upgrading the 2 km Hanford interferometer from eLIGO to aLIGO were set aside for construction of a full-scale aLIGO interferometer outside the United States due to the scientific benefits of increased spacing between detectors, e.g. improved detection confidence and source parameter measurements [176]. The first site chosen was near Perth, Australia, but lack of funding resulted in the decision to build the detector in western India, which still results in a factor of ~ 3 improvement in sky localisation of a detected signal [148]. The project is spearheaded by the Indian initiative in Gravitational-wave Observations (IndIGO) and LIGO India has been approved for construction by the Indian government and should be operational by 2020 [177–179].

The LIGO sites in Hanford and Livingston are still working towards reaching aLIGO design sensitivity, but there are already multiple stages of planned upgrades to the current interferometers. The immediate round of upgrades is called A+ and involves two discrete stages: the implementation of frequency dependent squeezing followed by the replacement of the test masses and suspensions along with a larger beam size within the cavities [180]. The first stage is tentatively planned for installation after the

completion of aLIGO's second observation run around mid 2017. A+ is then expected to operate for two to three years before beginning the second stage of upgrades [181].

The second stage of planned upgrades still requires years of research and development before implementation. Frequency-dependent squeezing has been shown to be successful in large scale interferometers with GEO 600 (as mentioned in 1.5.3), but to meet design sensitivity more consistent operation and greater levels of squeezing is needed. The new, larger test masses require a redesign of the suspensions and changes to the seismic isolation stages, and the larger beam size requires further stray-light controls as well as studies regarding parametric instabilities in the new system. Most notably, the test mass mirror coatings are planned to be upgraded in the second stage of A+ and there is no current viable improvement to the 25% Ti:Ta_2O_5/SiO_2 multi-layer coatings already in use in aLIGO (see chapter 2).

Following a number of years of coincident operation at A+ sensitivity, the LIGO detector sites are scheduled to undergo major facilities upgrades around 2025 and house a third generation detector called LIGO Voyager [181, 182]. Voyager is the last planned upgrade to the current LIGO vacuum enclosure, and it represents a significant departure from previous LIGO instruments with operation at cryogenic temperatures. It is meant to operate as LIGO's most sensitive detector design until the proposed construction of Cosmic Explorer (CE), a third generation gravitational wave detector built outwith current LIGO facilities [181]. The preliminary, optimistic, CE design consists of 40 km dual recycled Fabry-Perot interferometer arms with 2 MW of circulating power from a 220 W, 1550 nm laser. The design also proposes silicon test masses cooled to 123 K and operation with 10 dB of squeezing* [183].

1.6.5.2 ET

The Einstein Telescope (ET) is a proposed European third generation gravitational wave detector currently in a state of research and development following a European Commission conceptual design study [40]. ET is designed to push the limits of technologies and experience gained through two generations of interferometric detector operation. It will be constructed between 100 m to 200 m below ground and consist of three detectors, each having two independent, dual recycled Michelson interferometers with 10 km Fabry-Perot cavities for arms. The three dual interferometer, 10 km detectors are designed to fit together in a triangle, as shown in figure 1.10a. This tri-V detector configuration significantly improves the directional sensitivity and allows for

*squeezing is characterised by the percentage gain sensitivity, as seen by improvement in signal to noise ratio in decibels.

measurement of gravitational waves passing through the same plane as the detector, something current L-shaped interferometric detectors cannot resolve [184].

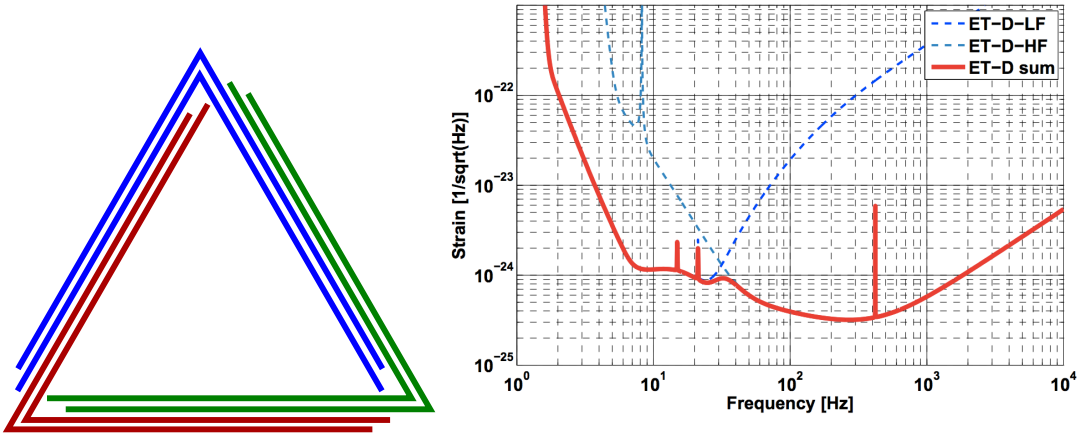

(a) (b)

Fig. 1.10 (a) The tri-V detector configuration for ET, with each detector (red, blue, and green) rotated 120° relative to one another. Each arm contains both a high and low frequency optimised interferometer, resulting in six individual V-shaped interferometers. (b) Combined strain sensitivity (ET-D-sum) for the low and high frequency (ET-D-LF and ET-D-HF) interferometers within each of the three V-shaped detectors, as reproduced from [40].

The advantage of a dual interferometer configuration is shown in figure 1.10b. Each interferometer is optimised for detection of sources at different frequencies, increasing the total sensitive bandwidth of the detector. One interferometer is designed to have peak sensitivity from ∼30 Hz to ∼10 kHz and be operated at room temperature using 60 cm diameter, 200 kg fused silica test masses with a proposed 3 MW of optical power in the arm cavities. The other interferometer is designed to be most sensitive from ∼1.5 Hz to ∼30 Hz and have silicon test masses* cooled to 10 K, an operating power of 18 kW at 1550 nm in the arm cavities, and detuned signal recycling in order to improve sensitivity over a narrow frequency band. Significant research and development is required to realise the proposed design for ET; among other technical challenges, mirror coatings with over an order in magnitude less thermal noise contribution are required to reach the proposed ET sensitivity limits.

*The size of the silicon test masses will be determined by manufacturing limits, but are tentatively designed to be >40 cm and ∼200 kg.

1.6.5.3 LISA

The Laser Interferometric Space Antenna (LISA) is a European Space Agency led space-based interferometric gravitational wave detector planned for launch in 2030. LISA consists of three identical spacecraft, each containing two free-falling test masses, oriented in an equilateral triangle with 2.5×10^6 km sides [110]. Three separate interferometers are created by the 2 W 1064 nm lasers within each spacecraft. Each vertex of the triangle creates a two-arm Michelson interferometer with the other two spacecrafts in the triangle, measuring the change in separation between the drag-free floating test masses [185]. Each spacecraft housing the test masses and optical benches is equipped with control and propulsion systems to ensure a purely gravitational orbit for the test masses. Figure 1.11 shows the spacecraft orientation and the planned orbit of LISA, which was chosen to minimise fluctuation in vertex angles and spacecraft separation distances while remaining close enough for effective communication [110].

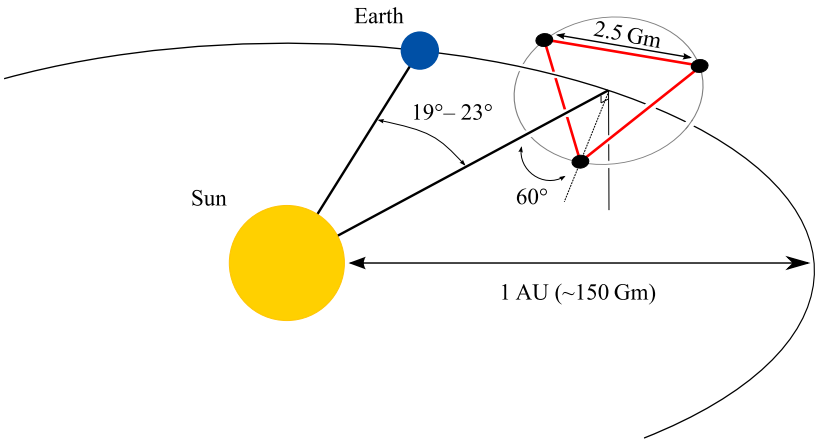

Fig. 1.11 LISA orientation and orbit (not to scale) [110].

LISA's design requirement is to be sensitive to gravitational waves with frequencies between 100 µHz and 0.1 Hz, with the goal of being sensitive between 20 µHz and 1 Hz. This frequency range will allow LISA to observe signals well below the frequencies measurable with ground-based detecters such as the inspiral and merger of supermassive black holes in the range of $\sim 10^3$ solar masses ($M_\odot$) to 10^6 $M_\odot$ and cosmological stochastic background signals [92]. Binary black hole systems whose merger would be observed by ground-based interferometers could potentially inspiral with frequencies previously in the LISA range, which could put LISA in the position of predicting merger observations for detectors on Earth weeks and months prior to their arrival [186].

The critical technologies required for the operation of LISA were tested with the launch of LISA Pathfinder in December of 2015 [187, 188]. The mission was an

enormous success, with LISA Pathfinder measuring an amplitude spectral density for frequencies between 0.7 mHz and 20 mHz five times lower than its mission goal and within a factor of about 1.25 of the requirement for LISA. LISA Pathfinder provided the proof of concept for viable space-based gravitational wave detectors.

1.7 Gravitational wave detections

The detection of gravitational wave signals by aLIGO represents a groundbreaking achievement in precision measurement, an extremely valuable chance to look into the nature of black holes, and a historic confirmation of the existence of gravitational waves. Six gravitational wave signals have been directly measured to date* Five of the signals match theoretical gravitational wave patterns originating from a binary black hole coalescence [2, 10, 11, 13, 14] and the other signal matched the predicted pattern of a binary neutron star coalescence [13].

The first gravitational wave ever directly measured was GW150914; on September 14$^{\text{th}}$ 2015 at 09:50:45 UTC the peak in spacetime strain from the merger of two black holes was seen at the aLIGO observatory in Livingston, Louisiana and seen 7 ms later at the observatory in Hanford, Washington [2]. The signal originated from the final inspiral and coalescence of a binary black hole system at a luminosity distance of $\sim$410 Mpc, or 1.37×10^9 ly. The black holes reached a peak orbit velocity of 180 000 km s^{-1} before merging and producing a single, final black hole. The periodic signal from the decaying orbit first entered the detectors' frequency band at 35 Hz and, with about 8 cycles over 0.2 ms, increased in frequency to 150 Hz, when the peak strain amplitude associated with the merger occurred [2]. The strain amplitudes and frequencies with respect to time for GW150914 can be seen for both the Hanford (H1) and Livingston (L1) detectors in figure 1.12. This detection is one of the great scientific achievements of this century and marks the start of gravitational wave astronomy.

The properties of this first detection, and those of the subsequent five confirmed detections, are given in table 1.1. The primary and secondary masses in table 1.1 refer to the size of the black holes in the binary system, and the final mass refers to the size of the black hole formed by the merger of the primary and secondary black holes. The chirp mass is one of the primary parameters used for calculating the black hole masses, and is defined as [193],

*A candidate signal, denoted LVT151012, was also measured but determined to be below the confidence level needed to unequivocally label it a detection. Its gravitational signal was consistent with a binary black hole inspiral and merger [189].

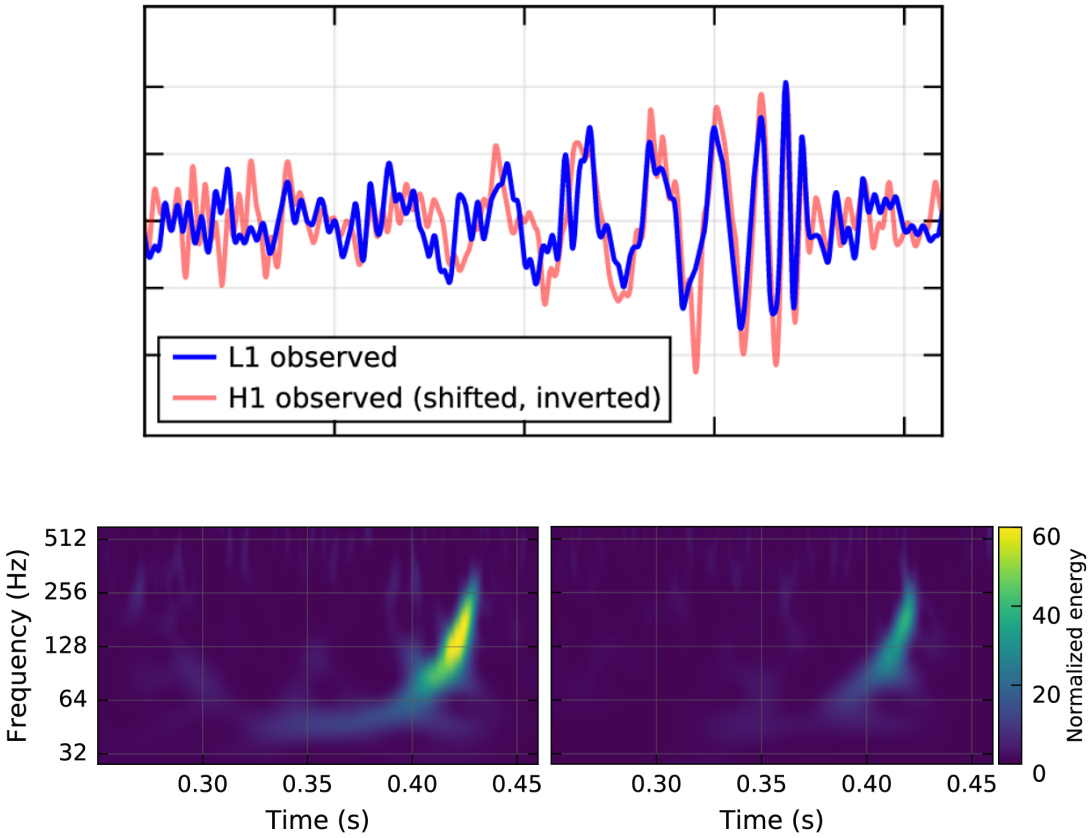

Fig. 1.12 Strain versus time (top) and frequency versus time (bottom: left H1, right L1) at the LIGO detectors during the observation of GW150914 [2]. The strain signal can be seen clearly within the noise of the detector due to the large amplitude of the incident wave. Both detectors show the characteristic frequency increase of a merging binary system.

Table 1.1 Properties and confidence levels of the five detected black hole coalescences and one detected binary neutron star coalescence [2, 10–14, 190, 191]. There tends to be a large uncertainty in luminosity distance because it is inversely proportional to the amplitude of the signal, which is also affected significantly by the binary's orbital inclination [192]. False alarm rate is reported with respect to how many years of continuous detector operation would be required before a false event of the same characteristics of the signal would occur.

	GW150914	GW151226	GW170104	GW170608	GW170814	GW170817 (BNS)
Primary mass, m_1 ($M_\odot$)	$36.2^{+5.2}_{-3.8}$	$14.2^{+8.3}_{-3.7}$	$31.2^{+8.4}_{-6.0}$	12^{+7}_{-2}	$30.5^{+5.7}_{-3.0}$	$1.36-2.26$
Secondary mass, m_2 ($M_\odot$)	$29.1^{+3.7}_{-4.4}$	$7.5^{+2.3}_{-2.3}$	$19.4^{+5.3}_{-5.9}$	7^{+2}_{-2}	$25.3^{+2.8}_{-4.2}$	$0.86-1.36$
Chirp mass, $\mathscr{M}$ ($M_\odot$)	$28.1^{+1.8}_{-1.5}$	$8.9^{+0.3}_{-0.3}$	$21.1^{+2.4}_{-2.7}$	$7.9^{+0.2}_{-0.2}$	$24.1^{+1.4}_{-1.1}$	$1.188^{+0.004}_{-0.002}$
Final mass, M_f ($M_\odot$)	$62.3^{+3.7}_{-3.1}$	$20.8^{+6.1}_{-1.7}$	$48.7^{+5.7}_{-4.6}$	$18.0^{+4.8}_{-0.9}$	$53.2^{+3.2}_{-2.5}$	–
Radiated GW energy ($M_\odot c^2$)	$3.0^{+0.5}_{-0.4}$	$1.0^{+0.1}_{-0.2}$	$2.0^{+0.6}_{-0.7}$	$0.85^{+0.07}_{-0.17}$	$2.7^{+0.4}_{-0.3}$	>0.025
Luminosity distance, (Mpc)	410^{+160}_{-180}	440^{+180}_{-190}	880^{+450}_{-390}	340^{+140}_{-140}	540^{+130}_{-210}	40^{+8}_{-14}
False alarm rate, (yr)	$>2\times10^5$	$>2\times10^5$	$>7\times10^4$	1.6×10^5	$>2.7\times10^4$	$>8\times10^4$
Signal-to-noise ratio	24	13	13	13	$31.2^{+8.4}_{-6.0}$	32.4

$$\mathscr{M} = \frac{(m_1 m_2)^{3/5}}{(m_1 + m_2)^{1/5}} = \frac{c^3}{G}\left(\frac{5}{96}\pi^{-8/3} f^{-11/3}\dot{f}\right)^{3/5}, \tag{1.10}$$

where f and $\dot{f}$ are the observed frequency and its derivative with respect to time.

The gravitational wave detections by aLIGO, and Advanced Virgo for GW170814 and GW170817, offer valuable astrophysical information. Both of the black holes in the binary system responsible for GW150914 are larger than any black holes measured through x-ray binary observation, and give the strongest evidence to date for the existence of 'heavy' ($\gtrsim 25\,\mathrm{M}_\odot$) stellar mass black holes, further confirmed with the measured masses of signals GW170104 and GW170814 [11, 14, 194]. The confirmed measurement of merging black hole binaries constrains cosmological models in that any valid model now must predict their formation and merger within a Hubble time, as well as altering significantly the population statistics for black holes in the Universe [189]. Further advances came with the detection of a binary star coalescence (GW170817), which was accompanied by electromagnetic observation of gamma ray bursts in the same locality, thereby confirming that binary neutron star mergers are progenitors of gamma ray bursts [26]. This detection also represents the first example of multi-messenger astronomy, where electromagnetic and gravitational wave observatories work in tandem to measure an astrophysical object/event and resulted in determining the Hubble constant to be roughly $70\,\mathrm{km\,s^{-1}\,Mpc^{-1}}$ [13].

1.8 Conclusion

The direct detection of gravitational waves has opened up a new era of multi-messenger astronomy and given further proof of Einstein's General Theory of Relativity. It also represents a monumental feat in metrology, with aLIGO sensitive to changes in the 4 km test mass separation as little as $\sim 2 \times 10^{-20}$ m, a length 10^5 times smaller than the diameter of a proton. Within the next year a worldwide network of second generation interferometric detectors will be concurrently taking data at similar sensitivity levels, which is likely to ensure multiple detections per year. However, with a gain of x in detector sensitivity corresponding to an x^3 increase in observable universe, it is important to continue to lower the noise sources limiting current generation gravitational wave detectors in order to increase the breadth of their science output.

Multiple noise sources contribute towards the overall sensitivity limit, but thermal noise in the test mass coatings will be a dominant noise source in the most sensitive frequency band of all future ground-based interferometric gravitational wave detectors.

It is therefore crucial to investigate relevant properties of materials currently used as test mass coatings in order to gain a better understanding of the processes behind coating thermal noise, as well as research possible future alternatives in order to obtain greater sensitivity and meet the design goals of future detectors. Of particular interest is the characterisation of the thermal noise properties of coating materials at cryogenic temperatures, since KAGRA and the future detectors ET, LV, and CE are designed for low temperature operation.

Chapter 2 will present a detailed look into the mechanisms behind coating thermal noise, and further chapters will chronicle the characterisation of coating materials currently used, as well as proposed alternatives, and their impact on coating thermal noise in future gravitational wave detectors.

Chapter 2

Coating thermal noise

2.1 Introduction

Thermally driven motion in the test masses, mirror coatings, and suspension fibres limits the sensitivity of interferometric ground-based gravitational wave detectors. Following the equipartition theorem, macroscopic motion in the test mass components arises from the mean $\frac{1}{2}k_{\mathrm{B}}T$ of thermal energy associated with each degree of freedom of molecules in a mechanical system. The magnitude of this thermally driven motion is similar to that of a gravitational wave signal at the detectors' most sensitive frequencies, and is known as Brownian thermal noise. Coating Brownian noise is particularly detrimental to detector sensitivity compared to suspension or substrate noise because the motion of the coatings is directly sampled by the laser light within the detector arm cavities [195].

The total thermal noise contribution from a mirror coating is a combination of Brownian noise with thermoelastic and thermo-refractive noises, two other major noise sources dependent on temperature fluctuations. All three properties vary significantly depending on the thermal and mechanical properties of the coating material. Thermoelastic and thermo-refractive noise from a given coating material can also change depending on the properties of the neighbouring coating layers in a multilayer stack and the substrate material. These two noise sources are closely related and can be combined and described as thermo-optic noise, which is not a limiting noise factor in advanced detectors but could become a dominant noise source if the test mass and/or coating materials are changed for the next generation of detectors [196]. Coating Brownian noise is the dominant source of thermal noise from the multilayer mirror coatings. It will continue to limit all current and future detectors at their most sensitive frequency, around 100 Hz, until new, lower loss coating materials are found.

2.1.1 Brownian noise

Macroscopic mechanical motion originating from random fluctuations in thermal energy was first described by the botanist Robert Brown in 1828 when he observed irregular movement of pollen and dust grains suspended in water [197]. It was not until Einstein's 1905 paper, however, that the origin of this motion was described mathematically and shown to be a result of stochastic collisions between the pollen particles and the surrounding water molecules [198]. Notable in this paper was the conclusion that the pollen grains lost kinetic energy with every molecular collision, which was the first ever description of a dissipative process originating from purely random fluctuations. About twenty years later an analogous thermally driven dissipation process was recorded by J. B. Johnson, who observed temperature-dependent spontaneous voltage fluctuations across conductors [199, 200]. This electronic noise was determined by H. Nyquist to originate from the thermal energy of electrons within the conducting material, the resistance of which determines the level of dissipation of electron thermal energy [201].

2.1.2 The Fluctuation-Dissipation Theorem

The stochastic, thermally driven fluctuations seen in both Brownian motion and Johnson-Nyquist noise represent a driving force in a linear system under thermal equilibrium. The subsequent energy loss caused by molecular collisions or electrical resistance represents irreversible dissipative mechanisms. Callen et al. generalised these examples with the Fluctuation Dissipation Theorem, which states that any linear system under thermal equilibrium and capable of dissipative processes will undergo thermally driven stochastic fluctuations, whose magnitude and frequency are characterised by the dissipative, i.e. real, part of the impedance, $Z(\omega)$, of the system, defined as [202–204]:

$$Z(\omega) \equiv \frac{F(\omega)}{\mathrm{v}(\omega)} \,, \tag{2.1}$$

where $\mathrm{v}(\omega)$ is the velocity of responsive motion within the system as a result of an applied force, $F(\omega)$. The power spectral density, $S_x(\omega)$, of this fluctuating, thermally-induced system displacement can be written in terms of the real part of the mechanical admittance $Y(\omega)$, which is equivalent to $Z^{-1}(\omega)$:

$$S_x(\omega) = \frac{4k_BT}{\omega^2}\Re\{Y(\omega)\} \,, \tag{2.2}$$

where k_B is Boltzmann's constant and T is the temperature of the driven system. It is therefore possible to predict the thermal noise of a system at a given frequency with knowledge of the real part of the mechanical impedance.

Sources of dissipation can be split into two categories: internal and external. In an interferometric gravitational wave detector, where we consider the test-mass and its suspension fibres as a mechanical system, external sources of dissipation include gas damping*, eddy currents, and energy loss through the suspension support structure (recoil damping) [205, 206]. These dissipative sources have been effectively eliminated through operation under high vacuum, using non-conductive components when possible, and careful design of the mirror/suspension support systems. External dissipative mechanisms in current detectors are insignificant compared to the damping processes within suspension, mirror, and coating materials. This internal friction is the dominant source of the mechanical impedance of the system, and, therefore, the primary contributor of thermal noise in gravitational wave detectors.

2.2 Internal mechanical dissipation

An ideal elastic material exhibits an instantaneous strain, ε, in response to an applied stress, σ†. Real materials, however, are anelastic and experience a lag in strain with respect to an applied stress. This delayed strain response builds over a finite relaxation time and is the origin of internal friction within a material [120, 207]. For a periodic stress, σ, of initial amplitude σ_0 and frequency f:

$$\sigma = \sigma_0 e^{i2\pi ft} \ , \tag{2.3}$$

the resulting strain in an anelastic material will be:

$$\varepsilon = \varepsilon_0 e^{i(2\pi ft-\phi)} \ , \tag{2.4}$$

where ε_0 is the initial strain amplitude and ϕ is a phase lag between the applied stress and a resulting strain. The strain response will have the same oscillation frequency as the causal stress but offset by ϕ, which is known as the mechanical loss angle and represents the fractional energy dissipated for each oscillation of the system [120].

*Gas damping is the momentum transfer between the mechanical system and ambient gas particles. It can be thought of as equivalent to viscosity-dependent drag on Brownian particles in a liquid [205].

†The relationship between stress and strain in an ideal solid can be defined using Hooke's law, where $\sigma = \varepsilon Y$ and Y is the Young's modulus, also known as the elastic modulus, of the material.

The internal friction characteristic of anelastic materials arises from a number of mechanisms. The amount of thermal energy dissipated during oscillating stress-strain interactions depends on point defects, dislocations and grain boundaries in crystalline materials [120, 205]. Thermal energy is also dissipated within amorphous and paracrystalline materials through these processes, as well as through changes in molecular structure dependent on temperature, stress, and the density of the material* [208–211].

2.2.1 Thermal noise associated with a resonant mode

The fractional energy loss associated with a single oscillation of a periodic system can be represented as the phase lag, ϕ, between an applied force, F, and the resulting displacement, x, of a mass, m. The mechanical origins of loss in this oscillating system can be thought of as a mass on an anelastic spring and described by a version of Hooke's law modified and extended to account for periodic damping [120]. The motion is then modelled as [205]:

$$m\ddot{x} = -k[1 + i\phi(\omega)]x + F \ , \tag{2.5}$$

where $k[1 + i\phi(\omega)]$ is a complex spring constant, x is displacement, and $\ddot{x}$ is acceleration. The displacement and acceleration of this oscillating system can be expressed in terms of the velocity, $\dot{x}$ [21]:

$$x = \frac{\dot{x}}{i\omega} \quad \text{and} \quad \ddot{x} = i\omega\dot{x} \ , \tag{2.6}$$

so the force applied to the oscillator moving according to equation 2.5 can also written in terms of the velocity:

$$F = \dot{x}\left[\frac{k(1 + i\phi(\omega)) - \omega^2 m}{i\omega}\right] \ . \tag{2.7}$$

The thermal displacement noise in this modelled system can be calculated using the Fluctuation Dissipation Theorem. First, the complex mechanical impedance is calculated by substituting equations 2.5 and 2.6 into equation 2.1:

$$Z(\omega) = \frac{k + ki\phi(\omega) - \omega^2 m}{i\omega} \ . \tag{2.8}$$

The impedance is the reciprocal of the admittance, which, when split into its real and imaginary parts, is given by:

*These processes are discussed in greater detail in section 4.4.1.

$$\Im\{Y(\omega)\} = \frac{\omega(k-\omega^2 m)}{(k-\omega^2 m)^2 + \phi^2(\omega)k^2} \tag{2.9}$$

and

$$\Re\{Y(\omega)\} = \frac{k\omega\phi(\omega)}{(k-\omega^2 m)^2 + \phi^2(\omega)k^2} \,. \tag{2.10}$$

The spring constant, k, is equivalent to $m\omega_0^2$ [205], so substituting the real part of the impedance into equation 2.2, and converting from angular frequency, gives the frequency dependent power spectral density of thermally-induced displacement noise from an oscillator with resonance at f_0 and mechanical loss, $\phi(f)$:

$$S_x(f) = \frac{k_B T}{2\pi^3 f m} \frac{f_0^2 \phi(f)}{\left(f_0^2 - f^2\right)^2 + f_0^4 \phi^2(f)} \,. \tag{2.11}$$

It is of interest to look at the thermal noise spectral density at frequencies above, below, and at the resonant mode frequency of the oscillatory system. Rearranging equation 2.11 assuming low loss materials ($\phi^2(f) << 1$) and a measurement frequency much greater than the resonant frequency ($f >> f_0$) gives:

$$S_x(f) = \frac{k_B T f_0^2}{2\pi^3 m} \frac{\phi(f)}{f^5} \,. \tag{2.12}$$

Looking at the other extreme, where measurement frequency is much less than that of the resonant mode, $f << f_0$, equation 2.11 becomes:

$$S_x(f) = \frac{k_B T}{2\pi^3 m f_0^2} \frac{\phi(f)}{f} \,. \tag{2.13}$$

In both cases the thermal displacement noise is directly proportional to the mechanical loss, so reducing the loss of an oscillatory system will decrease the thermal noise at frequencies away from resonance. For the case where the measurement frequency is on resonance, $f = f_0$, equation 2.11 becomes:

$$S_x(f_0) = \frac{k_B T}{2\pi^3 m f_0^3} \frac{1}{\phi(f_0)} \,, \tag{2.14}$$

where the thermal displacement noise is inversely proportional to the loss, so reducing mechanical loss increases the thermal motion at the resonance. Conservation of energy dictates that the total thermal motion within the system remains the same in all cases, so altering the mechanical loss just changes the relative magnitude of motion across a given frequency range. This is a crucial property of mechanically dissipative oscillators for reducing thermal noise in gravitational wave detectors; if the detector's mirrors

and suspensions are modelled as internally damped harmonic oscillators with a single resonant mode, then the thermal noise away from resonance is directly proportional to the mechanical loss. This effect is displayed in figure 2.1, which shows the thermally-induced displacement noise for single-mode mechanical oscillators of differing internal friction, where the amplitude spectral density ($m/\sqrt{Hz}$) is the square root of the power spectral density (m^2/Hz) given in equation 2.11. A greater thermal noise occurs on resonance for the lower loss oscillator, but this is offset by a significant reduction in noise at all frequencies other than the resonant mode. In reality the mirror and suspensions have many vibrational resonances*, but careful construction can push the resonant frequencies outwith the most sensitive bandwidth of the detectors. Thus, it is crucial to utilise low loss materials in the mirror assembly to push the energy dissipation away from detection frequencies and towards resonant modes far above or below this range.

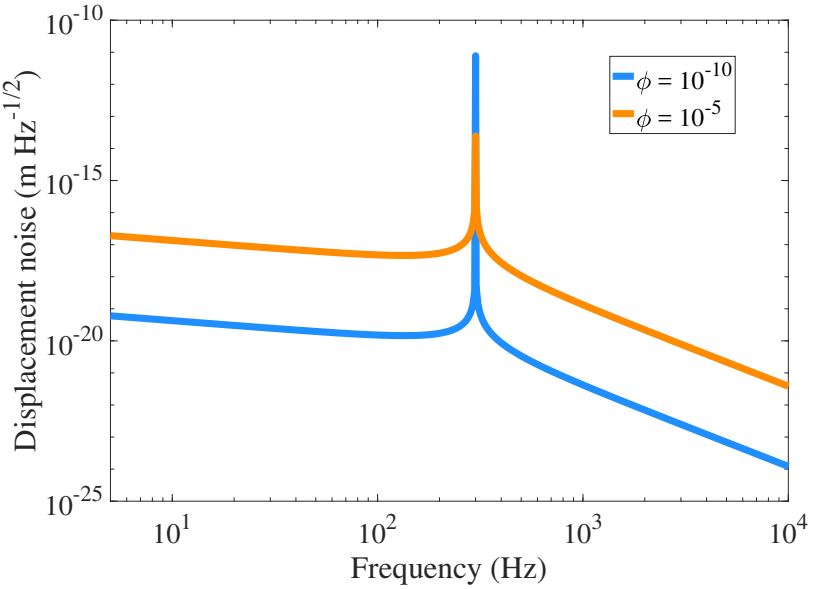

Fig. 2.1 Amplitude spectral density of thermally-induced displacement at 295 K for two 40 kg mechanical oscillators with 300 Hz resonances. The blue line represents the thermal noise of one of these oscillators with a mechanical loss of 10^{-10}, and the orange represents one with a loss of 10^{-5}.

2.2.2 Mechanical loss and the quality factor

The quality factor, Q is a common, dimensionless quantity used to describe the resonance peaks of harmonic oscillators and is defined as:

*These resonances are combinations of internal mirror modes, suspension fibre bending modes, and pendulum and bounce modes of the suspended system

$$Q \equiv \frac{f_0}{\Delta f} \equiv \frac{2\pi E_{\text{stored}}}{E_{\text{lost per cycle}}} , \tag{2.15}$$

where, E_{stored} is the total energy associated with oscillation within the system, $E_{\text{lost per cycle}}$ is the energy dissipated per cycle of oscillation, and Δf is the full width at half maximum of the resonant peak at frequency f_0. The width of a resonant peak, therefore, is inversely proportional to the energy loss on resonance; a high Q oscillator will exhibit a very narrow, tall peak and a low Q oscillator is characterised by a broad, short resonance peak.

As described in section 2.2, mechanical loss is the phase lag between an applied stress and the resulting strain in a material, and for an internally damped, oscillating system it is the ratio of the energy lost per cycle to the total stored energy in the system, i.e. [207]:

$$\phi(f) \equiv \frac{E_{\text{lost per cycle}}}{2\pi E_{\text{stored}}} . \tag{2.16}$$

Thus, the mechanical loss angle is the inverse of the quality factor, as defined by equation 2.15*. This means the loss angle of a material can be measured by determining the full width at half maximum of resonance peaks of an oscillating system comprised of said material. As shown in section 2.2.1, the thermally-induced noise of an internally damped system is proportional (off resonance) to the mechanical loss, so measurement of the resonant peaks allows for direct approximation of the thermal noise stemming from this anelastic process.

2.2.3 Thermoelastic loss

Thermoelastic loss is an internal source of anelastic energy dissipation originating from the distribution of temperature fluctuations in a material caused by a change in its shape. This deformation creates temperature gradients between warmer and cooler sections of the contracting and expanding material and the resulting heat flow across these gradients is a source of energy loss and, therefore, thermal noise [212]. An example of this motion-induced, oscillatory temperature gradient is shown in figure 2.2, where a beam is deflected to match the deformation caused by the $n = 2$ bending mode.

*It should be noted that the quality factor is defined only at a resonance, whereas the mechanical loss is a continuous function of frequency. In other words, Q is a property of a resonance and $\phi(f)$ is a property of the material.

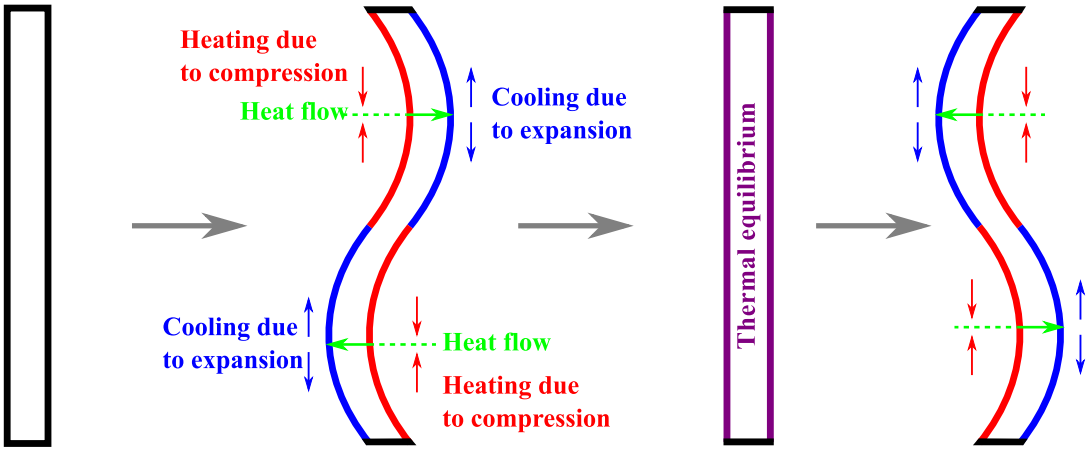

Fig. 2.2 Temperature gradients created across the width of a rectangular beam as a result of expansion and contraction due to vibration of the second resonant bending mode.

Thermoelastic energy dissipation (ϕ_{therm}) within an anelastic object oscillating at an angular frequency ω, such as the beam shown in figure 2.2, is given by [212, 213]:

$$\phi_{\text{therm}}(\omega) = \frac{Y\alpha^2 T}{\rho C}\frac{\omega\tau}{1+\omega^2\tau^2}\ , \tag{2.17}$$

where Y is the Young's modulus, α* is the linear thermal expansion coefficient, T is the temperature, ρ is the density, and C is the heat capacity. The thermal expansion coefficient of the material will determine the extent to which beam deformation will cool/heat the object during oscillation, and the resulting energy loss through heat flow can be seen to peak at a frequency determined by τ, the characteristic time it takes the heat to travel through the thickness of the beam. For a rectangular beam† of width t, τ is given by [120]:

$$\tau = \frac{t^2\rho C}{\pi^2\kappa}\ , \tag{2.18}$$

where κ is the thermal conductivity. This characteristic time, τ, is dependent on the geometry of the object under deformation. For comparison, the characteristic relaxation time for heat flow through a cylinder (such as a gravitational wave detector mirror suspension fibre) of diameter d_{f} is [212]:

$$\tau = \frac{d_{\text{f}}^2\rho C}{13.55\kappa}\ . \tag{2.19}$$

*As defined by $\alpha = L^{-1}\frac{dL}{dT}$, where L is the length in one axis of freedom and $\frac{dL}{dT}$ represents the change in this length with a change in temperature [214].

†A graph of thermoelastic loss versus temperature for various thicknesses and mode frequencies of silicon beams can be seen in section 4.2.2.1.

Partially as a result of the geometry-dependent τ, the thermoelastic noise spectral density is strongly dependent on the particular system of interest. The thermoelastic noise of the gravitational wave detector mirrors and coatings will be discussed in detail in section 2.4.1, but, to highlight the effect of equations 2.17 and 2.19, these thermoelastic models have led directly to reduction in the thermal noise in detector suspension fibres. The thermal expansion coefficient of silica can be shown to be dependent on stress such that α in equation 2.17 can be replaced [125]:

$$\alpha_{\text{effective}} = \alpha - \sigma_s \frac{\Lambda}{Y_{\text{rt}}} , \tag{2.20}$$

where σ_s is a static stress within a thin silica fibre, Y_{rt} is the Young's modulus at room temperature, and Λ is defined as $\frac{1}{Y_{\text{rt}}}\frac{dY}{dT}$. Applying the correct magnitude of static stress has been proven to result in a $\alpha_{\text{effective}}$ of zero, thus nullifying the thermal expansion within the suspension fibres and eliminating thermoelastic dissipation [126]. A similar technique of optimising thermal properties is used to reduce thermal gradient noise in the test mass mirror coatings within the detectors and is discussed in section 2.4.3.

2.3 Coating brownian noise

The thermal noise power spectral density given in equation 2.11 is relevant for calculating the noise contribution of a single resonant mode. Gravitational wave detector mirrors have many resonant frequencies, and initial calculations of the mirrors' total Brownian thermal noise involved summation of the noise from each of these resonances [205, 215]. This additive method assumed homogenous mechanical dissipation within the test mass mirrors, with the highly reflective coatings on the mirror face representing nothing more than a damping coefficient added to the internal friction of the bulk mirror substrate. However, with loss multiple orders of magnitude higher than the substrate, the coatings create an inhomogeneous loss distribution that breaks this assumption and renders the summation of noise from individual modes incorrect*, with initial calculations significantly underestimating the effect of the coatings on Brownian thermal noise within the mirrors [217, 218].

An alternative method that better takes into account the lossy mirror coating involves calculating the thermal noise directly from the detector readout [218–220]. The Fluctuation Dissipation Theorem is applied to the interferometer readout (directly

*The loss inhomogeneity created by the coatings actually results in a phase lag between dissipation on the surface of the substrate compared to the bulk, which alters the mode shape of a given resonant mode during oscillatory decay and can result in loss coupling between resonances. For a more detailed look into this process see [216].

observing the position of the test mass), where the Gaussian profile of the incident laser beam is thought of as a mechanical force on the mirror face and the noise arises from the dissipation of this imparted energy within the mirror. This results in the power spectral density of thermally-induced mirror face displacement being described by [218]:

$$S_x(f) = \frac{2k_B T}{\pi^2 f^2} \frac{W_{\text{diss}}}{F_0^2} \,, \tag{2.21}$$

where F_0 is the peak amplitude of the theoretical oscillating force modelled by the laser beam, and W_{diss} is the total power dissipated in the mirror in response to the applied force. If the radius of the laser beam used to measure displacement is small compared to that of the mirror, then the test mass can be approximated as half-infinite, and the Brownian noise power spectral density, $S_x^{\infty}(f)$, of a test mass substrate with mechanical loss $\phi_{\text{substrate}}$ can be shown to be [219]*:

$$S_x^{\infty}(f) = \frac{2k_B T}{\pi^{3/2} f} \frac{1-\nu^2}{w_r Y} \phi_{\text{substrate}} \,, \tag{2.22}$$

where ν and Y are the Poisson's ratio and Young's modulus, respectively, of the mirror substrate material, and w_r is the radius of a Gaussian† beam profile as defined by the point where the electric field amplitude falls to $1/e$‡ of the maximum value. Equation 2.22 assumes the ratio of the beam radius to mirror radius is very small, but for cases where w_r is increased the thermal noise estimation is still valid if scaled by a correction factor that depends on the relative change in the ratio [219, 220]. The most important result from the direct readout approach of thermal displacement noise calculation is the dependence of this noise on distance from the sampling laser beam. Whereas a source of high dissipation on the back side of a test mass must propagate its displacement effect through the bulk of the mirror to be observed by the interferometer laser beam, a very lossy material, such as a highly reflective coating stack, on the front of the mirror is directly sampled by this incident beam. In other words, the interferometer is more sensitive to the loss of the coatings than the loss of detector components further from the mirror face, e.g. the suspensions. Accounting for the energy dissipation within the mirror coatings, therefore, is of high importance for determining the thermal noise of an interferometer.

*This also assumed homogeneous loss within the test mass substrate [221].

†The interferometers utilise Gaussian beam profiles, for which 95% of the detector signal is contained within 60% of the mirror radius. Changing the beam profile could potentially increase the sampling radius and, therefore, reduce the thermal noise [222].

‡This is equivalent to the intensity dropping to $1/e^2$ of it maximum power.

A first approximation involved modelling the multi-layer coating stack as a thin surface layer of thickness d, where the mechanical properties of this 'coating' were the same as the substrate but with a different mechanical loss, ϕ_{coating}. The total thermal noise power spectral density, $S_x^{\text{total}}(f)$, of this compound mirror is given by [223]:

$$S_x^{\text{total}}(f) = \frac{2k_BT}{\pi^{3/2}f}\frac{1-\nu^2}{w_rY}\left(\phi_{\text{substrate}} + \frac{2d}{w_r\sqrt{\pi}}\frac{(1-2\nu)}{(1-\nu)}\phi_{\text{coating}}\right) . \tag{2.23}$$

Equation 2.23 successfully takes into consideration the loss inhomogeneity of a coated mirror by adding the corrective term containing coating dissipation. However, the mirror coating is far from homogeneous; it is comprised of stacked, alternating layers of materials with thermal and mechanical properties that differ significantly*. A more thorough calculation of the influence of the coating on thermal noise continues with the direct application of the Fluctuation Dissipation Theorem but accounts for the multilayer coating stack and gives a total thermal noise power spectral density of [164]:

$$S_x^{\text{total}}(f) = \frac{2k_BT(1-\nu^2)}{\pi^{3/2}fw_rY}\phi_{\text{effective}} , \tag{2.24}$$

where $\phi_{\text{effective}}$ is the effective mechanical loss angle of the mirror, comprised of a substrate and a highly reflective coating stack. It is derived as:

$$\begin{aligned}\phi_{\text{effective}} = \phi_{\text{substrate}} + \frac{d}{w_rY_\perp\sqrt{\pi}}\Bigg[&\left(\frac{Y}{1-\nu_\perp} - \frac{2\nu_\perp^2YY_\parallel}{Y_\perp(1-\nu^2)(1-\nu_\parallel)}\right)\phi_\perp \\ &+ \left(\frac{Y_\parallel\nu_\perp(1-2\nu)}{(1-\nu_\parallel)(1-\nu)}\right)(\phi_\parallel - \phi_\perp) \\ &+ \left(\frac{Y_\parallel Y_\perp(1+\nu)(1-2\nu)^2}{Y(1-\nu_\parallel^2)(1-\nu)}\right)\phi_\parallel\Bigg] ,\end{aligned} \tag{2.25}$$

where properties without subscripts refer to the substrate, and the subscripts $\parallel$ and $\perp$ denote coating material properties (Y, ν, and ϕ) for stresses parallel and perpendicular to the coating face, respectively. These directional properties are calculated for coating stacks comprised of alternating layers of material from [164]:

$$Y_\parallel = \frac{Y_1d_1 + Y_2d_2}{d_1+d_2} , \tag{2.26}$$

*See section 7.2.1 for specifics regarding the construction of a highly reflective multilayer coating.

$$Y_{\perp} = \frac{d_1 + d_2}{d_1/Y_1 + d_2/Y_2} \,, \tag{2.27}$$

$$\nu_{\perp} = \frac{\nu_1 Y_1 d_1 + \nu_2 Y_2 d_2}{Y_1 d_1 + Y_2 d_2} \,, \tag{2.28}$$

$$\phi_{\parallel} = \frac{Y_1 \phi_1 d_1 + Y_2 \phi_2 d_2}{Y_{\parallel}(d_1 + d_2)} \,, \tag{2.29}$$

and

$$\phi_{\perp} = \frac{Y_{\perp}(\phi_1 d_1/Y_1 + \phi_2 d_2/Y_2)}{(d_1 + d_2)} \,. \tag{2.30}$$

The Poisson's ratio in the direction parallel with the mirror face is the average of the ratios of the two coating materials: $\nu_{\parallel} = (\nu_1 + \nu_2)/2$.

From equations 2.25 and 2.24 it can be seen that the coating thermal noise is dependent on the stiffness of the substrate material, meaning that the same coating will exhibit different levels of thermal noise depending on the test mass material. A substrate with a high Young's modulus is beneficial, but, for a given substrate, the lowest noise is achieved by matching the Young's moduli of the substrate with the coating. Also of note is the dependence of coating thermal noise on $1/w_r^2$. The substrate thermal noise can also be seen to vary by $1/w_r$, so an increase in beam radius significantly reduces the thermally-induced displacement noise within the test mass mirrors. Of course, the thermal noise is also proportional to the operating temperature, as well as the mechanical loss of the substrate and coating materials. An ideal interferometer mirror in terms of coating Brownian noise, therefore, is a cooled, very large test mass with a low loss coating of nearly identical material properties. With the current design, it will be coating Brownian noise that limits aLIGO and Advanced Virgo in their most sensitive frequency band once they reach design sensitivity, thus making reduction of this noise source essential for all future upgrades and new detectors.

2.4 Coating thermo-optic noise

As discussed in section 2.2.3, thermoelastic loss is energy dissipation through heat flow across temperature gradients in anelastic materials originating from motion of the system. Thermoelastic noise is the result of statistical fluctuations in temperature causing temperature gradients that result in deformation of the mirror face and, there-

fore, displacement noise. Thermo-refractive noise arises from these same thermal fluctuations causing changes in the optical path length within coated mirrors due to the temperature dependence of the refractive index [224]. Due to their similar origins, thermoelastic and thermo-refractive noise are often combined and described as thermo-optic noise.

2.4.1 Thermoelastic noise

Thermal gradients arise in the mirror coating due to statistical temperature fluctuation, as well as from compression and tension from resonant mode motion. The resulting thermal expansion and contraction of the coating stack shifts causes a displacement noise within the interferometer, the power spectral density of which is given by [195, 224]:

$$S_x^{\mathrm{TE}}(f) \approx \frac{8k_B T^2}{\pi^{3/2} f} \frac{d^2}{w_r^2} (1+\nu_\mathrm{s})^2 \frac{\overline{C}_\mathrm{c}^2}{C_\mathrm{s}^2} \frac{\alpha_\mathrm{s}^2}{\sqrt{\kappa_\mathrm{s} C_\mathrm{s}}} \tilde{\Delta}^2 \ , \tag{2.31}$$

where C is the specific heat capacity, κ is the thermal conductivity, and α is the thermal expansion coefficient. Subscripts 's' and 'c' denote substrate and coating, respectively, and $\tilde{\Delta}$ is a dimensionless averaging of material properties defined as:

$$\tilde{\Delta} \equiv \frac{C_\mathrm{s}}{2\alpha_\mathrm{s}\overline{C}_\mathrm{c}} \left(\frac{\overline{\alpha}_\mathrm{c}}{1-\overline{\nu}_\mathrm{c}} \left[\frac{1+\overline{\nu}_\mathrm{c}}{1+\nu_\mathrm{s}} + (1-2\nu_\mathrm{s}) \frac{\overline{Y}_\mathrm{c}}{Y_\mathrm{s}} \right] \right) - 1 \tag{2.32}$$

The detector mirror coatings are comprised of multiple materials, so the coating properties in equations 2.31 and 2.32 are averaged over the relative thickness of each coating material to create an effective homogenous coating with properties representative of the multilayer stack. These averaged properties are denoted by raised bar, and the averaging is done using the equation [195]:

$$\overline{X}_{a,b} \equiv \frac{d_\mathrm{a}}{d_\mathrm{a}+d_\mathrm{b}} X_\mathrm{a} + \frac{d_\mathrm{b}}{d_\mathrm{a}+d_\mathrm{b}} X_\mathrm{b} \ , \tag{2.33}$$

where a and b are the two coating materials. It can be seen from equation 2.32 that $\tilde{\Delta}$ tends towards zero as the thermal and mechanical properties of the coating and substrate become identical. Thus, if the thickness-averaged coating properties are the same as the mirror substrate then there is no coating thermoelastic noise.

2.4.2 Thermo-refractive noise

Thermo-refractive noise is dependent on the change in refractive index with temperature, $\beta = \frac{dn}{dT}$, in the same way thermoelastic noise depends on the thermal expansion coefficient of the coating stack. The optical path length of the laser light is lengthened or shortened depending on changes in refractive indices of the coating layers due to thermal gradients within the coating. Unlike Brownian or thermoelastic noise, thermo-refractive noise does not result from mechanical displacement of the laser-sampled mirror face, but rather from phase fluctuations caused by artificial lengthening of the sampling laser beam path within the roughly one coating bilayer of beam penetration. The power spectral density of this noise source is given by [225, 226]:

$$S_{x,\beta}^{\mathrm{TR}}(f) = \frac{\beta_{\mathrm{eff}}^2 \lambda^2 k_B T^2}{\pi^{3/2} w_r^2 \sqrt{f \rho_{\mathrm{s}} C_{\mathrm{s}} \kappa_{\mathrm{s}}}} , \tag{2.34}$$

where λ is the laser wavelength and T is the mean temperature within the mirror. β_{eff} is the effective change in refractive index of the multilayer coating stack with respect to temperature, and, for alternating $\lambda/4$ thick layers of low and high index (n_{L} and n_{H}) coating materials, is defined as:

$$\beta_{\mathrm{eff}} = \frac{n_{\mathrm{H}} n_{\mathrm{L}} (\beta_{\mathrm{H}} + \beta_{\mathrm{L}})}{4(n_{\mathrm{H}}^2 - n_{\mathrm{L}}^2)} . \tag{2.35}$$

It is of interest to note that unlike thermoelastic noise, the thermo-refractive noise given by equation 2.34 is not dependent on the coating thickness.

2.4.3 Thermo-optic noise

Thermoelastic and thermo-refractive noises both arise from temperature gradients within the test mass mirror, particularly within the thin coating layer on the front face directly. sampled by the laser. Because of their shared origin mechanism, these two distinct noise sources are highly correlated and can be combined and described as thermo-optic noise [196, 227, 228]. First, the power spectral density of temperature fluctuations, $S_{\mathrm{TO}}^{\Delta T}(f)$, is calculated from the Fluctuation Dissipation Theorem to be [226]:

$$S_{\mathrm{TO}}^{\Delta T}(f) = \frac{2 k_B T^2}{\pi^{3/2} w_r^2 \sqrt{\kappa_{\mathrm{s}} C_{\mathrm{s}} \rho_{\mathrm{s}} f}} . \tag{2.36}$$

The fluctuations in phase observed by the laser beam within the interferometer is then calculated, effectively combining the mechanical changes in test mass size from

thermoelastic effects and the change in path length as a result of the thermo-optic effects. Combining the two effects takes the form of a scaling factor to the temperature fluctuation noise given by equation 2.36, and the power spectral density of this thermo-optic noise, $S_{\mathrm{TO}}^{\Delta z}(f)$, is approximated by [196]:

$$S_{\mathrm{TO}}^{\Delta z}(f) \simeq S_{\mathrm{TO}}^{\Delta T}(f)\left(\tilde{\alpha}_{\mathrm{c}} d - \tilde{\beta}_{\mathrm{c}}\lambda - \tilde{\alpha}_{\mathrm{s}} d\frac{\overline{C}_{\mathrm{c}}}{C_{\mathrm{s}}}\right) , \tag{2.37}$$

where d is the coating thickness, λ is the wavelength, C is the heat capacity, and 's' and 'c' correspond to the substrate and coating, respectively. The bar over C_{c} represents the thickness-averaged value following equation 2.33. $\tilde{\alpha}$ represents an effective thermal expansion coefficient given by*:

$$\tilde{\alpha}_{\mathrm{X}} \sim 2\overline{\alpha}_{\mathrm{X}}(1+\overline{\nu}_{\mathrm{X}}) , \tag{2.38}$$

where ν is the Poisson's ratio. The change in refractive index with temperature of the coating, $\tilde{\beta}_{\mathrm{c}}$, is similar to β_{eff} given in equation 2.35 but is altered to include a $\frac{1}{2}\lambda$ thick silica cap layer on top of the alternating $\frac{1}{4}\lambda$ coating layers and takes into account the effect of thermal expansion on $\frac{\mathrm{d}n}{\mathrm{d}T}$; changes that more accurately represent the mirror coatings used in current detectors. This new $\tilde{\beta}_{\mathrm{c}}$ is defined as [196]:

$$\tilde{\beta}_{\mathrm{c}} \simeq \frac{B_{\mathrm{H}} + B_{\mathrm{L}}\left(2\left(n_{\mathrm{H}}/n_{\mathrm{L}}\right)^2 - 1\right)}{4(n_{\mathrm{H}}^2 - n_{\mathrm{L}}^2)} , \tag{2.39}$$

where B_{X} is the fractional change in optical path length with respect to temperature in high (n_{H}) or low (n_{L}) index coating material and is given by $B_{\mathrm{X}} = \beta_{\mathrm{X}} + \tilde{\alpha}_{\mathrm{X}} n_{\mathrm{X}}$.

The crucial result from equation 2.37 is the opposite effects on the magnitude of the noise power spectral density from thermoelastic ($\tilde{\alpha}_{\mathrm{c}} d$) and thermo-refractive ($\tilde{\beta}_{\mathrm{c}}\lambda$ and $\tilde{\alpha}_{\mathrm{s}} d\frac{\overline{C}_{\mathrm{c}}}{C_{\mathrm{s}}}$) loss components. Given the correct coating material properties the two noise sources cancel each other out, thus significantly reducing the total thermal noise of the test mass mirrors. This has been shown to be the case for the aLIGO mirror coatings, where thermo-optic noise is effectively irrelevant due to the nearly equal and opposite effects of thermoelastic and thermo-refractive noise from the multilayer coating stack consisting of SiO_2 (n_{L}, and cap layer) and 25% Ti:Ta_2O_5 (n_{H}) [196].

*This is a simplified $\tilde{\alpha}$ assuming the substrate and coating properties are similar, for a more thorough derivation and an un-simplified $\tilde{\alpha}$ see [195, 196].

2.5 Conclusions

Thermally-induced displacement noise is a primary limiting factor in the sensitivity of interferometric gravitational wave detectors*. The thermal phase noise at the laser output is a result of three primary mechanisms: thermoelastic noise stems from a change in the size of the mirrors due to thermal expansion and contraction, thermo-refractive noise from changes to the effective optical path length due to thermally altered refractive indices, and Brownian thermal noise arrises due to internal friction during thermal energy dissipation within the anelastic mirror materials. All thermally-induced noise sources are found to be strongly dependent on the thin coating applied to the front face of the test mass mirrors. Direct application of the Fluctuation Dissipation Theorem to the interferometer readout shows that the dissipation within the highly reflective multilayer mirror coating has a larger effect on the noise sources than that within the test mass or suspensions; this is due to the direct interface of the coatings with the sampling laser beam within the interferometer.

Accurate estimations of coating thermal noise (equations 2.24, 2.31, and 2.34) can lead to mitigation techniques. For example, thermo-optic noise is the combination of the elastic and refractive thermal noises, which can be estimated using equation 2.37 and shown to be eliminated with careful choice of coating materials. Brownian thermal noise, on the other hand, has no similar counteractive physical processes; reduction of this thermal noise source comes from increasing the laser beam radius (the noise scales by the inverse of the radius squared), choosing materials with decreased mechanical loss, or reducing the operating temperature of the interferometer.

The beam radius was increased for the aLIGO and Advanced Virgo upgrades, and future detectors are designed with further increases in test mass diameter to accommodate even larger beam radii†. Fused silica test mass substrates used in GEO, aLIGO, and Advanced Virgo have mechanical loss on the order of 10^{-8}, which is sufficiently low to suppress Brownian noise in the detection frequency range. The sapphire used for test masses in KAGRA and the crystalline silicon planned for use in ET and future LIGO detectors also exhibit sufficiently low internal fiction. However, coating mechanical loss is many orders of magnitude greater than that of the substrate and, as mentioned previously, more important due to its proximity to the sampling laser. Finding new coatings that are within the current, stringent optical requirements but with significantly lowered mechanical loss is the focus of current research and essential for sensitivity improvements to all interferometric gravitational wave detectors.

*Visual representation of the various detector noise sources is shown in section 1.4.

†See section 1.6 for a more in-depth review of planned detectors and upgrades.

Reducing the interferometer operation temperature directly lowers thermal noise; a strategy that increases design complexity but has been proven to work in large-scale prototype detectors [173] and is currently implemented in the KAGRA detector and planned for use in the ET detector as well as future aLIGO upgrades and LIGO detectors. However, the mechanical loss of many coating materials is temperature dependent and unknown at the planned operating temperatures. Coating Brownian noise cannot be estimated without accurate characterisation of the internal friction of these materials. Measuring the mechanical loss angle of current coatings, as well as potential replacement coating materials, is therefore of high importance for reducing the thermal noise currently limiting detector sensitivity. Furthermore, knowledge of the change in mechanical loss with respect to temperature gives valuable insight in the structural origins of internal friction, thus giving better understanding of the root causes of thermally-induced displacement noise. Chapter 3 will discuss the theory and methods behind characterising the temperature-dependent mechanical loss of coatings, with the goal of finding low loss materials to reduce the Brownian noise contribution from the test mass coating stack.

Chapter 3

Experimental methods for coating characterisation

3.1 Introduction

As discussed in Chapter 2, the magnitude of thermal noise within a gravitational wave detector is directly related to the mechanical dissipation of the highly reflective thin-film mirror coatings on the interferometer test masses. It is important to characterise the mechanical loss of materials in the current mirror coatings in order to more accurately quantify the sensitivity limits stemming from thermal noise within the current detectors. In addition to being necessary for thermal noise predictions of promising new coatings, loss measurements can also further understanding of energy dissipation mechanisms within thin-films. This chapter describes the methods used for depositing a material as a thin-film coating, measuring the mechanical loss of a coating, and determining the stress of a coating once deposited.

Coating loss measurements involve the excitation of resonant vibrational modes of a substrate coated with the material of interest and monitoring the natural decay of vibrational amplitude due to energy loss mechanisms within the system. Coating loss is then calculated by comparing the losses of the uncoated and coated cantilevers. Mechanical loss results presented in further chapters were all found through measuring the ringdown of coated cantilever resonators.

Compressive or tensile stresses within thin-film coatings are calculated from measurements of the radius of curvature of the coated cantilever, which deflects from a flat, uncoated state based on the imparted stress of the coating. It is thought that a number of inconsistent experimental results from the same coating using different measurement techniques, as well as differences between predicted and measured loss

values, could stem from the varying amounts of internal stress created by depositing a thin-film coating on a substrate with differing material properties [229–231]. Combined measurement of the mechanical loss and coating stress may lead to a better understanding of the relation between coating stress and internal friction of a material, which has been suggested to be a causal relationship in amorphous solids [232].

It should be noted that stringent optical requirements for coatings used in gravitational wave detectors means there is more than just mechanical loss to consider when researching new coating materials [16]. This thesis will not discuss measurement of optical properties in detail, but in later sections discussing optimised coatings for future detector upgrades it is crucial to take into account properties such as absorption and reflectivity which, if found lacking, eliminate a material from consideration. For information about characterising coating absorption see [233].

3.2 Sample preparation

Here, the coating deposition methods used to create coatings studied in this thesis will be discussed, as well as the sample substrates upon which these coatings are deposited.

3.2.1 Coating deposition methods

Physical vapour deposition (PVD) describes a wide range of coating deposition methods where a solid or liquid material is vaporised and the atoms/molecules transported to a substrate where they condense into a thin film. The method of material vaporisation, environment in which the vapour travels/condenses, and treatment of the substrate surface all differ depending on the method of PVD. Each deposition method will produce coatings with characteristic properties that can vary for a given material. Current gravitational wave detector test mass coatings are deposited by ion beam sputtering, which will be discussed along with a number of possible alternative sputtering methods for which mechanical loss measurements are presented in later chapters. Crystalline coatings, a possible alternative for future detectors [229, 234, 235], are created through a process known as molecular beam epitaxy (MBE), which will not be discussed in detail*.

*For information on MBE see references [236–238].

3.2.1.1 Ion beam sputtering

Sputtering PVD processes vaporise coating materials via direct bombardment from atomic-sized particles. The momentum transfer from incident ions dislodges atoms or molecules from a target material, which then condense on the substrate, forming a thin film. Ion beam sputtering (IBS) is a specific type of sputtering PVD where high energy ablating ions are created away from the target surface via an ion gun. Figure 3.1 shows the layout of an IBS coating chamber, which is held under vacuum during deposition. Metallic oxide coatings can be created by sputtering from a pure target and bleeding oxygen into the chamber in order to oxidise the sputtered material en route to, and at, the surface of the substrate. Standard IBS does not include external heating of the substrate, but the substrate can reach a temperature of $\sim$100 °C during deposition [239, 240].

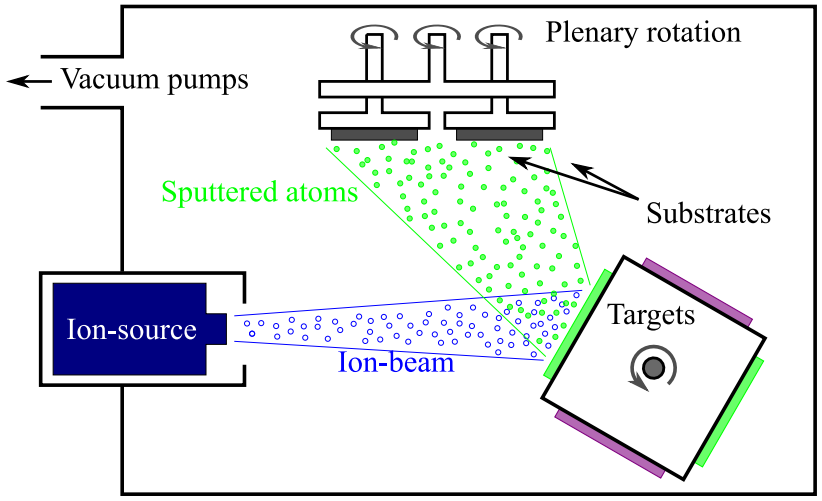

Fig. 3.1 Schematic of an ion beam sputtering chamber. Dual ion beam sputtering would have a second ion gun with its beam aligned to bombard the substrate surface, thus increasing the surface energy during coating growth.

Ion beam sputtering has been proven to create coatings with extremely low optical losses from absorption and scatter, which is why both aLIGO and Advanced Virgo have test masses coated via IBS [241]. IBS coatings have also been shown to have low mechanical loss when compared to other deposition methods, and can be sputtered such that the absorption is below instrument requirements for advanced detectors [16]. The high energy with which an IBS sputtered material reaches the substrate allows for greater surface mobility, which results in denser coatings with greater adhesion. Ion beam sputtered atoms incident on the substrate have kinetic energy on the order of 10 eV, which is $\sim$100 times greater than thermal evaporation coatings and $\sim$10 times greater than glow discharge coating techniques such as magnetron sputtering.

Increasing surface mobility and allowing coating atoms to migrate to optimal positions in a minimum energy configuration is thought to be related to low mechanical loss in some coatings, e.g. aSi deposited at high temperatures [242–245].

IBS is highly customisable in terms of sputter rate and ion energy, with variables including differences in ion source accelerating grid separation and curvature, variation in aperture sizing for the ion beam, and angle of incidence of the ion beam on the target material. This can be disadvantageous in that two different IBS coatings of the same material may differ slightly in terms of their physical and optical properties depending on the specific conditions within the coating deposition chambers [246]. However, this capability for variation in deposition parameters allows for fine tuning of the coating process and better customisation opportunities. Another advantage of ion beam sputtering is the ease with which multilayer coatings can be created. The ablation ions are not created at the surface of the target, but rather arrive at the sputtering target from an external source, so an arbitrary number of materials can be rotated sequentially in front of the ablating ion beam without breaking vacuum or significantly interrupting the flow of ions during a single coating run [239, 242].

3.2.1.2 DC magnetron sputtering

DC magnetron sputtering is an alternative PVD method. A glow discharge plasma is used to sputter atoms from a target material and magnets are used to contain electrons stripped from the target material near to the surface of the target. The 'trapped' electrons near the target surface increase the chance of further ionisation, creating denser plasma near the sputtering target material and, in turn, a steep rise in target ion bombardment [247–249]. As shown in figure 3.2a, the basic magnetron sputtering system holds the dense plasma region just above the target material, with the substrate receiving comparatively little energy.

It is beneficial for coating density and adhesion to have the sputtered atoms condensing on the substrate in a sufficiently energetic environment [242]. Strengthening the outer magnets in the magnetron system creates an unbalanced magnetic field, which extends the region of dense plasma far enough to energise the substrate surface during deposition, as shown in figure 3.2b. Adding additional sets of magnet-target pairs and creating a closed magnetic field around a rotating substrate holder further increases coating uniformity and sputter rates [250]. This is shown in figure 3.2c and is representative of the coating chamber used to produce the DC magnetron coatings discussed in Chapter 6. Metallic oxide coatings can be produced in this system by periodically passing the substrate through an atomic oxygen plasma. DC magnetron

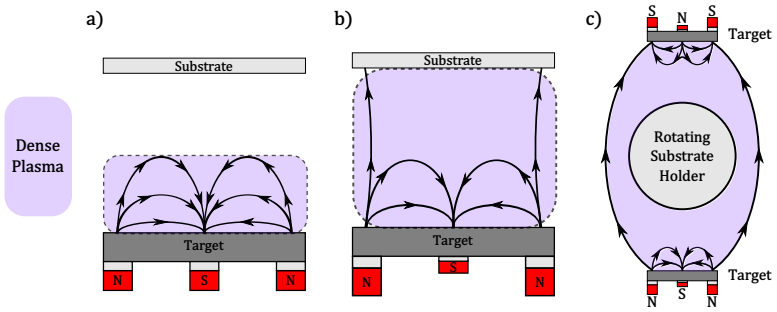

Fig. 3.2 Simplified schematic of magnetron sputtering systems. DC magnetron sputtering refers to the direct current source used to ionise the inert gas. Electric insulators require a radio frequency oscillating power supply in order to maintain a consistent sputtering plasma. (a) Basic, balanced magnetron sputtering. (b) Unbalanced magnetron sputtering, with outer magnetic poles strengthened relative to the central magnetic pole and the dense plasma extended to the substrate surface. (c) Multi-magnetron, closed loop sputtering system.

sputtering reaches temperatures of ∼100 °C at the substrate during deposition and produces films with very consistent layer thickness but with lower packing density than IBS systems [247, 250].

3.2.1.3 Reactive low voltage ion plating

Ion plating, also known as ion-assisted deposition or ion vapour deposition, describes a wide range of PVD techniques where the substrate surface is bombarded with atomic-sized particles during film growth [251]. The coating material can be vaporised via a number of methods, e.g sputtering or thermal evaporation, during ion plating. Reactive low voltage ion plating (RLVIP) vaporises the coating material using a low voltage electrical arc between an argon plasma source and a crucible containing this material [252]. Figure 3.3 shows a representative RLVIP coating chamber, where the coating material is evaporated via electron bombardment from a nearby e-beam source. Oxygen can be leaked into the chamber near the crucible to oxidise the coating during deposition.

A potential difference is created between the crucible and the insulated substrate holder, creating strong acceleration for the positive, evaporated coating ions. Coating atoms incident on the substrate can have high kinetic energy (∼30 to 50 eV) which, similarly to IBS, results in a significant amount of surface mobility for the evaporated coating atoms on the substrate and leads to a dense coating. The substrate is heated to ∼250 °C during RLVIP, which has been shown to provide further surface mobility and

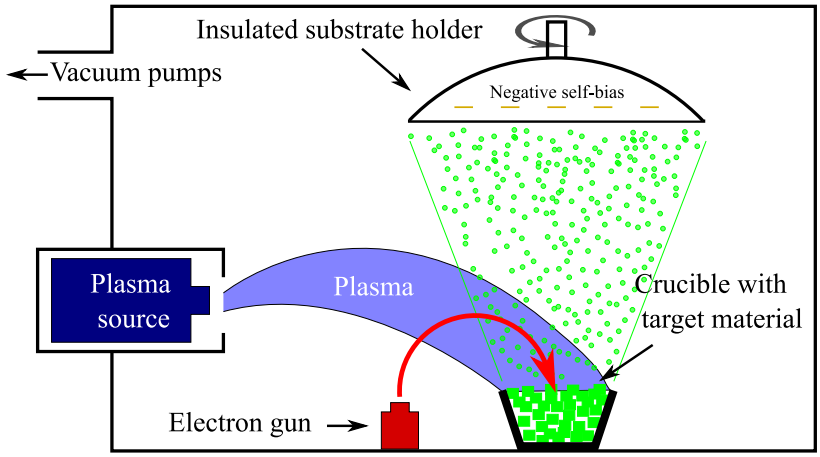

Fig. 3.3 Diagram of RLVIP coating deposition chamber. RLVIP is a combination of evaporative and sputtering techniques.

facilitate coating atoms condensing in a preferred, low energy state, which may result in lower coating mechanical loss [245].

3.2.2 Substrates

Substrate material and geometry are chosen based on the specific properties of the coating being measured. The substrate can affect certain properties, such as coating stress or growth structure, or it can limit measurement of other properties like mechanical loss and absorption. Measuring coating loss requires very low loss substrate materials in shapes that allow for a sufficient portion of total mechanical energy stored in the resonant modes of the sample to be stored in the coating. A greater ratio of energy contained in the coating as opposed to the substrate results in clearer distinction between the two materials' internal dissipation. Cantilevers were first used for coating mechanical loss characterisation by Berry and Pritchett in 1975 [253] and continue to be a productive substrate geometry due to the high amount of total energy stored in the coating and the large range of vibrational eigenfrequencies with which to observe internal dissipation [229, 254–259].

3.2.2.1 Silica cantilevers

Fused silica has extremely low mechanical loss at room temperature, so it is widely used as a substrate material for coating mechanical loss measurements; many previous and current loss experiments use 7.62 cm diameter, 0.254 cm thick machined and polished silica discs [158, 163, 165]. Some of the measurements presented in Chapter 6 used a different silica substrate geometry in the form of laser-welded cantilevers. The

cantilevers were constructed from two separate silica pieces: a 45 mm × 5 mm blank silica blade, which is typically ∼150 µm thick, and a 10 mm × ∼10 mm × 1 mm silica block. A 100 W CO_2 laser was used to weld 1 mm to 3 mm of the thin silica blade to the the top face of the thicker block; the weld joint can be seen in figure 3.4. The length of the finished cantilevers will vary depending on the size of the welded portion.

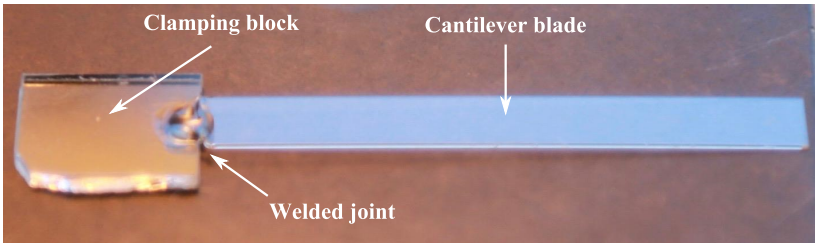

Fig. 3.4 Silica cantilever blade laser-welded to a silica clamping block.

The thick block is necessary because it provides a clamping point for the sample while the thin cantilever blade is electrostatically driven to excite a resonance and allowed to freely decay during mechanical loss measurements. The large difference in thickness between the blade and the clamping block reduces stick-slip loss at the interface between the clamp and the sample; a significant amount of energy might be dissipated at this interface if the cantilever was affixed without a clamping block, which acts to isolate the bending motion of the cantilever from the clamping system [260]. The clamping block also provides a sturdy base during handling and holding the thin cantilever blades for coating and experimental characterisation. Uncoated welded silica cantilevers exhibit a loss of about 1 to 5×10^{-6} depending on the individual cantilever and the measured bending frequencies.

3.2.2.2 Silicon cantilevers

Low thermal conductivity and poor low temperature mechanical loss render welded silica cantilevers unsuitable as substrates for measuring coating loss at cryogenic temperatures. Etched crystalline silicon cantilevers were used instead due to a thermal conductivity high enough for fast and accurate temperature changes and the absence of a peak in dissipation at low temperatures. The cantilevers were chemically etched by Kelvin NanoTechnology (KNT) [261] from 0.5 mm thick polished single crystal silicon wafers, creating cantilevers with a 0.5 mm thick clamping block and cantilever blades ∼70 µm thick (can vary wafer to wafer). Figure 3.5 shows a representative diagram for one of these silicon cantilevers. While a proven method for producing cantilever blades, the etching process is time consuming and expensive, and it creates uneven thicknesses across the length of the cantilever. An alternate method of creating

silicon cantilever blades through hydroxide-catalysis bonding cleaved silicon blades to silica clamping blocks is discussed in Appendix A. These bonded cantilevers, however, failed to match the low loss of the etched blades, which were used for all low temperature mechanical loss measurements presented in this thesis.

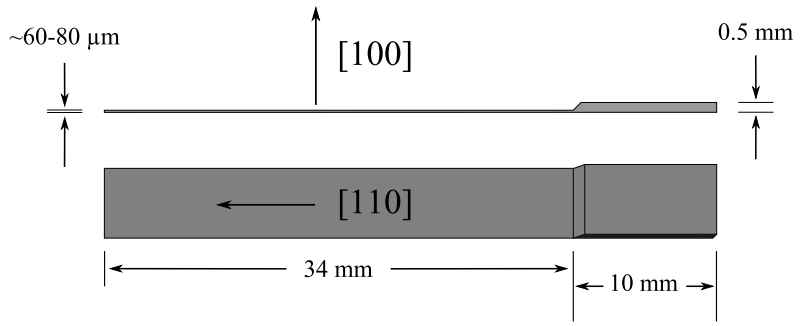

Fig. 3.5 Diagram of an etched silicon cantilever with relevant silicon crystal axis orientation. Coatings are applied to the un-etched, bottom side of the cantilever due its better surface roughness.

Etched crystalline silicon cantilevers achieve mechanical loss values from mid 10^{-7} to low 10^{-6} at temperatures between 10 K and ~150 K, which is well below the loss of bulk silica at these temperatures (mid 10^{-4} to low 10^{-3} [262]) and sufficiently low for characterising the mechanical loss of many amorphous thin-film coatings [263]. Thermoelastic loss* associated with heat flow within the silicon cantilevers during bending mode vibration significantly increases the loss above ~150 K (especially for high frequency modes) [214] and is the limiting source of internal dissipation up to room temperature.

Single crystal bulk silicon has been shown to exhibit lower mechanical loss than is seen with the etched cantilevers. At low temperatures the difference is due to the presence of thermally grown silicon dioxide on the cantilever. It has been shown that a thermal oxide layer of ~20 nm is beneficial for sputtered film adhesion [229]. This thermally grown SiO_2 film is a limiting source of loss at low temperatures and the loss increases significantly with greater oxide thicknesses, displaying a similar broad dissipation peak to that of bulk silica. This is especially an issue for post-deposition heat treatments approaching 1000 °C, as discussed in more detail in Chapter 4. A primary reason for the loss discrepancy at higher temperatures (above ~150 K) is the elevated thermoelastic loss of thin flexures compared to large, bulk substrates. In the frequency range of cantilever bending modes (0.5 to 30 kHz), equations 2.17 and 2.18 in section 2.2.3 show a significant decrease in 'high' temperature thermoelastic

*See section 2.2.3 for more information about thermoelastic loss.

loss once the object thickness is greater than ∼1 mm*. Further difference in intrinsic dissipation between bulk silicon and cantilevers is thought to stem from excess surface loss on the cantilevers as a result of the etching process [263, 264].

3.2.2.3 Ellipsometry

The thicknesses of both sputtered films and thermal oxide layers on silicon cantilevers were measured using a Sentech SE850 spectroscopic ellipsometer [265]. Ellipsometry is a non-destructive, indirect optical measuring technique for characterising thin film thicknesses and refractive indices. It works by emitting collimated, polarised light of varying wavelengths onto a sample at a known incidence angle and measuring the ellipsometric angles Ψ and Δ, which are defined by the ratio of the complex Fresnel equations r_s and r_p, corresponding to parallel and perpendicular polarised light, respectively [266–268]:

$$\rho = \frac{r_p}{r_s} = \tan(\Psi)e^{i\Delta} , \tag{3.1}$$

where

$$\tan(\Psi) = \frac{|r_p|}{|r_s|} \tag{3.2}$$

and

$$\Delta = \delta_p - \delta_s , \tag{3.3}$$

where δ_x represents the change in phase of the light polarised in the x direction. The angles Ψ and Δ are measures of the change in amplitude and phase, respectively, of the light after refraction through the coating and reflection back to the detector. If the wavelength-dependence of the sample material's refractive index is known, then the thickness of the sample can be determined from measurements of Ψ and Δ and use of equations 3.1 through 3.3 as well as the Fresnel equations.

Figure 3.6 shows example ellipsometer measurements, where three silicon samples with varying thicknesses of thermally grown SiO_2 were probed with wavelengths from 320 to 790 nm at an incident angle of 70°. There is only a difference of about 35 nm between each thermal oxide thickness from 15 to 94 nm, but there is a marked difference in both Ψ and Δ for the three thicknesses. Ellipsometry is accurate to the

*The opposite is true in this frequency range for thermoelastic loss with respect to thickness on the micrometer scale. This is shown in figure 4.2 in section 4.2.2.1, where an increase in cantilever thickness from 50 µm to 80 µm results in higher cantilever thermoelastic loss across all temperatures.

sub-nanometre when the refractive indices are well known, as is the case for crystalline silicon and thermally grown silicon dioxide. It should be noted that the reason behind the observed deviation in measured Ψ and Δ from the model at wavelengths below $\sim$400 nm is unknown but thought to originate from an inaccurate silicon dioxide model; the refractive index of SiO_2 changes very little from wavelengths of 400 nm to 800 nm but increases rapidly with decreasing wavelengths below 400 nm. It is reasonable to assume that the silicon dioxide model has a change in refractive index in this 'volatile' wavelength range not matching that of the measured, thermally grown silica on top of the etched silicon cantilevers.

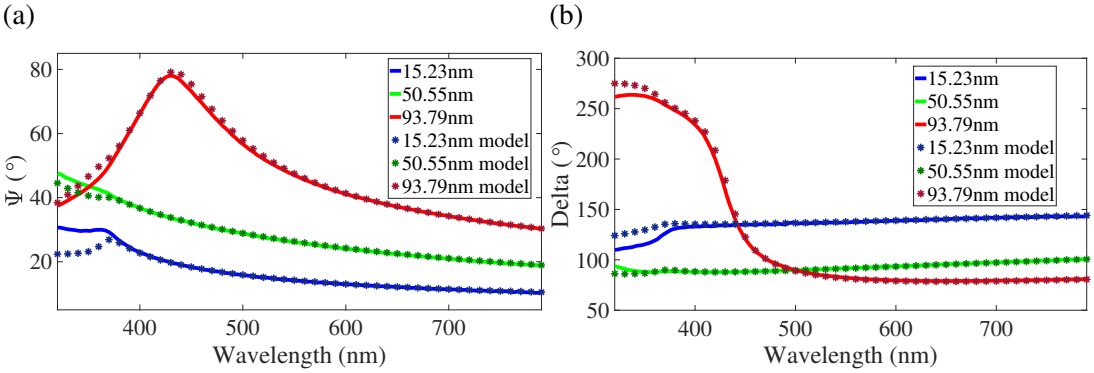

Fig. 3.6 Ellipsometer measurements of the thermal oxide on three different cantilever samples. (a) Psi is related to the amplitude, and (b) Delta the phase shift, of the light after reflection off the sample.

3.3 Temperature-dependent coating mechanical loss

3.3.1 Cantilever loss analysis

As discussed in Chapter 2, mechanical loss is the energy dissipated per cycle of motion in an oscillating system, normalised to the total energy within the system. Physical oscillations within a system are induced by exciting resonance at eigenfrequencies, which are determined by substrate geometry and material properties. The mechanical loss angle of a given sample (cantilevers in this case) can be determined by measuring the time dependent amplitude decay, $A(t)$, of a freely resonating eigenmode at frequency f:

$$A(t) = A_0 e^{-\pi f t \phi(f)} , \tag{3.4}$$

where A is the amplitude at time t and A_0 is the amplitude at $t = 0$. The characteristic decay time, τ, for equation 3.4 represents the time at which amplitude has reduced by a factor of $1/e$ from A_0, and is inversely proportional to the total loss of the resonating sample for this mode frequency:

$$\tau = \frac{1}{\phi(f)\pi f} \,. \tag{3.5}$$

Cantilevers have two primary forms of eigenmodes: bending modes and torsional modes, both of which are shown in figure 3.7 and can be excited by the experimental apparatus described in section 3.3.2. The frequencies at which a cantilever of length L and thickness t_s has bending mode resonances can be found using the formula [269]:

$$f_n = \Gamma^2 \frac{t_s}{4\pi\sqrt{3}L^2} \left(\frac{Y_s}{\rho}\right)^{\frac{1}{2}} \,, \tag{3.6}$$

where n is the mode number, and Y_s and ρ are the Young's modulus and density of the cantilever material. Γ represents a mode-dependent constant; Γ is 1.875, 4.694, 7.853, 10.996 and 14.137 for modes $n = 1$ to 5 and is approximated by $\frac{\pi}{2}(2n-1)$ for modes greater than $n = 5$. Equation 3.6 is used to find the bending modes measured via the method described in section 3.3.2 based on approximate cantilever thicknesses and known substrate material properties. A more accurate thickness of the cantilever can be determined using equation 3.6 once f_n is found for a number of modes.

(a) (b)

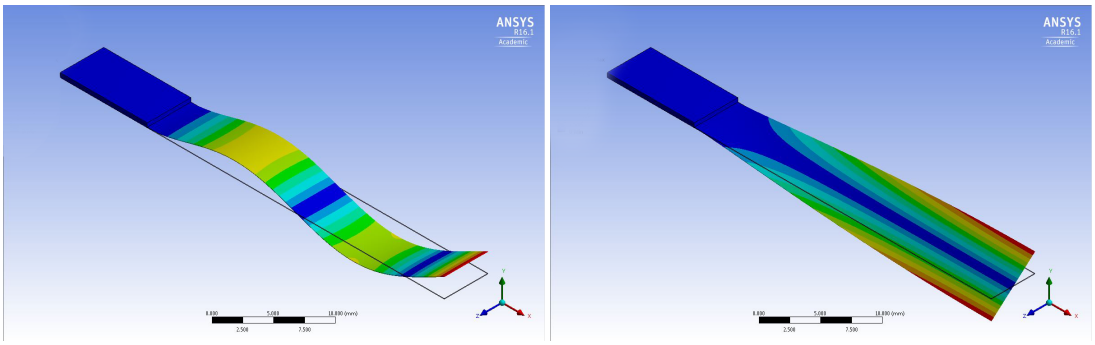

Fig. 3.7 Cantilever substrate eigenmodes, as modelled using ANSYS finite element analysis software. The undeflected cantilever position is given by a black outline, and the colour gradient of the cantilever represents total deflection (blue is minimum, red maximum). Both models are silicon cantilevers with dimensions shown in figure 3.5 and represent (a) the third bending mode (1.356 kHz) and (b) the first torsional mode (1.046 kHz).

The measured loss angle found via equation 3.5 represents the total dissipation of the sample. In the case of a coated cantilever, the total energy lost per cycle of oscillation is comprised of the sum of energy lost within the substrate and energy lost within the thin-film coating:

$$E_{\text{lost, coated}} = E_{\text{lost, substrate}} + E_{\text{lost, coating}} \ . \tag{3.7}$$

It follows from equation 2.16 that dividing equation 3.7 by $2\pi E_{\text{stored, coated}}$ gives the mechanical loss for the coated cantilever:

$$\phi(f)_{\text{coated}} = \frac{E_{\text{lost, substrate}}}{2\pi E_{\text{stored, coated}}} + \frac{E_{\text{lost, coating}}}{2\pi E_{\text{stored, coated}}} \ . \tag{3.8}$$

Coatings usually comprise less than 1% of the coated cantilever thickness, so it can be assumed that the total energy stored within the coated cantilever is approximately equal to the energy stored in the substrate:

$$\phi(f)_{\text{coated}} \simeq \phi(f)_{\text{substrate}} + \frac{E_{\text{lost, coating}}}{2\pi E_{\text{stored, substrate}}} \ . \tag{3.9}$$

The second term in equation 3.9 is equivalent to $\phi(f)_{\text{coating}}$ multiplied by the ratio of energy stored in the coating to the energy stored in the substrate. If this energy ratio is known, then the mechanical loss of a thin-film coating on a cantilever can be calculated from measurements of a bare and a coated substrate [270]:

$$\phi(f)_{\text{coating}} \simeq \frac{E_{\text{stored, substrate}}}{E_{\text{stored, coating}}} \left(\phi(f)_{\text{coated}} - \phi(f)_{\text{substrate}}\right) \ . \tag{3.10}$$

Energy storage and dissipation differ between torsional and bending modes*. There is evidence that torsional cantilever modes have significantly reduced thermoelastic effects, but torsional modes were not included in the coating mechanical loss results presented in Chapters 4-6 so will not be covered in detail within the scope of this thesis. It should be noted, however, that the vibrational frequencies of torsional modes can sometimes overlap with bending mode frequencies during measurements. This is thought to be a significant source of error for some bending mode measurements, as will be discussed in section 4.3.1.

The energy ratio for coated cantilever bending modes can be found by considering a beam of thickness t_s, length L, and width u, with a thin coating layer of thickness t_c. When the beam is bent to form an arc of angle θ, as shown in figure 3.8, elastic strain

*The energy ratio for a torsional mode can be approximated from equation 3 within [271].

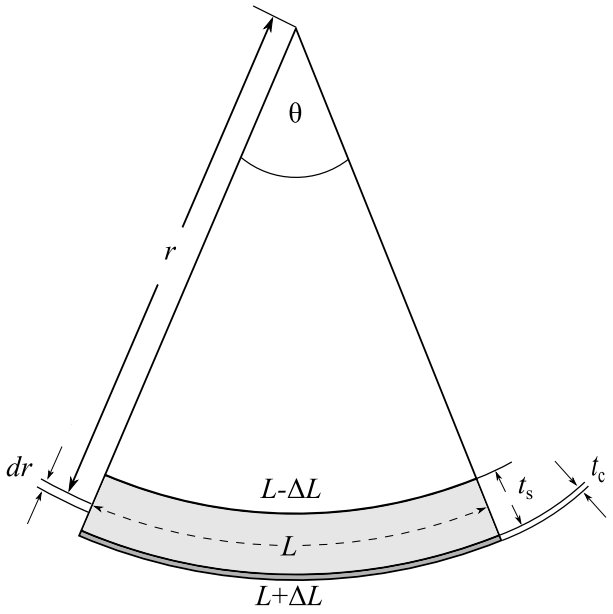

Fig. 3.8 A beam of thickness t_s and length L curved to a radius r. A coating of thickness t_c is applied to one side and lengthened to $L+\Delta L$ by the beam deflection. The dotted line represents the neutral line, where there is no change in length during bending. Above this line the beam is under compression, and below the line the beam is under tension

energy is stored in both the coating and the bulk substrate. The energy in the coating, E_c, as it is stretched from length L to $L+\Delta L$ can be described by

$$E_c = \frac{Y_c t_c u}{2L}\Delta L^2 \,, \tag{3.11}$$

where ΔL can be shown to be $\frac{1}{2}t_s\theta$ and Y_c is the Young's modulus of the coating [272]. In order to find the energy stored in the bulk of the beam substrate, it is assumed that the shorter half of the beam in compression has stored energy equal to that of the longer half of the beam under tension. The energy stored within a small slice of the substrate under tension can be given as:

$$dE = \frac{Y_s u \Delta L^2}{2L} dr \,, \tag{3.12}$$

where Y_s is the Young's modulus of the substrate, and ΔL is equal to $(r-r_0)\theta$. Substituting for ΔL and integrating over the full tensile half of the deflected beam gives:

$$\frac{E_s}{2} = \int_r^{r+\frac{t_s}{2}} \frac{Y_s u \theta^2}{2L}(r-r_0)^2 dr \;=\; \frac{1}{48}\frac{Y_s u \theta^2 t_s^3}{L} \,. \tag{3.13}$$

Multiplying equation 3.13 by 2 gives the total stored elastic strain energy within the substrate. Dividing this strain energy by equation 3.11 results in the ratio of energy stored within the substrate to that stored in the coating:

$$\frac{E_s}{E_c} = \frac{Y_s t_s}{3 Y_c t_c} \ . \tag{3.14}$$

Equation 3.10 can now be rewritten such that the mechanical loss of a coating on a cantilever can be calculated solely from material properties of the coating and substrate and measurements of bending mode energy dissipation of the coated and uncoated cantilever:

$$\phi(f)_{\text{coating}} \simeq \frac{Y_s t_s}{3 Y_c t_c} \left(\phi(f)_{\text{coated}} - \phi(f)_{\text{substrate}} \right) \ . \tag{3.15}$$

3.3.2 Experimental method for measuring cantilever mechanical loss

3.3.2.1 Measurement apparatus and technique

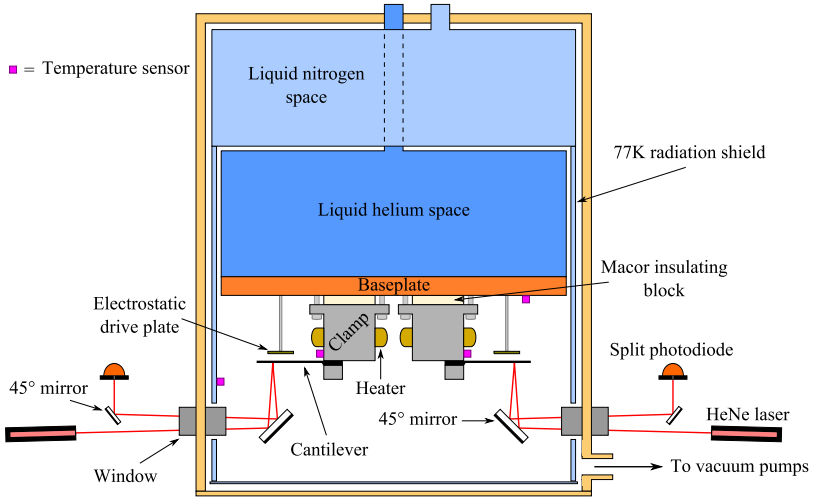

Fig. 3.9 A schematic diagram of the cryostat with dual clamps and optical lever readouts. The liquid nitrogen space is a cylindrical shell with an internal volume of 4.37 L and the liquid helium space is a cylinder with a volume of 4.39 L. A combination of roughing and turbo vacuum pumps keeps pressure in the ∼10 L measurement space below 10^{-5} mbar during cooling and measurement.

Cryogenic cantilever mechanical loss measurements were made using the setup shown in figure 3.9. Room temperature loss measurements with silica cantilevers were taken using a similar apparatus and technique but without any of the temperature

regulation hardware or software. Cantilevers were clamped in a two-piece stainless steel clamp, where one piece is a large ($4 \times 3 \times 5$ cm) base with flanges for rigid attachment to the base of the measurement space and the other is a small ($4 \times 1 \times 1$ cm) piece able to be tightened over the cantilever clamping block using two M4 hex screws. The compression under which cantilevers are clamped directly affects the efficiency with which the cantilever clamping block isolates the energy loss within the cantilever blade. Loose clamping of the sample results in excess stick-slip energy loss at the clamp-cantilever interface, but too much sample compression when affixed at room temperature can result in cracks or breakage of the clamping block when cooled to 10 K due to the differing thermal expansion of crystalline silicon and stainless steel. The surfaces of the clamp in contact with the cantilever were polished and then buffed to a mirror finish to reduce the likelihood of breakage because of over tightening. Polishing was done using a Struers Labo-Pol-4 lapping machine with 1 µm grit polish. The pieces were then buffed with Brasso metal polish.

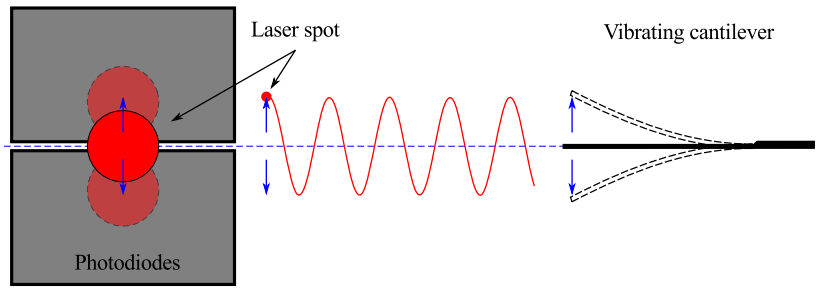

Fig. 3.10 A split photodiode detector, aligned with the return laser spot from the optical lever shone incident in the middle of the two photodiodes. The laser spot oscillates across the photodiodes at the same frequency as the vibrating cantilever.

Once the samples were clamped, the cryostat was pumped down to below 10^{-5} mbar in order to reduce gas damping to a negligible level during cantilever vibration [253]. The cantilever vibrations were monitored using an optical lever system, where a HeNe laser was shone through an infrared filtered window* in the cryostat and reflected off a 45° mirror onto the top face of the clamped cantilever, where the spot was then reflected back onto the same mirror and out of the cryostat. Any small oscillation of the cantilever blade causes lateral movement of the return spot, which was incident on a split photodiode (shown in figure 3.10) and converted to a sinusoidal voltage signal corresponding to the frequency and amplitude of cantilever oscillation.

Cantilever resonances were excited using an electrostatic drive plate positioned about 2 mm to 5 mm below the free end of the clamped cantilever. Electrostatic drives

*The filtered window reduces the influx of ambient heat into the cryostat chamber.

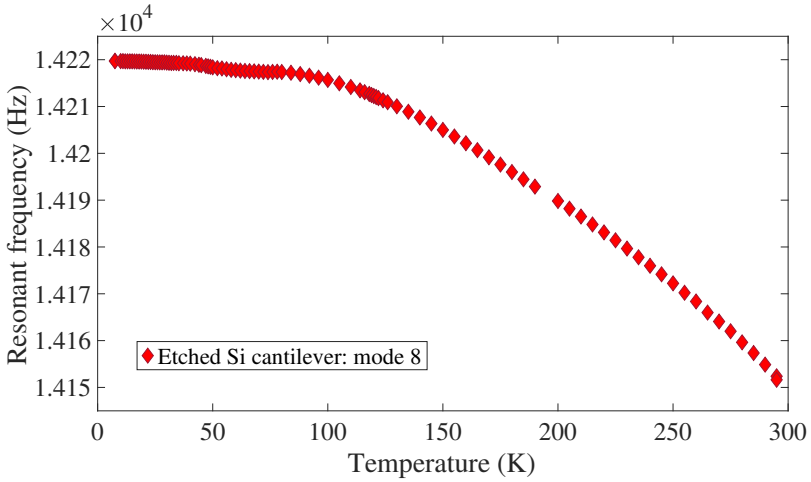

Fig. 3.11 Change in resonant frequency with respect to temperature for the eighth bending mode of an etched silicon cantilever. Each mode experiences a similar percentage change in resonant frequency over this temperature range.

create inhomogeneous electric fields that induce a force on nearby dielectric materials proportional to the inverse square of the distance, and are used to both control the position of and dampen excitations within dielectric mirrors [273, 274]. The drive plate consisted of a circuit board with two sets of copper electrodes positioned as an interlocking 'comb', where one set was grounded and the other was attached to a high voltage source. An oscillating high voltage signal ~ 3 Hz to 6 Hz below the targeted mode frequency was sent to the electrostatic drive and then swept upwards in frequency until a peak was seen in the cantilever deflection amplitude, whereafter the voltage signal was dropped to zero and the cantilever allowed to freely resonate. This sweeping technique was necessary to follow the shift in resonant frequency with respect to measurement temperature, which is shown for an uncoated silicon cantilever in figure 3.11 and occurs due to the temperature-dependent variation of the cantilever's Young's modulus [263]. A schematic of the drive used to excite cantilever resonances can be seen in figure 3.12. The DC offset and root mean square of the oscillatory voltage varied depending on the mode frequency, separation between the drive plate and the cantilever, and the position of the laser spot on the face of the cantilever in relation to mode nodes and antinodes.

Once mode frequencies were confirmed and room temperature loss shown to be limited by thermoelastic loss, which is indicative of clamp quality and adequate vacuum pressure, both cryogen spaces in the cryostat were filled with liquid nitrogen and the baseplate, samples, and nitrogen shield cooled to $\sim$77 K. Liquid nitrogen was then removed from the helium space and replaced with liquid helium. The

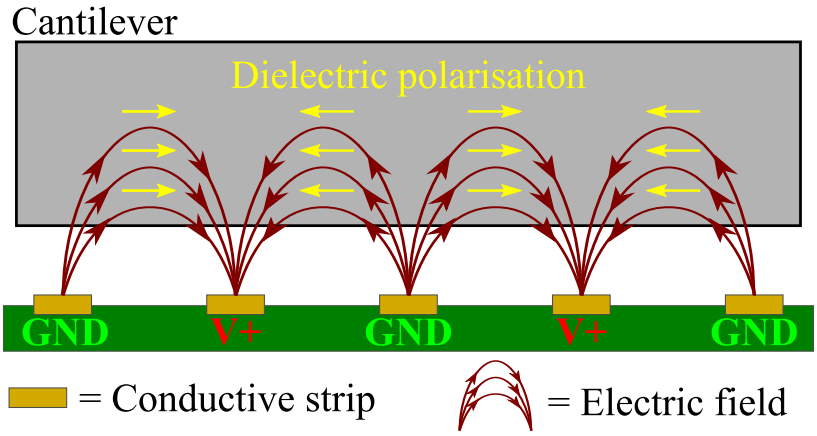

Fig. 3.12 Simplified schematic of the electrostatic drive used to excite resonances of the dielectric cantilevers.

baseplate reached ∼5 K but samples only reached a minimum temperature of ∼8 K due to the heating power of the laser and stray radiation entering through the filtered cryostat windows. Temperatures were monitored using calibrated Lakeshore DT-670-SD silicon diode temperature sensors, which were located on the nitrogen shield, baseplate, and cantilever clamp, and are rated at an accuracy of ±12 mK from 1.4 K to 77 K and ±22 mK from 77 K to 300 K [275].The temperature along the length of the cantilever was taken to be the same as that at the clamping block due to the high thermal conductivity of silicon*.

Loss measurements were first carried out at 8 K, after which the samples were heated to the next temperature step using two resistive heaters attached to the clamp and measured again; measurement temperatures and step sizes are shown in table 3.1. Temperatures were controlled using a Lakeshore 340 PID temperature controller, with a maximum power output of 25 W (50 V at 2 A) [277]. Each cantilever mode was measured twice at every temperature step.

3.3.2.2 Data acquisition

Early measurements were conducted with one sample clamped and measured during each cooling cycle and controlled with a LabView software program created by Ronny Nawrodt, a former member of IGR. The system was then upgraded to measure two samples simultaneously and the majority of results presented in chapters 4, 5, and 6

*The thermal conductivity of crystalline silicon is strongly temperature dependent. It is ∼424 W/(m K) at 5 K, reaches a maximum of ∼5140 W/(m K) at 25 K and then decreases with higher temperatures, reaching ∼148 W/(m K) at 300 K. Listed values are quoted with a maximum of 10% error. [276]

Table 3.1 Temperature steps for cryogenics mechanical loss measurements. Extra fidelity was chosen for temperatures below 50 K and around 120 K, which encompasses the possible temperatures of future cryogenic gravitational wave detectors as well as areas of interest for coating structural changes seen through mechanical loss. Measurements at a new temperature step began only after the sensors at the cantilever clamp registered a temperature within ± 0.05 of the set temperature, with a change in temperature of less than 0.01 $\mathrm{K\,h^{-1}}$ for 1 K and 1 K steps, and a change in temperature of less than 0.1 $\mathrm{K\,h^{-1}}$ for 4 K and 5 K steps.

Sample temperature range (K)	Temperature step size (K)
8-50	1
50-80	2
80-100	4
100-110	5
110-114	4
114-118	2
118-122	1
122-126	2
126-130	4
130-295	5

were obtained with this new, improved setup. The upgrade consisted of duplicating the hardware necessary for sample clamping, temperature control, excitation, and observation, as well as altering the LabView software to accommodate an extra sample measurement channel.

Temperature control remained the same, with the only addition being a second heater channel and monitor; both samples are kept at the same temperature through all temperature steps. The single channel photodiode voltage monitor previously operated only when the sample was under excitation or free decay and was otherwise ignored. This was a problem for the dual channel setup, since the photodiode outputs could not be independently measured at will. The issue was overcome by having both photodiode voltage signals monitored constantly and frequency/amplitude data pulled from the data stream when needed. This can be seen in figure 3.13b as a digital oscilloscope screen in the user interface page for sample excitation and ringdown. The sampling rate needed to be reduced to 100 kHz in order to maintain efficient running in this configuration.

(a)

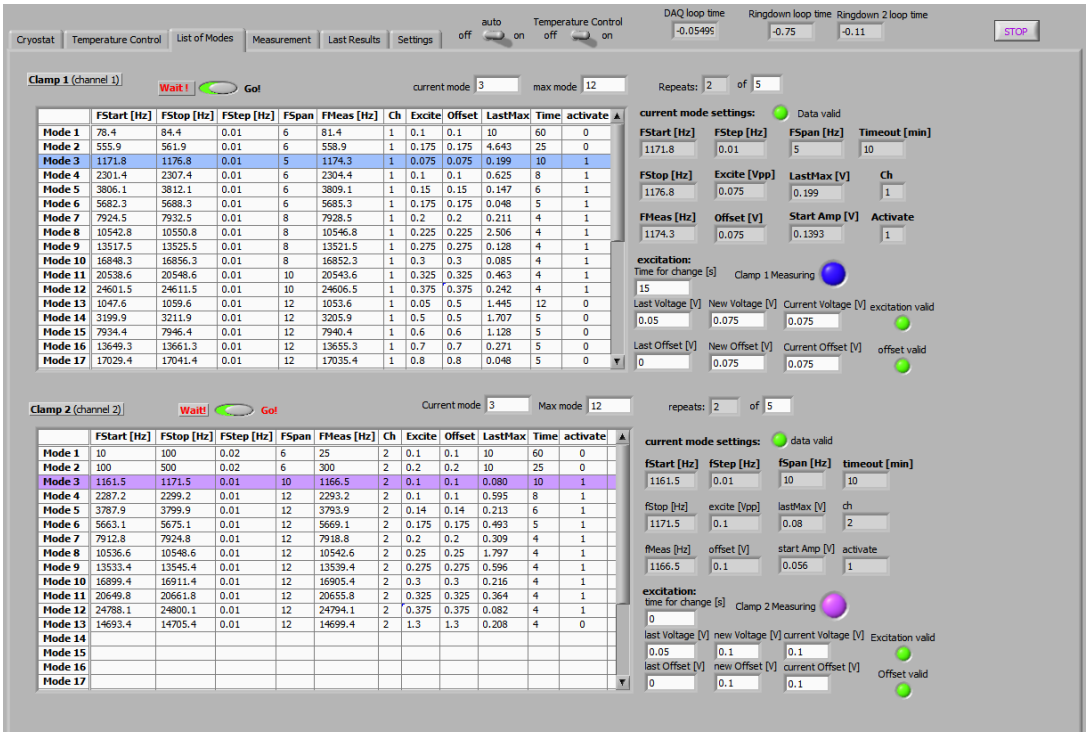

(b)

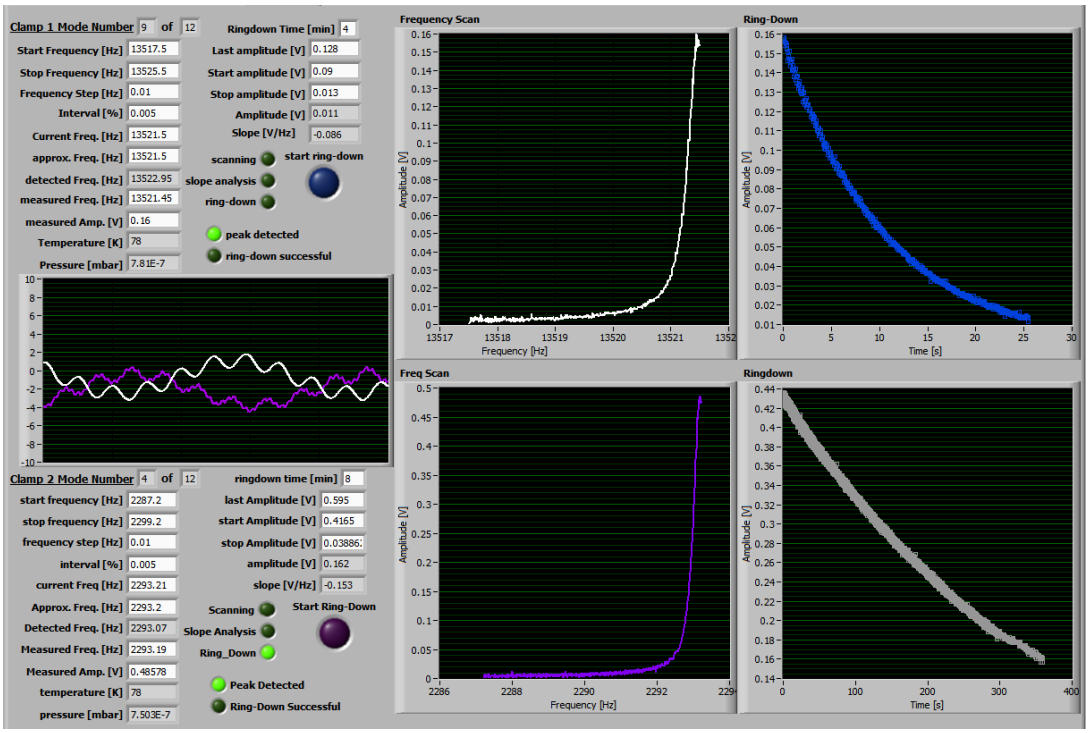

Fig. 3.13 (a) Mode tables for both clamps under simultaneous measurement. (b) Measurement screen for dual clamp upgrade, where the top and bottom pair of graphs represent clamps one, and two, respectively.

The new system allows for fully independent, simultaneous mode incrementing, ringing up, and ringing down for two samples at each temperature step, thus doubling the rate of measurement for the cryostat without requiring extra cryogens or increasing the time at each temperature step. The user interface for this simultaneous sample measurement can be seen in figure 3.13a.

One possible source of error with the dual channel measurement system could be energy transfer between the two resonating cantilevers with similar mode frequencies. Both clamps are attached to the same baseplate through rigid screws, so resonant vibrations of one cantilever could possibly effect the ring down of the other cantilever. The majority of samples measured during the same cooling cycle were chosen to have significantly different thicknesses for this reason. However, figure 3.14 shows the amplitude decay of two clamped cantilevers with nearly identical mode frequencies, where the cantilevers were measured one at a time, at the same time, and with one sample delayed to begin excitation while the other is already ringing down. While there is an observable difference between the ringdowns, this difference is well within the spread of values seen between multiple measurements of one sample mode. In other words, any change in exponential decay and, subsequently, mechanical loss caused by energy transfer between clamps is less than the expected measurement uncertainty.

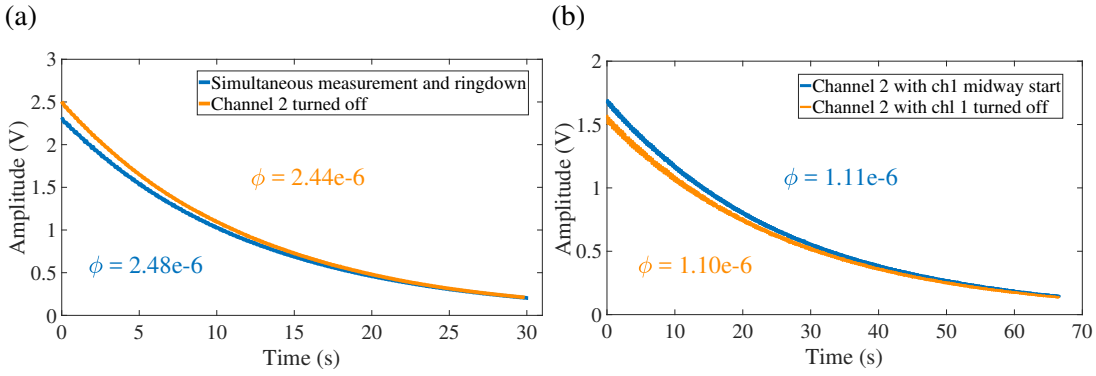

Fig. 3.14 Ringdowns after excitation of nearly identical mode frequencies of bare silicon cantilevers held at 80 K in the dual clamp cryostat. (a) Graph of two mode 8 ringdowns from channel one showing one measurement without the second clamp operating and another where the same mode is measured at the exact same time on channel two. (b) Graph of two mode 8 ringdowns from channel two showing one measurement without channel one operating and another where the same mode is measured on channel one halfway through the channel two measurement. Both tests show a change in loss of less than 2%, which is consistent with measurement differences in a single clamp cryostat.

3.4 Coating stress from sample curvature

3.4.1 Theory

Stress in optical coatings is of interest due to its possible influence on coating mechanical loss and, thus, thermal noise [232]. Additionally, recent results suggest multilayer coatings measured on silica disc substrates have a mechanical loss value that differs from the loss measured using thin silicon cantilever substrates [278]. One possible explanation for this discrepancy could be stress within the coating and the resulting, differing curvatures of substrates.

The deposition of thin-film coatings on a relatively thick substrate produces a combination of thermal and intrinsic stress. The thermal stress component arises from deposition temperature parameters and the difference in the thermal expansion coefficients between the substrate and film. The combination of these elements can be seen in the relation [279]:

$$\sigma_{\text{coating}} = \sigma_{\text{I}} + (\alpha_{\text{s}} - \alpha_{\text{c}})\, B_{\text{c}} \Delta T \ , \tag{3.16}$$

where σ_{I} is the intrinsic stress in the coating, ΔT is the difference between measurement and deposition/heat-treatment temperature, α_{s} and α_{c} are the thermal expansion coefficients of the substrate and coating, and B_{c} is the biaxial modulus of the coating and is defined as: $B_{\text{c}} = \frac{Y}{1-\nu}$, where Y and ν are the Young's modulus and Poisson ratio of the coating material. As previously mentioned, coating deposition often takes place at elevated temperatures, so the subsequent cooling to room temperature produces a thermal stress. This thermal stress can be seen to change while the sample changes temperature [280]. The intrinsic stress is thought to originate due to the films formation in a state of non-equilibrium [281].

Both the intrinsic and thermal stress in a deposited coating can be seen by the physical deflection of the substrate, as shown in figure 3.15. Biaxial compression/tension in the coating and the corresponding tension/compression in the substrate reach an equilibrium state, which results in macroscopic curvature of the coated sample [282]. The curvature of a substrate can therefore be used to determine the magnitude of the stress present in the corresponding thin-film coating. The stress-curvature relation can be shown to be described by a modified version of Stoney's equation [283]:

$$\sigma_{\text{coating}} = \frac{B_{\text{s}} t_{\text{s}}^2}{6 t_{\text{c}}} \left(\frac{1}{R} - \frac{1}{R_0} \right) \ , \tag{3.17}$$

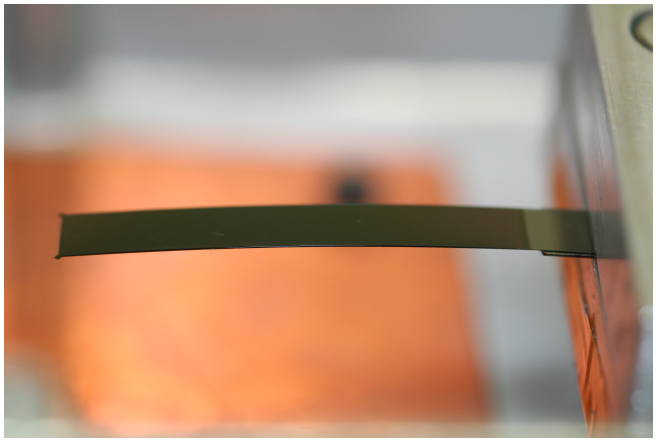

Fig. 3.15 Curvature induced in a ∼74 µm thick silicon cantilever due to compressive stress from the deposition of 5.22 µm of niobia via DC magnetron sputtering. The cantilever is curved to a radius of ∼23 cm.

where σ_{coating} is the stress in the coating, t_c and t_s are the thicknesses of the coating and substrate, B_s is the biaxial modulus of the substrate, R is the radius of curvature of the coated cantilever, and R_0 is the radius of curvature of the cantilever prior to coating. R_0 is assumed to be infinite for the cantilevers used in measurements, as they are sufficiently flat to be of negligible curvature prior to coating [280].

While the origin and nature of the stress components within a thin-film coating are not fully understood [232, 279], the magnitude and sign of the coating stress can be determined through equation 3.17, which only requires knowledge of the substrate material properties and experimental determination of the radius of curvature of a coated sample.

3.4.2 Experimental apparatus

Cantilever radii of curvature were determined with the apparatus shown in figure 3.16, where a laser beam was split into two parallel beams a distance x apart using a beam-splitter and a 45° mirror and shown incident on the curved sample. The parallel beams reflect off the face of the cantilever and travel a distance, L, to a screen behind the laser. In order to achieve a longer path length, the laser light is bounced between multiple mirrors after being reflected from the curved cantilever. This provides a much larger distance over which the beams deviate, thus reducing the error of the final separation measurement. L is the total beam path after reflection off the sample and is comprised of multiple distances, l_n, which represent the reflections within the folded mirror system. Figure 3.16 shows three reflections, one off the sample and two from perpendicular mirrors, and thus L is the sum of l_1, l_2, and l_3. The final separation

distance, D, of the reflected beams is measured on a screen kept perpendicular to the incident beams.

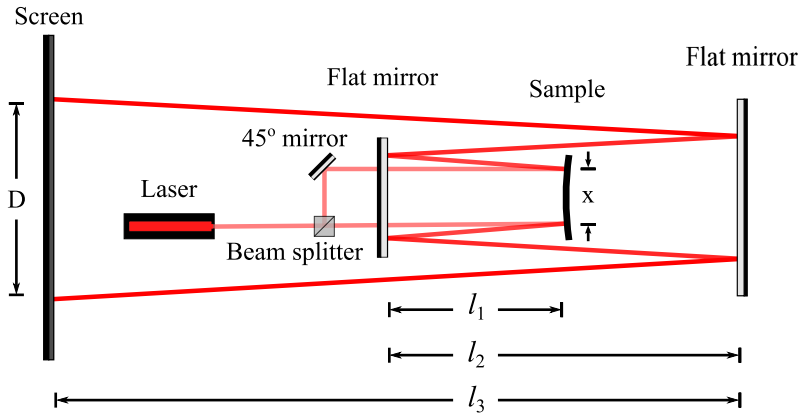

Fig. 3.16 Radius of curvature measurement apparatus. Both beam paths are shown to diverge for the sake of clarity; measurements were taken such that the un-split portion of the laser beam was reflected upon itself to reduce the beam spot size error on the separation distance D.

The radius of curvature of the cantilever, R, was calculated with the relation:

$$R = \frac{2Lx}{\delta}\,, \tag{3.18}$$

where x is the initial separation of the parallel beams and δ is the distance of the beam deflection, defined by $\delta = D - x$. D will be negative in cases where the curvature of the cantilever causes the reflected beams to cross. Concave samples result in negative radius values, and convex samples are measured as positive. This corresponds to compressive and tensile stress values when the laser beam is reflected off the coated side of the cantilever [280, 284].

Each sample was measured up to seven times to ensure accurate radius values. The initial separation of the parallel beams (x) was set at the full length of the cantilever for one measurement and then reduced to $\sim$2.5 cm for the rest, which were moved across the face of the sample. This ensured that the radius was sampled from multiple sections of the cantilever, giving insight into the consistency of the curvature along the length of the cantilever, while the full cantilever length radius measurement benefited from a smaller error due to the larger initial beam separation distance. The system was realigned for each change in x and was found to produce a dual beam deviating from parallel by $\pm$2.0 mm over a distance of 18.177 m. The dominant source of error in the multi-reflection system is the measurement of the initial beam separation, x, which is 8% for a separation of 2.5 cm. Calibration was carried out in the form of radius

measurements for three mirrors of known curvatures: 100 cm, 30 cm, and 20 cm. All three radii measurements were within 2% of the manufacturer specifications.

3.5 Conclusion

Ion beam sputtered coatings are the current standard for the highly reflective multilayer mirror coatings on the test mass mirrors within gravitational wave detectors. This form of physical vapour deposition has been shown to produce high quality thin-films, but other deposition techniques, such as the similarly ablative magnetron sputtering techniques or the evaporative but highly energetic ion plating deposition, have the potential to produce coatings of interest for research into both thin-film structure and improved mechanical loss for better mirror coatings.

Coating mechanical loss can be calculated from the material properties of the coating and the substrate and measurements of the sufficiently low loss substrate prior to coating and post-deposition. The cantilever substrate geometry ensures minimal energy transfer between the resonating sample and its clamp, improving the accuracy of mechanical loss measurements. Welded, fused silica cantilevers are used for room temperature mechanical loss measurements due to their high room temperature quality factor and insignificant thermoelastic loss contribution. Etched, crystalline silicon cantilevers are used for mechanical loss measurements at cryogenic temperatures because of their lower loss and higher thermal conductivity than fused silica at low temperatures. A system was designed to allow characterisation of two coatings simultaneously during one thermal cycle from 8 K to 295 K without any interference due to energy coupling between samples, thus improving the rate at which coating mechanical loss can be measured.

Coatings deposited on either substrate material will induce stress due, in part, to differing thermal expansion coefficients between the coating and substrate. This stress can be calculated from the radius of curvature of the coated cantilevers, since the coating stress has a corresponding strain that manifests as deflection of an otherwise straight cantilever blade. Understanding the change in stress in relation to changes in mechanical loss may give an insight into the mechanisms behind coating internal energy dissipation and, consequently, thermal noise in gravitational wave detectors.

Chapter 4

Mechanical characterisation of ion-beam sputtered silica

4.1 Introduction

Ion beam sputtered amorphous silica has remained unchanged as the low index layer in multilayer test mass coatings for second generation detectors due to its excellent optical properties and low room temperature mechanical loss, which has been previously shown to be strongly dependent upon post-deposition heat treatment, with minimum loss occurring after annealing at ∼950 °C [285]. The multilayer IBS SiO_2/Ti:Ta_2O_5 coatings require heat treatment to improve both loss and optical properties for use in aLIGO and Advanced Virgo. Optical absorption, a primary limiting factor in coating materials for use in the detectors, usually decreases with some amount of post-deposition heat treatment. This heat treatment temperature is currently limited to 500 °C by the tantalum pentoxide layers, which have a low crystallisation temperature and are also the dominant source of mechanical loss within the coating stack [158, 256].

Future detector designs include operation at cryogenic temperatures of ∼10 K to 20 K or ∼120 K*. Bulk fused silica has been well characterised at low temperatures and exhibits a broad peak in mechanical loss between 30 K and 40 K, where the mechanical loss increases from 1×10^{-8} to 1×10^{-9} at room temperature up to $\sim 1 \times 10^{-3}$ at the low temperature peak [208, 262, 286, 287]. Previous studies of thin film silica have shown that the method of film growth greatly affected the low temperature mechanical loss characteristics: the presence of a low temperature peak was absent from electron-

*See section 1.6.5, and references thereof, for more details on future detectors designs.

beam evaporated SiO_2*, but thermal oxide growth on silicon and IBS SiO_2 heated to 600 °C both exhibited a low temperature mechanical loss peak [258, 271].

Combined with the low temperature loss peaks seen in pure and titania doped tantalum pentoxide [229, 256, 280] it would follow that the loss of a multilayer coating stack with IBS silica layers would display a low temperature peak in mechanical loss. However, the temperature dependent mechanical loss of mulitlayer silica/tantala coating stacks has been measured in multiple experiments and the results were equivocal. A clearly defined peak was apparent in measurements of silicon cantilevers coated with the IBS multilayer coating by Laboratoire des Matériaux Avancés (LMA) and heat-treated at 500 °C [229, 231], but the same IBS coating stack deposited on sapphire discs by both the JAE (annealed) and NAOJ† (not annealed) seemed to display no peak in loss with five measurements between 4 K to 80 K [230].

Extensive mechanical loss studies after a wide range of post-deposition heat treatment temperatures have been performed between 10 K to 300 K for Ta_2O_5 and Ti:Ta_2O_5, as well as for potential future high index coating materials, and have resulted in better understanding of coating structure and mechanical loss [229, 256, 259, 280]. The loss of silica has been characterised after heat-treatment at 600 °C [258], but has largely been overlooked in favour of research into high index materials. Measurements of the temperature dependent mechanical loss of amorphous silica with incremental heat treatment from deposition temperature to the optimum anneal for room temperature loss at ∼950 °C would therefore be valuable for better understanding the dissipation mechanisms within thin film silica, as well as for obtaining accurate mechanical loss values at low temperatures for comparisons and thermal noise calculations related to coating stacks for use in cryogenic detectors. It would also give a much more comprehensive starting point from which to understand the significant differences in mechanical behaviour between bulk and thin-film silica, which could be crucial in producing future coating materials. This chapter presents the mechanical loss of IBS silica from ∼10 K to 200 K as well structural characterisations intended to gain a better understanding of the link been the internal structural changes through heat treatment and coating mechanical loss.

*Electron-beam sputtered silica loss results presented by White and Pohl showed no peak in their measured temperature range (0.05 K to 100 K) [271]. A peak could exist above these temperatures, as the loss was increasing at the upper range of measurement temperatures.

†Japan Aviation Electronics Industry, Ltd. and National Astronomical Observatory of Japan, respectively.

4.2 Sample preparation

4.2.1 Coated samples

Eight silicon cantilevers etched from the same wafer were coated by IBS with 511 ± 4 nm of amorphous silica by Advanced Thin Films (ATF) [240]. No active substrate heating was used during deposition, but the substrates reached a maximum temperature of $\sim 90\,^{\circ}$C during the sputtering process. All of the cantilevers were heated at $1000\,^{\circ}$C for 15 minutes prior to coating in order to grow a thin layer of thermal oxide, which aids in coating adhesion and consistency [229]. The 15 minute bake resulted in an average of $\sim$19 nm of thermal oxide on each side of the cantilever. It was found that the etched side of the coated cantilevers* had an increase in silica thickness of 47 ± 5 nm after deposition of the 511 nm coating on the opposite side. Dry thermal oxide growth on [100] crystalline silicon is well modelled for thicknesses at and above 20 nm and has been shown to be strongly pressure and temperature dependent [288, 289]. The growth rate is insignificant at temperatures below $700\,^{\circ}$C, where the rate reaches less than 1 nm per hour [290]. Thermal oxide growth on the substrate is therefore insignificant at the temperatures reached during deposition. Furthermore, the diffusion rate of oxygen atoms into the oxide-silicon interface decreases with lower atmospheric pressure, limiting oxide growth in vacuum [289]. It was therefore assumed that the $\sim$47 nm of silica seen on the etched side of the cantilever was 'overspill' of sputtered atoms during deposition, so it was added to the other $\sim$511 nm to create a total coating thickness of 558 ± 6 nm, which is the final value used to calculate mechanical loss for all heat treatments. A representative coating-oxide-cantilever thickness profile can be seen in figure 4.1.

Post-deposition heat treatment was carried out in atmosphere, where samples heat-treated at or below $600\,^{\circ}$C were heated from room temperature to the desired temperature over the span of $\sim$ 1 hour and held at a constant temperature for 4 hours before cooling to room temperature overnight. Table 4.1 shows the post-deposition heat treatments with corresponding sample numbers, cantilever thickness, and total thickness of thermal oxide between the silicon cantilever and the IBS silica coating. Samples 7 and 4 were put into the oven at the desired temperature ($800\,^{\circ}$C and $950\,^{\circ}$C, respectively) in order to minimise the growth of thermal oxide on the uncoated side of the cantilever during ramp up; both samples were allowed to cool overnight. Significant thermal oxide growth was observed via ellipsometry measurements of sample 4 heat-

*Cantilevers are coated on the non-etched side of the blade due to increased surface roughness as a result of the wet-etch process [280].

Table 4.1 ATF IBS SiO_2 silicon cantilever sample properties. Cantilever thicknesses were calculated from equation 3.6 using the bending mode frequencies found during mechanical loss measurements. Listed heat treatments correspond to presented results. Samples that were measured without any post-deposition heat treatment are labelled AD (as deposited). Thermal oxide thickness is a combination of the oxide grown prior to coating and any measured increase in silica thickness after heat treatment (increase only seen in 950 °C treated samples.)

Heat treatment (°C)	Sample number	Cantilever thickness (μm)	Total thermal oxide thickness (nm)
AD	3	81.1 ± 0.2	33 ± 3
300	7	80.5 ± 0.4	41 ± 4
	8	80.4 ± 0.3	44 ± 5
450	11	80.5 ± 0.1	41 ± 3
600	3	81.1 ± 0.2	33 ± 3
800	7	80.5 ± 0.4	41 ± 4
950	3	81.1 ± 0.2	88 ± 10
950	4	61.2 ± 0.2	188 ± 14

treated to 950 °C, and therefore a second sample (3) was heat-treated at 950 °C without the elongated cooldown period.

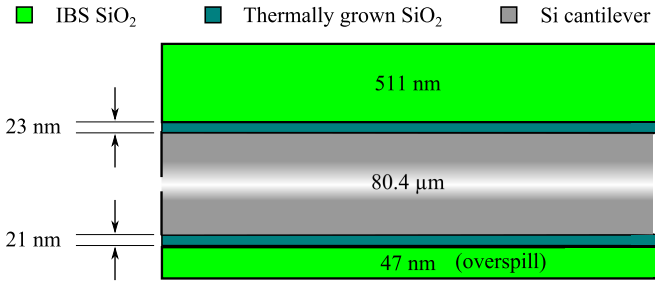

Fig. 4.1 Diagram showing the thickness profile of coated sample 8 (300 °C heat treatment. Thicknesses are not to scale.

The post-deposition heat treatment temperatures listed in table 4.1 were chosen based on previous room and low temperature mechanical loss studies of IBS silica coatings and optimum annealing temperatures for absorption and mechanical loss in high index coating materials of interest. An exception was the 800 °C heat treatment, which was added later to better understand the significant structural changes in the coating seen between the 600 °C and 950 °C heat treatments, as will be shown in section 4.3.

4.2.2 Control samples

Four uncoated silicon cantilevers were kept as control samples to represent the mechanical loss of the substrate during coating loss calculations (as described in section 3.3.1). The efficacy of a control sample in mimicking the substrate loss of a coated sample is dependent on two factors: matching cantilever thicknesses to accurately replicate higher temperature loss, where substrate thermoelastic loss is the dominant dissipation mechanism; and matching thermal oxide thicknesses to replicate loss at low temperatures, where internal dissipation is dominated by the thermal oxide loss peak. The loss of uncoated control samples in these two temperature regimes is discussed in detail in the following sections.

4.2.2.1 Thermoelastic loss control matching

Thermoelastic loss in the uncoated silicon substrate is the dominant source of dissipation at temperatures above $\sim$185 K at the lowest frequency modes and, as shown in figure 4.2, is frequency and thickness dependent; it increases with both mode frequency and cantilever thickness for the frequencies of interest in loss calculations ($\sim$1 to 30 kHz). Thermoelastic loss dominates measured loss values at temperatures as low as $\sim$130 K for the tenth bending mode (around 28 kHz for 80 µm thick cantilever), where a coating loss below 1×10^{-4} is unable to increase the loss of the cantilever enough to be accurately measured above the thermoelastic dissipation*. The control cantilevers were all fabricated from the same silicon wafer as the coated cantilevers, ensuring similar thicknesses and, therefore, similar mode frequencies and thermoelastic loss. As shown in tables 4.1 and 4.3, most of the cantilevers differed in thickness by about 1 µm. The resulting difference in thermoelastic loss between the coated and uncoated cantilevers was within the uncertainty in the calculated thermoelastic loss. One coated cantilever (#4) and one control sample (#9) were significantly thinner than the rest, but were closely matched to each other enabling an accurate estimate of the substrate loss for the coated sample.

The measured mechanical loss data for a number of control samples had gaps† at high temperatures (200 K to 300 K). In these cases the loss of the control sample was

*The inability to distinguish between substrate thermoelastic loss and coating mechanical loss can be seen in figure 4.6 in section 4.3

†The automated measurement system used to collect loss data at each temperature (described in section 3.3.2) occasionally failed to track the change in mode frequency with increased temperature due to a change in cantilever curvature or excitation amplitude. If this occurred at times where the system was not monitored, eg overnight, no loss data would be available for these modes at the measured temperature steps. High frequency modes are more susceptible to this phenomenon due to their greater frequency change with temperature and decreased exponential decay constant, τ.

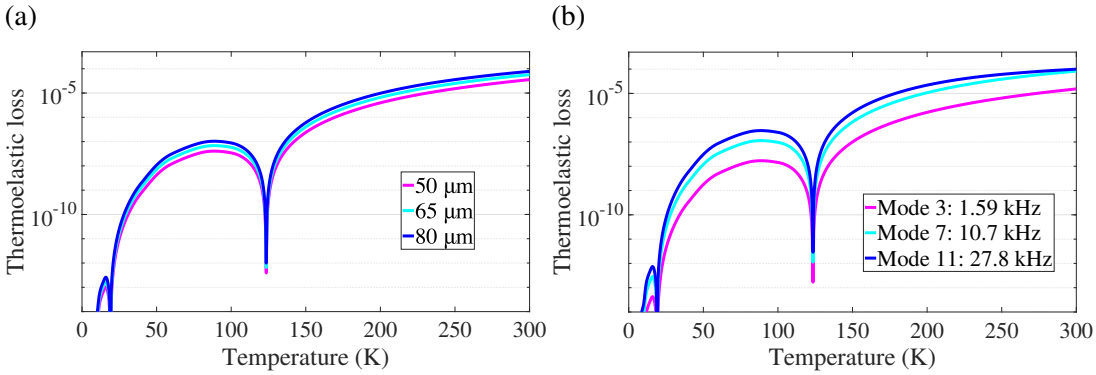

Fig. 4.2 Thermoelastic loss with respect to (a) cantilever thickness, where the frequency remains constant (10 000 Hz) and (b) mode frequency, where the thickness remains constant (80 µm). The troughs in thermoelastic loss correspond to silicon's thermal expansion coefficient passing through zero as it changes from positive to negative at 18 K and then back to positive at 120 K.

estimated to be above the calculated thermoelastic loss of the sample by a constant amount that was dependent on mode frequency. These estimates were first checked against modes with complete loss/temperature datasets before being applied to the incomplete control data. The difference between measured control mechanical loss and the expected thermoelastic loss of the substrate changed mode to mode, but the absolute difference was $\sim 5 \times 10^{-7}$ on average.

4.2.2.2 Thermal oxide loss control matching

Internal friction within the thermally grown amorphous SiO_2 on the faces of the cantilever is the dominant source of the measured loss at temperatures below the influence of cantilever thermoelastic loss. A thermal oxide layer was grown on all of the control samples in the same manner as the coated samples in order to account for the influence of this oxide layer when calculating coating loss. The effect of increasing thermal oxide thickness on the low temperature mechanical loss of a silicon cantilever is shown in figure 4.3, where the magnitude of the loss peak can be seen to be proportional to the oxide thickness. Figure 4.3 also illustrates that thermal oxide thickness has little to no effect on the cantilever mechanical loss above ~120 K where thermoelastic loss in the silicon begins to be the dominant source of dissipation.

The thickness, x_o, of thermally induced amorphous silica growth on crystalline silicon due to diffusion of oxygen in a dry environment has been shown by Deal and Grove to be modelled as a function of time, t, for relatively long oxidation times and thick oxides by [288]:

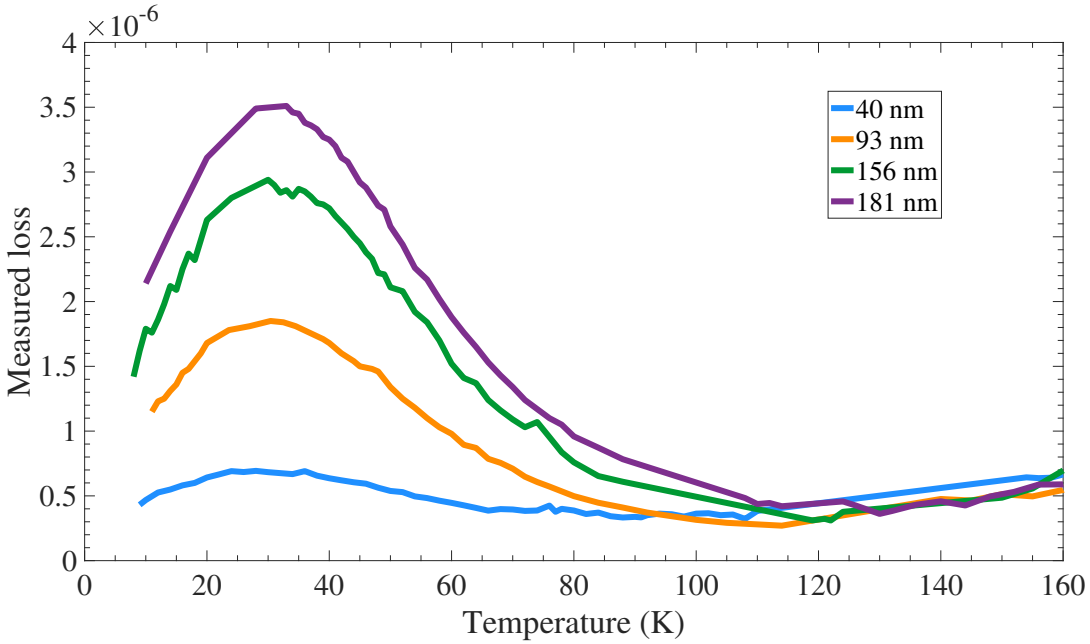

Fig. 4.3 Low temperature mechanical loss peak from various thicknesses of thermally grown oxide on silicon cantilevers. Curves shown are from control samples 9 (blue), 10 (orange), and 12 (green, purple). Sample 12 was heated to grow 156 nm of thermal oxide, and then a further 15 nm was added to better match oxide thicknesses of coated sample number 4 after a 950 °C heat treatment (see tables 4.1 and 4.3).

$$x_o(t) = \frac{A}{2}\left(\sqrt{1+\frac{(t+\tau)}{(A^2/4B)}}-1\right), \tag{4.1}$$

where $\tau = (x_i^2 + Ax_i)/B$ is a corrective time shift based on the initial oxide thickness, x_i. A and B are physically based parameters relating to oxidant equilibrium concentration and diffusivity, the number of oxidant molecules per unit volume of oxide layer, and surface processes at the Si-SiO_2 interface [291, 292]. Both A and B are experimentally determined to be temperature (T) dependent in accordance with the Arrhenius expressions [293, 294]:

$$B = B_0 e^{-E_a/k_B T} \qquad \text{and} \qquad \frac{B}{A} = \left(\frac{B}{A}\right)_0 e^{-E_a^*/k_B T}, \tag{4.2}$$

where k_B is the Boltzmann constant, B_0 and $(B/A)_0$ are experimentally determined pre-exponential constants, and E_a and E_a^* are the activation energies associated with the combination of physical processes contained within B and B/A, respectively. For dry oxidation E_a is equal to 1.24 eV and E_a^* is equal to 2.0 eV. Table 4.2 gives the A and B values for a range of temperatures.

Table 4.2 Arrhenius parameters for Deal and Grove thermal oxide growth model. Values are relevant for dry oxide growth at atmospheric pressure for <100> silicon [294].

Oxidation temperature (°C)	A (μm)	B (μm^2/hr)
800	0.370	0.0011
920	0.235	0.0049
1000	0.165	0.0117
1200	0.040	0.045

The Deal and Grove model, as implemented through use of equation 4.1, was tested for applicability with a set of 12 uncoated silicon cantilevers each heated at 1000 °C for varying times from 20 min to 240 min. Comparison of the predicted and measured oxide growth is shown in 4.4. The measured oxide thicknesses were found to be within 10% of the predicted oxide thicknesses for most growth times. The gap between experimental and predicted thicknesses for the longer growth times is thought to be a result of the continued opening of the oven for sample removal at the shorter baking times. Oxide growth at 990 °C is included in figure 4.4 to show the potential effect of a drop in oven temperature, and it can be seen that this better represents the thicknesses for the longer growth times.

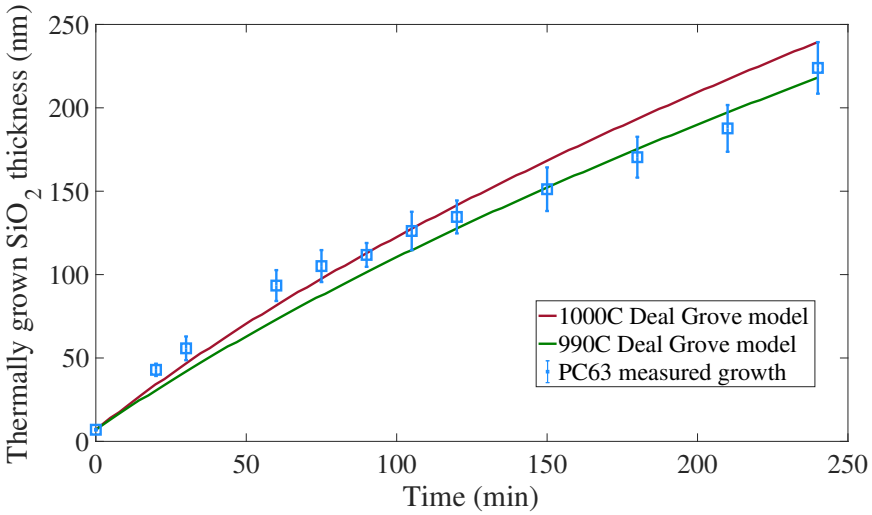

Fig. 4.4 Thermal oxide growth on bare silicon cantilevers compared to the Deal Grove growth model. Models for growth at 990 °C and 1000 °C are included. Cantilevers were baked at nominally 1000 °C.

Following the Deal Grove model, the rate of dry thermal oxide growth on <100> silicon at temperatures below 700 °C should be insignificant. This was experimentally confirmed for the etched silicon cantilevers, where control sample 9 showed no change

Table 4.3 Properties of uncoated silicon samples used as control data for mechanical loss calculations of IBS SiO_2. Cantilever thicknesses were calculated from equation 3.6 using the bending mode frequencies found during mechanical loss measurements. Total thermal oxide is a combination of measured growth on both sides of the cantilever after the dry oxide formation in a 1000 °C oven at atmospheric pressure and oxygen concentration.

Sample number	Cantilever thickness (μm)	Time at 1000 °C (min)	Total thermal oxide thickness (nm)
9	64.1 ± 0.1	20	40 ± 2
10	80.6 ± 0.2	20	41 ± 3
		60	93 ± 10
12	81.0 ± 0.2	20	43 ± 3
		115	181 ± 14

in thermal oxide thickness on either side after heat treatment at 600 °C. For a cantilever heat-treated at 800 °C for four hours in air, e.g. coated sample 7, the model predicts roughly 5 nm of thermal oxide growth. Post heat treatment measurements of sample 7 showed no significant increase in oxide thickness, but the predicted 5 nm oxide growth is within the uncertainty in measuring oxide thickness across the length of both cantilever faces. It can be concluded that no significant thermal oxide growth occurred on coated samples heat-treated up to 800 °C. Therefore measurements of uncoated samples 9, 10, and 12 were used to represent the substrate loss during coating mechanical loss calculations for coated samples with post-depositions heat treatments at or below 800 °C*. It should be noted that the control samples did not undergo any heat treatment after the initial oxide growth performed for all samples.

At temperatures above 800 °C there is predicted to be significant (»5 nm) oxide growth over time scales approaching the duration of post-deposition heat treatment for coated samples. For example, 20 nm of thermal oxide should double in thickness after 70 min at 950 °C. Coated sample 4 exhibits the predicted growth, with ∼140 nm of oxide forming during post-deposition heat treatment at 950 °C on top of the ∼40 nm present prior to coating. At ∼ 25% of the total coating thickness, this thermal oxide layer would be expected to significantly impact the mechanical loss of the heat-treated, coated sample. A similar thickness of thermal oxide was grown on one of the control samples in order to account for this influence: uncoated sample number 12 was baked at

*Loss data from sample 9 was omitted above ∼180 K due to a large difference in thickness compared to the coated cantilevers and the corresponding thermoelastic loss mismatch

1000 °C* for 115 min (an initial 20 min plus an additional 95 min) to grow 181 ± 14 nm of thermal oxide, thus providing an accurate representation of the substrate loss for the coated, 950 °C heat-treated sample number 4. There was a ∼20 µm difference in thickness between samples 12 and 4 that was not expected to affect the magnitude of loss at low temperatures, where dissipation within the oxide layers is the dominant source of mechanical loss. Measured loss data from sample 9, which was much closer to sample 4 in thickness, was used for coating loss calculations at temperatures above ∼ 180 K, where oxide loss is negligible in comparison to cantilever thermoelastic loss.

As previously mentioned, coated sample 3 was heat-treated at 950 °C for 4 hours but without the standard, elongated cooldown period in order to reduce the thermal oxide growth. This resulted in 88 nm of total oxide thickness on the sample, so control sample 10 was heated to grow ∼90 nm of oxide in order to accurately match the increase in substrate loss for sample 3.

4.3 Results

The mechanical loss of IBS silica between 10 and 295 K after a range of post-deposition heat treatments was calculated from loss measurements of the samples listed in tables 4.1 and 4.3, following procedures described in Chapter 3. Samples were measured between ∼1 and 28 kHz, corresponding to cantilever bending modes 3 through 11. Figures 4.5 and 4.6 illustrate the measurement process, showing data for the 3rd mode of the as-deposited and 800 °C heat-treated coatings, respectively, with the measured loss of the uncoated control sample and of the coated cantilever, the expected cantilever thermoelastic loss, and the calculated coating loss shown. The coating can be seen to significantly increase the loss of the silicon cantilever at low temperatures, where the thermal oxide peak from the uncoated cantilever can also be observed at about 30 K. It can also be seen that there is a gap in control loss between about 120 K to 150 K for both samples shown in figures 4.5 and 4.6. The loss in this region was interpolated for coating loss calculations, as too few control samples had enough consistent loss data in the region to estimate the loss. The coating loss is seen to change across all measured temperatures between these two heat treatments, with one notable change being the inability to resolve coating loss in the thermoelastic region for the 800 °C heat treatment.

As mentioned in section 4.2.2, the effect of a coating with mechanical loss lower than 1×10^{-4} cannot be distinguished from measurements of uncoated cantilevers

*1000 °C was chosen over 950 °C in order to increase the oxide growth rate.

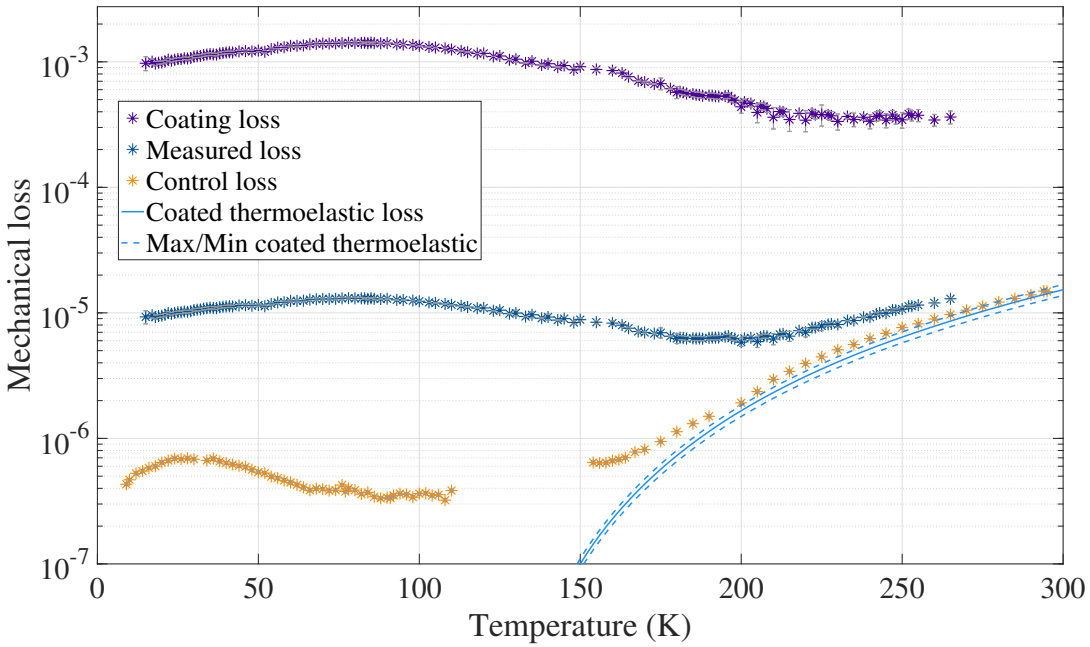

Fig. 4.5 Mechanical loss measurements of mode 3 (∼1.59 kHz) of AD sample 3. Purple represents coating mechanical loss as calculated at each temperature step from the mechanical losses of the coated sample (blue) and the control sample (orange). Thermoelastic loss of the cantilever is shown in light blue; a thickness difference of 1 µm between the control and coated sample means that the difference in thermoelastic loss is insignificant. Thermoelastic loss becomes negligible at temperatures below ∼150 K, as can be seen in figure 4.2.

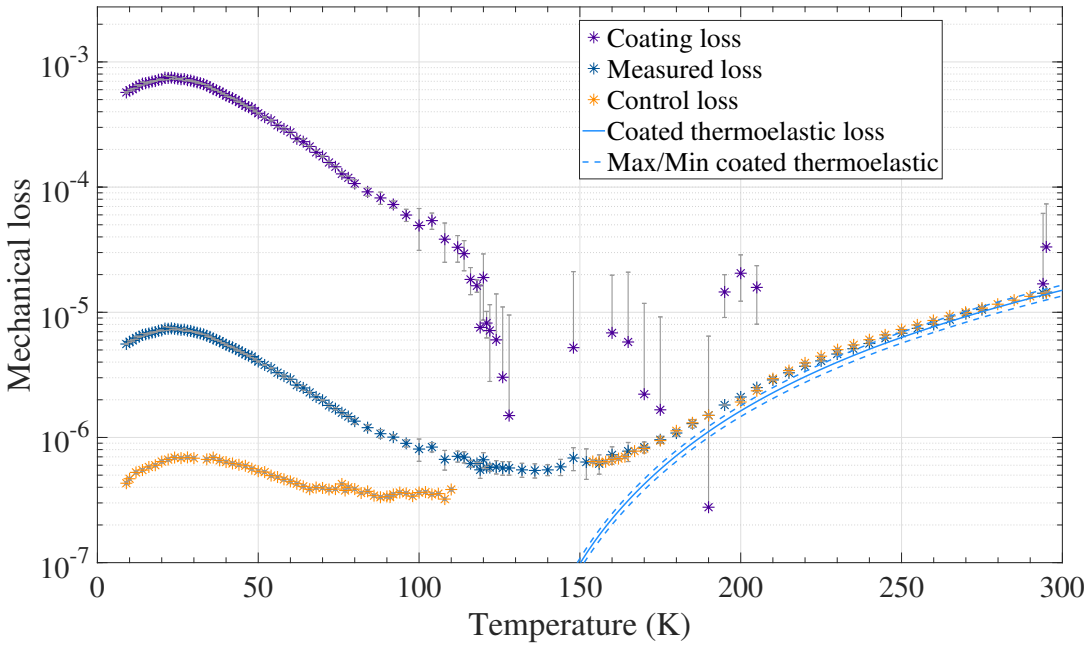

Fig. 4.6 Calculated, measured, control, and thermoelastic losses of mode 3 (∼1.58 kHz) of 800 °C heat-treated sample 7. Measured and control loss becoming indistinguishable at ∼150 K is characteristic of heat treatments above 450 °C. A zoomed-in depiction of this region is shown in figure 4.7.

above ∼185 K due to the influence of thermoelastic loss in the substrate. As-deposited and 300 °C heat-treated IBS SiO_2 has loss high enough to be the dominant source of dissipation across the measurement temperature range, but with post-deposition heat treatment above 300 °C the coating loss above ∼200 K decreases to a point where the dominant source of loss is substrate thermoelastic loss. Thus we are sensitive to sources of error such as differences in control/coated cantilever thicknesses or statistical measurement uncertainty, which can result in erroneously reporting an unphysical, negative coating loss. This effect is highlighted in figure 4.7, which shows the same loss presented in figure 4.6 but over a much smaller temperature range. There is also evidence that cantilever curvature due to stress can reduce the thermoelastic loss of a coated silicon cantilever [295]. This could explain the lower loss consistently measured at high temperatures in the coated cantilever compared to the uncoated substrate, which is an effect present in the one mode of the 800 °C heat treatment shown in 4.7 but prevalent across measured mode frequencies of samples heat-treated above 300 °C.

Samples were clamped and measured multiple times when possible in order to limit gaps in loss data and eliminate spurious peaks in measured data arising due to coupling between clamping block resonances and certain mode frequencies. Figure 4.8

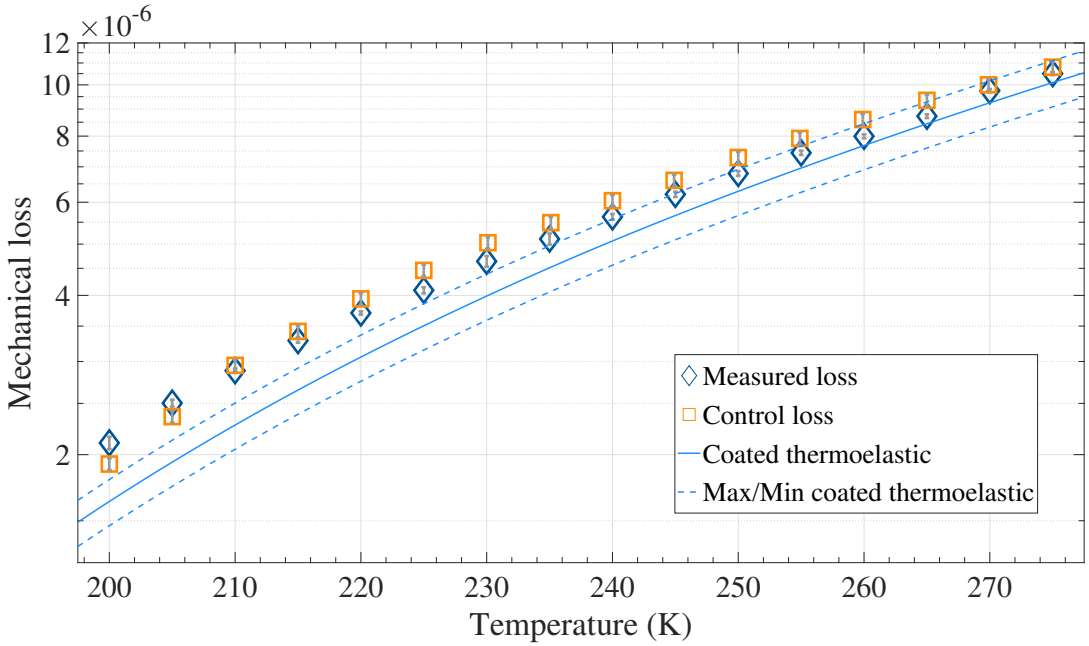

Fig. 4.7 Enlarged view of figure 4.6 showing measured, control, and thermoelastic losses over a 75 K range dominated by thermoelastic loss. Measured and control loss becoming indistinguishable at ∼150 K is characteristic of heat treatments above 450 °C.

shows loss measurements of the same bending mode from two different measurement cycles, where the first clamping produced extremely scattered and unreliable data and the second clamping resulted in clear and consistent measured loss. The results presented in this section are a combination of multiple measurement cycles when possible, but values from only one clamping were used where the loss from another set of measurement was found to be artificially high, such as the first clamp shown in figure 4.8.

The uncertainty in coated cantilever mechanical loss at each temperature step was calculated from the spread of measured loss values, which came from both repeat measurements during the same clamp at a given temperature step and measurements from successive clamps and measurements of the same sample. The mean of the measured results was taken to be the mechanical loss for temperature steps where there were three or more measurements, with the error bars representing the sample standard deviation. Temperature steps with only two measurements are presented with their average value as the loss and each measurement representing a maximum or minimum possible value. The mean deviation of values with three or more measurements is assigned to losses at temperature steps with only one measurement. The uncertainty in control sample loss was derived from the spread of loss values at each temperature

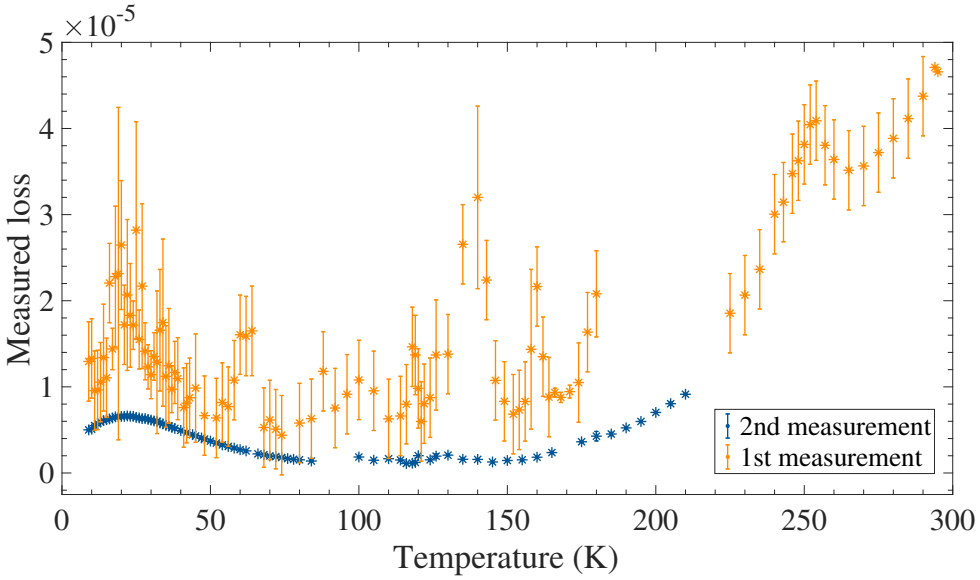

Fig. 4.8 Measured mechanical loss of 600 °C heat-treated sample number 3 from two different clamps and temperature cycles.

Table 4.4 Material properties used for calculating coating mechanical and thermoelastic loss [276, 286, 296, 297]. Thermal conductivity, specific heat capacity, and thermal expansion are strongly temperature dependent; listed values are for room temperature calculations (full range of values can be found in [276]).

Property	Silica	Silicon
ν	0.17	0.27
Y (GPa)	72	166
ρ ($\mathrm{kg\,m^{-2}}$)	2202	2330
α ($\mathrm{K^{-1}}$)	5.10×10^{-7}	2.54×10^{-6}
κ ($\mathrm{W\,m^{-1}\,K^{-1}}$)	1.38	140
C ($\mathrm{J\,kg^{-1}\,K^{-1}}$)	746	705

step for a bare cantilever with multiple clamps. Four modes of control cantilever 12 were analysed and found to have an average spread in mechanical loss of 2.5%. This percentage uncertainty was applied to all control data, as the low mechanical loss of bare cantilevers leads to a prohibitively long ringdown time and, thus, only single loss measurements at every temperature step. Error bars on the calculated coating mechanical loss were formed from a combination of measurement errors for both the coated and uncoated cantilevers, where the uncertainty in each was added in quadrature for every temperature step. The systematic uncertainty in calculated coating loss due to uncertainty in the Young's modulus of both coating and substrate has been omitted, as both properties remain within a few percent of the room temperature values over the temperature range of the experiment and the maximum systematic uncertainty for a given temperature step would be below 5% [276, 286, 298, 299].

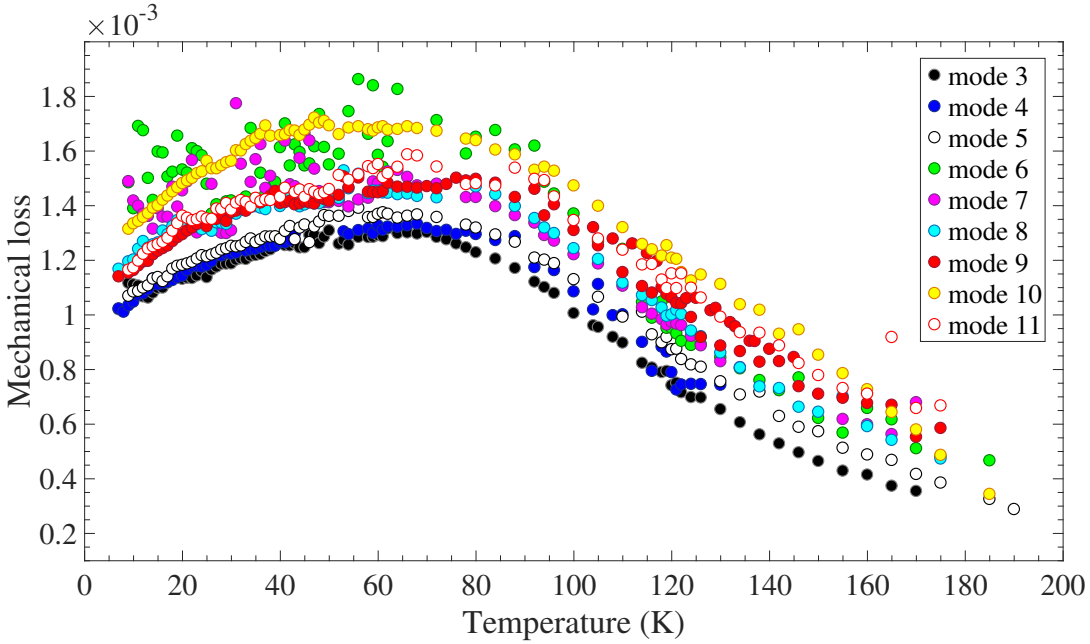

Fig. 4.9 Calculated coating mechanical loss for all measured modes of samples 7 and 8 after heat treatment at 300 °C. Consistency in temperature dependent loss across mode frequencies is evident, as is an increase in magnitude of loss with frequency. Error bars have been omitted for clarity but can be seen in figures 4.11 through 4.18.

Figures 4.9 and 4.10 show the calculated coating loss for all measured cantilever modes of samples heat-treated at 300 °C and 950 °C, respectively. The coating mechanical loss can be seen to be frequency dependent for all heat treatments, with higher frequency modes tending to result in higher coating mechanical loss; this is also the case for the loss of heat treatments not shown. While some modes exhibit minor scattering of loss data from adjacent temperature steps, the loss from all heat treatment

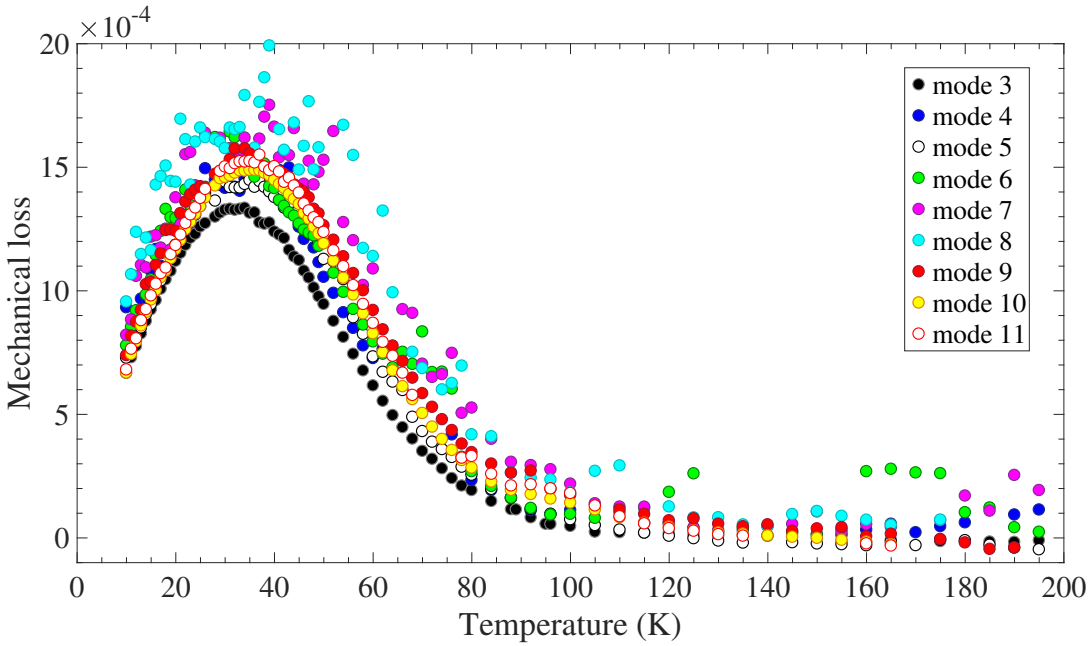

Fig. 4.10 Calculated coating mechanical loss for all measured modes of sample 4 after heat treatment at 950 °C. The broadly consistent temperature dependent loss remained after heat treatment, as did the increase in magnitude with frequency. Error bars have been omitted for clarity but can be seen in figures 4.11 through 4.18.

temperatures show consistent loss shape and magnitude across measured cantilever vibrational frequencies. Measurements at different frequencies with be analysed in more detail in section 4.3.1.

4.3.1 Effects of heat treatment on the mechanical loss of IBS SiO_2

Figures 4.11 through 4.18 show the calculated coating mechanical loss across all heat treatments for bending modes 3, 4, 5, 6, 8, 9, 10, and 11. Modes 3 and 9 (figures 4.11 and 4.16) produced the clearest depiction of changes in loss with heat treatment. Measurements of mode 7 have been omitted from this chapter due to a lack of available data across multiple heat treatments. The most likely explanation is energy coupling with the sixth torsional mode, which was found through FEA modelling to be nearly identical in frequency to the seventh bending modes at some temperatures and within 150 Hz across the entire measurement temperature range.

The as-deposited coating exhibited a large, broad loss peak centred around 80 K to 100 K depending on mode frequency. The magnitude of the loss was greater than 10^{-3} for a majority of temperatures below 200 K, but varied with frequency to a greater degree than the coating after any post-deposition heat treatment. It should be noted that loss data for the as-deposited coating was consistently found to have a higher

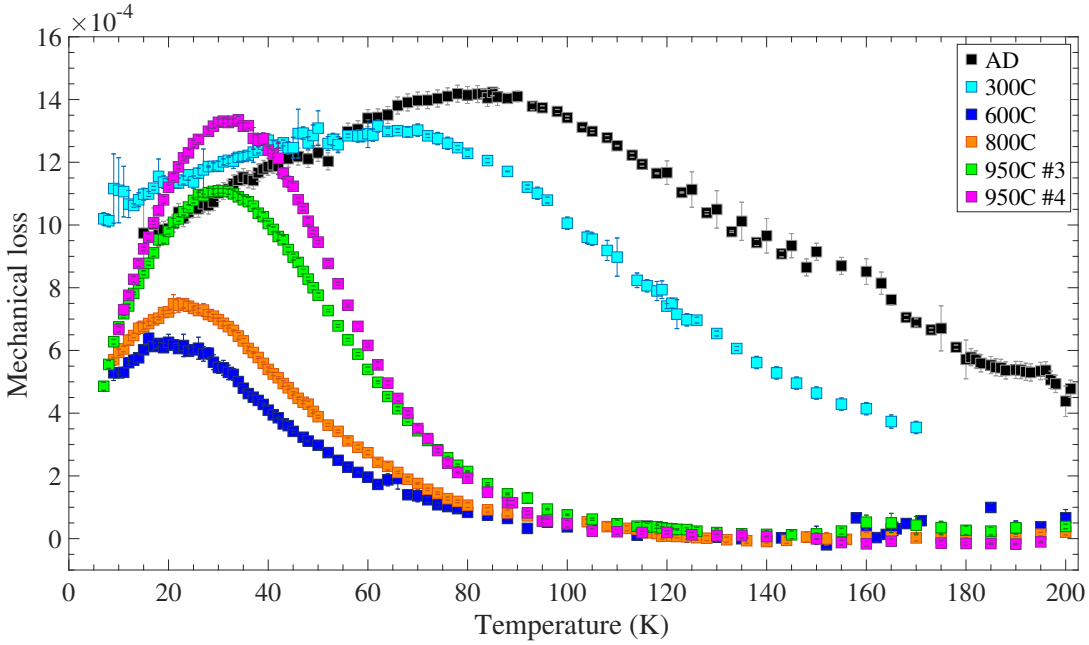

Fig. 4.11 Coating mechanical loss from all available heat treatments, as calculated from measurements of mode 3 (∼1.6 kHz).

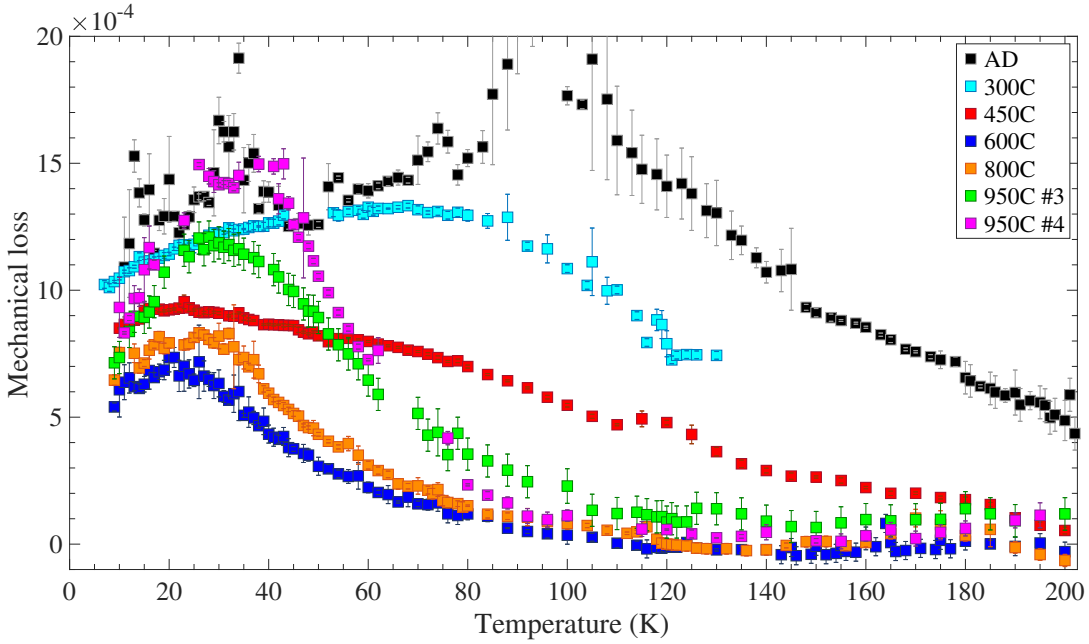

Fig. 4.12 Coating mechanical loss from all available heat treatments, as calculated from measurements of mode 4 (∼3.1 kHz).

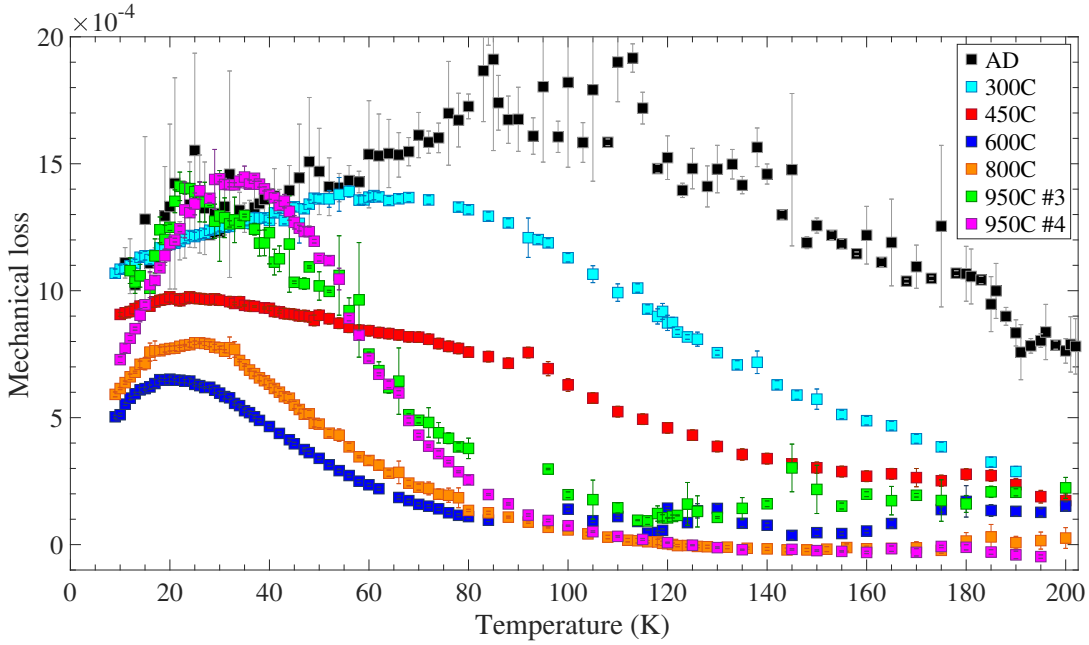

Fig. 4.13 Coating mechanical loss from all heat treatments, as calculated from measurements of mode 5 (∼5.1 kHz).

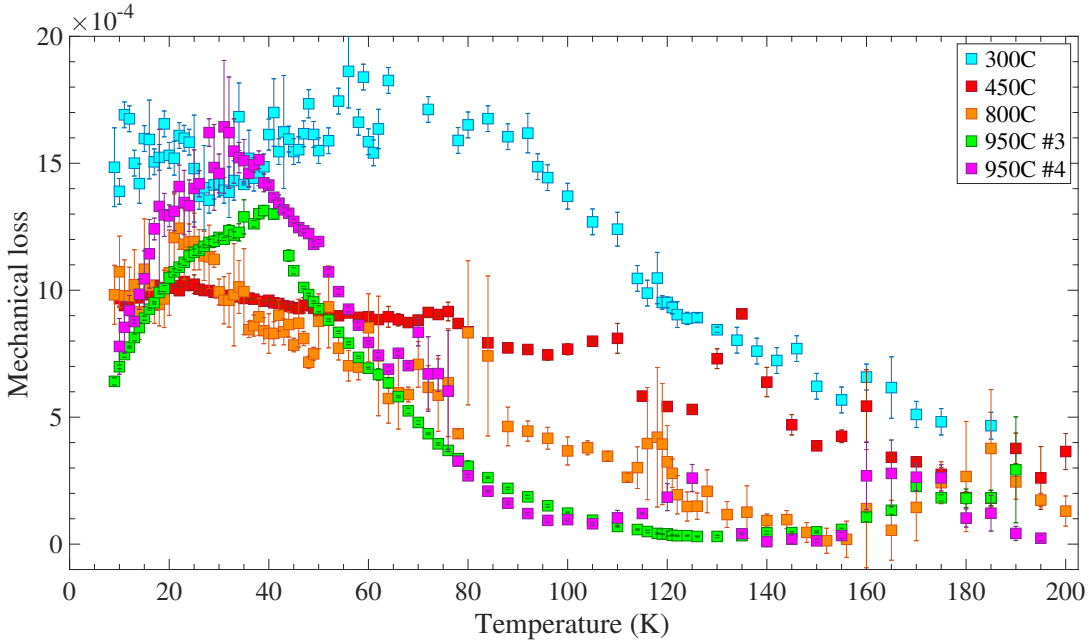

Fig. 4.14 Coating mechanical loss from all available heat treatments, as calculated from measurements of mode 6 (∼7.6 kHz).

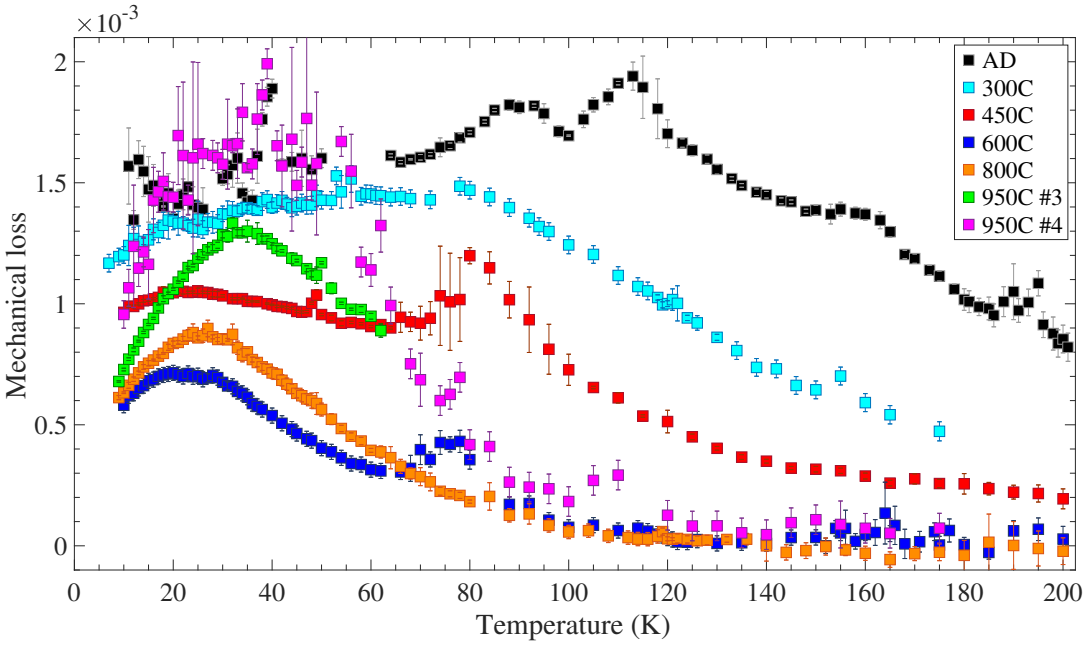

Fig. 4.15 Coating mechanical loss from all heat treatments, as calculated from measurements of mode 8 (∼14 kHz).

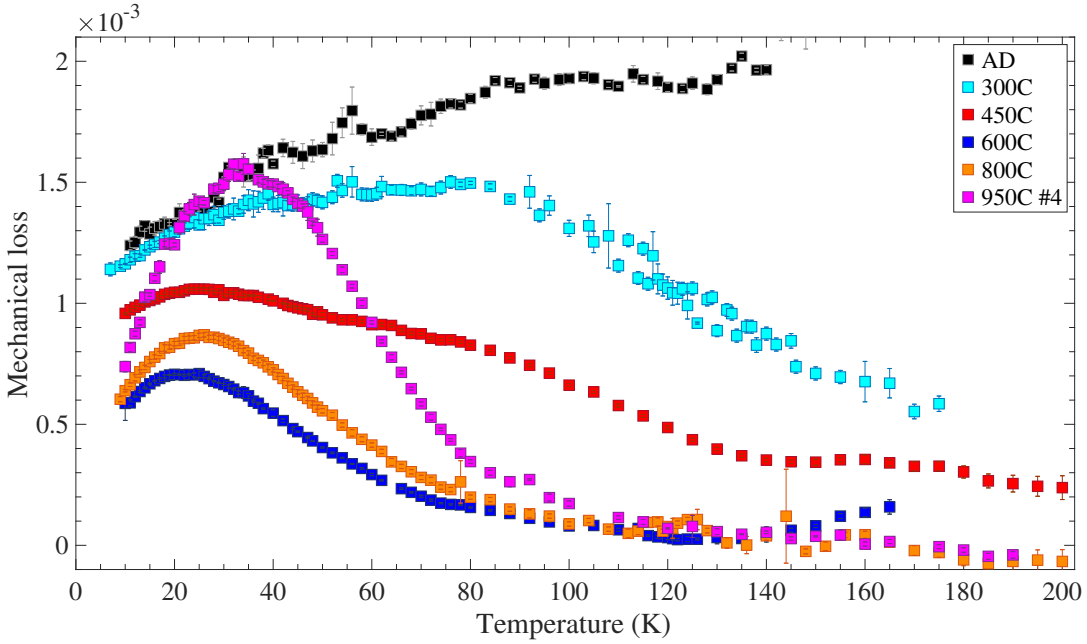

Fig. 4.16 Coating mechanical loss from all available heat treatments, as calculated from measurements of mode 9 (∼18 kHz).

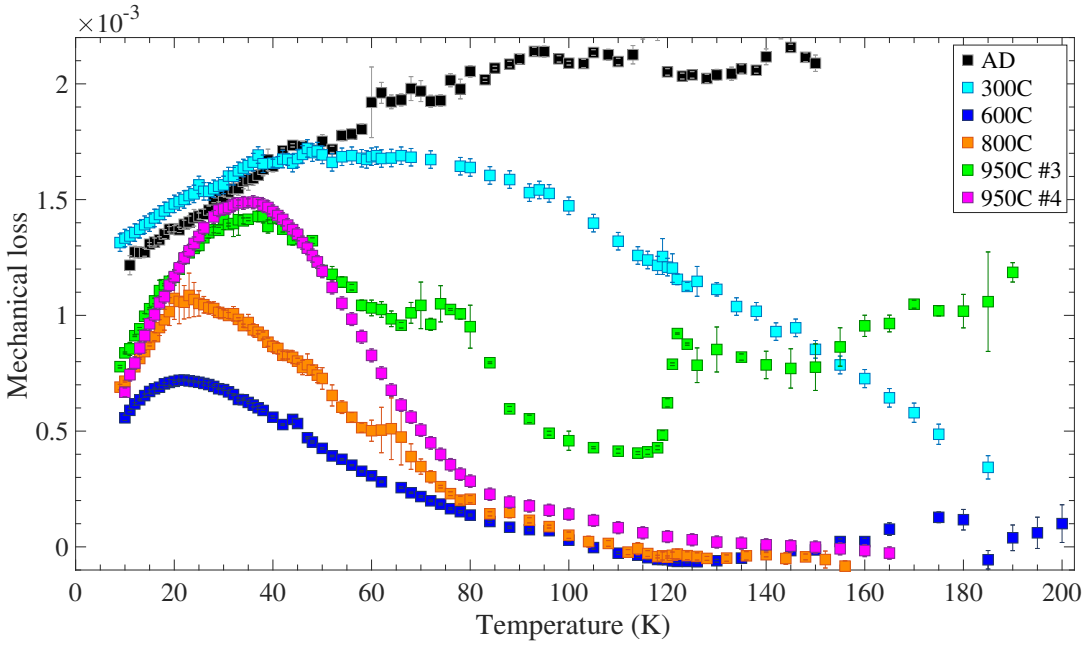

Fig. 4.17 Coating mechanical loss from all available heat treatments, as calculated from measurements of mode 10 (∼23 kHz).

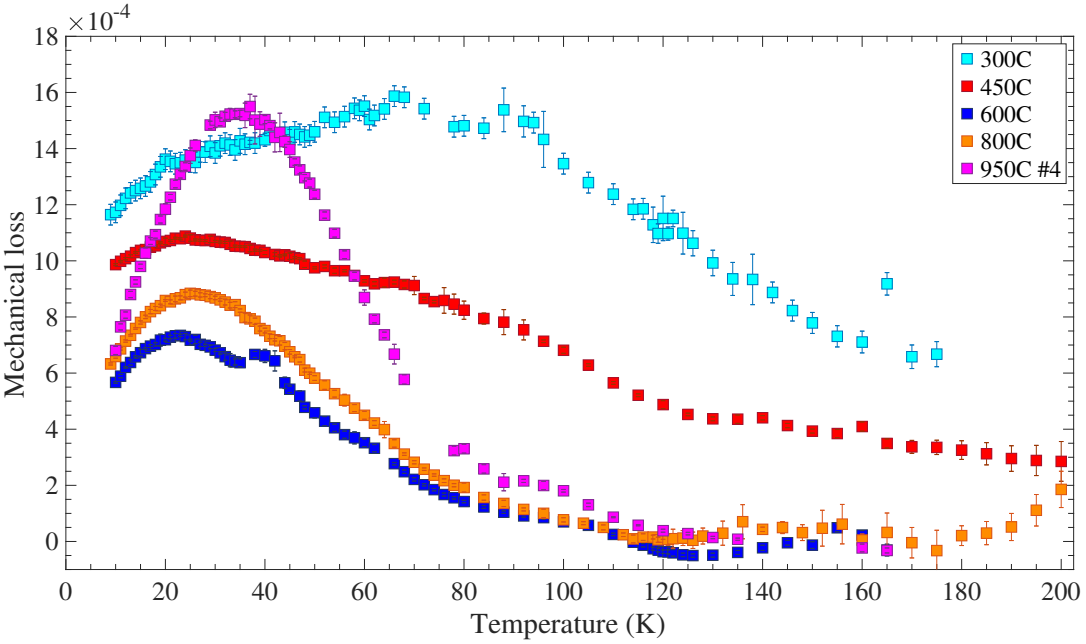

Fig. 4.18 Coating mechanical loss from all available heat treatments, as calculated from measurements of mode 11 (∼28 kHz).

than usual degree of scatter and it was difficult to obtain clear measurements for most mode frequencies despite multiple clampings. This can be seen in figures 4.12 and 4.13, where there are large uncertainties in the calculated coating loss for modes 4 and 5, and in figure 4.15, where there are seemingly spurious peaks notable in the data. The inconsistencies also resulted in a lack of usable data for modes 6 and 11 despite multiple measurements of the sample.

The most notable effect of 300 °C heat treatment was a significant drop in coating mechanical loss compared to the as-deposited coating for temperatures above 60 K. A broad peak is still present in the loss data, but the decrease in coating loss resulted in a more defined loss curve and a peak loss temperature decreasing by about 20 K to centre around 60 K. Coating loss at temperatures below ∼40 K remained unchanged after the 300 °C heat treatment.

Heat treatment at 450 °C resulted in decreased coating mechanical loss across all measured temperatures and a significant suppression of the broad loss peak in the mid-temperature range. It also led to the emergence of a different, sharper loss peak between 20 K and 25 K. The features and small peaks seen in modes 4, 5, 6, and 8 (figures 4.12 through 4.15) are thought to be clamping effects that would be eliminated with more measurements*.

The silica coating heat-treated at 600 °C displayed the lowest mechanical loss of any heat treatment, with the magnitude decreasing by about a factor of 2 at 10 K and by a factor of ∼15 at 100 K compared to the coating as deposited. The loss profile is dominated by a well-defined peak centred around ∼20 K, and there is no evidence of the broad, mid-range peak seen in lower temperature heat treatments. IBS silica heat-treated at 600 °C has been previously studied by Martin et al. [258] and comparison to these results will be presented in section 4.6.

Further heat treatment at 800 °C resulted in very similar overall loss shape as the 600 °C heat treatment, but with an increase of roughly 30% in the magnitude of the loss peak and a shift upward in peak loss temperature of about 5 K across all modes. It is unclear if the sharp peak seen in the 600 °C and 800 °C heat treatments was present in all previous annealing states of the coating but masked by the broad loss peak centred around 90 K, or whether the low temperature peak was created through increased post-deposition heat treatments and then shifted/increased through further annealing. It appears that the mid-range 450 °C heat treatment shows some evidence of the low temperature peak, but it could be that the magnitude of the broad loss peak

*The 450 °C heat-treated sample number 11 only had one measurement before breaking.

was asymmetrically suppressed, with coating loss above 40 K decreasing faster with heat treatment than loss at lower temperatures.

Heat treatment at 950 °C produced a significant increase in the magnitude of the sharp, low temperature loss peak and a further shift upward in peak loss temperature. Coating loss above 100 K remained unchanged for both 950 °C heat treatments (samples 3 and 4) compared to lower annealing temperatures, but the change in peak loss differed between the two heat-treated samples*. Sample 4 exhibited higher peak loss for most modes where there was comparable data, where the sample 3 peak more consistently remains below the broad loss peak seen in the AD and 300 °C samples.

Figure 4.19 shows the change in cantilever mode frequency with respect to measurement temperature for bending mode five of all coated and heat treated samples. The frequencies differ between samples based on the cantilever thickness and slight variations between clampings, so the change in frequency is shown relative to the mode frequency measured at 10 K. Comparison of the frequency trends between heat treatments is valuable given the observed changes in loss. The consistency in mode frequency change between all heat treatments of the silica confirms that little change to the coating's dY/dT or $d\rho/dT$ occurred with annealing. An uncoated cantilever is included in figure 4.19 as reference, but the coating had such little effect on the frequency trend that it is effectively indistinguishable from the coated samples†. It should be noted that the slight spread in relative change between heat-treated samples is well within the spread seen between uncoated cantilevers.

The heat-treatment measurement series are compared to the loss of bulk fused silica in figure 4.20. Even with the discrepancy in loss between the 950 °C samples, the amorphous coating tends toward the loss characteristics of bulk amorphous silica with increased heat treatment. The peak loss temperature of the bulk loss in figure 4.20 is greater than that seen in the IBS silica, but the bulk measurements were taken at a vibrational frequency ∼80 kHz higher than the coated cantilever results‡. This would be expected to shift the peak upwards in temperature [300, 301]. IBS SiO_2 heat-treated to 950 °C has been shown to produce the minimum loss at room temperature, with heat treatments past 1000 °C resulting in an increase of the coating loss [285]. The progression of low temperature coating loss in IBS silica with heat treatments shown in this section give evidence that the 950 °C annealed coating reaches a structure as

*It should be reiterated that the 300 °C coating loss was comprised of measurements from two different samples that produced nearly identical loss, so there was no reason to suspect that two different samples heat-treated at the same temperature should exhibit different loss.

†An example of coatings having a noticeable effect on mode frequency with respect to temperature is shown in section 5.4.2.

‡The bulk data was chosen due its use in comparing previous coating loss results [258, 271].

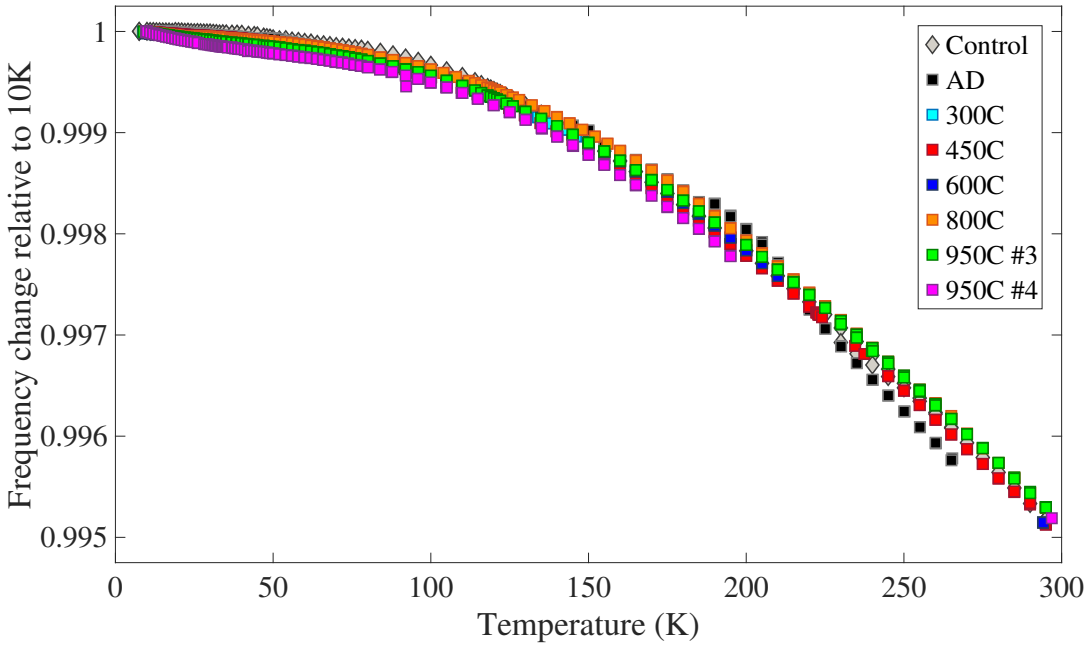

Fig. 4.19 Relative change in cantilever mode frequency with respect to measurement temperature for all heat treatments of IBS silica. All curves are from mode 5, which varies depending on the cantilever thickness but is around 5 kHz. The frequency change for an uncoated cantilever is included for comparison.

close to bulk silica as can be created with heat treatment of an IBS film. It should be emphasised, however, that all other heat treatments exhibited a significant difference in loss behaviour than bulk silica, and understanding the reason behind this difference is crucial for producing better coatings.

4.4 Analysis and discussion

Characterisation of the temperature dependent mechanical loss of IBS SiO_2 after multiple heat treatment temperatures is important for coating thermal noise estimations and comparison to other coating loss studies. In addition, studying the effect of heat treatment temperature on the temperature-dependent loss of IBS silica can provide valuable insight into the structural origin of loss mechanisms, as well as provide further understanding of amorphous materials. This section will delve into the structural characteristics of the amorphous silica that can be determined by its low temperature mechanical loss, and will discuss the stress internal to the coating and compare the IBS silica loss and structure to SiO_2 coatings deposited through different methods.

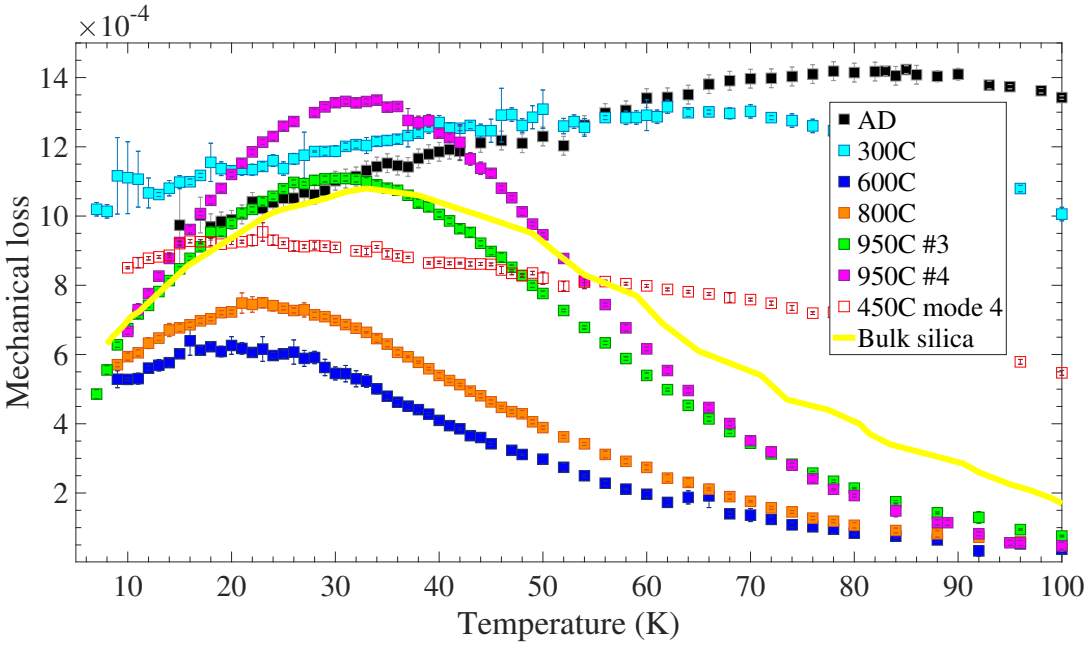

Fig. 4.20 IBS SiO_2 coating mechanical loss, as calculated from measurements of mode 3, compared to the mechanical loss of bulk SiO_2. Bulk data corresponds to measurements at 86 kHz, as presented by Cahill and Van Cleve [302].

4.4.1 Origin of mechanical loss in amorphous coatings

The movement of atoms and molecules between energy states separated by potential energy barriers is thought to be the primary source of mechanical loss (as well as thermal conductivity and heat capacity) within amorphous materials [303]. At low temperatures (less than 10 K) dissipation follows a quantum tunnelling model [209, 301, 304, 305], where particles can access other local energy minima without the energy required to overcome the potential energy barrier height*. Above 10 K relaxation processes are dominated by thermal activation, where the energy required to cross the potential barrier comes from thermal energy in the material or absorption of a thermal phonon [303]. An experimental characteristic of thermally activated loss processes is that the peak mechanical loss temperature increases at higher measurement frequencies. Heat treatments of IBS SiO_2 at and above 450 °C show such peaks, which if assumed to be a product of Debye relaxation, where the anelastic relaxation response to a changing energy field is characterised by a single relaxation time, then the mechanical loss as a function of frequency may be described by the relation [120, 307, 308]:

$$\phi(\omega) = \Delta \frac{\omega\tau}{1+(\omega\tau)^2} , \tag{4.3}$$

*Whereas potential energy barrier heights can be on the order of meV, tunnelling in amorphous solid requires less than 10^{-4} eV [306]

where Δ is a constant dependent on the magnitude of dissipation, and τ is the relaxation time, which describes the time required for the dissipative system to return to equilibrium after some external perturbation. The origin of the dissipation in equation 4.3 is unspecified, but for thermally activated loss processes this relaxation time is given by the Arrhenius equation [120]:

$$\tau = \tau_0 e^{E_a/k_B T_{peak}} , \tag{4.4}$$

where k_B is the Boltzmann constant, T_{peak} is the temperature at which the loss peak is at a maximum, and τ_0 is the characteristic time associated with attempts at overcoming the potential energy barrier, the height of which is determined by the activation energy, E_a. Activation energy is the minimum energy required for a system to undergo a change in state and can be characterised by the height of the potential barrier between two minima of potential energy wells. Figure 4.21 shows an example of an asymmetric double potential well, or two level system (TLS), where an atom or molecule would reside at the potential energy minima associated with energies E_1 or E_2 and need an influx of energy to cross the barrier of height V. A simpler representation would be a symmetric double well, but this would be incongruent with the linear increase in temperature of the peak mechanical loss with relation to frequency [303].

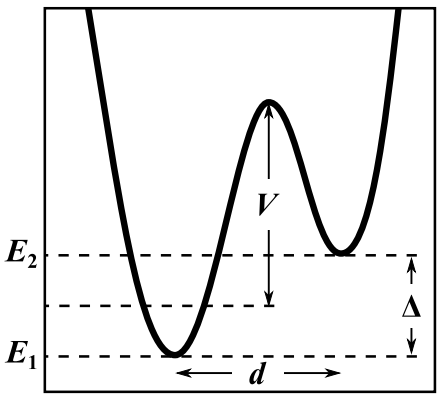

Fig. 4.21 Asymmetric double potential well, potential energy vs configuration space.

It can be seen from equation 4.3 that such dissipation peaks should occur when $\omega\tau = 1$, so when combined with equation 4.4 one obtains the relation:

$$\ln(\omega) = -\frac{E_a}{k_B}\frac{1}{T_{peak}} - \ln(\tau_0) . \tag{4.5}$$

The activation energy associated with a peak in mechanical loss can therefore be determined from a linear fit of the natural log of angular mode frequency versus the reciprocal of the temperature at which the loss peak is at a maximum. The extreme

peak fitting function in Origin [309] was used to determine T_{peak} for heat treatments of IBS SiO_2 at and above 450 °C, where a well-defined loss peak dominates the low temperature mechanical loss. This method utilises a four parameter Gumbel probability density function and was chosen due to its ability to accurately fit the asymmetric peaks seen in the data. It should be noted that the fitting of the mechanical loss versus temperature data does not represent any physical property in and of itself, and the method was chosen due to its ability to match the asymmetry seen in the loss peaks. The peak temperature was determined from the mean of a number of peak fits with differing temperature ranges. The uncertainty in peak temperature was then determined by the standard deviation of the fitted peaks with respect to the mean. The uncertainty in measurement frequency (vertical axis) was insignificant, with mode frequencies known to within a half of a hertz. This represents a relative error of less than a 0.05% for mode 3, the lowest frequency bending mode analysed, and will decrease for higher modes as they increase in frequency.

Table 4.5 shows T_{peak} and the corresponding measurement frequencies for all available modes of the 450 °C, 600 °C, 800 °C, and 950 °C heat treatments. A number of modes were omitted from the fitting process, as these lacked measured control loss data at the correct mode frequency. Gaps in low temperature control data were filled with measured loss from the mode above or below in order to provide a close match in the magnitude of calculated loss. This, however, could potentially alter the peak temperature of the coating loss by laterally shifting the calculated loss values. The high oxide thicknesses of the 950 °C heat treatments would be particularly susceptible to this effect.

The values in table 4.5 were used to plot the natural log of angular measurement frequency versus inverse peak loss shown in figure 4.22 following equation 4.5, and the activation energies and corresponding rate constants for each heat treatment were determined from the slopes and y-intercepts of the fits. The slopes and intercepts were determined through weighted least squares linear regression, where the weighting of each data point was the inverse of its variance in $1/T_{peak}$. Uncertainties in calculated E_a and τ_0 correspond to a one sigma confidence in the fitted slope and y-intercept. The activation energies and rate constants for each heat treatment are listed in table 4.6.

Figure 4.22a shows the Arrhenius analysis for the coating heat-treated at 450 °C. The data for this heat treatment exhibits a considerable spread in $\ln \omega$ versus inverse T_{peak}, illustrating the benefit of the weighted regression, which yields a 26% uncertainty in E_a compared to a 41% uncertainty when calculating E_a from an unweighted linear regression. The 600 °C heat-treated IBS silica shown in figure 4.22b can be seen to have the best fit, where all of the inverse peak temperatures scaled linearly with the

Table 4.5 Temperatures and the associated measurement frequencies corresponding to the maximum magnitude of the low temperature loss peak in heat-treated IBS silica. Mode numbers correspond to the cantilever bending modes, where the frequency given is that measured at the peak temperature.

Mode	Frequency (Hz)	T_{peak} (K)	Mode	Frequency (Hz)	T_{peak} (K)
	450 °C			950 °C sample 3	
4	3102	22.69 ± 0.09	3	1768	30.10 ± 0.28
5	5122	23.83 ± 0.32	4	3484	29.95 ± 0.38
8	14189	23.89 ± 0.18	6	8629	32.80 ± 0.26
11	27766	25.26 ± 0.26	8	16046	34.10 ± 0.35
			10	25822	34.41 ± 0.24
	600 °C			950 °C sample 4	
3	1596	20.51 ± 0.33	3	1200	31.95 ± 0.38
4	3127	20.61 ± 0.30	4	2360	32.61 ± 0.88
5	5162	21.01 ± 0.29	5	3903	33.70 ± 0.40
8	14295	21.90 ± 0.24	9	13826	34.96 ± 0.17
10	22891	22.20 ± 0.16	11	20933	34.21 ± 0.12
11	27963	22.43 ± 0.22			
	800 °C				
3	1591	23.24 ± 0.21			
4	3112	24.32 ± 0.37			
5	5129	25.07 ± 0.50			
8	14169	25.52 ± 0.39			
11	27688	25.97 ± 0.25			

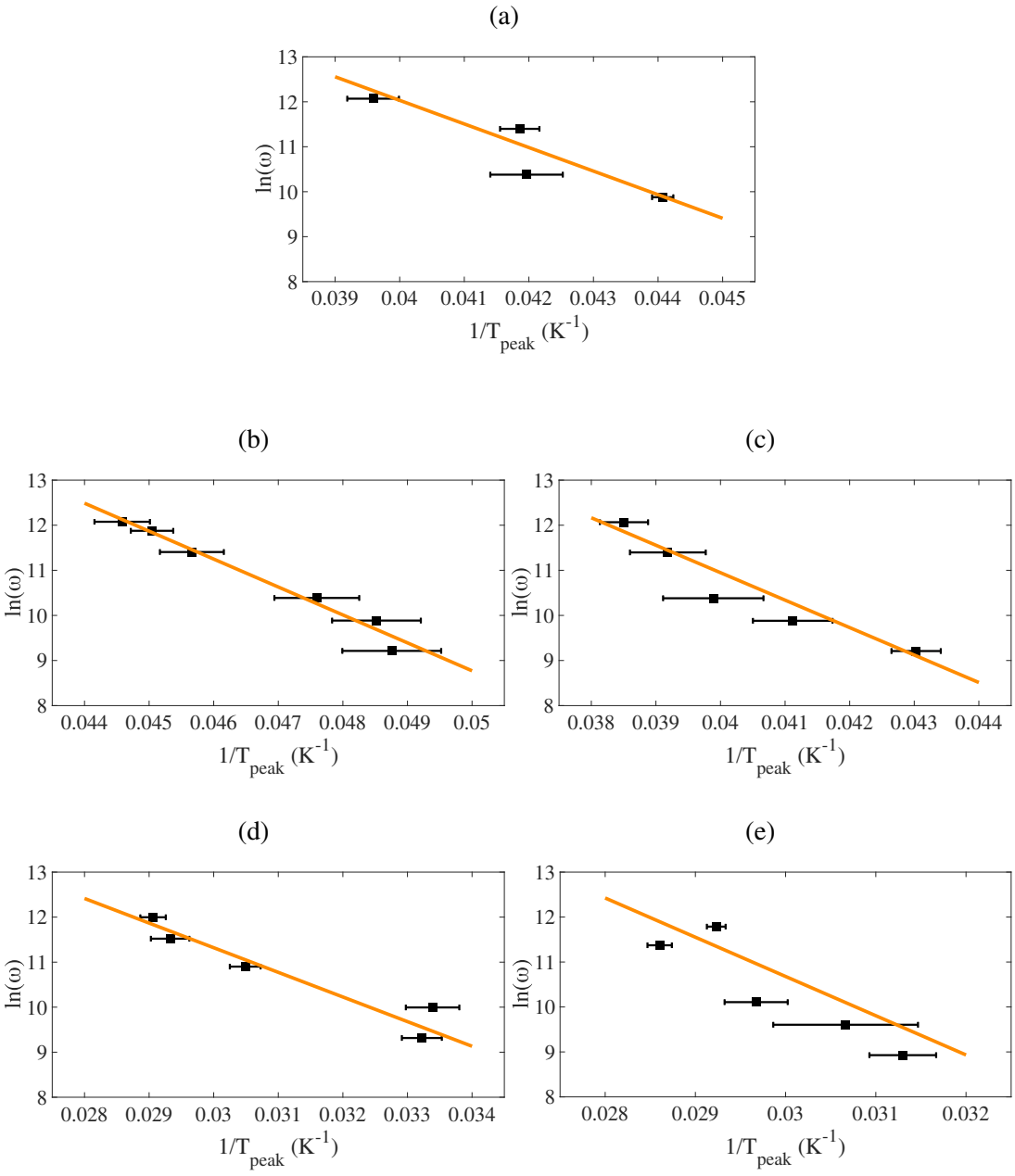

Fig. 4.22 Linear fits of the natural log of peak frequency versus inverse of the peak temperature, as listed in table 4.5 for (a) 450 °C, (b) 600 °C, (c) 800 °C, (d) 950 °C sample 3, and 950 °C sample 4.

Table 4.6 Activation energy, E_a, and characteristic time, τ_0, for all heat treatments.

Heat treatment	E_a (meV)	τ_0 (s)
450 °C	45.2 ± 11.8	$(45.9 \pm 8.2) \times 10^{-16}$
600 °C	53.4 ± 4.1	$(55.4 \pm 3.1) \times 10^{-19}$
800 °C	52.5 ± 7.7	$(46.7 \pm 4.9) \times 10^{-17}$
950 °C 3	47.1 ± 8.3	$(90.4 \pm 9.6) \times 10^{-14}$
950 °C 4	75.2 ± 47.6	$(98.0 \pm 4.3) \times 10^{-17}$

natural log of measurement frequency and no mode was outwith the fitted line given the uncertainty in T_{peak}. This resulted in the lowest uncertainty in activation energy and rate constant, at 8% and 6%, respectively. The 800 °C heat treatment, shown in figure 4.22c had about a 15% uncertainty in activation energy due to modes 4 and 5, which had T_{peak}s increasing in temperature at a greater rate than that determined by the rest of the modes (3, 8, and 11). Despite having the lowest fitting uncertainty for its peak temperatures, sample 3 heat-treated at 950 °C had an 18% uncertainty in E_a. This was due to the peak temperature for mode 4 being greater than the lower frequency mode 3. There was no reason to omit mode 4, especially given the high fidelity, low uncertainty peak fit.

The Arrhenius fitting for these four heat treatments resulted in calculated activation energies between 45.2 and 53.4 meV, with all values within fitting uncertainties of each other. There was no observed trend of activation energy with heat treatment, leading to the conclusion that E_a remained the same throughout heat treatment of the sample. Previous measurements have shown the activation energy associated with the low temperature loss peak in bulk silica to be in the range of 44 meV to 52 meV [208, 310], and IBS SiO_2 heat-treated at 600 °C to have an E_a of 32.1 ± 2.9 meV for the observed low temperature peak [258]. The results presented in table 4.6 for all but the 950 °C heat-treated sample 4 fall within the range of measured bulk silica, but do not agree with the calculated activation energy for the low temperature loss peak in IBS SiO_2 deposited by The Commonwealth Scientific and Industrial Research Organisation (CSIRO) and presented by Martin et. al. [258]. It should also be noted that the rate constant calculated for the low temperature in peak in CSIRO IBS SiO_2 was found to be $18 \pm 1 \times 10^{-14}$ s, five orders of magnitude lower than that calculated for ATF IBS SiO_2 after the same heat treatment. The effect of this disparity will become apparent in section 4.6.

Another notable result from the Arrhenius fitting is that the activation energy associated with the low temperature peak in the 950 °C heat-treated sample 4 differed

significantly from those calculated from the rest of the heat treatments, including the other 950 °C heat-treated sample. It can be seen in figure 4.22e that the two most well-defined low temperature peaks (from modes 9 and 11) do not agree with the linearly increasing inverse peak temperature seen in the other heat treatments. The peaks for modes 9 and 11 were very well-defined, leading to both being weighted heavily in the linear regression. The significant decrease in T_{peak} for mode 11 resulted in a 63% uncertainty in E_{a}. Omitting mode 11 as an outlier gives an activation energy of 80 ± 8 meV, which corresponds to a much better linear fit, but an activation energy significantly higher than that calculated for the other heat treatments*. One possible explanation for the anomalous results for 950 °C sample 4 could be the use of a much thicker cantilever for the low temperature control loss. As discussed in section 4.2.2, sample 4 was much thinner than the rest of the measured samples but had significantly higher thermal oxide layer present after heat treatment. The oxide layer was accounted for during mechanical loss calculations by using a control sample with matching thermal oxide growth, but this sample was about 20 µm thicker than sample 4. The difference in thickness resulted in disparities between measured mode frequencies (steadily increasing from a ∼500 Hz difference for mode 3), which could shift T_{peak} because of the frequency dependence of the peak.

4.4.1.1 Barrier height distribution

Activation energies were only calculated for samples heat-treated above 450 °C, as there were no sufficiently defined temperature peaks in the AD or 300 °C samples. Even the sharply-defined peaks of the 950 °C heat-treated samples were wider and less symmetric than the theoretical Debye peaks that should accompany a single thermal activation energy; this can be seen in figure 4.23 for the 600 °C, 800 °C, and 950 °C heat treatments. Unlike perfectly crystalline materials†, glasses contain many degrees of structural freedom and are characterised by a distribution of two level systems rather than one asymmetric potential and a single Debye peak [306]. Figure 4.24 shows an example of such an energy landscape, where a number of TLS combine to create a distribution of barrier heights, $g(V)$, and well asymmetries, $f(\Delta)$. In this case the activation energies found through equation 4.5 and presented in the previous section represent the average barrier heights of a number of the dominant TLS [311].

Internal friction within an amorphous solid is the result of thermally induced transferring of particles between potential energy minima in a TLS distribution [245].

*Omitting mode 9, for comparison, results in an activation energy of 124 ± 38 meV.

†In a perfect crystal each atom is constrained by symmetry to occupy a single potential minimum [306]

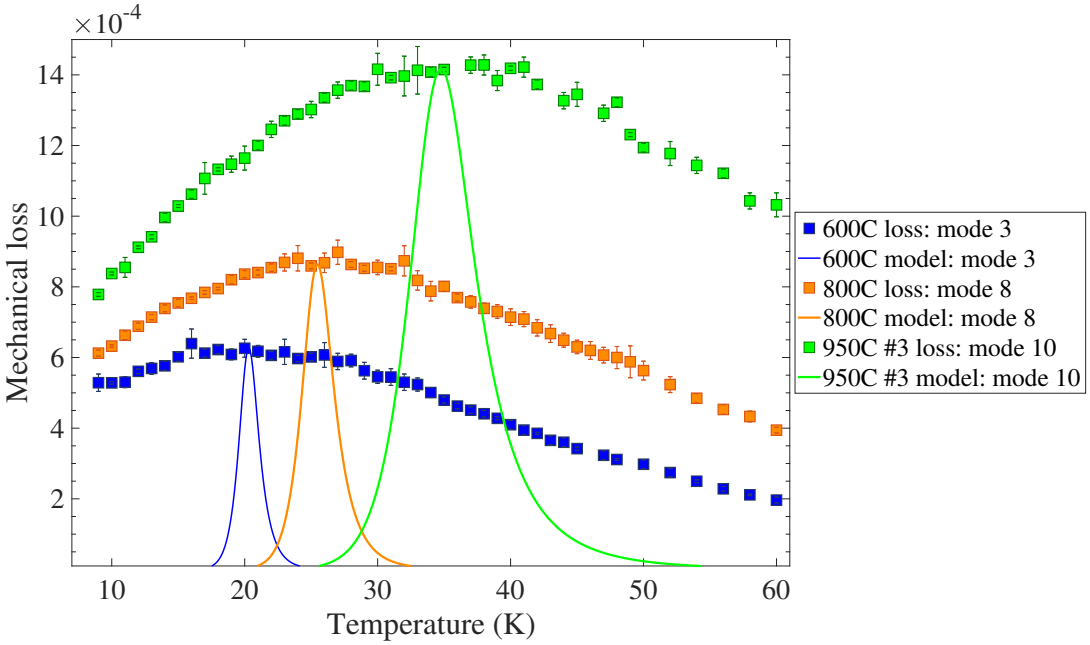

Fig. 4.23 Silica coating loss peaks from 600 °C, 800 °C, and 950 °C heat treatments and their corresponding, theoretical Debye peaks from Arrhenius fits. Mode 3 (1.60 kHz) is shown for 600 °C, 8 (14.2 kHz) for 800 °C, and 10 (25.8 kHz) for 950 °C sample 3.

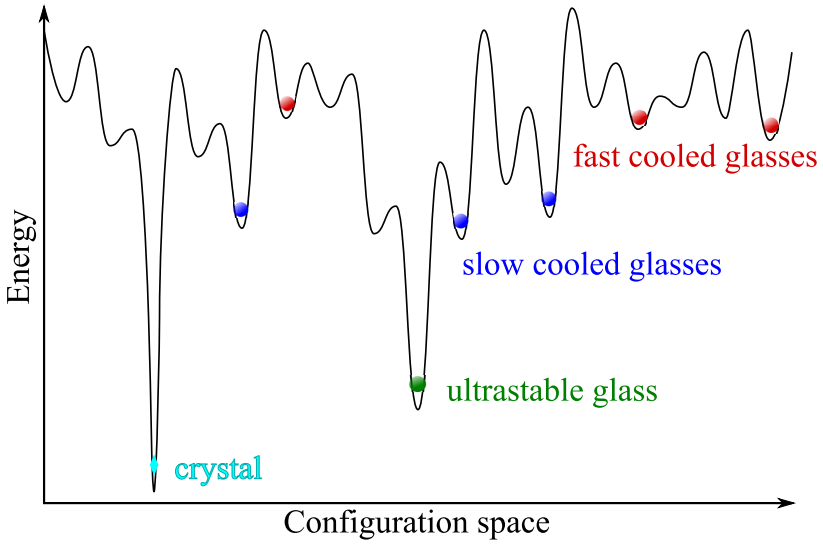

Fig. 4.24 One dimensional potential energy landscape of an amorphous solid, where atoms/molecules (red, blue, and green spheres) are shown to reside within differing areas of local potential energy barrier heights depending on conditions during coating formation. Slow deposition rate, high temperature/energy deposition, and slow cooling of a coating allows sufficient particle mobility to reach the lowest potential energy minima and create an ultra-stable, i.e. ultra low-loss amorphous coatings [243, 244, 312].

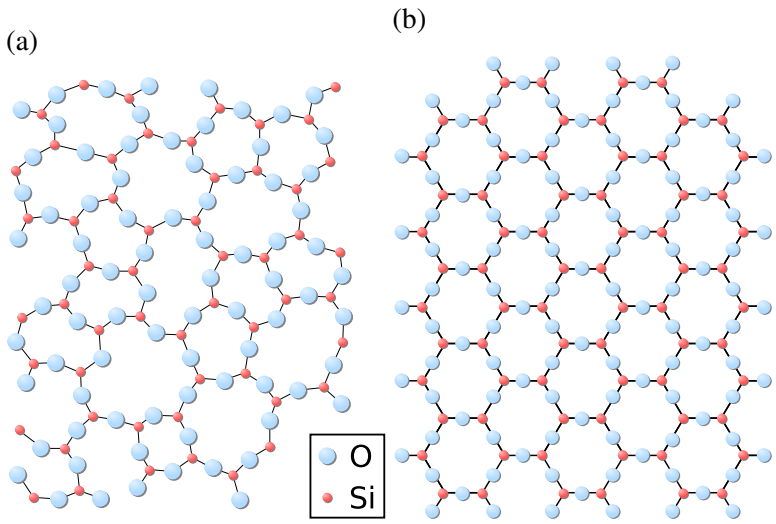

Fig. 4.25 Atomic structure of (a) amorphous and (b) crystalline SiO_2 [316].

The wide low temperature loss peak in silica is thought to arise from a distribution of TLS within the amorphous material. Figure 4.25b shows the atomic structure of crystalline quartz, which can be seen to be highly ordered, with constraints in terms of possible bond angles and lengths. Figure 4.25a shows one possible snapshot of an amorphous silica structure, which can be seen to posses significantly more disorder due to its under-constrained bond angles and lengths. It is the disorder in the amorphous silica that is thought to be the cause of the increased mechanical loss due to structural relaxation associated with mechanically coupled TLS [262]. These TLS could correspond to a number of physical processes, with the distribution in their parameters related to the disorder inherent in an amorphous material. For example, thermally induced barrier height 'hopping' could correspond to the flipping of Si-O bond angles between possible equilibrium states [208], rearranging between multiple stable bond lengths between Si-O-Si structures [313], or the rotation of tetrahedral SiO_4 structures between stable orientations [306, 314]. Recent studies have also shown that TLS could also correspond to larger scale reorientation of groups of ordered atoms within the potential energy landscape, even well below glass transition temperatures [211, 315].

The distribution of barrier heights and asymmetries created by any of the structural models laid out above can be shown to predict mechanical loss in an amorphous solid from the following relationship [303]:

$$\phi = \frac{\gamma^2}{k_B T C_{ii}} \int_0^\infty \int_0^\infty \frac{\omega\tau}{1+(\omega\tau)^2} \mathrm{sech}^2\left(\frac{\Delta}{2k_B T}\right) f(\Delta) g(V)\, d\Delta dV \,, \tag{4.6}$$

where γ is a constant related to the coupling of defect mechanisms to an applied strain, C_{ii} is the relevant elastic constant for the measured mode shape*, and ω is the angular frequency of the measured mode. Potential well asymmetries should fluctuate in time at temperatures nearing the glass transition (T_{glass})† due to large scale structural changes, but at energies much less than $2k_{\text{B}}T_{\text{glass}}$ the distribution of well asymmetries can be assumed to be static, with $f(\Delta)$ equal to a constant f_0 [303]. $g(V)$ can be assumed to be temperature independent at temperatures much less than T_{glass}, which allows equation 4.6 to be rearranged to relate dissipation to the distribution of barrier heights [317]:

$$\phi = \frac{\pi\gamma^2 f_0}{C_{ii}} k_{\text{B}} T g(V) \,, \qquad \text{where} \qquad V = -k_{\text{B}} T \ln(\omega\tau_0) \,. \tag{4.7}$$

Equation 4.7 can be used to experimentally determine the distribution of barrier heights within an amorphous coating through measurement of mechanical loss as a function of temperature. This analysis was applied to the coatings heat-treated at 450 °C, 600 °C, 800 °C, and 950 °C. Figure 4.26 shows the calculated barrier height distribution for all the measured modes of 600 °C heat-treated IBS silica; the frequency dependence in the link between measurement temperature and barrier height seen in equation 4.7 counteracts the frequency dependence in mechanical loss, leading to nominally identical barrier height distributions for all mode frequencies, as would be expected. As mentioned in section 4.3.1, mode 7 produces anomalous mechanical loss results across all samples and heat treatments. It was thought that there was significant energy coupling with a torsional mode rather than measurement of a purely bending mode for the 600 °C heat-treated sample, which can be seen in figure 4.26 where the mode 7 distribution is an outlier compared to the other seven measured modes.

Knowledge of the product of barrier height and well asymmetry distribution with respect to potential barrier height for an amorphous coating gives valuable insight into the internal mechanisms behind its mechanical loss, specific heat, and thermal conductivity [210, 211, 304, 315, 319, 320]. Figure 4.27 shows the change in barrier height distributions for all heat treatments of IBS SiO_2 as compared to bulk silica. Similar to the trend seen in mechanical loss shown in figure 4.20, it can be seen that the distribution of barrier heights associated with low temperature mechanical loss in the ATF IBS silica tends towards that of bulk, fused silica with increased post-deposition heat treatment.

*The values for C_{ii} and γ were taken from the literature to be 3.3×10^{-4} and 0.9 eV for fused silica [317]

†$\sim$1500 K for SiO_2 [318]

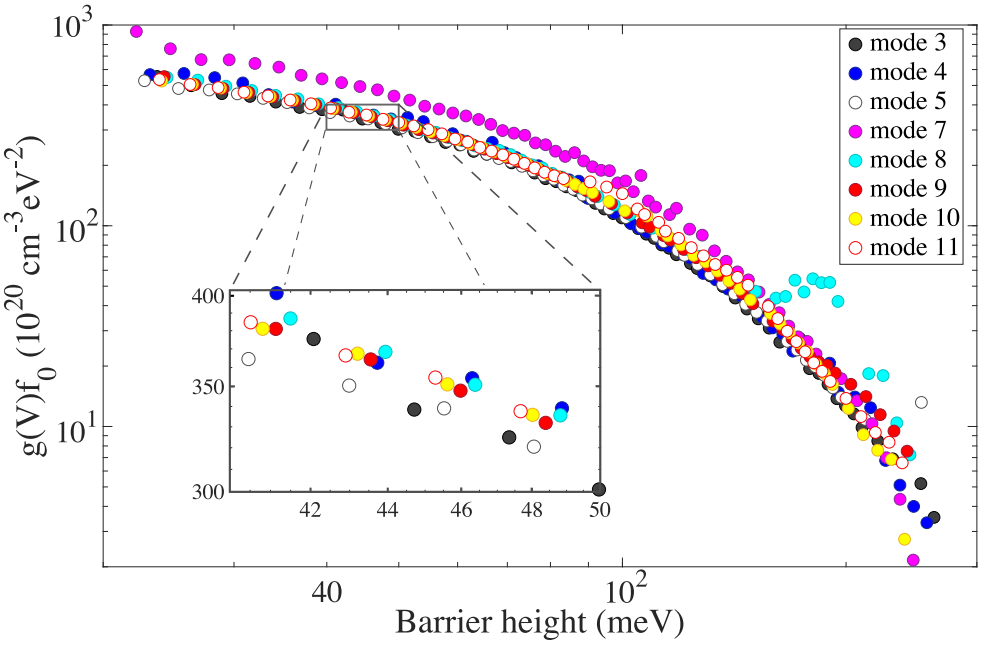

Fig. 4.26 Barrier height distribution times f_0 versus barrier height for all available modes of 600 °C heat-treated IBS SiO_2.

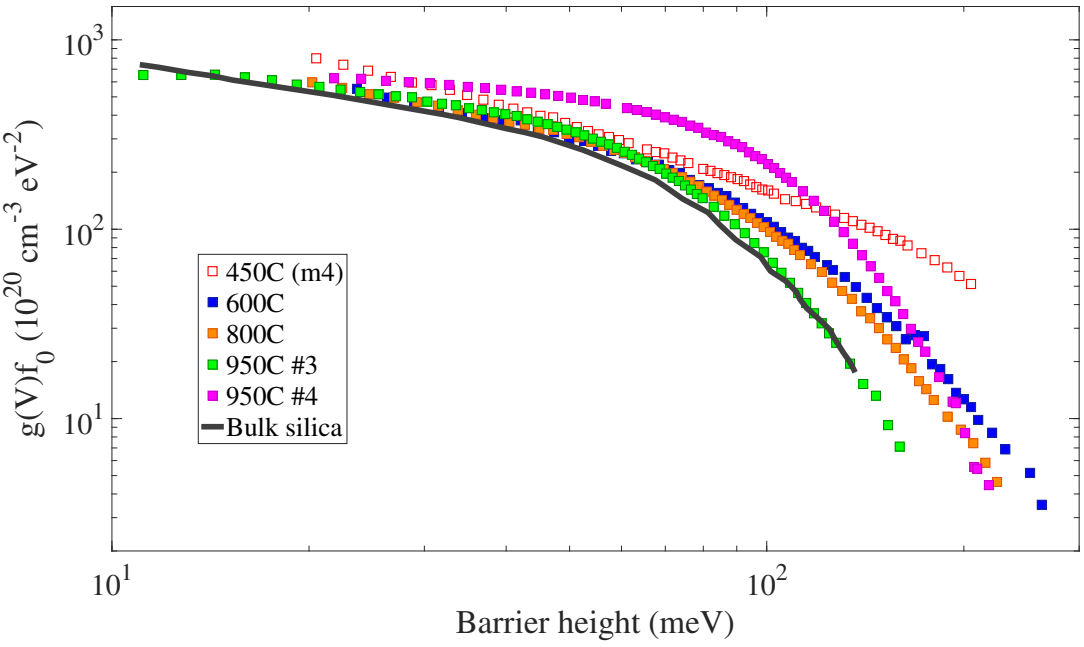

Fig. 4.27 Product of barrier height and well asymmetry distribution versus barrier height for bulk silica and all heat treatment temperatures of ATF IBS SiO_2, as calculated from mode 3 (mode 4 for 450 °C) loss between 10 K to 100 K. Bulk data corresponds to measurements at 86 kHz between 10 K to 100 K, as presented by Cahill and Van Cleve [302].

A number of interesting shifts in barrier height distribution occurred during the transition towards a bulk silica potential energy landscape with heat treatment. The number of barriers at all energies decreased for the coating heat-treated at 600 °C compared to the coating heat-treated at 450 °C, with a more significant decrease seen at the higher energies than the low energies.

The 800 °C heat-treated sample continued to have a lower overall $g(V)f_0$ than the 450 °C sample's distribution and had a nearly identical number of barriers as the 600 °C sample at all energies up to ∼80 meV. The highest energy barrier heights within the 600 °C distribution did not remain after heat treatment to 800 °C. The temperature dependent mechanical loss of the 800 °C and 600 °C heat-treated coatings were nearly identical as well, with the slight increase in mechanical loss seen in the 800 °C sample seeming to correspond with a small decrease in potential barrier heights within the energy landscape after the higher temperature anneal.

Sample 3 heat-treated to 950 °C continued the trend in barrier height energy reduction seen for the 600 °C and 800 °C heat treatments; there is a significant decrease in distribution of energies greater than ∼70 meV. This heat treatment increased slightly the number of barriers in the mid-energy range and then appeared to have lowered the distribution of energies below ∼25 meV compared to the 800 °C sample. These changes induced by the 950 °C heat treatment resulted in the barrier height and well asymmetry distribution of the thin film silica to very closely resemble that of bulk SiO_2 for all energies. In other words, the increase in the low temperature mechanical loss peak seen in 950 °C IBS SiO_2 to match that observed in bulk silica corresponds to a marked reduction in the distribution of high energy barriers observed in the lower temperature heat treatments.

Values plotted in figure 4.27 for sample 4 heat-treated at 950 °C continue to highlight the disparity between the two 950 °C heat-treated samples. There can be seen to be similarities in $g(V)f_0$ between the two samples (as well as with bulk silica), with sample 4 appearing to have a similar distribution of barrier heights between low and high energy as sample 3, just with more barriers at each potential energy. However, the large uncertainty in activation energy presented in section 4.4.1 and the anomalous nature of the temperature dependent mechanical loss and associated barrier height distribution for sample 4 leads to low confidence in conclusions drawn from either calculated values for this 950 °C sample.

Sample 4 aside, a link between increase in low energy barrier heights with a sharpening of the peak mechanical loss at low temperatures was seen with increased heat treatment of the ATF IBS silica. This agrees with computational modelling of silica films, where a high density of two-level systems with small barrier heights results

in a large, peaked value of modelled mechanical loss at low temperature [211]. This correlation leads to the conclusion that an ideal $g(V)f_0$ for low temperature coating mechanical loss would be dominated by high energy barrier heights, where the low thermal energy prevents minima hopping between potential wells. The opposite would therefore be desirable for mechanical loss at room temperature, as evidenced by 950 °C heat treatment resulting in the largest and most narrow low temperature loss peak as well as the lowest room temperature mechanical loss.

4.4.2 Coating stress

Mechanical loss is the time delay between an applied stress and the resulting strain, which, as described in the previous section, could be related to a number of physical deformations from bond orientation changes to medium and large range molecular motion. It is thought that internal stresses within an amorphous material can therefore decrease the mechanical loss angle by increasing potential barriers of coating defects, thereby reducing their associated thermal activation and tunnelling processes [232]. A possible correlation between coating stress and mechanical loss would provide further structural understanding of mechanical loss, as well as explain contradicting results between the same coating on differing substrates [229, 278].

Measurements of the radii of curvature (ROC) and subsequent calculation of coating stresses for all cantilevers coated with SiO_2 were carried out following the procedure described in section 3.4.2. As discussed in section 4.2.1, the coated cantilevers were found to have 511 nm of IBS silica on their flat side and a further ∼47 nm of IBS silica overspill onto the etched side. The total thickness was therefore increased for coating mechanical loss calculations, but the overspill should have a counteracting effect on the cantilever curvature caused by the coating. In fact, coating substrates on both sides is a common practice for eliminating sample curvature*. The ROC, and thus coating stress, was therefore assumed to be from 464 ± 6 nm of IBS silica. By the same logic, thermal oxide growth should have no effect on the final coating stress.

Coating stresses for all heat treatments are shown in table 4.7†, where the negative values correspond to compressive stress. This compressive stress in the coating can be

*It is questionable whether this results in a reduction of stress, as recent models have shown that balancing the stress by coating both sides of a cantilever leaves the substrate in a very highly stressed state, where the stress neutral line (where compressive and tensile meet to form a line of zero stress) is centred but the magnitude of stress at each coating-sub interface is much higher than if allowed to relax through curvature in a single-side coated cantilever [295].

†The sample numbers do not necessarily match heat treatments as listed in table 4.1. ROC measurements taken during the initial stages of the experiment were discarded after a 'flat' mirror in the curvature measurement was found to have a non-zero ROC.

Table 4.7 Coating stress and coated cantilever radius of curvature for heat-treated samples of ATF IBS silica. Negative stress corresponds to compressive rather than tensile stress in the coating.

Heat treatment (°C)	Sample	Radius of curvature (cm)	$\sigma_{coating}$ (MPa)	$\sigma_{thermal}$ (MPa)	$\sigma_{intrinsic}$ (MPa)
AD	1	48 ± 4	-858 ± 67	-14 ± 1	-844 ± 67
300	1	67 ± 5	-611 ± 51	-49 ± 4	-562 ± 51
	7	82 ± 3	-642 ± 26		-593 ± 26
	8	84 ± 6	-622 ± 45		-573 ± 45
450	11	154 ± 13	-343 ± 29	-75 ± 6	-268 ± 30
	5	149 ± 13	-360 ± 31		-285 ± 32
600	1	174 ± 12	-235 ± 17	-102 ± 8	-133 ± 19
800	1	179 ± 13	-228 ± 18	-137 ± 10	-91 ± 21
	7	233 ± 23	-227 ± 23		-90 ± 25
950	3	183 ± 17	-290 ± 32	-163 ± 12	-127 ± 34
	4	108 ± 7	-280 ± 46		-117 ± 48

seen to steadily decrease with higher heat treat temperatures up to 800 °C, where it appears to plateau before increasing slightly after 950 °C. The coating stress calculated from measured ROC can be thought of as a combination of intrinsic stress ($\sigma_{intrinsic}$) created by the deposition process and thermal stress ($\sigma_{thermal}$) due to differences in thermal properties between the coating and substrate [279, 281]. Intrinsic stress originates from a number of interconnected sources*, but thermal stress can be shown to be a linear function of the temperature difference, ΔT, between the measurement temperature and the deposition or heat treatment temperature:

$$\sigma_{thermal} = (\alpha_s - \alpha_c) B_c \Delta T \ , \tag{4.8}$$

where α_s and α_c are the coefficients of thermal expansion of the substrate and coating, respectively, and B_c is the biaxial modulus of the coating (defined as $Y_c/(1-\nu_c)$). From equation 4.8 it is clear that the thermal stress increases linearly with heat treatment, and since the room temperature thermal expansion coefficient of the silica coating is greater than that of the silicon substrate the thermal stress is compressive. Intrinsic stress, therefore, decreases with continued heat treatment of the coating. This is illustrated in figure 4.28.

*The intrinsic stress is strongly dependent on the coating deposition parameters, e.g. sputter rate and ion energy [321].

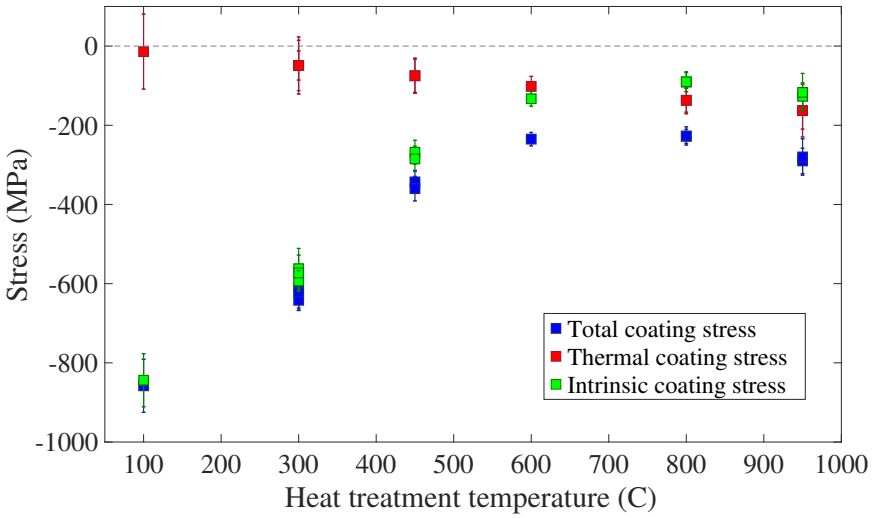

Fig. 4.28 Thermal, intrinsic, and total coating stress for all heat treatments of IBS SiO_2. All of the coating stresses are compressive and are given in table 4.7.

The intrinsic stress is of interest for comparing to room temperature silica loss measurements taken on silica discs, where the coating stress induced by thermal expansion mismatch with silicon cantilever substrates would not apply. Figure 4.29 displays a comparison of intrinsic coating stress and room temperature coating loss with respect to heat treatment temperature. The intrinsic coating stress is compressive, but the magnitude of stress is shown to highlight its decrease with heat treatment temperature. There appears to be a correlation between the stress and loss, where a decrease in loss accompanies a decrease in the magnitude of coating stress. This is the opposite effect of that observed in [232], where higher stress in silicon nitride coatings corresponded to lower mechanical loss. It is not mentioned whether the silicon nitride stress is compressive or tensile, so it possible that compressive stress is detrimental to loss while tensile improves it, but there is not enough evidence at this time to definitively claim causation.

4.5 Reactive low voltage ion-plated SiO_2

As described in Chapter 3, section 3.2.1.3, reactive low voltage ion plating (RLVIP) is a high energy coating deposition method that is thought to produce coatings as dense and homogenous as IBS films [252]. RLVIP is of interest as an alternative deposition method because of the substrate reaching temperatures of $\sim$250 °C during the ion-plating process. The high temperature deposition (compared to $\sim$100 °C for IBS) is thought to endow coating particles with enough energy to migrate towards

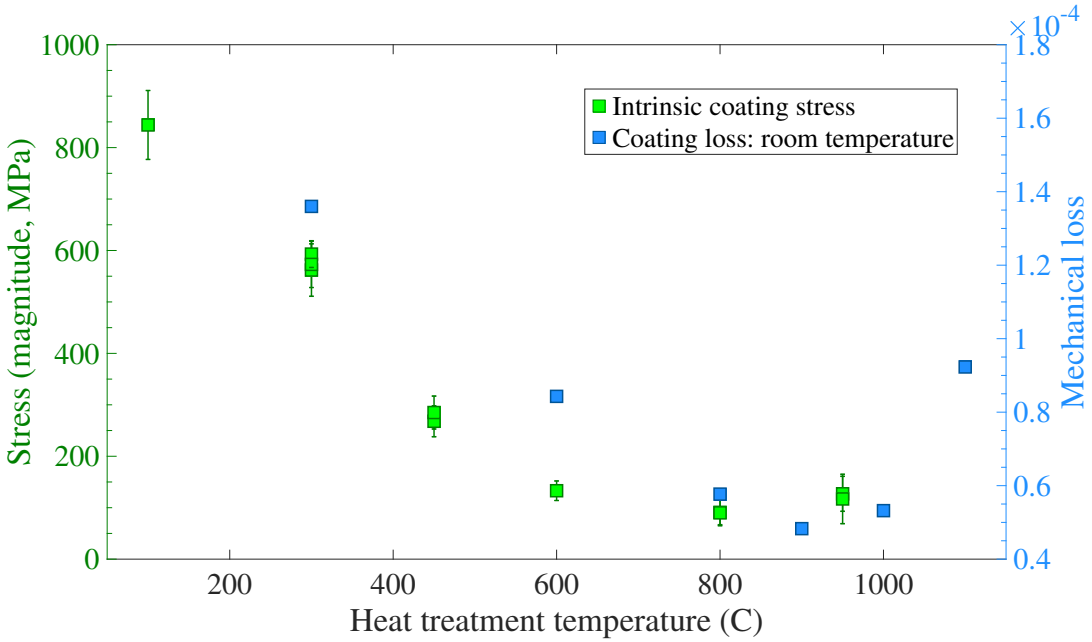

Fig. 4.29 Magnitude of intrinsic stress and room temperature loss versus heat treatment temperature for IBS SiO_2. All stress values correspond to the intrinsic compressive stress given in table 4.7. Coating mechanical loss values are from [285] and correspond to a 500 nm thick IBS silica coating measured on a silica disc.

the lowest available potential energy position prior to being trapped under further particles or fully solidifying on the surface of the substrate [244]. In an idealised state, high surface energy during deposition could allow the coating particles to explore regions of the potential energy landscape that would result in an ultra-stable glass (as previously illustrated in figure 4.24 [243]. Evidence of the link between high temperature deposition and a reduction in TLS has been presented by Liu et. al. [245] for e-beam deposition of amorphous silicon. The high energy of incident coating particles, elevated substrate temperature during deposition, and IBS-like dense deposited coating points towards RLVIP as a possible alternative deposition method for improving the mechanical loss of amorphous silica, particularly at the low temperatures of future cryogenic gravitational wave detectors. It is also of interest in terms of further investigation of deposition parameters and structural properties with respect to coating mechanical loss*.

Five silicon cantilevers etched from the same wafer were coated with RLVIP SiO_2 by Tafelmaier [252]. Similar to the overspill seen with the ATF IBS SiO_2, the RLVIP

*Recent experimentation [246] with slow deposition rate IBS SiO_2 has shown significant structural change compared to the standard deposition rate, as well as an accompanying reduction in room temperature mechanical loss, further motivating studies of deposition parameters with respect to coating loss. The relative deposition rate of RLVIP to these IBS studies is currently not known.

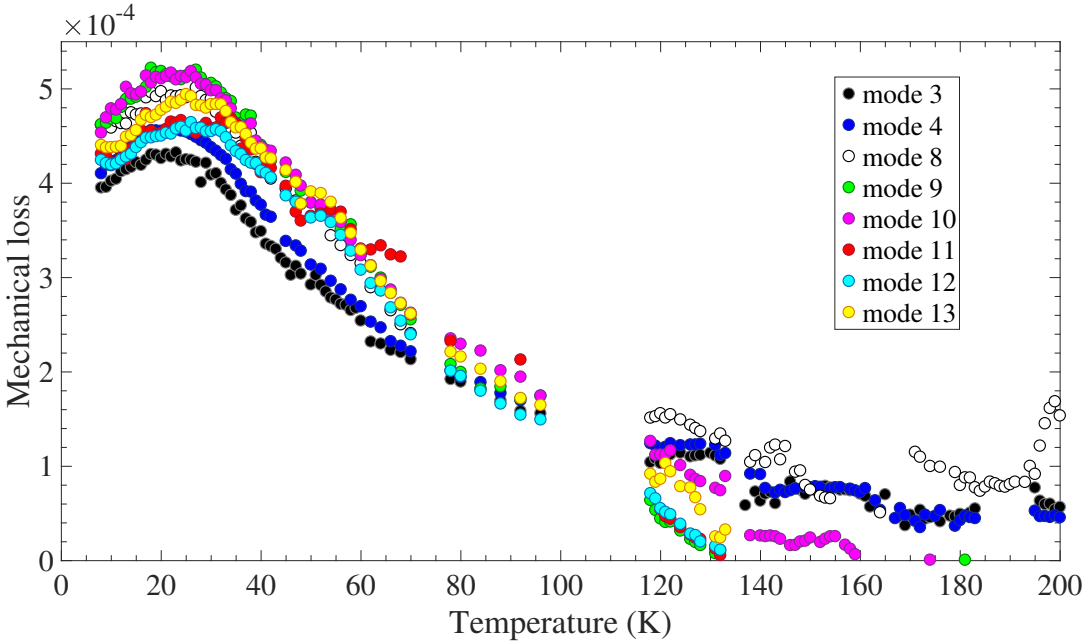

Fig. 4.30 Temperature dependent coating mechanical loss of RLVIP SiO_2 as calculated from seven measured modes.

deposition resulted in ∼28 nm of silica overspill onto the backside of the cantilever. This resulted in a total coating thickness of 528 ± 7 nm, with a total thermal oxide thickness of about 34 nm. Temperature dependent mechanical loss measurements were performed for two clamps/temperature cycles of the as-deposited RLVIP SiO_2 on a 60.3 ± 0.8 µm silicon cantilever (sample 8). Figure 4.30 shows the temperature dependence of calculated coating loss for seven measured modes*. Error bars were omitted in figure 4.30 for clarity, but the uncertainty in loss below 150 K was notably low (≤5%), with excellent agreement between the two clampings/measurement cycles for the presented modes. The coating loss exhibits a clearly defined loss peak at around 20 K to 25 K and steadily decreasing loss from 30 K to 140 K.

Figure 4.31 compares the coating loss calculated for the AD RLVIP silica to coating the loss for all heat-treatments of the IBS silica. It is important to note that the ∼250 °C deposition temperature would make the as-deposited RLVIP silica most appropriately matched to the 300 °C IBS silica in terms of thermal history. However, the ion-plated silica clearly has significantly lower loss at all temperatures compared to the AD, 300 °C, and 450 °C heat-treated IBS coating, as well as showing no evidence of a broad loss peak centred in the 60 K to 90 K range. While the RLVIP coating loss is higher that of IBS heat-treated above 450 °C at temperatures above ∼50 K, the

*Modes 5, 6, and 7 were omitted due to excess measured loss and inconsistent data between measurement cycles (similar to that shown in figure 4.8).

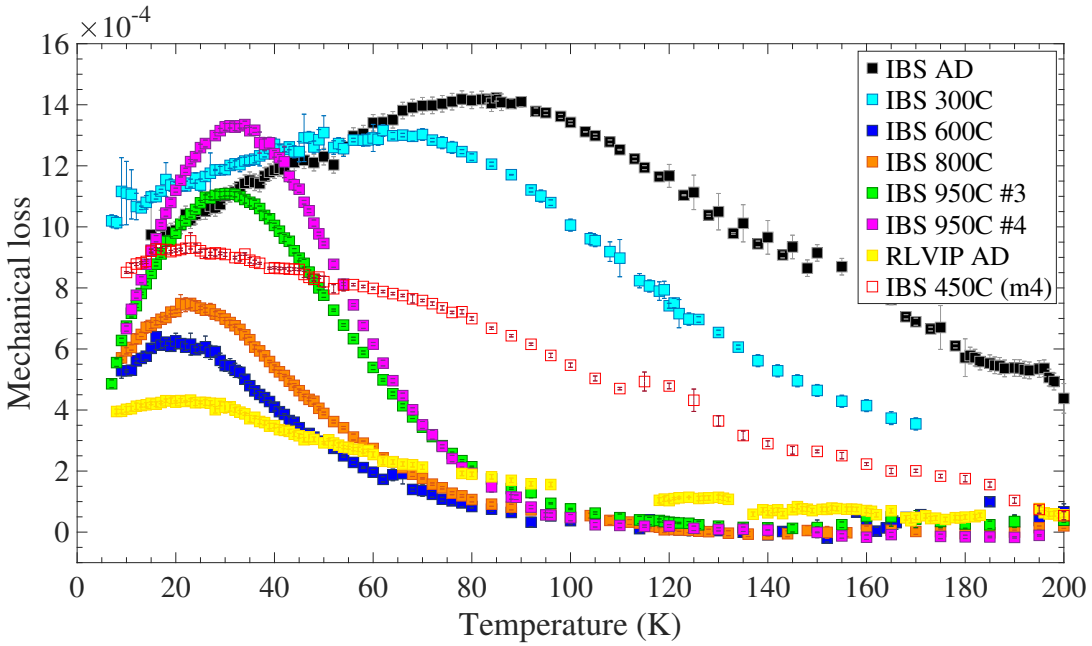

Fig. 4.31 Cryogenic mechanical loss of AD RLVIP SiO_2 and all heat treatments of IBS SiO_2. Coating loss was calculated from mode 3 for all heat treatments and coatings except for the 450 °C heat-treated IBS SiO_2, where mode 4 was used.

ion-plated silica as deposited exhibited lower coating loss below 50 K than any of the IBS heat treatments; the 600 °C heat treatment produced the lowest loss for IBS silica but was still about 50% higher at 20 K than the RLVIP silica. Figure 4.32 is included to show that there is no measurement effects contributing to the loss differences. The change in mode frequency with respect to measurement temperature for the RLVIP silica sample is nearly identical to that of the IBS silica.

Similar to the heat-treated IBS SiO_2, the RLVIP silica has a peak in mechanical loss around 20 K, which was analysed in the manner described in section 4.4.1 to calculate the associated activation energy and rate constant. Table 4.8 shows T_{peak}

Table 4.8 Thermally activated peak loss temperatures for AD RLVIP SiO_2.

Mode	Frequency (Hz)	T_{peak} (K)
3	1196	20.97 ± 0.06
4	2349	21.72 ± 0.05
8	10671	22.78 ± 0.16
9	13652	23.16 ± 0.25
10	16978	23.07 ± 0.14
12	24626	24.47 ± 0.35

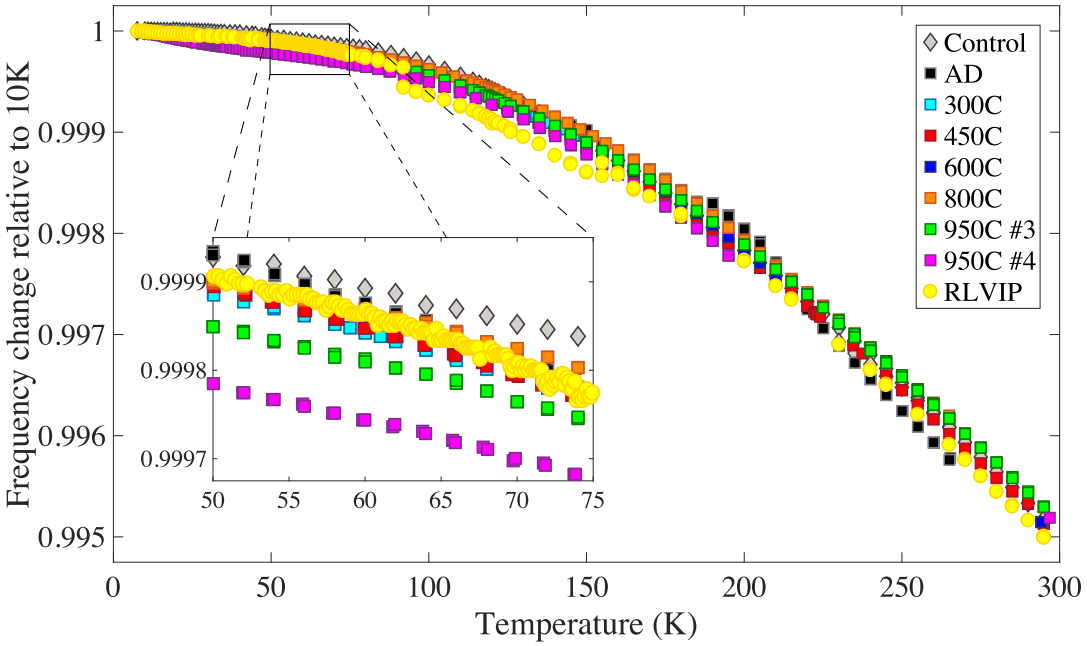

Fig. 4.32 Relative change in cantilever mode frequency with respect to measurement temperature for all heat treatments of IBS silica and the RLVIP silica. All curves are from mode 5, which varies depending on the cantilever thickness but is around 5 kHz. The discontinuity in the RLVIP silica data from about 90 −150 K is an artefact of the measurement technique, where extended periods of rest at a given temperature (78 K in this case) can alter the measured mode frequency. It is the relative change in frequency, i.e. the shape of the curve, that is relevant for comparison between heat treatments, so this slight change in mode frequency is irrelevant and not indicative of any structural feature of the coating. If the curve from this temperature range were scaled to match the relative frequency change in the temperature ranges prior to and following it, there would be a consistent, unbroken trend.

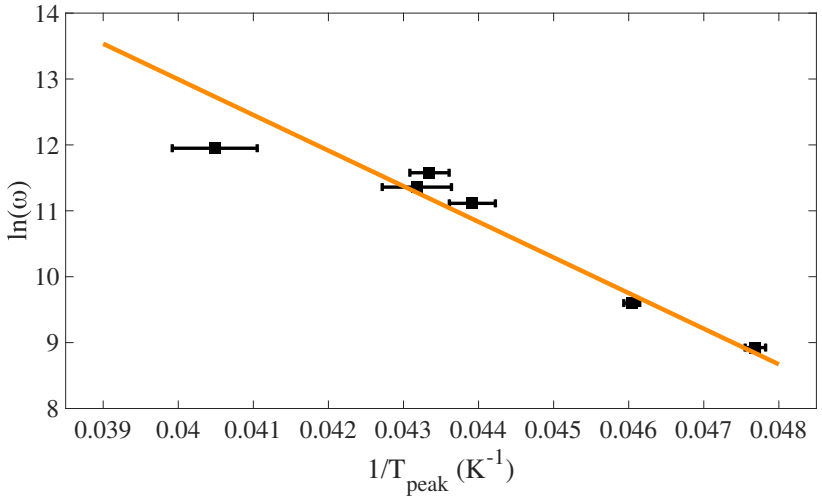

Fig. 4.33 Arrhenius plot for AD RLVIP SiO_2 using T_{peak}s and measured frequencies shown in table 4.8.

Table 4.9 Radius of curvature and coating stress for all RLVIP SiO_2 samples.

Sample	Radius of curvature (cm)	ϕ_{coating} (MPa)
3	68 ± 6	-428 ± 134
4	69 ± 6	-423 ± 132
6	69 ± 6	-423 ± 133
7	63 ± 6	-462 ± 145
8	42 ± 3	-691 ± 55

and measurement frequency for all measured modes with control data of matching frequency. As is indicative of thermally activated loss processes, the peak loss temperature increased with measurement frequency for all but mode 10. An Arrhenius plot utilising these fitted T_{peak} values is shown in figure 4.33, where the low frequency modes had relatively large weighting due to their extremely low uncertainty in peak temperature. The activation energy of the low temperature peak was 46.6 ± 5.8 meV with a rate constant of $92.4 \pm 8.3 \times 10^{-17}$ s. This E_a agrees with that calculated for the peaks in IBS silica and is within the range of activation energies found for bulk silica. The barrier height distribution determined by τ_0 will be shown in section 4.6.

As mentioned in section 4.4.2, there is a possible correlation between coating stress and temperature dependent mechanical loss. Given the significant difference in mechanical loss between the IBS and RLVIP silica without any heat treatment, it is of interest to see the native stress within the RLVIP coating. Table 4.9 contains the radii of curvature and coating stresses for all 5 cantilevers coated with RLVIP silica. Notable in comparing the magnitude of stress between coated samples is the disparity between sample 8 and the rest of the coated samples. Sample 8 was the only cantilever for which the thickness was confirmed through mode frequency measurements. Cantilever thicknesses for the rest of the samples were assumed to be within 12 µm* of cantilever 8, so the stress values presented in table 4.9 are calculated with identical thicknesses, with the uncertainty accounting for a possible increase or decrease coating thickness of 12 µm. This wide thickness range and accompanying large uncertainty fails to rectify the difference in stress between the samples. However, sample 8's apparent elevated stress could be explained by the cantilever being an outlier in thickness for the wafer, similar to cantilever 4 in the ATF silica coating run. If samples 3 through 7 in table

*6 µm is the average deviation of cantilever thicknesses for cantilevers from the same wafers studied in this thesis.

4.9 were 77 µm thick (well within the range of cantilevers from a single wafer) rather than the 60 µm as assumed, then the stresses for all coated samples match given the measured radii of curvature.

Further evidence for the validity of -691 ± 55 MPa as an accepted value for the stress in the as-deposited RLVIP can be seen in figure 4.39 in the next section, where the ion-plated silica is plotted with respect to its deposition temperature at 250 °C and found to fall within the trend of stress reduction with heat treatment of the silica coating. This agreement is particularly interesting given the stark difference in loss between this coating and the heat-treated IBS SiO_2. The initial conclusion is that the ion plating changes the silica coating structure in a way to reduce the loss without having a significant effect on the coating stress. The thermal stress should be the same for both coatings, so it would be the intrinsic coating stress for which high temperature deposition matches the effects seen with post-deposition heat treatment.

Continued measurement of the RLVIP silica samples would be extremely valuable to determine the validity of not only RLVIP as a valid alternative to IBS but also the model of ultra-stable vapour deposited glasses produced via increased surface mobility during deposition at elevated temperatures. The difference in loss seen between the 300 °C heat treated IBS silica and the RLVIP SiO_2 clearly points towards interesting differences between the application of thermal energy to a coating during the sputtering process as opposed to after deposition. Other experiments aimed at understanding the effects of heated substrate deposition are focused on high index coatings such as amorphous silicon or tantalum pentoxide, where there is evidence that heating the substrate during deposition improves the room temperature mechanical loss as deposited, with further improvement through post-deposition heat treatment [322, 323]. However, IBS tantalum pentoxide, previously shown to begin crystallising after heat treatment at 600 °C [256], exhibited signs of crystallisation during deposition at 480 °C [324]. It is possible that tantala is unable to reach the stage of an ultra-stable glass due to a relatively low crystallisation temperature. Thin film SiO_2 has resisted crystallisation at temperatures up to 1200 °C [285], so silica-based deposition experiments, whether through RLVIP or IBS, are therefore highly valuable in testing whether an ultra-stable glass is attainable through high surface energy deposition alone.

While further measurements of heat-treated RLVIP silica will be of interest for comparison with IBS SiO_2, the reduction in loss seen with as-deposited RLVIP silica already makes it a valuable substitution material in considering future mirror coating designs. Amorphous silicon is currently likely to be used as a high index coating layer

in future, cryogenic detectors, but it requires heat treatment at 400 °C to 500 °C in order to minimise absorption* [259, 325, 326].

If the temperature dependent mechanical loss of RLVIP SiO_2 after a ∼450 °C heat treatment remains similar to that seen with the coating as deposited, then using RLVIP rather than IBS SiO_2 would significantly improve the thermal noise of the multilayer mirror coatings in future detectors operating below 50 K, such as the proposed Einstein Telescope. Chapter 7 will discuss the thermal noise implications of different coating combinations in more detail.

4.6 Deposition comparisons

The parameter space of coating deposition variables–deposition rate, ion-beam energy, intra-chamber substrate motion, etc.–is large enough that the same coating technique can produce thin films with different properties. Even nominally the same input parameters can result in differences in mechanical loss of the IBS coating when produced in different coating chambers [246]. This section will compare IBS silica coatings produced from a number of different deposition chambers while also including the RLVIP silica to provide context for its properties presented in section 4.5.

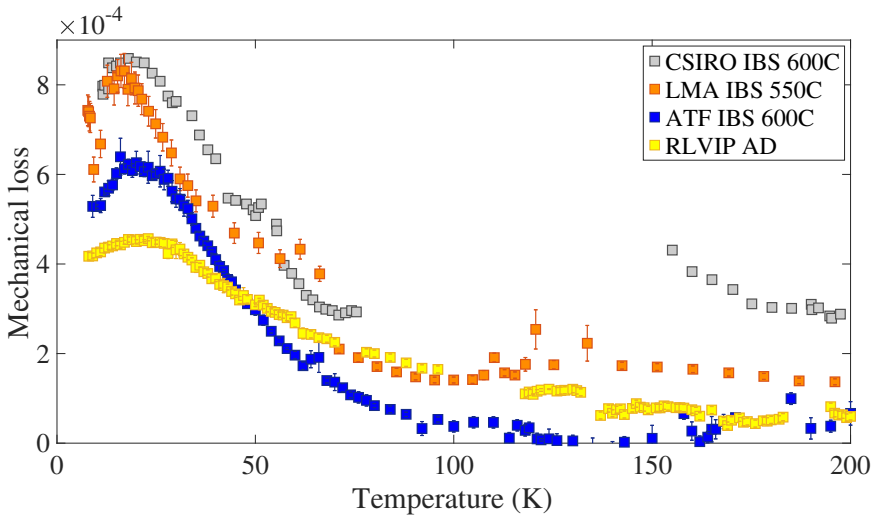

Fig. 4.34 Temperature-dependent mechanical loss of as-deposited RLVIP SiO_2 and heat-treated IBS SiO_2 coatings deposited in three different sputtering chambers. All loss is from measurements of cantilever bending mode 3.

Figures 4.34 through 4.37 show the temperature dependent mechanical loss of 600 °C IBS amorphous silica deposited in three different sputtering chambers, as well

*Measurements of the RLVIP SiO_2 absorption are preliminary but have shown levels less than 3 ppm, well within the range for further decrease through heat treatment towards that of IBS silica.

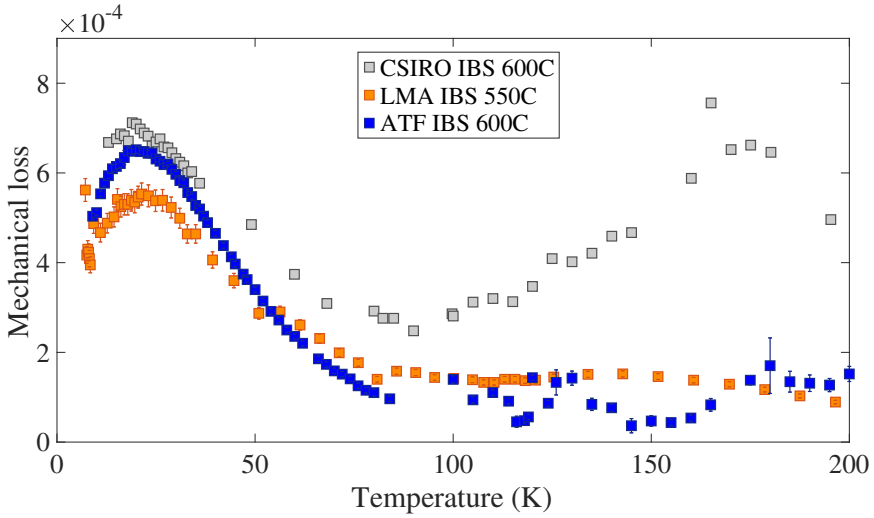

Fig. 4.35 Temperature-dependent mechanical loss of heat-treated IBS SiO_2 coatings deposited in three different sputtering chambers. All loss is from measurements of cantilever bending mode 5.

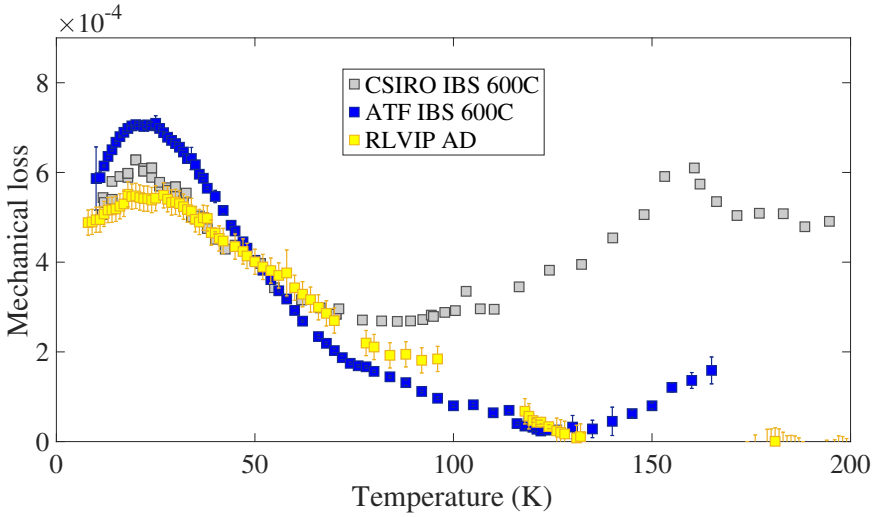

Fig. 4.36 Temperature-dependent mechanical loss of as-deposited RLVIP SiO_2 and heat-treated IBS SiO_2 coatings deposited in two different sputtering chambers. All loss is from measurements of cantilever bending mode 9.

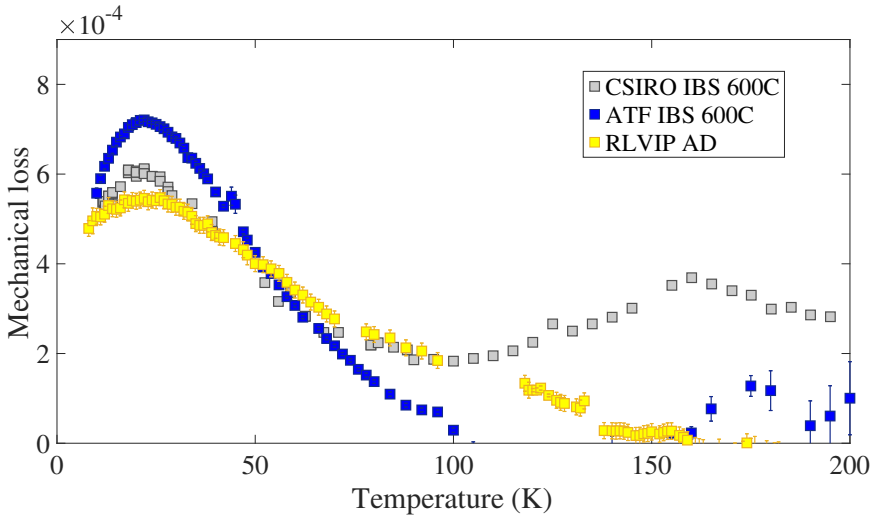

Fig. 4.37 Temperature-dependent mechanical loss of as-deposited RLVIP SiO_2 and heat-treated IBS SiO_2 coatings deposited in two different sputtering chambers. All loss is from measurements of cantilever bending mode 10.

as the AD RLVIP SiO_2. The three IBS silica films are from ATF (presented in this thesis), CSIRO [258], and LMA [327]. Figure 4.34 shows the loss at ∼1 kHz (mode 3) for all these coatings. As was shown in figure 4.31, the RLVIP exhibits the lower loss below 50 K than IBS silica. The ATF SiO_2 had the lowest loss of the three IBS coatings at this frequency and temperature range, with the LMA and CSIRO loss having comparable magnitudes. Above 50 K, the LMA silica can be seen to have similar loss to the RLVIP silica, where both are roughly double the loss of the ATF IBS coating. The CSIRO silica had a large gap in data in this temperature range, but a peak in loss around 150 K is apparent and the magnitude of the loss above 50 K is about five times that of the ATF silica.

Figure 4.35 shows the loss of the three IBS coatings as calculated from mode 5; the RLVIP silica did not have any loss data for this mode frequency. Both the LMA and CSIRO coatings display reduced mechanical loss compared to mode 3 at the lowest temperatures, with about a 33% reduction in mechanical loss at 20 K for the LMA IBS silica and ∼20% for the CSIRO. The loss above 50 K remained nearly the same as mode 3, although the peak in loss for the CSIRO coating seems centred around 175 K rather than 150 K. The ATF silica appears to fluctuate in loss in this temperature region, with what could be a peak at a similar spot as the CSIRO, but the relative loss increase at the peak and the preceding ∼60 K temperature steps is much less pronounced than the CSIRO, which sees the 'high' temperature peak loss match that of the loss peak at 25 K.

Figures 4.36 and 4.37 (modes 9 and 10) show nearly identical trends, where the CSIRO silica now has lower loss at the 25 K than the ATF IBS SiO_2. In both cases the RLVIP silica continued to have the lowest in mechanical loss at the peak temperature, but for modes 9 and 10 it is only about 15% lower than the CSIRO loss, as compared to over 50% lower for the CSIRO loss from mode 3. No LMA silica data was available for modes 9 and 10.

While the origins of the differences are not fully understood, figures 4.34 through 4.37 show evidence that there is variability in coating properties even when deposited using the same sputtering technique. The losses of all three differ significantly at the low temperature peak, and the CSIRO and LMA silica coatings display greater change in loss at low temperatures with respect to measurement frequency than the ATF coating. All three behaved differently above 50 K, particularly the CSIRO silica, which contained a loss peak at about 150 K not seen in the other coatings.

Computational modelling of amorphous silica could give an explanation behind the high temperature peak, as recent modelling results have come close to replicating the CSIRO $\sim$150 K peak while maintaining a low temperature loss peak [211]. All previous modelling efforts utilised a TLS distribution comprised of uncorrelated barrier height and asymmetry distributions [303, 315, 317, 320, 328–330]. This 'separable' distribution was found to greatly overestimate coating loss above 20 K so was altered to have an asymmetry cutoff of 0.1 eV, which was an arbitrary value chosen because it forced a low temperature peak in the modelled loss that better matched experimental silica loss [315, 320]. The separable-cutoff TLS distribution gives a temperature dependent loss very close to that of the LMA silica coating at 1 kHz, with a 20 K peak of about 8×10^{-4} and a plateau of about 2×10^{-4} above 100 K. However, the cutoff energy is an ad hoc decision and a separable TLS distribution is not justified given the correlated nature of barrier heights and assymetries with respect to relaxation time of a material. A fully correlated TLS distribution adds computational requirements but it better represents the TLS model used to describe mechanical loss in a material. Modelling coating loss with the correlated TLS distribution produces a peak at 115 K similar in shape to that seen at 150 K for the CSIRO coating, but adds an extra peak at 12 K that is both sharply defined and large (1.3×10^{-3}) [211]. The new, correlated TLS distribution model is a step forward in terms of marrying theory with computational results, but the accuracy of these models is dependent on the experimental results which they attempt to replicate; two out of the three IBS silica coatings shown here do not match the loss produced by the current iteration of this model, so little is currently explained by the computational loss modelling, but future results are of high interest.

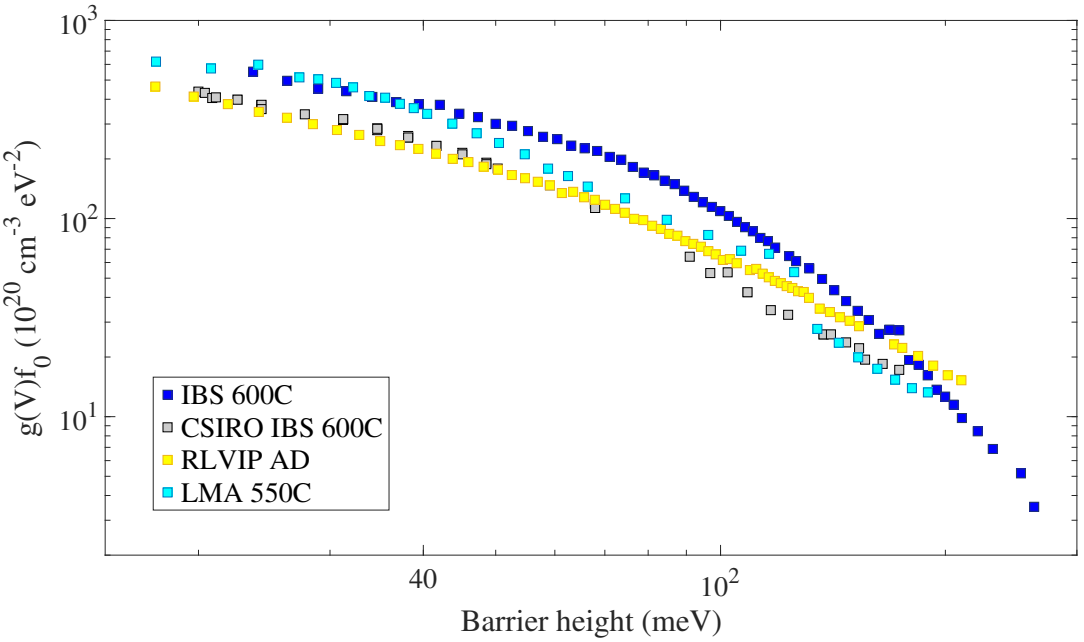

Fig. 4.38 Barrier height distribution for 550 °C heat-treated LMA IBS SiO_2, 600 °C heat-treated CSIRO IBS SiO_2, AD RLVIP, and 600 °C heat-treated ATF IBS SiO_2. All calculated coating values are from mode 3.

One possible origin of the difference in CSIRO silica loss in this higher temperature region is the difference in film thickness; whereas the LMA and ATF coatings were both nominally 500 nm, the CSIRO IBS silica was 1 µm thick*. Other origins of the difference may be highlighted by looking beyond mechanical loss. Figure 4.38 shows the barrier height distributions for RLVIP silica as deposited, 600 °C heat-treated CSIRO, 550 °C heat-treated LMA IBS silica, and 600 °C heat-treated ATF IBS SiO_2. CSIRO E_a and τ were taken from Martin et. al. [258] to be 32.1 ± 2.9 meV and $1.8 \pm 0.1 \times 10^{-13}$ s, respectively. The rate constant used to determine barrier heights for the LMA silica was $4.3 \pm 0.4 \times 10^{-14}$ s, which was determined through an Arrhenius fit of the peak temperature and measurement frequency for three measured modes and, as such, was an estimation. The dominant activation energy of the low temperature, thermally activated loss peak in heat-treated LMA silica was calculated from the slope of the estimated Arrhenius fit and found to be 32.0 ± 3.5 meV. This matches the activation energy associated with the loss peak in CSIRO silica, and might explain the greater similarity between these IBS coatings than with the ATF IBS silica in terms of $g(V)f_0$.

*Differences in calculated coating loss with respect to coating thickness will be shown in Chapter 5 with respect to measurements of an Al_2O_3 coating.

The ATF silica can be seen to have more barriers at all energies above ∼40 meV than the LMA or CSIRO coatings, which share similar overall distributions. The CSIRO silica seems to have a similar number of high energy barriers but fewer low energy barriers than the LMA coating. All three ∼600 °C heat-treated IBS silica barrier height distributions were different than the AD RLVIP silica, which displayed a similar spread of barrier heights to the 450 °C ATF SiO_2 shown in figure 4.27, but with fewer barriers at all potential energies. This was similar to the loss profile of the two coatings shown in figure 4.31, where the shape of the RLVIP loss mirrored that of the 450 °C ATF IBS loss but lower in magnitude across all temperatures.

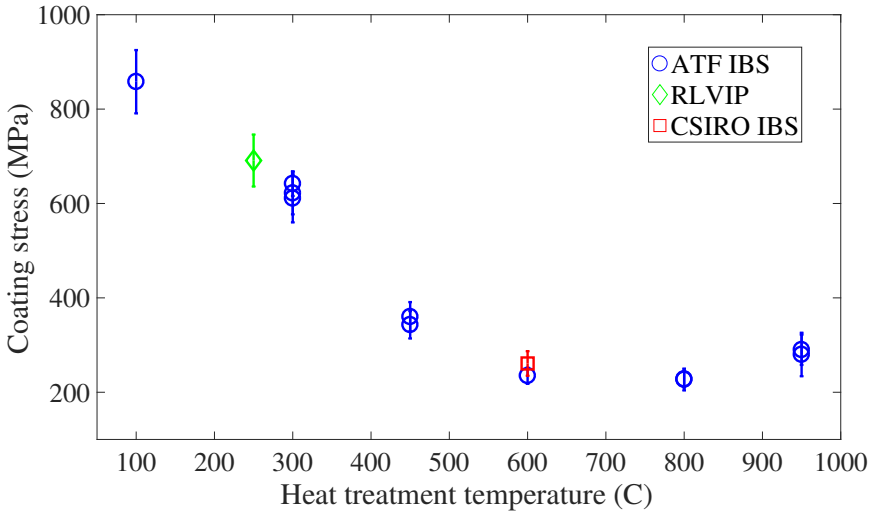

Fig. 4.39 Magnitude of coating stress for AD RLVIP silica, 600 °C CSIRO IBS silica, and all heat treatments of ATF IBS SiO_2. All of the coating stress was compressive, which is normally denoted as negative, but is shown as positive to demonstrate the reduction in coating stress with heat treatment.

While the mechanical loss and barrier height distribution showed little agreement between silica depositions, the coating stresses with respect to heat treatment shown in figure 4.39 display similarities between the measured coatings. Coating stress for the LMA IBS SiO_2 was not available, but the stress in the CSRIO cantilever (-261 ± 26 MPa) was found to be within measurement uncertainty of the 600 °C ATF silica*, and the AD RLVIP plotted based on its deposition temperature fits within the trend of reduction in the ATF IBS silica stress with heat treatment.

One material property not known was the coatings' relative densities. A 1% change in density can result in up to a 50% change in rigidity (shear modulus) and a 0.01

*The CSIRO coating was 1 µm thick and deposited on a ∼50 nm silicon cantilever; its coating stress agreeing with the matching heat treatment of ATF silica assuaged concerns over assumptions of relative coating-substrate thickness upon which the modified Stoney's equation was predicated.

difference in Poisson's ratio, and for bulk silica the density is strongly dependent on the temperature at which the silica was fused [300]. There was also found to be a strong link between density and mechanical loss through TLS modelling of thin film silica [211]. Coating density could differ for a number of reasons, the trapped water content, for example, can be a factor with 0.96 ppm decrease in density for every 1 weight ppm of water in the glass [331]. However, the difference in mechanical loss between coating chambers at LMA corresponded to a 10% difference in coating density [246], which could point towards slight differences in deposition chambers resulting in altered coating density even with the same IBS parameters. Measurement of the densities of the three IBS coatings and the RLVIP coating compared in this section would therefore be of high interest. Furthermore, while comprehensive investigation of temperature dependent mechanical loss for the CSIRO and LMA IBS silica coatings would be of interest to see if the trends in loss and barrier height distribution are consistent even with slightly different magnitudes of loss, the continued heat treatment and measurement of RLVIP silica remains a high priority in order to investigate the change in coating loss for a silica coating already exhibiting low temperature mechanical loss than any measured IBS coating.

4.7 Conclusions

The mechanical loss of IBS SiO_2 was characterised from 10 K to 300 K for the coating in an as-deposited state, as well as for post-deposition heat treatments at 450 °C, 600 °C, 800 °C, and 950 °C. A consistent changing of the shape and magnitude of the low temperature coating loss occurred with increasing heat treatment temperature. A broad, high loss peak was seen in the coating as deposited and decreased in magnitude with heat treatment until disappearing after 600 °C. Simultaneously, a sharp peak below 50 K began to emerge, increased in magnitude, and shifted upwards in temperature with increased heat treatment temperature. The shape and magnitude of the low temperature loss peak tended towards the loss peak observed in bulk silica loss with heat treatment; the 950 °C heat treatment displayed loss very similar to bulk SiO_2. Heat treatments above 450 °C had mechanical loss too low to be measured above 200 K. These samples displayed nearly identical loss from 100 K to 200 K. These trends were apparent in all measured modes except number 7, which often displayed evidence of energy coupling with a torsional mode.

One sample heat-treated at 950 °C was found to have anomalous coating loss, activation energy and barrier height distribution. The results were included but assumed

to be an artefact of either the sample breaking during measurement or the high oxide thickness relative to the IBS coating. Measuring another sample heat-treated to 950 °C would be valuable to confirm this assumption.

IBS silica heat-treated at 600 °C was found to have the lowest loss across all measured temperatures, which corresponded with the largest proportion of high energy barrier heights of any heat treatment. The barrier height distribution of silica heat-treated from 450 °C to 950 °C tended toward that of bulk silica in a similar manner to that seen in the mechanical loss measurements. Above 600 °C the coating can be seen to gain increasing numbers of low energy barriers and lose access to the low potential wells seen by the 600 °C heat-treated coating. The activation energy associated with the low temperature loss peak in the heat-treated silica was found to be consistent within uncertainty across heat treatments and in the range from 45 meV to 53 meV, which agrees with the E_a for bulk (and RLVIP) silica but not with previous measurements of IBS SiO_2 coatings deposited by CSIRO and LMA. The coating stress, however, was found to be consistent between the CSIRO and ATF silica coatings, with the ATF silica having high compressive coating stress (-858 ± 67 MPa) that reduced with heat treatment to match that of the CSIRO silica (about -260 MPa) after a 600 °C heat treatment.

RLVIP silica as deposited was found to have lower loss below 50 K than any heat treatment of the IBS silica coating. It displayed no evidence of the broad loss peak seen in the AD, 300 °C, and 450 °C heat treatments of ATF IBS silica. This may point towards high temperature deposition producing greater changes in loss than possible through post-deposition heat treatment, and is worth further investigation. It is of high interest to heat-treat the RVLIP silica coating to observe the change in loss and barrier height distribution with this high energy, heated substrate coating technique. The stress in the RLVIP coating was found to be in the range expected for an IBS silica coating heat treatment at the RLVIP deposition temperature.

Greater understanding of correlations between structural changes and temperature dependent mechanical loss moves the field closer to understanding the causal origins of mechanical loss in thin film coatings. The inverse relationship between loss at 30 K and at room temperature for increased heat treatments of silica seen in this chapter gives a much fuller picture of the physical changes in silica coatings with post-deposition annealing. The comprehensive loss data also enables significantly increased accuracy in the design of future coating stacks, where absorption in the high index layer may require heat treatments, and therefore loss estimations, at temperatures besides the 600 °C samples already measured. These new values also provide crucial references for statistical modelling of mechanical loss within amorphous solids, a

rapidly improving field that could be a powerful tool for understanding the difference in material behaviour observed between bulk and thin-film form, as well as for choosing new coating materials for future cryogenic gravitational wave detectors.

Chapter 5

Mechanical characterisation of ion-beam sputtered aluminium oxide

5.1 Introduction

Coating thermal noise from the multilayer mirror coatings in gravitational wave detectors is currently dominated by the high index 25% Ti:Ta_2O_5 layers; the low index SiO_2 layers have comparatively insignificant mechanical loss at room temperature. As a result, the majority of coatings research has concentrated on reducing the mechanical loss of the high index coating layer through further doping or replacing the tantalum pentoxide [229, 259, 280]*. With the proposed switch to cryogenic operation temperatures the relative thermal noise contribution of the low index layer is significantly increased due the low temperature peak in loss for silica, which is discussed in detail in Chapter 4. It is therefore of increasing importance to find possible alternatives for silica as a low index coating layer for cryogenic gravitational wave detectors, particularly given the emergence of potentially viable high index replacement materials such as amorphous silicon [259, 326, 332].

Ion-beam sputtered (IBS) amorphous alumina (Al_2O_3) has been studied previously and ruled out as a viable room temperature low index coating layer due to its higher loss and refractive index than amorphous silica [163]. However, the low temperature mechanical loss has not been characterised, and alumina could be a viable replacement for silica in cryogenic detectors if found to have lower loss near potential operating temperatures ($\sim$10, 20, and 120 K). The refractive index of alumina coatings can vary depending on the deposition technique and substrate from 1.52 to 1.76 [333, 334]. The refractive index of ALD amorphous alumina at 1064 nm on a silicon substrate was

*See Chapter 6 for a more in-depth look into high index coating research.

found to be 1.63 [335], which is the value assumed for IBS alumina studied in this thesis. Compared to the refractive index of 1.45 for silica, this would result in more coating layers to achieve the same reflectivity as the current coating stack, resulting in a thicker coating and, therefore, a likely increase in thermal noise. However, if the mechanical loss of alumina is significantly lower at cryogenic temperatures then the extra layers may not matter in terms of overall thermal noise contribution. Furthermore, the dependence of both thermo-optic and coating Brownian noise on the relative Young's modulus of coating layers with respect to the substrate could result in alumina providing better noise characteristics as a low index coating layer; the cryogenic detectors will utilise bulk silicon or sapphire substrates, with both materials having greater Young's moduli than that of the fused silica currently used.

The viability of alumina as a coating material rests on it having significantly lower mechanical loss at temperatures between 10 and 130 K than IBS silica. Two sets of etched silicon cantilevers were coated with IBS Al_2O_3 in order to characterise the temperature-dependent coating loss for a series of post-deposition heat treatments. The two sample sets were coated with different thicknesses of alumina, 505 nm and 2.02 µm*, in order to investigate any possible dependence of the mechanical loss on the coating thickness, which could be an intrinsic property of the coating or occur as a result of stress and curvature in the cantilever. This chapter presents the temperature dependent mechanical loss of both thicknesses of alumina, as well as its change in stress, with respect to heat treatments between 300 °C and 800 °C.

5.2 Sample preparation

Amorphous alumina thin-film coatings were deposited onto silicon cantilever substrates via ion beam sputtering by ATF using an aluminium sputtering target [240]. Similar to the silica coatings presented in Chapter 4, there was no active substrate heating during deposition, but temperatures up to ∼90 °C were reached during the sputtering process. Two different coating thicknesses were deposited, resulting in eight cantilevers with a 2.02 ± 0.02 µm thick coating and eight cantilevers with a 505 ± 8 nm thick coating. No overspill of IBS alumina was found through ellipsometer measurements of the back (etched) side of the coated cantilevers.

Four samples from each coating thickness were heat treated by ATF, with two samples annealed at 300 °C and two more at 400 °C. Their heat treatment profile consisted

*The requested deposition thicknesses were 500 nm and 2.00 µm, with the extra 5 and 20 nm, respectively, of alumina measured post-deposition.

Table 5.1 ATF IBS Al_2O_3 coated silicon cantilever samples. Cantilever thicknesses were calculated from the bending mode frequencies found during mechanical loss measurements. Each coating thickness deposition run included sample numbers 1 through 12; duplicate sample numbers between coating thicknesses do not mean that the 505 nm samples were coated with extra alumina to reach 2.02 µm.

Heat treatment (°C)	2.02 µm		505 nm	
	Sample	Thickness (µm)	Sample	Thickness (µm)
AD	1	72.9 ± 0.1	2	59.8 ± 0.1
300	7	60.3 ± 0.4	7	50.8 ± 0.1
300 (24 h)	7	60.3 ± 0.4	1	60.0 ± 0.2
400	11	60.5 ± 0.1	10	55.1 ± 0.2
600 (24 h)	3	54.6 ± 0.1	3	60.5 ± 0.1
800 (24 h)	10	61.7 ± 0.1	4	61.3 ± 0.1

of 90 minutes of ramp up time, a 60 minutes plateau at the maximum temperature, then 60 minutes of ramp down time. All other heat treatments were performed with a ramp up of about one hour followed by a 24 hour plateau at temperature and then an overnight ramp down to room temperature. The samples measured during this experiment and their corresponding heat treatments are shown in table 5.1.

All samples were baked in atmosphere at 1000 °C prior to coating to grow a layer of thermal oxide. The cantilevers coated with 2.02 µm IBS alumina had an average oxide thickness of ∼84 nm prior to coating, and those coated with 505 nm had a pre-coated average oxide thickness of ∼58 nm. This oxide thickness, as measured through ellipsometry, did not increase after the cantilevers were coated. Cantilevers from each wafer underwent the 1000 °C thermal oxide growth stage but were not coated in order to provide control data for coating loss calculations. The 2.02 µm control sample was 59.8 ± 0.2 µm thick with about 95 nm of total oxide thickness, and the 505 nm control sample was 59.6 ± 0.1 µm with about 40 nm of thermal oxide. Gaps in control sample data in temperature range dominated by thermoelastic loss (∼ 150 to 300 K) were interpolated based on standard differences seen between expected and measured thermoelastic loss for uncoated samples with full data sets. All but four of the cantilever samples listed in table 5.1 were within one micron of their corresponding control cantilevers, and therefore required no scaling of the control data. Samples 1 and 3 for the 2.02 µm coating and 1 and 10 for the 505 nm differed in thickness by at least five microns. The control data for these samples was increased or decreased in

Table 5.2 Range of Young's modulus values for thin film alumina deposited via a number of PVD techniques, as well as a polycrystalline bulk alumina sample (PC bulk). RE is reactive evaporation, PLD is pulsed laser deposition, RMS is reactive magnetron sputtering, and ALD is atomic layer deposition. A γ suffix represents deposition in a state of partial or full crystallinity (cubic).

Deposition method	Film thickness (μm)	Young's modulus (GPa)
RE	0.35	100 [336]
E-beam	0.35	120 [337]
ALD	0.5	200 [338]
PC bulk	2540	309 [339]
RMS	0.3 to 1.2	140 [340]
	1.0 to 2.0	105 to 170 [341]
	1.0 to 2.0	110 to 220 [342]
	0.2 to 3.0	177 to 219 [343]
RMS-γ	1.0 to 2.0	300 [342]
	2.0	350 [344]
PLD-γ	1.0	320 to 360 [345]

the thermoelastic region according to the thickness of the coated sample following the method described in Chapter 4 (section 4.2.2).

5.2.1 Young's modulus of thin-film Al_2O_3

Previous mechanical loss studies of IBS alumina as the low index layer in multilayer mirror coatings assumed the Young's modulus to be 400 GPa, which is identical to bulk, crystalline sapphire [163, 195]. This assumption was necessary due to an absence of Young's modulus characterisation of IBS alumina films in the literature. However, Al_2O_3 films formed by other deposition methods, particularly magnetron sputtering, have been extensively studied and the range of Young's moduli from these investigations is summarised in table 5.2. It can be seen that even coatings deposited in a crystalline state (RMS-γ and PLD-γ) remain well below the bulk alumina modulus used in previous studies.

One possible explanation for the large disparity in stiffness shown in table 5.2 could be the nature of amorphous alumina formation: alumina is a non-quench glass, meaning that Al_2O_3 cannot be formed in an amorphous state via rapid cooling from a liquid state [346]. Amorphous alumina can be created using PVD, but some deposition techniques have shown evidence of polycrystalline structures, even at deposition

temperatures below 100 °C. Ion beam assisted IBS alumina deposited at 100 °C, however, has been shown to be amorphous [347, 348]. Even so, the hardness of alumina films have been found to increase with post deposition heat treatment as the film transitions from an amorphous to a crystalline structure [349].

The transition temperature from amorphous film to a crystalline structure has been shown to depend strongly on both the deposition method and deposition temperature, where some amorphous films crystallise after heat treatments as low as 570 °C and others can resist crystallisation at annealing temperatures up to 1200 °C [348–351]. Ion beam assisted IBS alumina has been shown to be amorphous at deposition temperatures below 500 °C and to have a post deposition heat treatment phase transition path of a-Al_2O_3 $\xrightarrow{800\,°C/6h}$ γ-Al_2O_3 $\xrightarrow{1000\,°C/6h}$ γ-Al_2O_3+α-Al_2O_3 $\xrightarrow{1200\,°C/6h}$ α-Al_2O_3, which is very similar to the thermal behaviour of pulsed reactive magnetron sputtered alumina [347]. It was therefore assumed that the structure of IBS Al_2O_3 is most comparable to RMS films and the Young's modulus taken to be 200 GPa. This value is within the upper range of the measured RMS stiffnesses, but was chosen due to the increased density and uniformity seen in IBS compared to magnetron sputtered films, as well as the relatively high heat treatment temperatures used for this experiment.

5.3 Results

The mechanical loss between between 10 K to 295 K of 505 nm and 2.02 µm thick IBS Al_2O_3 was calculated after a range of post-deposition annealing temperatures following the procedures detailed in Chapter 3. Figure 5.1 shows the expected thermoelastic loss, measured control and coated cantilever loss, and calculated coating loss for a 505 nm IBS alumina sample. The same set of measured and calculated loss can be seen for the 2.02 µm thick coating in figure 5.2. The samples were heat treated at 600 °C and 800 °C, respectively, but are broadly representative of the measured versus calculated data from all samples and heat treatments studied for each thickness.

Unlike the silica coatings presented in Chapter 4, the IBS alumina loss remained well above that of the bare silicon control at temperatures above 100 K. This resulted in greater coating loss fidelity in the mid-range temperatures. However, it can be seen in figure 5.1 that the measured sample loss is affected by the thermoelastic loss of the control sample at temperatures above ∼200 K, where the loss increases in conjunction with the rise of substrate thermoelastic loss. The frequency dependence of thermoelastic loss resulted in this influence being magnified for higher frequency modes. The same effect was not present for the 2.02 µm alumina coating, which can

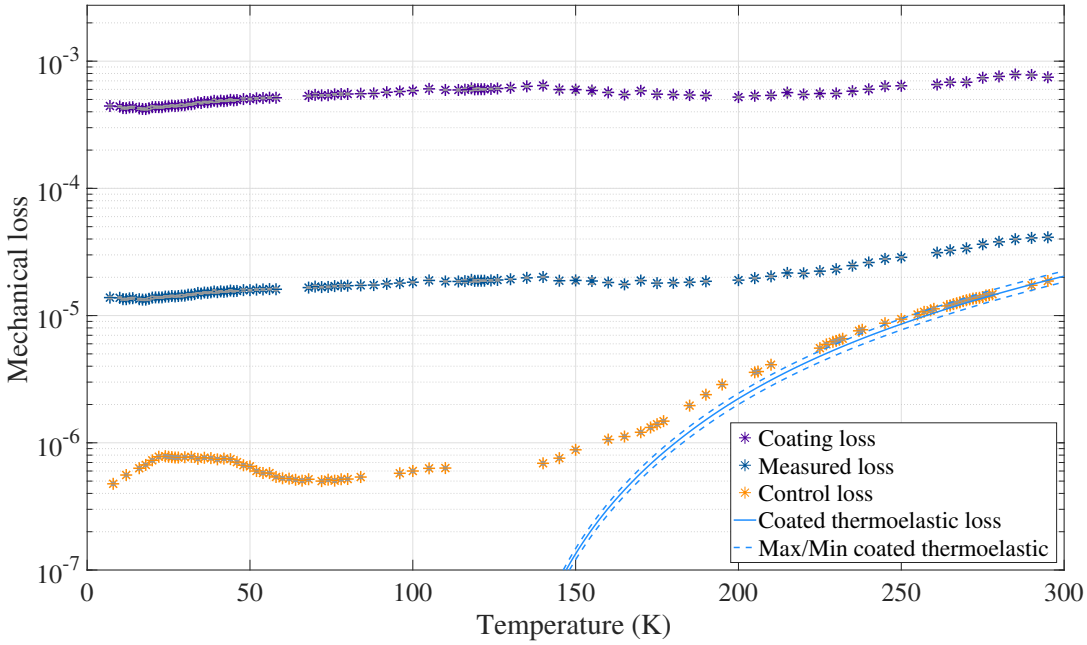

Fig. 5.1 Control, measured, and calculated loss for 505 nm of 600 °C heat treated Al_2O_3. Shown values are from mode 5 (∼3.8 kHz).

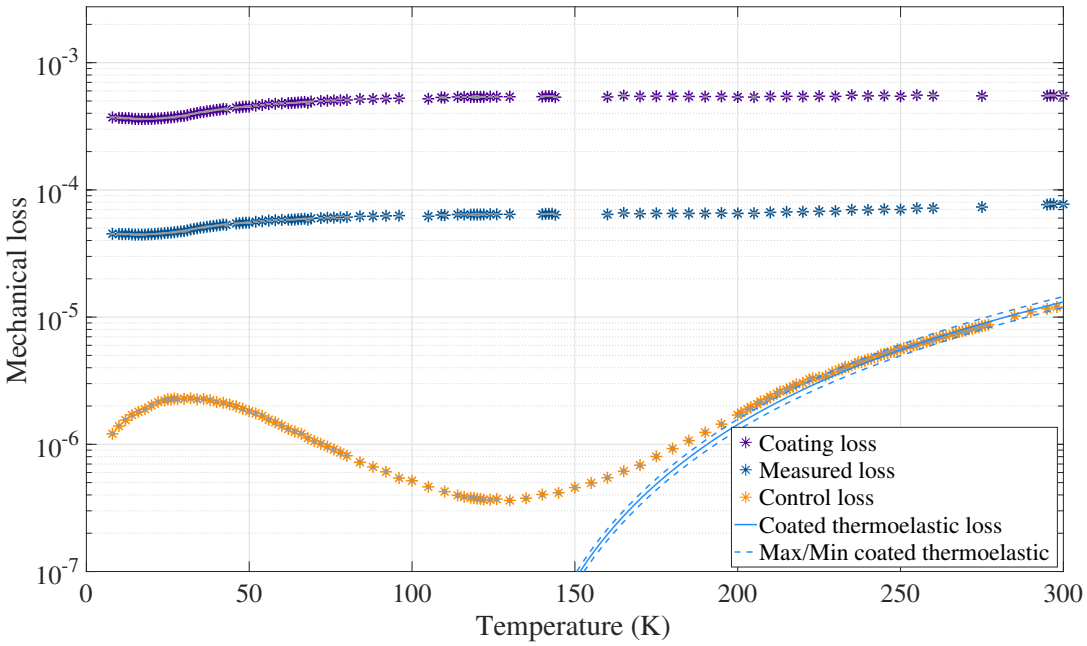

Fig. 5.2 Control, measured, and calculated loss for 2.02 µm of 600 °C heat treated Al_2O_3. Shown values are from mode 4 (∼2.4 kHz).

be seen in figure 5.2 to be unaffected by the increased substrate thermoelastic loss at high temperatures. This is a result of the thicker coating having about four times the relative energy dissipation compared to the 505 nm sample, thus increasing the gap in measured loss between the control cantilever and the coated sample.

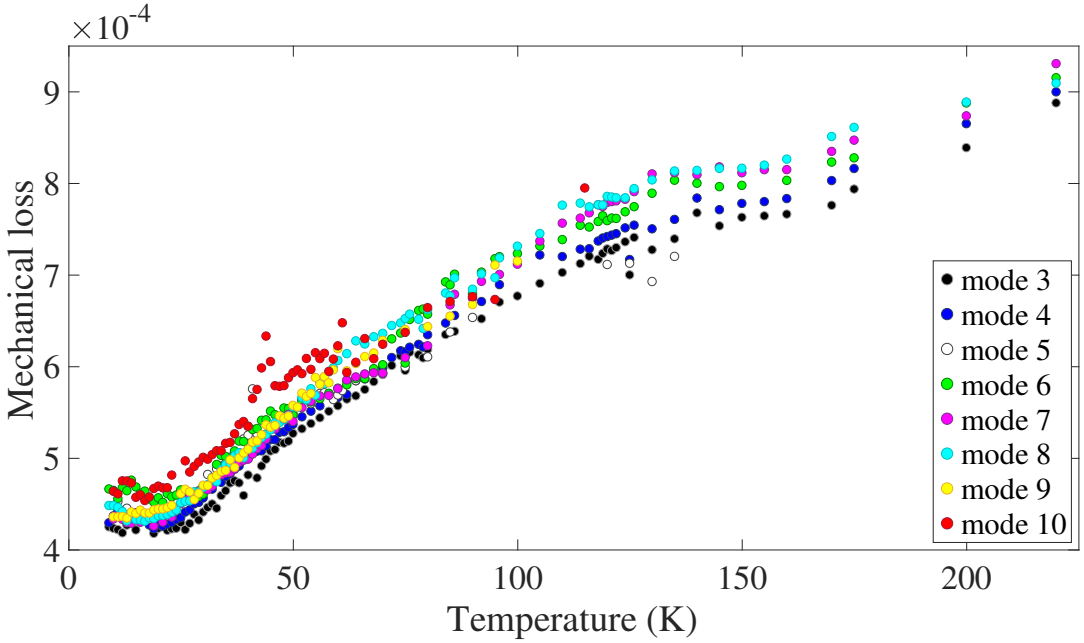

Fig. 5.3 Coating loss from all measured modes of 505 nm Al_2O_3 without heat treatment.

Figures 5.3 and 5.4 show coating loss for 505 nm Al_2O_3 as deposited and 2.02 µm Al_2O_3 heat treated at 400 °C, respectively, where the loss was calculated from all measured cantilever bending modes. Both loss compilations show consistent loss trends between measured modes, as well as evidence of increased loss accompanying higher frequency modes. This was the case for all measured samples of both coating thicknesses.

Figures 5.5 and 5.6 show coating loss for all heat treatments of 505 nm thick alumina, where each graph represents coating loss calculated from one measured mode frequency (modes 4 and 8, respectively). Below 25 K the loss can be seen to be nearly identical regardless of heat treatment temperature; all samples agree to within 10% in this temperature range. This region is also notable for exhibiting a slight trough in loss just below 20 K, which is clearly defined for all heat treatments.

Heat treatment of the Al_2O_3 produced changes in the magnitude of loss above the low temperature trough region, but after an initial reduction in loss following heat treatment at 300 °C, only minor changes were observed at higher heat treatment temperatures. Further annealing at 400 °C and 600 °C produced slight variations in

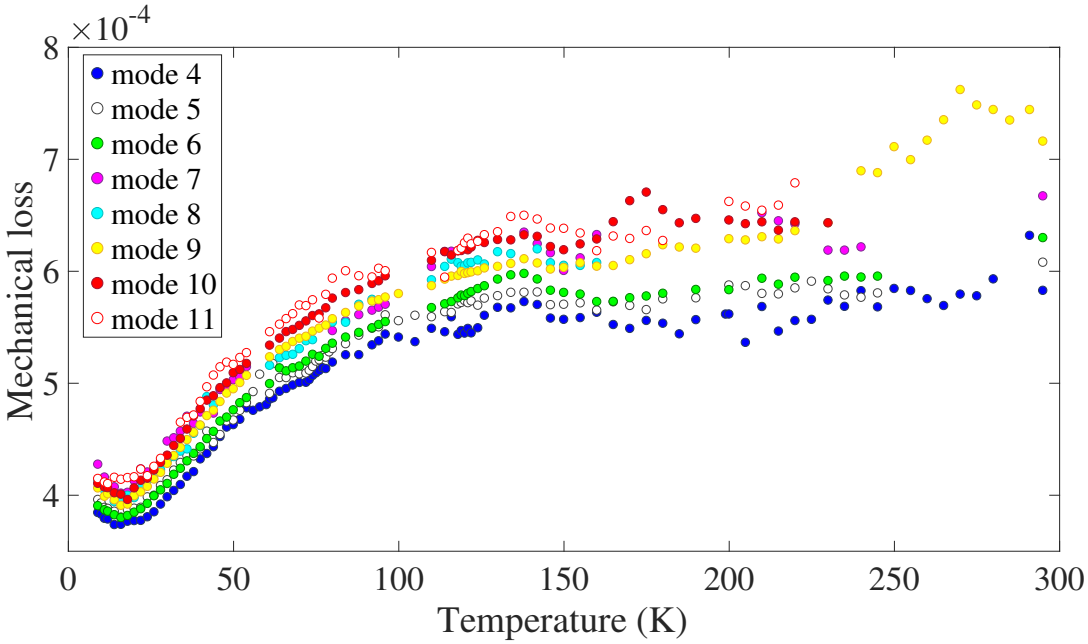

Fig. 5.4 Coating loss from all measured modes of 2.02 µm Al_2O_3 after heat treatment at 400 °C.

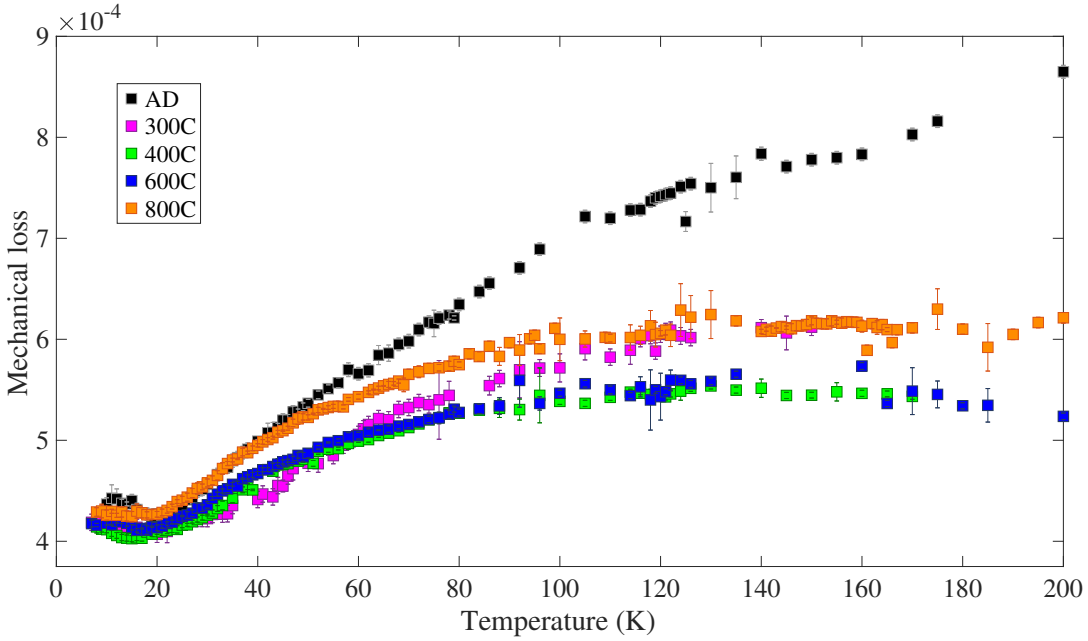

Fig. 5.5 Coating loss from all heat treatments of 505 nm IBS Al_2O_3, as calculated from mode 4 (∼1.9 to 2.3 kHz).

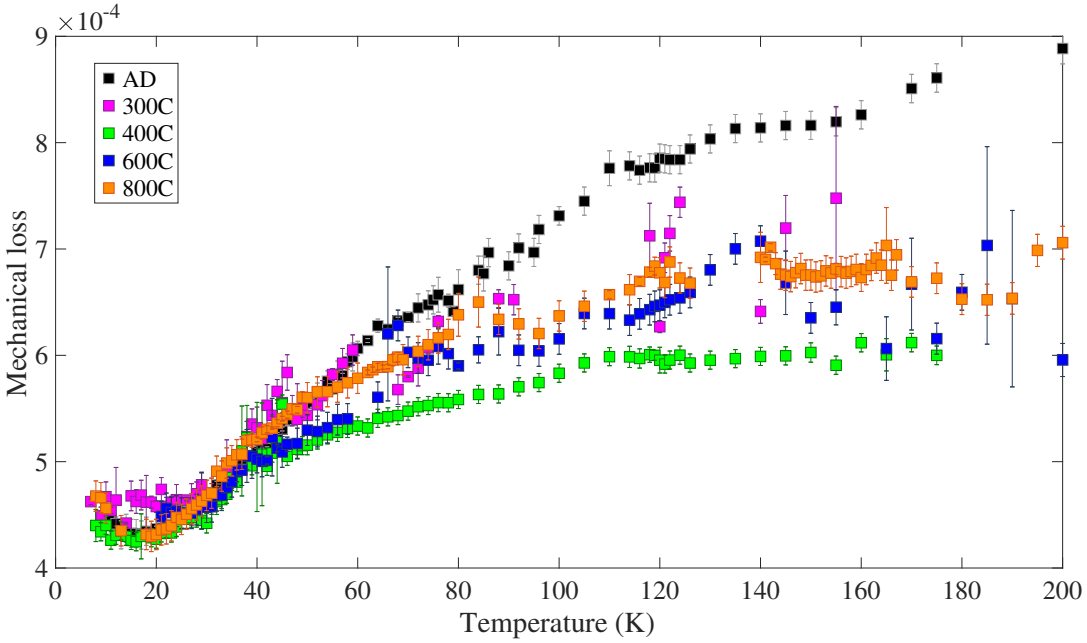

Fig. 5.6 Coating loss from all heat treatments of 505 nm IBS Al_2O_3, as calculated from mode 8 (∼8.9 to 10.7 kHz).

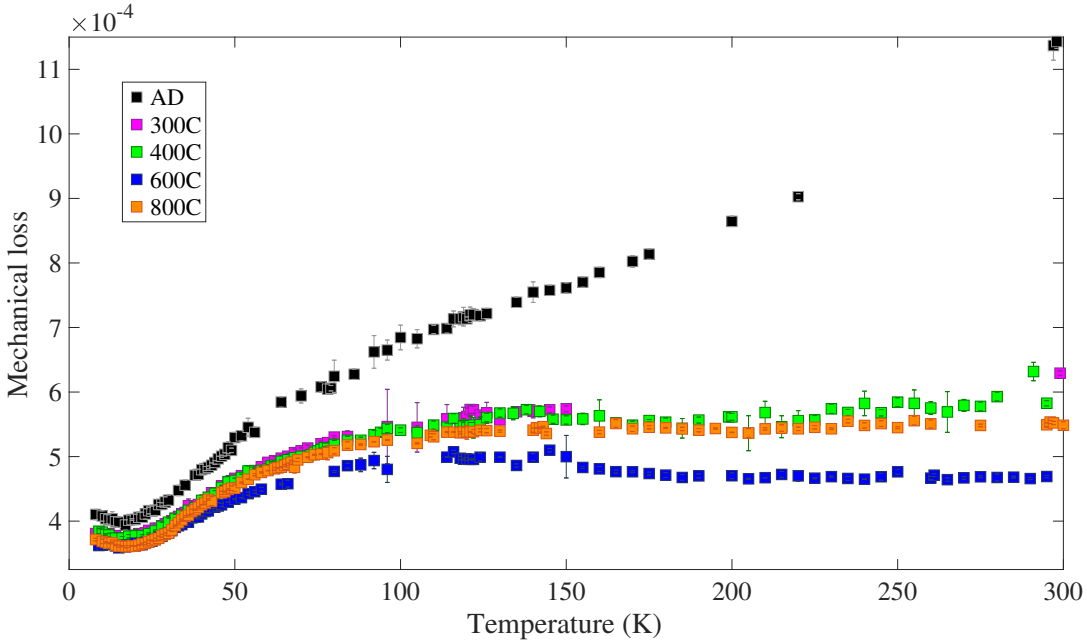

Fig. 5.7 Coating loss from all heat treatments of 2.02 µm IBS Al_2O_3, as calculated from mode 4 (∼2.1 to 2.8 kHz).

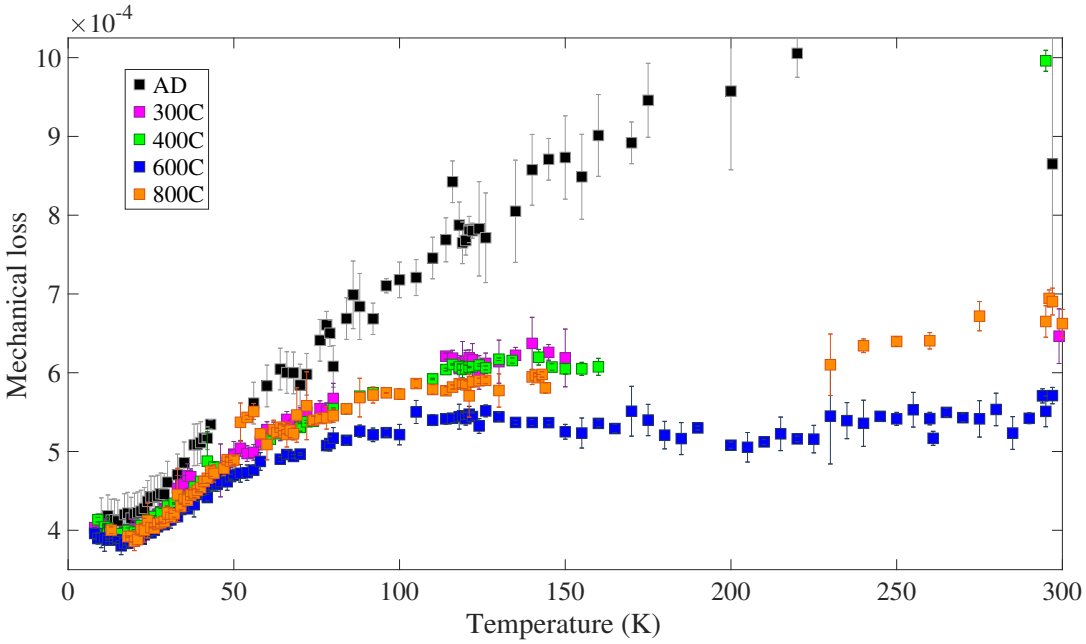

Fig. 5.8 Coating loss from all heat treatments of 2.02 µm IBS Al_2O_3, as calculated from mode 8 (∼9.6 to 12.8 kHz).

mechanical loss from ∼40 to 200 K, but no significant changes in the overall loss trend occurred. In other words, the gradual increase and then plateau of mechanical loss seen after heat treatment at 300 °C remained for all further heat treatments.

There is some evidence, seen in figure 5.5, that the 800 °C heat treatment resulted in an increase in loss compared to the lower temperatures. As outlined in section 5.2.1, 800 °C is the temperature at which IBS alumina begins to transition from amorphous to crystalline, so the slight increase in loss at this heat treatment temperature could be indicative of the early stages of crystallisation within the 505 nm coating. Furthermore, ion-assisted IBS alumina coatings have shown increased surface roughness after 800 °C heat treatment, which could be responsible for the slight increase in mechanical loss for this heat treatment of the ATF IBS alumina [347].

Figures 5.7 and 5.8 show the same loss versus heat treatment curves as 5.5 and 5.6 but for the 2.02 µm thick coating. Similar to the thinner alumina coating, the 2.02 µm Al_2O_3 increases in loss with measurement temperature in an as-deposited state, and it follows a temperature dependent loss trend of trough-rise-plateau for all heat treated samples. Heat treatment can also be seen to have little to no effect on coating loss at the low temperature trough region. Unlike the 505 nm thick alumina, the 2.02 µm coating clearly exhibits the lowest loss after 600 °C and shows no difference in loss after heat treatment at 800 °C. Notable as well is the improved fidelity of the 2.02 µm loss; single mode heat treatment loss comparisons for the 2.02 µm alumina coating were

Table 5.3 Coating stress and coated cantilever radius of curvature for heat treated samples of ATF IBS alumina. Negative stress corresponds to compressive stress in the coating. Positive values indicate tensile coating stress.

Heat treatment (°C)	2.02 µm		505 nm	
	ROC (cm)	σ (GPa)	ROC (cm)	σ (GPa)
AD	22 ± 2	-461 ± 35	53 ± 3	-504 ± 35
300	–	–	90 ± 7	-301 ± 23
300 (24 h)	24 ± 2	-279 ± 21	59 ± 4	-331 ± 25
400	27 ± 2	-251 ± 19	96 ± 7	-236 ± 17
600	173 ± 11	32.3 ± 2.1	245 ± 17	112 ± 8
800	48 ± 3	147 ± 10	134 ± 8	210 ± 13

more consistent between modes and had significantly less measurement error for each heat treatment. It is unknown why the thicker coating had this reduced measurement uncertainty.

5.4 Analysis

The characterisation of temperature dependent coating loss for a range of heat treatments of IBS Al_2O_3 is valuable for judging its merit as a low index coating in future coating designs. This section will compare the loss results to those presented for silica in Chapter 4, as well as delve deeper into the features seen between Al_2O_3 thicknesses and heat treatment parameters. Measurements of the coating stress for all heat treatments of both thicknesses is also presented.

5.4.1 Stress

The radius of curvature was measured and coating stress calculated using the procedures described in section 3.4 for all of the studied alumina coatings. Since there was no evidence of alumina overspill on the coated samples, the coating thicknesses used in stress calculations match those used for calculating loss. No oxide growth was measured on the back side of the cantilevers, and the pre-coating thermal oxide thickness was equal on both sides of the cantilevers, so it was assumed that any curvature induced by thermally grown SiO_2 would cancel itself out. A summary of all radii and coating stress is given in table 5.3.

Both coating thicknesses share similar stress trends, with a continued change in stress after increased-temperature heat treatments and a transition from compressive to tensile stress occurring between the 400 °C and 600 °C heat treatments. They differ, however, in that the 2.02 µm alumina displayed lower stress at all heat treatments except the 400 °C. The disparity was more pronounced after the transition from compressive to tensile stress, where the 505 nm alumina had over three times the coating stress as the thicker coating after 600 °C and 30% higher stress after 800 °C*.

5.4.2 Thickness dependent mechanical loss

The 2.02 µm coating was found to exhibit lower loss than the 505 nm coating across all measured temperatures for all heat treatments, and the difference was found to increase with heat treatment. Figure 5.9 shows the loss of the coatings as deposited and the difference can be seen to be minimal, with less than a 10% difference in loss across the measured temperature range and nearly indistinguishable loss from 50 to 100 K. Figures 5.10 and 5.11 show the 300 °C and 400 °C heat treatments, respectively, and display a gradual increase in loss disparity with heat treatment culminating in a clear and distinct difference in loss of about 20% across all measured temperatures after heat treatment at 800 °C, which is shown in figure 5.12. The 600 °C annealed coating loss fits within this trend as well and can be seen in figures 5.21 and 5.22 in section 5.4.4. Figure 5.13 shows the difference in loss between the two thicknesses at 10 K, 20 K, and 120 K to summarise the changes seen between the thicknesses after each heat treatment. While the magnitude of the difference is relatively small, there is a clear trend of the 505 nm coating having higher loss than the thicker coating, with this difference increasing in conjunction with increased heat treatment temperatures.

The relative energy dissipated within a thin-film coating compared to the bulk substrate is dependent on the coating thickness, as shown in section 3.3.1. If the coatings remain homogenous and isotropic then there should be no thickness dependence with regards to mechanical loss. It was therefore expected that the 505 nm and 2.02 µm IBS alumina coatings would produce identical temperature dependent mechanical loss results. The trends shown in figures 5.9 through 5.13 clearly show otherwise, and understanding the origin of the loss disparity could provide insight into connections between coating structure and loss.

A potential origin of the loss difference could be an increase in surface defects on the coatings. It has also been shown that high temperature annealing of alumina coatings increases the surface roughness of the films [347], and high surface roughness

*A graph of the results shown in table 5.3 is presented in section 5.4.4.2 (figure 5.23)

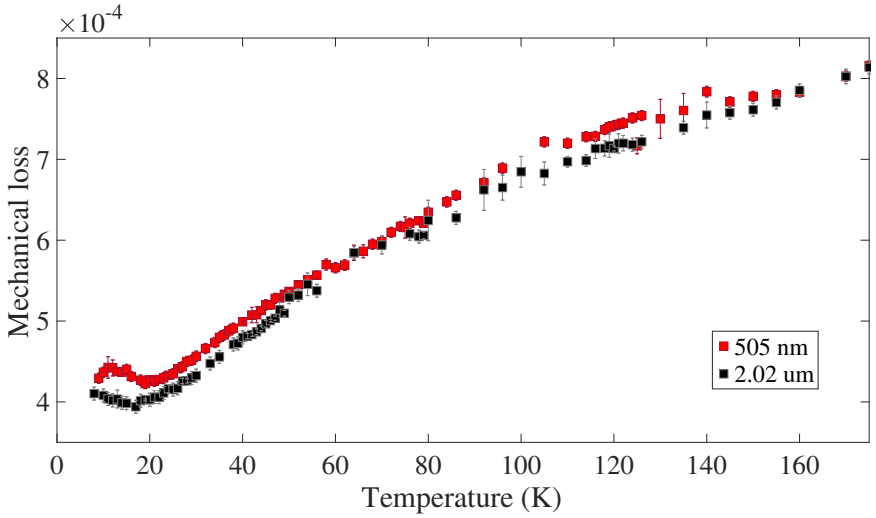

Fig. 5.9 Coating loss of 2.02 µm versus 505 nm Al_2O_3 without heat treatment and calculated from mode 4: 2.8 kHz and 2.3 kHz, respectively.

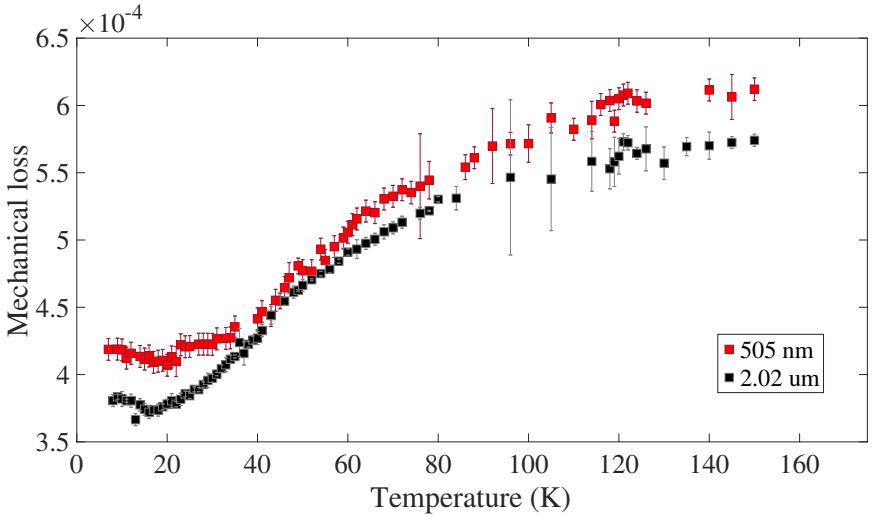

Fig. 5.10 Coating loss of 2.02 µm versus 505 nm Al_2O_3 heat treated at 300 °C and calculated from mode 4 (2.3 kHz for both thicknesses).

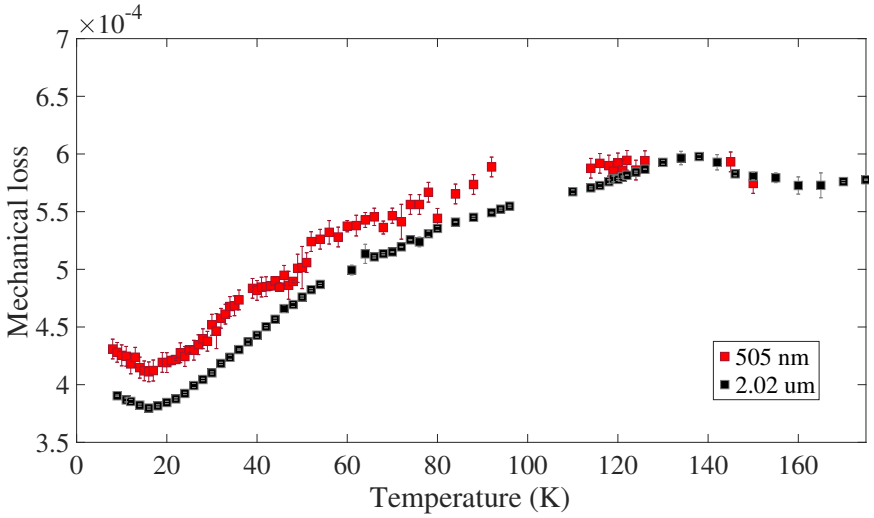

Fig. 5.11 Coating loss of 2.02 µm versus 505 nm Al_2O_3 heat treated at 400 °C and calculated from mode 6: 5.7 kHz and 5.2 kHz, respectively.

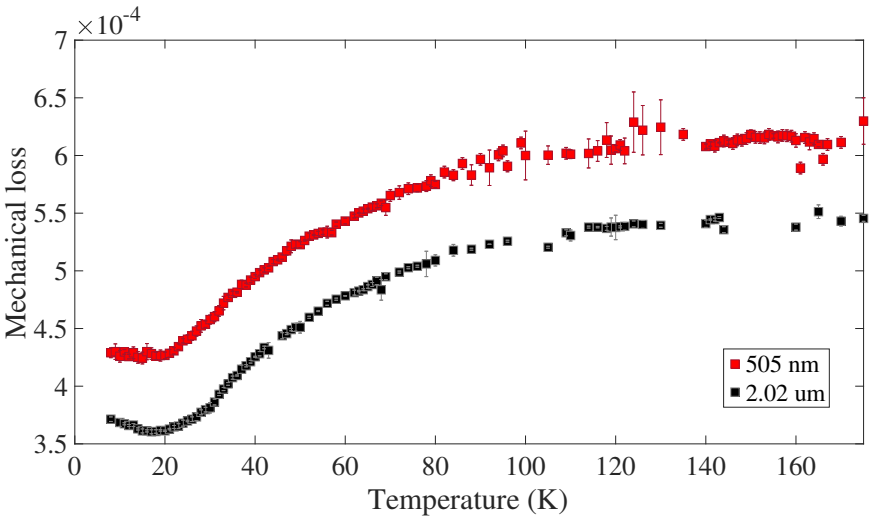

Fig. 5.12 Coating loss of 2.02 µm versus 505 nm Al_2O_3 heat treated at 800 °C and calculated from mode 4: 2.4 kHz and 2.3 kHz, respectively.

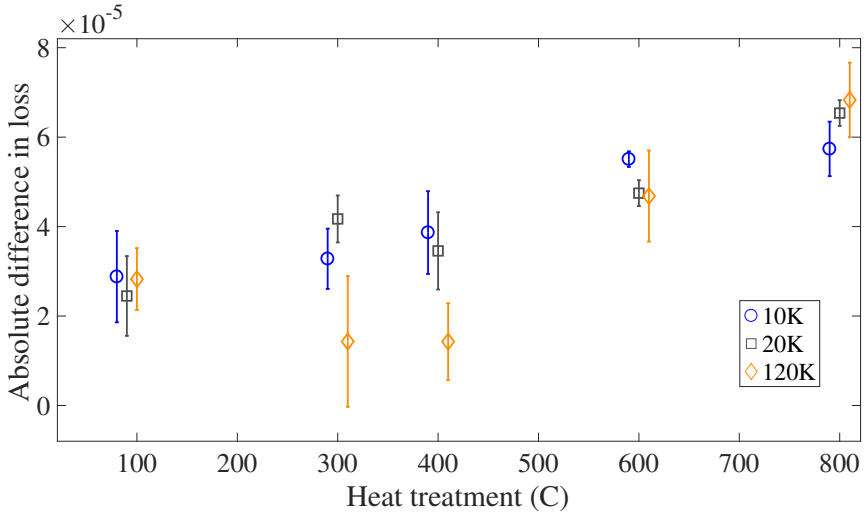

Fig. 5.13 Absolute difference in loss between the 505 nm and 2.02 µm thick alumina samples at 10 K, 20 K, and 120 K with respect to heat treatment temperature. The temperature for the as-deposited coating loss difference is 90 °C, which is roughly the temperature reached during deposition. The 10 K and 120 K values are shifted left and right, respectively, by 10 °C for the sake of clarity.

has been linked to increased mechanical loss for both silicon cantilever and silica disc substrates [264, 352]. While the surface roughness of the IBS alumina coatings are unknown, the greater surface to volume ratio of the thinner coating would lead to this being a more pronounced effect for the 505 nm alumina and could serve to raise its loss above that of the thicker coating.

A possible cause for the increase in difference with heat treatment could be a changing Young's modulus. Heat treatment of pulsed magnetron sputtered alumina has been shown to result in increased hardness just before and during the transition from amorphous Al_2O_3 to γ-Al_2O_3 [349]. If this hardening effect occurs for IBS alumina and thicker coatings were found to be more susceptible*, then the increased Young's modulus for the 2.02 µm coating would bring its current calculated loss down with increased heat treatment. This is supported by the loss of the thicker coating exhibiting a greater change with heat treatment than the 505 nm coating.

Linked to changes in coating stiffness is the stress in the coating and substrate. The room temperature coating stress displayed in table 5.3 shows inconsistent changes in magnitude with heat treatment and little evidence for correlation between the changes in coating stress and the increased difference in mechanical loss between thicknesses with continued heat treatment of the samples. However, during loss measurements

*Thinner coatings have been shown to resist crystallisation to a greater extent than thicker coatings of the same material [353, 354].

it was noticed that the alumina samples significantly changed in curvature over the course of the measurement cycle. This could possibly be a result of changing thermal stress with measurement temperature.

Figures 5.14 and 5.15 show the change in mode frequency (relative to its starting value at 10 K) with respect to measurement temperature for mode 4 of the 505 nm and 2.02 µm samples, respectively. The 505 nm samples emulate closely the frequency changes seen for an uncoated cantilever, with consistent relative frequency change with respect to temperature between all heat treatments. It should be noted that the 800 °C heat-treated sample contains a second curve visible from 78 K to ∼140 K, which is an artefact of re-cooling the cryostat to measure loss in this range. The origin of this frequency change is unknown, but there is no correlated change in the mechanical loss when this frequency change occurs. One potential reason for the shift could be elastic hysteresis in the clamping block from the contraction, expansion, and re-contraction of the steel clamping block during re-cooling.

The 2.02 µm coated samples, on the other hand, show marked changes in the mode frequency reduction. All of the samples differ significantly from the uncoated cantilever below 150 K. The 600 °C and 800 °C heat treatments display significantly altered trends compared to the bare cantilever across the full temperature range, where both samples produced a much more linear decrease in frequency with temperature. The discontinuity seen in the 400 °C heat-treated samples is a product of long rest times in between measurements and is not a noteworthy feature; in this case the cryostat was held at 78 K for an extended period of time.

Figure 5.16 shows the same frequency change versus temperature analysis but for multiple measurement cycles of the same sample: the 300 °C heat treatment of the 2.02 µm alumina. This figure highlights the altered trend in mode frequency seen for the 2.02 µm thick alumina samples, but is also included to show the consistency in frequency change between multiple measurements. The third clamp contains a discontinuity (similar to that seen in the 400 °C sample in figure 5.15) where the cryostat was held at 78 K for an extended period of time prior to resuming measurements, the trend in this temperature range is consistent with the other cycles, just shifted downwards in relative frequency. The trend in frequency change is clearly consistent between measurements, so the differences seen in figures 5.14 and 5.15 cannot be attributed to variations from temperature cycles. Figure 5.16 also includes two different uncoated cantilevers to show the consistency of frequency change in uncoated cantilevers, even of different thicknesses (56 and 60 nm).

It can be concluded from the changes in mode frequency with respect to temperature in the 2.02 µm coating that something is happening to the thick alumina during

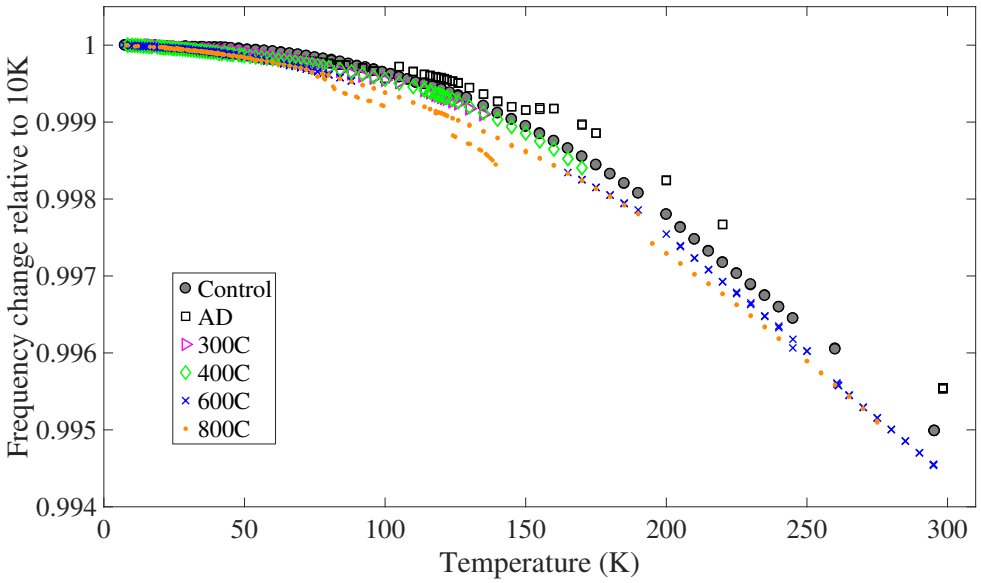

Fig. 5.14 Relative change in mode frequency with respect to temperature for mode 4 from all heat treatments of the 505 nm thick alumina. Uncoated silicon cantilever data is included for comparison.

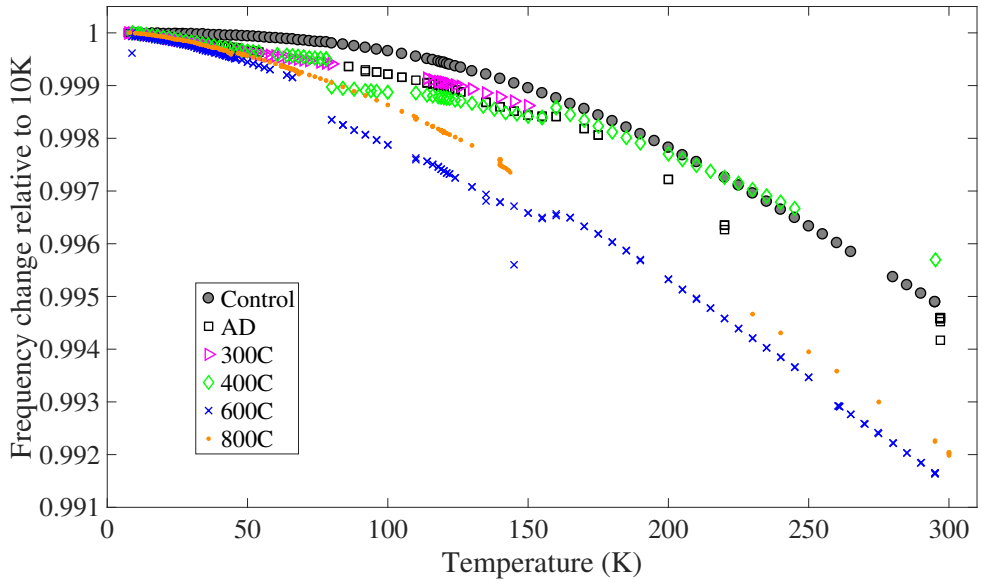

Fig. 5.15 Relative change in mode frequency with respect to temperature for mode 4 from all heat treatments of the 2.02 µm thick alumina. Uncoated silicon cantilever data is included for comparison.

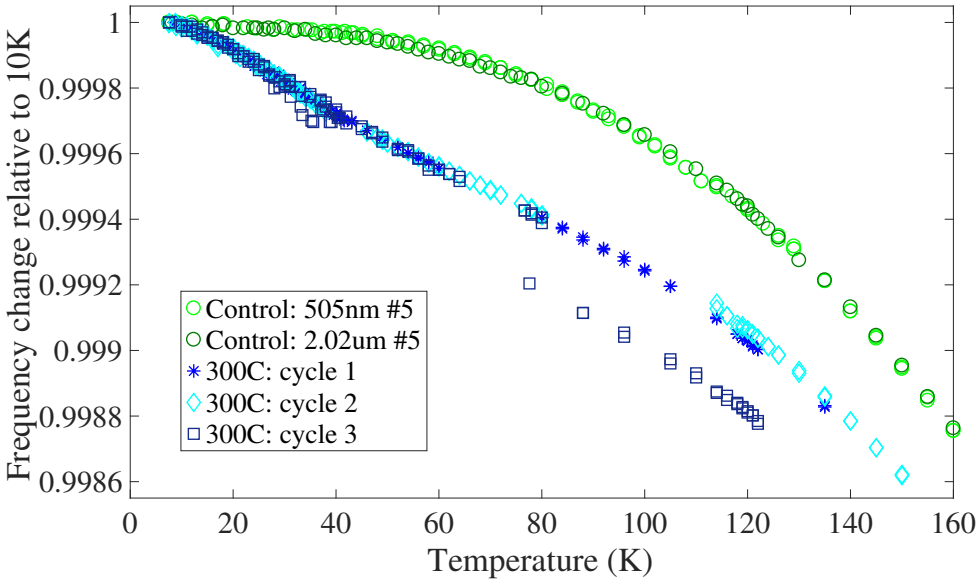

Fig. 5.16 Relative change in mode frequency with respect to temperature for three separate measurement cycles of 300 °C heat-treated 2.02 µm Al_2O_3. Uncoated silicon cantilever data is included for comparison.

heat treatment that is not occurring during heating of the thinner coating. This can also be seen in the loss, where the 2.02 µm coating appears to undergo a greater change in coating loss than the 505 nm. It is unclear why this observed frequency effect would result in lower mechanical loss, but, particularly for the 600 °C and 800 °C heat treatments, there is a significant reduction of loss that accompanies the more rapid change in frequency with respect to measurement temperature. The mode frequency is dependent on the square root of the ratio of Young's modulus to density, so if dY/dT and $d\rho/dT$ were to be thickness dependent, and also change with heat treatment at a different rate depending on coating thickness, then this would explain loss differences observed between the 505 nm and 2.02 µm Al_2O_3. Measurement of the stress with respect to temperature would be valuable in providing further evidence for this hypothesis.

5.4.3 300 °C heat treatment comparison

It was of interest to test the dependence of loss on heat treatment times given the difference between the ∼2 hour ATF heat treatment used for the 300 °C and 400 °C heat treatments (described in detail in section 5.2) and the 24 hour anneal used for the 600 °C and 800 °C samples. In order to test the validity of comparing samples heat treated under different conditions, it was decided to compare the temperature dependent loss of two samples, each heat treated at the same temperature (300 °C) but

for different times; this comparison was performed for the 505 nm coating. Another, similar comparison was performed for a 2.02 µm coating heat treated by ATF, which was measured for temperature dependent loss, heat treated for an additional 24 hours at 300 °C, and then measured again.

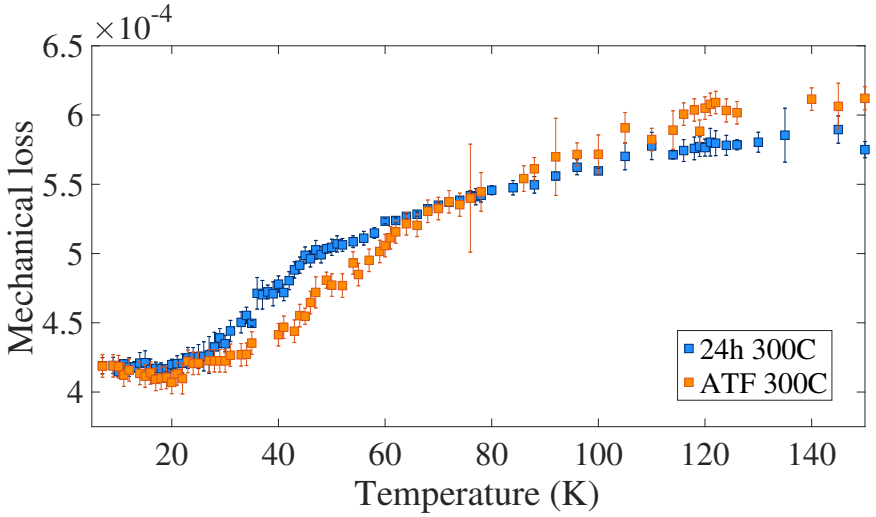

Fig. 5.17 Coating loss from mode 4 (2.29 kHz) of 505 nm Al_2O_3 heat treated at 300 °C for 24 h versus loss from mode 4 (1.19 kHz) of another 505 nm thick coating sample heat treated at 300 °C for ∼1 h by ATF.

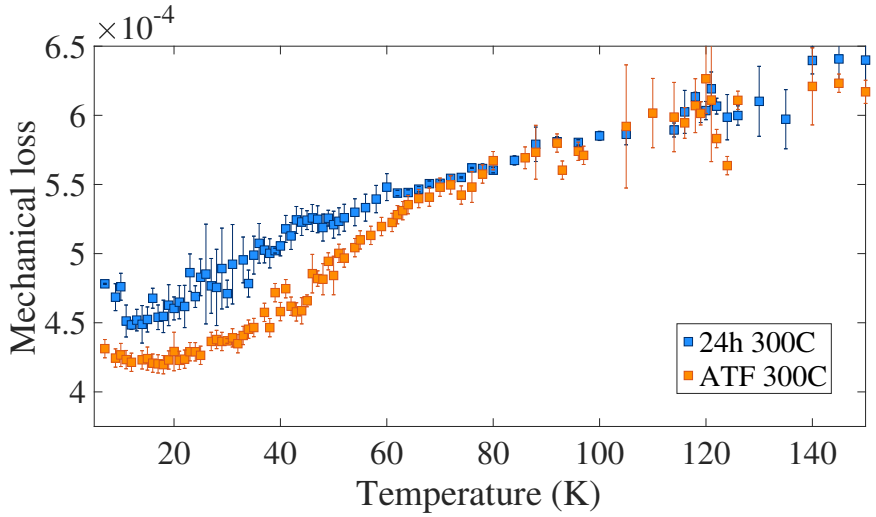

Fig. 5.18 Coating loss from mode 5 (3.80 kHz) of 505 nm Al_2O_3 heat treated at 300 °C for 24 h versus loss from mode 5 (3.22 kHz) of another 505 nm thick coating sample heat treated at 300 °C for ∼1 h by ATF.

Figures 5.17 and 5.18 show the loss comparison for 505 nm samples heat treated by ATF and separate samples annealed for 24 hours. The two heat treatments produce a large separation in loss values between 30 and 60 K, with the 24 hour heat treatment

exhibiting higher loss. The loss disparity in both figures reaches near 10% for some temperature steps, but the differences are inconsistent between measured modes and are difficult to confidently ascribe to the continued heat treatment; particularly given that the measured loss was from two different samples, neither of which had as-deposited loss data to check for a loss difference before heat treatment.

Figures 5.19 and 5.20 show coating loss for 2.02 µm alumina heat treated at 300 °C by ATF for about one hour compared to the same sample heated at 300 °C for an additional twenty four hours. The 24 hour heat treatment appears to have systematically lowered the loss of the sample (opposite to the effect seen in the 505 nm samples), and there is a noticeable separation in loss values between the two heat treatments from 40 K upwards. However, the difference in loss never exceeds 5% and the two data sets are consistent enough to be considered in agreement within normal variations between multiple clamps of the same sample.

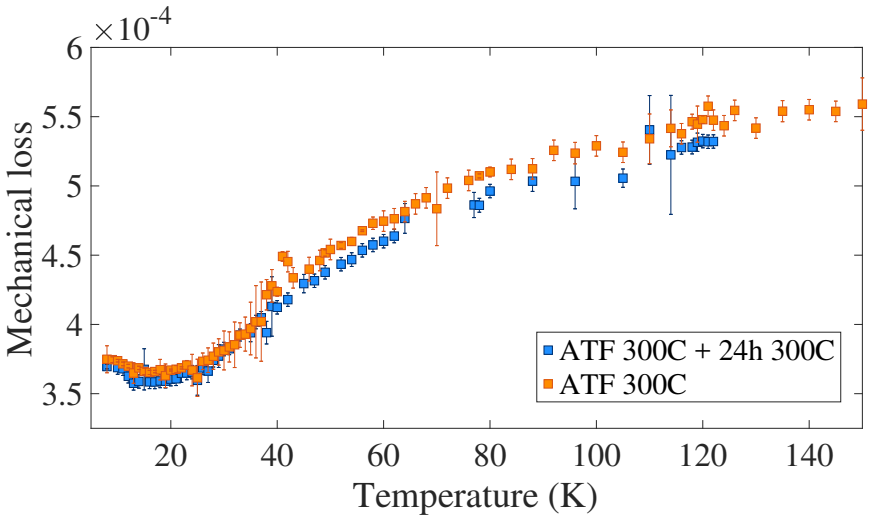

Fig. 5.19 Coating loss calculated from mode 3 (1.19 kHz) of 2.02 µm Al_2O_3 heat treated by ATF at 300 °C for ∼1 h versus the loss of the same coating sample heat treated for an additional 24 h.

Unfortunately this heat treatment comparison experiment was designed and performed prior to observing both the difference in loss between alumina coatings of differing thicknesses discussed in section 5.4.2 and the relatively little change in loss profile of alumina with heat treatment at temperatures below 800 °C. The disparity in loss between the two coating thicknesses was far greater than the differences observed when heat-treating for different times. This, combined with the relatively insignificant change in loss of alumina with heat treatment, as well as opposite findings for the 2.02 µm and 505 nm experiments, leads to the results being inconclusive. There may be a slight change in the temperature dependent loss of alumina coatings heat treated

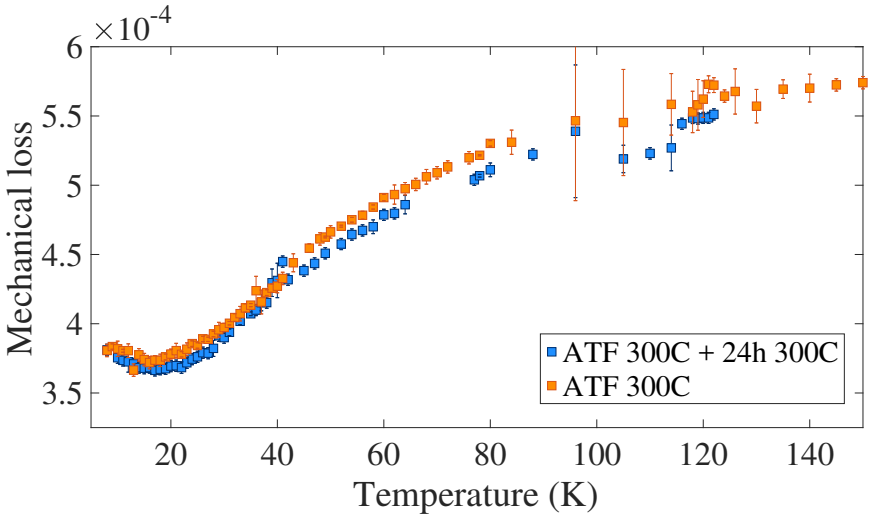

Fig. 5.20 Coating loss calculated from mode 4 (2.33 kHz) of 2.02 µm Al_2O_3 heat treated by ATF at 300 °C for ∼1 h versus the loss of the same coating sample heat treated for an additional 24 h.

for differing amounts of time, but it is not a limiting factor in comparing different annealing temperatures. A similar experiment but with more comparison samples of a coating with pronounced changes in loss, eg silica or tantalum pentoxide, would be valuable in providing a more rigorous look at the effects of heat treatment ramp up/down and plateau times on temperature dependent mechanical loss.

5.4.4 Comparison to SiO_2

5.4.4.1 Mechanical loss comparisons

The primary motivation for characterising the temperature dependent mechanical loss of IBS Al_2O_3 was to determine its potential as a replacement low refractive index layer for the multilayer mirror coatings in future cryogenic gravitational wave detectors. With a higher refractive index than silica, the mechanical loss benefits of alumina need to outweigh the increased thermal noise from additional layers required to match reflectivity. Figures 5.21 and 5.21 show the loss of both alumina coating thicknesses compared to the IBS and RLVIP SiO_2 coatings presented in Chapter 4, as calculated from modes 3 and 4, respectively. Both the IBS silica and alumina loss in the figures are from the 600 °C heat treated samples in order to match the current aLIGO coating stack post deposition heat treatment as closely as possible; the RLVIP silica loss is from the coating measured as deposited. It can be seen in both figures that the alumina loss is lower than the IBS silica at 10 K and significantly lower at 20 K. The RLVIP silica is comparable to the alumina at temperatures below 40 K, with a maximum

difference of about 10% at 20 K. The loss of Al_2O_3 is comparatively very high at 120 K, with both thicknesses displaying about five times the loss of the RLVIP silica coating and well above five times the loss of the IBS silica.

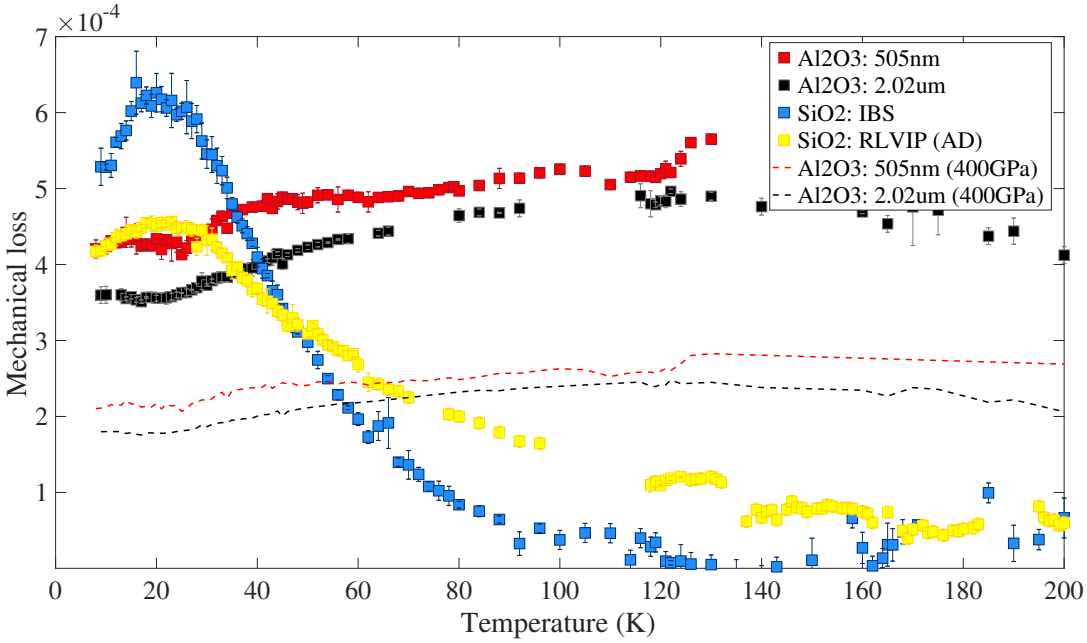

Fig. 5.21 Low temperature loss of IBS Al_2O_3 and SiO_2, both heat treated at 600 °C. The as-deposited RLVIP SiO_2 loss is included for comparison as well. All loss calculated from mode 3. Dotted lines represent the coating loss of both thicknesses of IBS alumina if the Young's modulus of the coating matches that of bulk sapphire (400 GPa).

Figures 5.21 and 5.22 also show (dotted lines) the loss of the 505 nm and 2.02 µm thick alumina coatings if the Young's modulus of the films were to match that of bulk sapphire. As discussed in section 5.2.1, this is not a realistic estimation, but the loss from such an assumption is shown to highlight both the necessity for nanoindentation of alumina films and the hazards of assuming bulk material stiffness for thin film coatings. The higher Young's modulus reduces the loss at all temperatures by 50%, artificially bolstering Al_2O_3 in loss comparisons with other low index coatings. The Young's modulus of the coating layers and the mirror substrate material factors into the thermal noise associated with a coating stack, so the larger Young's modulus of 400 GPa–much larger than silica at 72 GPa– would also have an effect on the theoretical change in detector sensitivity associated with any improvements in coating thermal noise. In other words, the bulk Young's modulus assumption results in significant underestimation of coating thermal noise. The potential of alumina as a low index replacement for improved coating thermal noise will be investigated in Chapter 7,

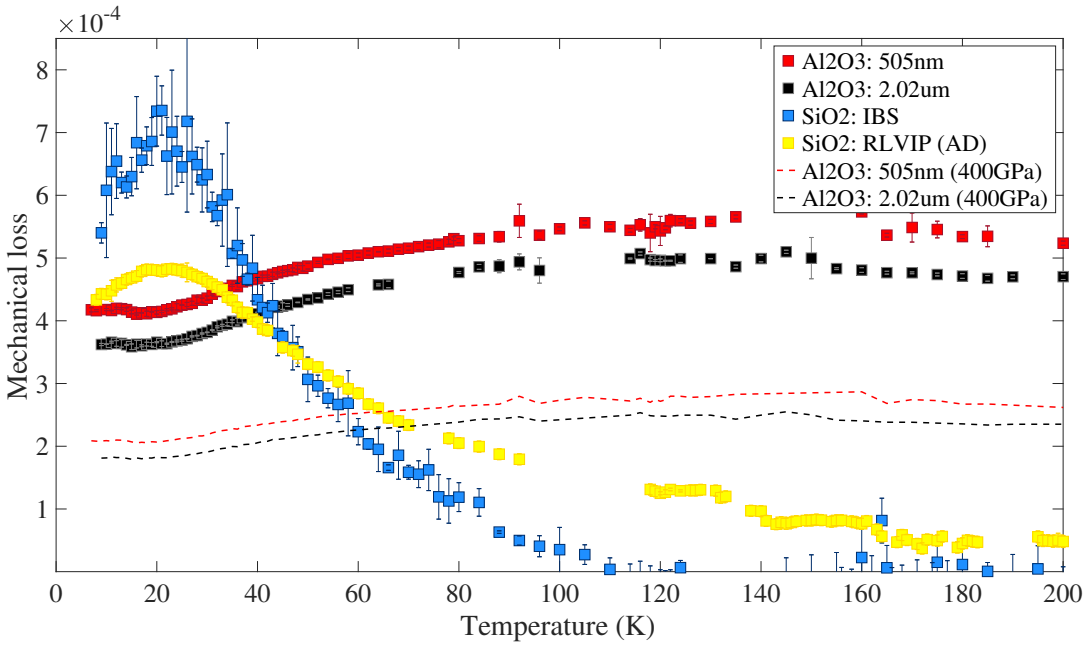

Fig. 5.22 Low temperature loss of IBS Al_2O_3 and SiO_2, both heat treated at 600 °C. The as-deposited RLVIP SiO_2 loss is included for comparison as well. All loss calculated from mode 4. Dotted lines represent the coating loss of both thicknesses of IBS alumina if the Young's modulus of the coating matches that of bulk sapphire (400 GPa).

but it was worth noting here the importance of an accurate elastic modulus for both mechanical loss calculations and thermal noise estimates. An investigation into the Young's modulus of thin-film IBS Al_2O_3 is of the utmost importance.

5.4.4.2 Stress comparison

The clearest difference between stress in heat treated SiO_2 and Al_2O_3 coatings is the transition from compressive to tensile stress seen in the alumina coatings. The comparative transition of coating stress in the two materials with continued heat treatment is shown in figure 5.23. The magnitude of stress in both coatings decreases linearly from an as-deposited state until heat treatment at 450 °C, after which the silica appears to plateau at ~ -230 GPa for the 600 °C and 800 °C anneals and the alumina continues in a roughly linear manner through a point of zero stress and increasing in tensile stress. There is a difference between the magnitude of tensile stress in the 505 nm and 2.02 µm alumina coatings, but the trend is consistent between the two thicknesses and very different from that seen in the silica coatings.

Notable as well is the lack of correlation between alumina loss and coating stress, compared to the apparent connection between temperature dependent loss and coating

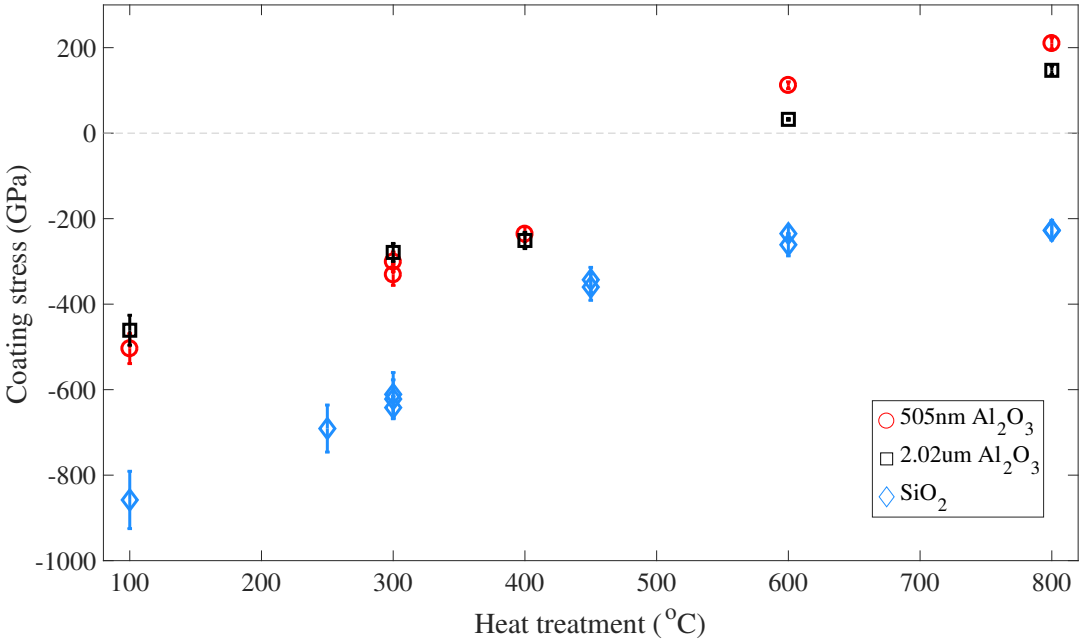

Fig. 5.23 Coating stress in silica and alumina coatings. Both thicknesses of the IBS Al_2O_3 are shown, and the silica stress includes both CSIRO and ATF IBS SiO_2 as well as the RLVIP SiO_2.

stress seen in IBS silica and discussed in section 4.4.2. Combined with the lack of a defined activation energy for TLS within the alumina coating, its lack of correlation between stress and loss could be further evidence of a difference in internal relaxation mechanisms between the two coating materials.

5.5 Conclusions

Amorphous IBS Al_2O_3 was considered as a possible alternative to SiO_2 as the low index coating layer in highly reflective multilayer mirror coatings given the increase in mechanical loss of silica at the operating temperatures of future cryogenic detectors. Alumina's mechanical loss was found to be thickness dependent, with 2.02 µm thick coatings displaying increasingly higher loss with continued heat treatment compared to that of the 505 nm coatings. Both thicknesses of IBS alumina exhibited a significant decrease in loss after heat treatment at 300 °C, but relatively little change in loss was observed for further heat treatments up to 800 °C, with no change at all for temperatures below ∼50 K. An experiment to test differences in loss with respect to heat treatment time at 300 °C was inconclusive, likely in part due to this lack of significant change in loss with increased temperatures.

Unlike the mechanical loss, the stress within the alumina coatings changed significantly with subsequent heat treatments, with both coating thicknesses containing more than 450 GPa of compressive stress in their as deposited state and transitioning to tensile stress after heat treatment at 600 °C. There appeared to be no correlation between mechanical loss and stress for the alumina coatings, and, especially compared to IBS silica, they exhibited a consistent change in stress with each increasing heat treatment.

Both coating thicknesses of alumina were found to exhibit lower mechanical loss than IBS silica below 40 K but significantly higher loss at temperatures above 100 K. However, comparisons between the mechanical loss of silica and alumina depend strongly on knowledge of the Young's modulus for IBS Al_2O_3. The assumption of a value at 200 GPa adds significant systematic error to all the reported loss values, particularly given the possible evidence of increased stiffness with heat treatment. A systematic study of the change in Young's modulus with heat treatment is essential for evaluating alumina as a possible low index coating material.

Chapter 6

Temperature dependent mechanical loss of high index coating materials

6.1 Introduction

Reflectance in multilayer coatings is determined by both the number of layer pairs and the difference in refractive indices of the materials comprising said pair. A large difference in refractive indices of the layer materials allows for higher reflectivity with less coating pairs, i.e. a thinner coating, which is beneficial because thermal noise is directly proportional to coating thickness. The current, advanced gravitational wave detector coating is comprised of amorphous silica for the low index layers ($n \approx 1.45$) and 25% titania doped tantalum pentoxide ($n \approx 2.03$) for the high index layers. The coating used in the first generation of detectors contained pure Ta_2O_5, but it was shown that doping with TiO_2 reduced the room temperature mechanical loss by $\sim 40\%$ [165]. Even with the $\sim 40\%$ reduction, tantala dominates the mechanical loss of the multilayer coating and is therefore the primary source of thermal noise within the coating at room temperature*. 25% Ti:Ta_2O_5 displays a loss peak at low temperatures comparable in magnitude to that seen in amorphous silica [254]. It is therefore of primary importance to find a material suitable for replacing the high index layer for both upgrades to the current, room temperature detectors and new coatings for future, cryogenically cooled detectors.

Extensive studies have been carried out to further improve on 25% Ti:Ta_2O_5 as the high index layer, but it has been a decade since the last significant reduction in coating thermal noise was achieved through titania doping [165]. Continued measurement

*The loss of silica at room temperature is about 5×10^{-5} [158], compared to the 2.3×10^{-4} for titania doped tantala [355].

of the loss characteristics of new materials is important, but investigations into the structural origins of mechanical loss could provide more valuable results with regards to discovering a new, low loss coating and is crucial given the detector upgrade and construction timelines. This chapter studies the loss characteristics of a number of new coating materials and deposition methods in order to test their validity* as replacement high index layers. It also presents loss comparisons of new coating techniques with a growing body of work on tantalum pentoxide in the hope of eventually finding a correlation between deposition parameters and thermal history with loss and coating structure.

6.2 Ion-beam sputtered materials

Ion-beam sputtering is the current standard for the mirror coatings in gravitational wave detectors. It is a high energy deposition method that has hitherto not been surpassed as a technique for producing homogenous coatings with sufficiently low scatter, and the only deposition chamber currently capable of sputtering coatings for detector test masses utilises IBS [356]. It is therefore of significant interest to look first to coating materials deposited by IBS as replacements for the current high index 25% Ti:Ta_2O_5 layers. This section will present results from four different high index materials produced through ion-beam sputtering.

6.2.1 High deposition temperature tantalum pentoxide

As discussed in section 4.4.1.1, mechanical loss in thin films is thought to originate from thermally induced transitions between asymmetric double well potentials, with the distribution of two-level systems (TLS) comprised of barrier heights and barrier asymmetries serving as predictors of loss in an amorphous solid. It is thought that coatings formed with increased surface mobility during deposition could reach a lower potential energy landscape once cooled, reducing the number of TLS present in the cooled glass [243, 244]. Post-deposition heat treatment works to accomplish a similar goal, but 'trapped' particles within a coating structure are limited in changing their local energy landscape by neighbouring particles; those at the surface during deposition have a significantly increased volume of configuration space to explore for the lowest energy states. Increasing the substrate temperature during deposition allows

*Absorption and other optical properties are also crucial in determining the practicality of a coating material, but mechanical loss is a limiting material property with regards to implementation viability and is the primary focus of this thesis.

for greater surface mobility and more effective formation of coatings in their lowest energy states, the ideal state being an ultra-stable glass that is at an energy landscape effectively devoid of TLS. The use of deposition temperatures approaching 400 °C has been shown to significantly reduce the loss of e-beam evaporated amorphous silicon coatings, thought to be a result of this increased surface mobility and a reduction in two-level systems [245]. It is therefore of interest to explore elevated substrate temperature deposition for potential thermal noise improvement through reduced coating loss*, with current experiments focusing on Ta_2O_5 due to the wealth of previous research on the coating material under standard deposition conditions.

Ion-beam sputtered coatings, such as those presented in Chapters 4 and 5, reach substrate temperatures of about 90 °C during sputtering purely as a result of the deposition process. Silica disc substrates have been heated beyond this natural plateau during deposition to 150 °C, 250 °C, 400 °C, and 480 °C to test the effect on room temperature loss, which was found to decrease for all elevated substrate temperatures compared to unheated deposition but, unfortunately, with little difference among the elevated substrate temperatures [324]. Also of note was the continued decrease in loss with post-deposition annealing, even at temperatures below the heating during deposition. This implies that elevated deposition temperatures and post-deposition annealing are not analogous, with each producing different structural changes. While not producing dramatic reduction in mechanical loss, the elevated deposition temperatures are clearly producing significant structural changes, so observing the loss behaviour at cryogenic temperatures is of value for a fuller picture of this new variable space in the coating deposition process.

A number of elevated deposition temperature IBS tantalum pentoxide samples were produced by The University of the West of Scotland (UWS), from which an etched silicon cantilever with a 577 ± 20 nm thick coating both deposited at and then heat treated at 300 °C was measured following procedures described in section 3.3.2. Figure 6.1 shows the coating loss† below 200 K calculated from all measured modes of the ∼68 µm thick coated sample. The change in loss with respect to temperature is consistent between measured modes, with a peak in loss at about 40 K. One notable feature is the consistency in magnitude for all modes below 40 K compared to the spread in magnitude above the peak temperature, where the loss appears to be more strongly frequency dependent.

*There is also evidence that high temperature deposition of tantalum pentoxide results in an increased refractive index, which could result in thermal noise reduction even if the loss remains unchanged by reducing the number of coating layers required for high reflectivity [357]

†The Young's modulus was assumed to be the same as IBS Ta_2O_5, 140 GPa

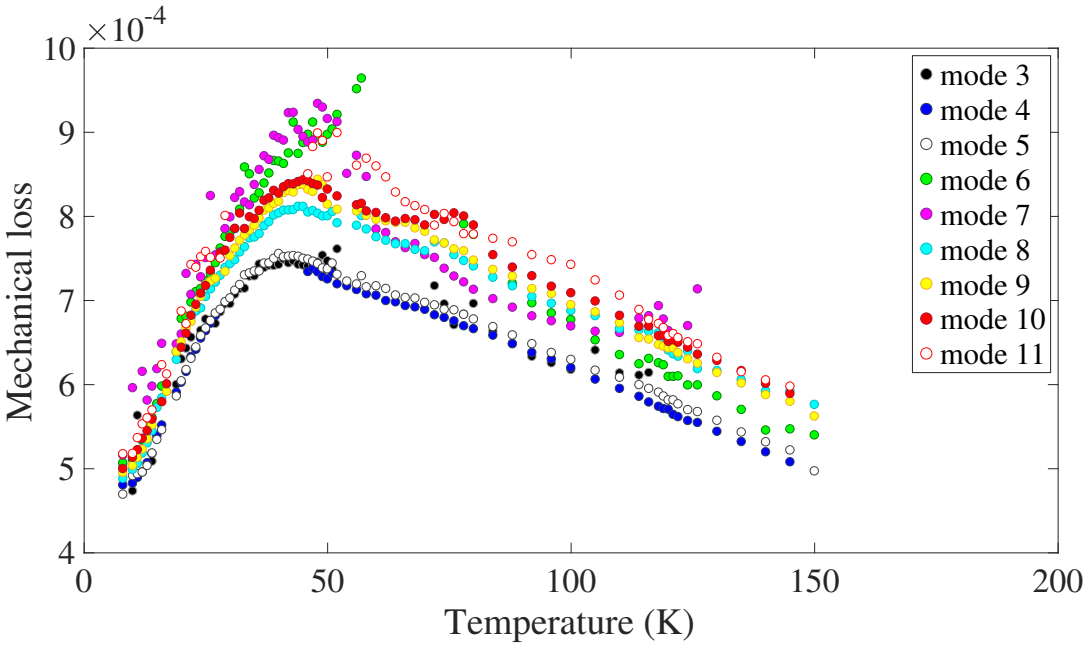

Fig. 6.1 Coating loss from modes 3 through 11 (1.28 – 23.5 kHz) of 300 °C heat treated IBS Ta_2O_5 deposited at 300 °C.

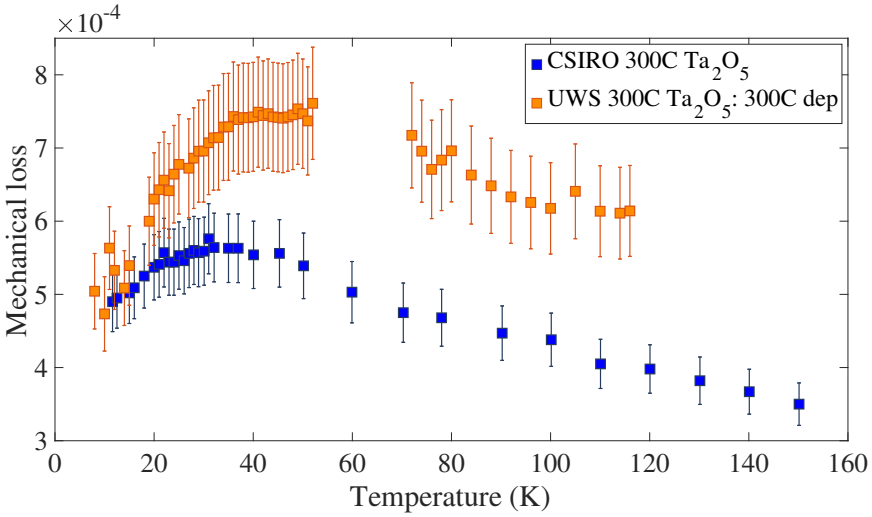

Fig. 6.2 300 °C heat treated IBS Ta_2O_5 loss from coatings deposited without substrate heating (CSIRO, data from [256]) and deposited at 300 °C (UWS). The loss is calculated from mode 3, which is 1.28 kHz for the UWS tantala and 1.00 kHz for the CSIRO.

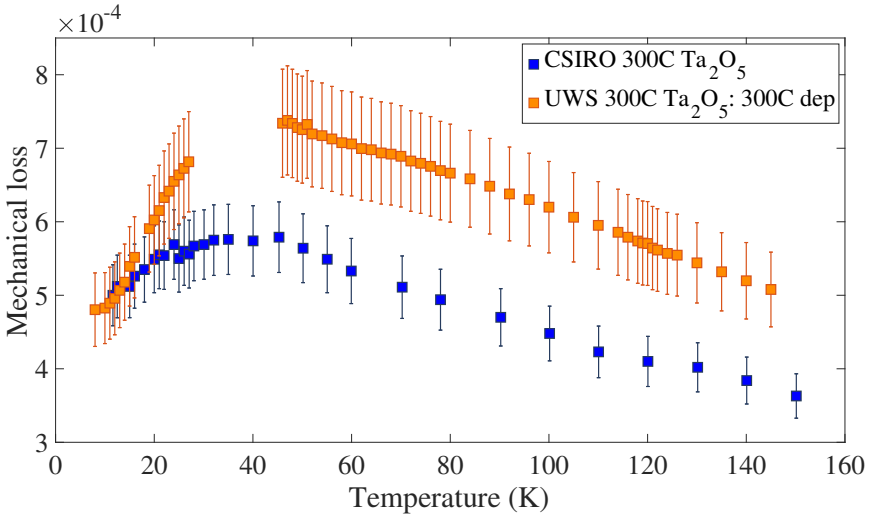

Fig. 6.3 300 °C heat treated IBS Ta_2O_5 loss from coatings deposited without substrate heating (CSIRO, data from [256]) and deposited at 300 °C (UWS). The loss is calculated from mode 4, which is 2.55 kHz for the UWS tantala and 1.90 kHz for the CSIRO.

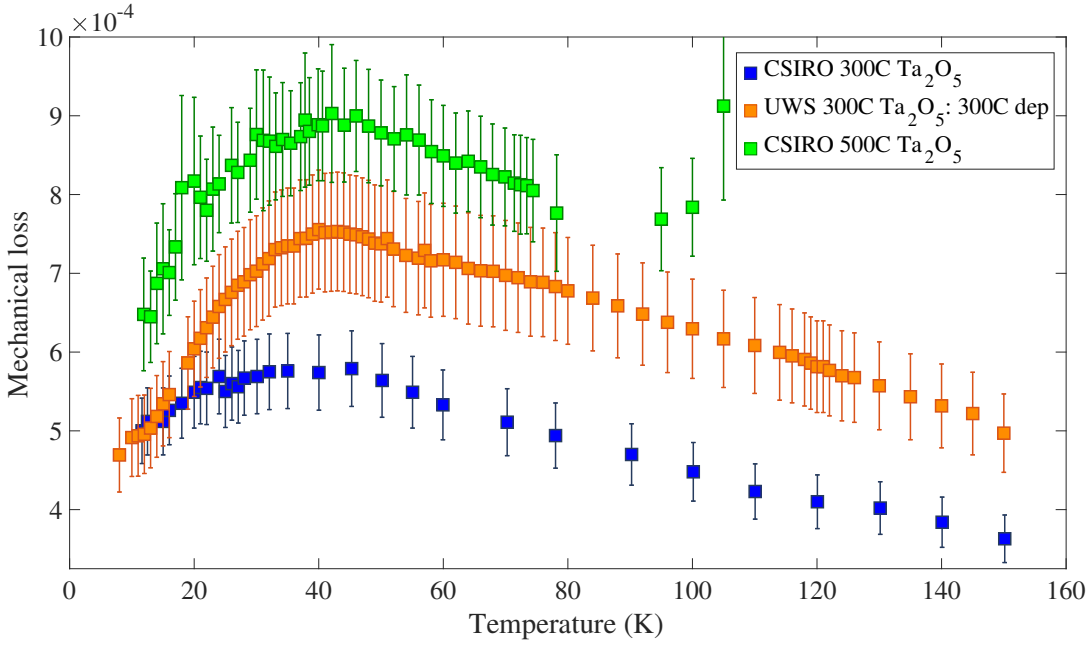

Fig. 6.4 300 °C heat treated IBS Ta_2O_5 loss from coatings deposited without substrate heating (CSIRO, data from [256]) and deposited at 300 °C (UWS). The loss is calculated from mode 5, which is 4.26 kHz for the UWS tantala and 3.2 kHz for the CSIRO. The 500 °C heat treatment for CSIRO Ta_2O_5 is included for comparison as well (data also from [256]).

Figures 6.2 (mode 3) and 6.3 (mode 4) show the loss of the elevated deposition Ta_2O_5 compared to standard IBS Ta_2O_5 (sputtered by CSIRO [256]), where both coatings have been heat treated at 300 °C. A 10% systematic uncertainty stemming from unknown Young's modulus has been added to the loss from tantala deposited at 300 °C. This was done in response to the significant structural changes apparent from the room temperature loss results for high temperature deposition tantala and comprises the majority of the uncertainty in results; the statistical measurement uncertainty was extremely low across measured temperatures for all modes ($\sim$2%). Even with the wide range of expected Young's moduli (126 to 154 GPa), the 300 °C deposited tantala has higher loss at all temperatures above 30 K; the loss below 20 K is nearly identical.

A significant difference, other than the magnitude of loss, is the shifted peak loss temperature for the 300 °C deposited Ta_2O_5. Figure 6.4 (mode 5) highlights this difference as, unlike modes 3 and 4, it has data at every temperature step for the elevated temperature tantala. The two measured cantilevers differed in thickness, resulting in a higher measured frequency at each mode for the elevated temperature tantala. This could result in a slight lateral shift in peak temperature, but would be in the order of tenths of a Kelvin rather than the observed 5 to 10 K shift. Figure 6.4 also includes the loss of the CSIRO tantala after a 500 °C heat treatment, which has a peak temperature closer to that of the 300 °C deposition temperature Ta_2O_5. This could provide evidence of the elevated deposition temperature having a structural effect greater than post-deposition heat treatment at the same temperature, similar to the decrease in crystallisation temperature with deposition temperatures nearing 500 °C.

Continued measurement of the temperature dependent loss of IBS tantala deposited at varying deposition temperatures would serve to provide a wider lens through which to view the structural changes in coatings with applied thermal energy. Current tantala results do not yet match the TLS-reduced ultrastable glass formation seen in the theoretical models. Further research may point towards incremental loss improvements through an optimised combination of heated substrate deposition and post-deposition heat treatment, and significant structural changes with little effect on loss at room temperature may become apparent with cryogenic mechanical loss measurements. Measurement of the coating stress would also be of interest, since the higher deposition temperature should lead to a greater amount of thermal coating stress in the coating.

6.2.2 68% Ti:Ta_2O_5

Doping pure Ta_2O_5 with titanium dioxide during coating deposition has been shown to significantly reduce the mechanical loss of the coating [165]. TiO_2 has a high

elastic modulus, atomic compatibility with tantalum pentoxide, and stability in an amorphous state, and an optimum dopant concentration of 25% was found for use in the aLIGO and Advanced Virgo highly reflective multilayer mirror coatings to reduce the coating thermal noise contribution while maintaining the optical properties required for reaching design sensitivity [16]. It is of interest, however, to investigate the changes in optical and mechanical properties that occur with differing doping percentages in order to gain a better understanding of the origins of coating loss and its relation to structural and chemical differences. The temperature dependent mechanical loss of tantala doped with titania percentages of 14% and 52% has been characterised both as-deposited and after heat treatment at 400 °C and 600 °C, respectively [229, 280]. Measurement of samples coated with 68% Ti:Ta_2O_5* should provide a systematic look at the effect of titania doping percentages on the loss of tantalum pentoxide.

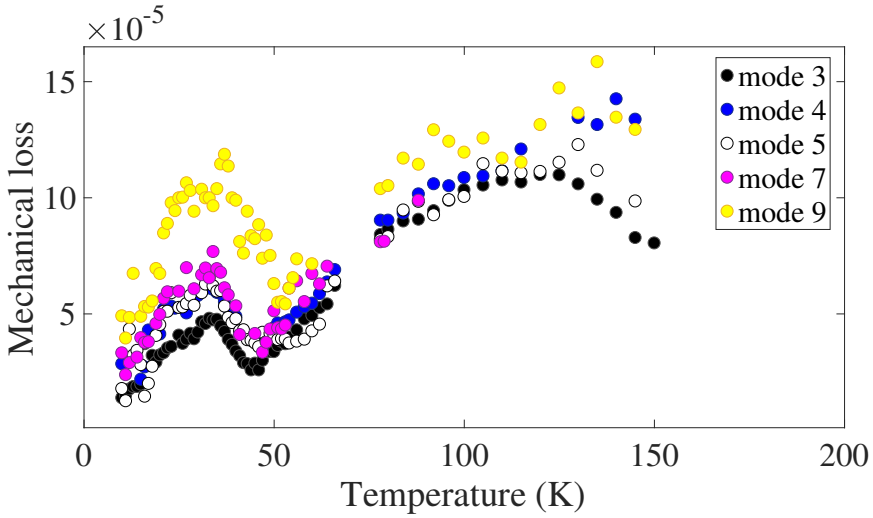

Fig. 6.5 IBS 68% Ti:Ta_2O_5 coating loss calculated from all measured modes: 500 °C heat treatment.

It should be noted that the Young's modulus of this coating is unknown, but previous nano-indentation studies of titania-doped tantala found greater variance in Young's modulus between heat treatment temperatures of identical coatings than between 0%, 14%, and 52% titania doping percentages [280]. A value of 140 GPa was, therefore, used in all loss calculations, as well as for comparison coating curves from previous measurements. The Young's modulus of pure, thin-film TiO_2 is 151 GPa [358], so this assumption would, at most, impart about an 8% systematic uncertainty in loss

*The nominal doping percentages were 25%, 55%, and 75%. Electron energy loss spectroscopy (EELS) measurements later revealed the actual stoichiometry to be 14%, 52%, and 68% titania, which are the percentages quoted throughout this thesis. Results for titania-doped tantala presented in [229, 280] refer to the nominal percentages.

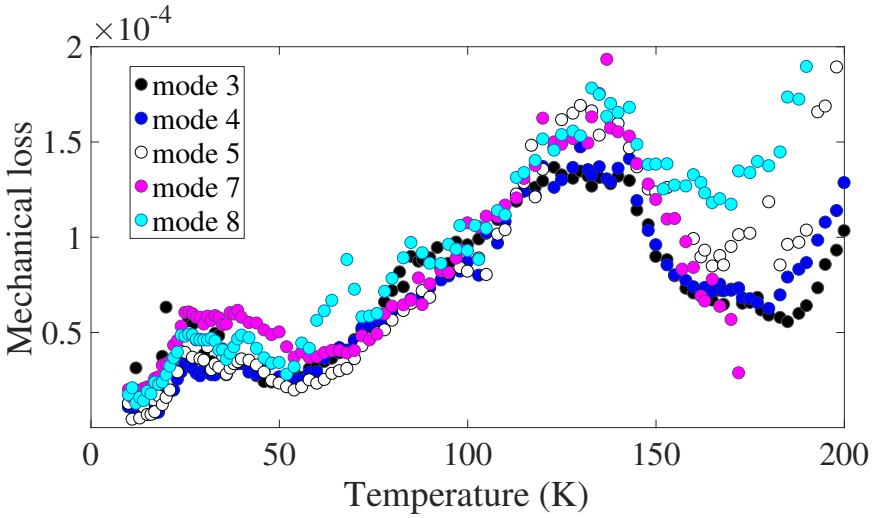

Fig. 6.6 IBS 68% Ti:Ta_2O_5 coating loss calculated from all measured modes: 600 °C heat treatment sample 2.

given the worst case of the coating having the stiffness of titania rather than tantalum pentoxide.

The loss of 500 ± 10 nm of 68% Ti:Ta_2O_5 has been measured for the coating as-deposited, as well as after heat treatment at 600 °C where it was found to exhibit anomalous loss characteristics, with loss nearly an order of magnitude lower at the low temperature peak after heat treatment (this can be seen in figure 6.8). Two additional samples were measured to confirm the drastic loss reduction; one (70.1 µm thick) was heat-treated at 600 °C to compare directly with the extraordinary sample (70.2 µm thick), and another (66.5 µm thick) was annealed at 500 °C in an attempt to track the reduction in loss. Figures 6.5 and 6.6 show the coating loss from these samples after heat treatment at 500 °C and 600 °C, respectively. Both figures contain loss calculated from all measured bending modes of the coated sample. A peak in mechanical loss at ∼35 K can be seen for both heat treatments, with the loss increasing afterwards to create another, much broader peak in the loss between 100-150 K.

Figure 6.7 shows the loss from these samples (labelled sample 2 for the 600 °C) compared to the previous measurements of the coating loss as-deposited and after heat treatment at 600 °C. It can be seen clearly that the seemingly anomalous reduction in loss with heat treatment is, in fact, characteristic of 68% Ti:Ta_2O_5. The losses of the 500 °C and both 600 °C heat-treated samples are nearly indistinguishable and significantly lower than the loss of the coating without heat treatment. The reduction in loss with heat treatment is particularly apparent when compared with other titania doping percentages.

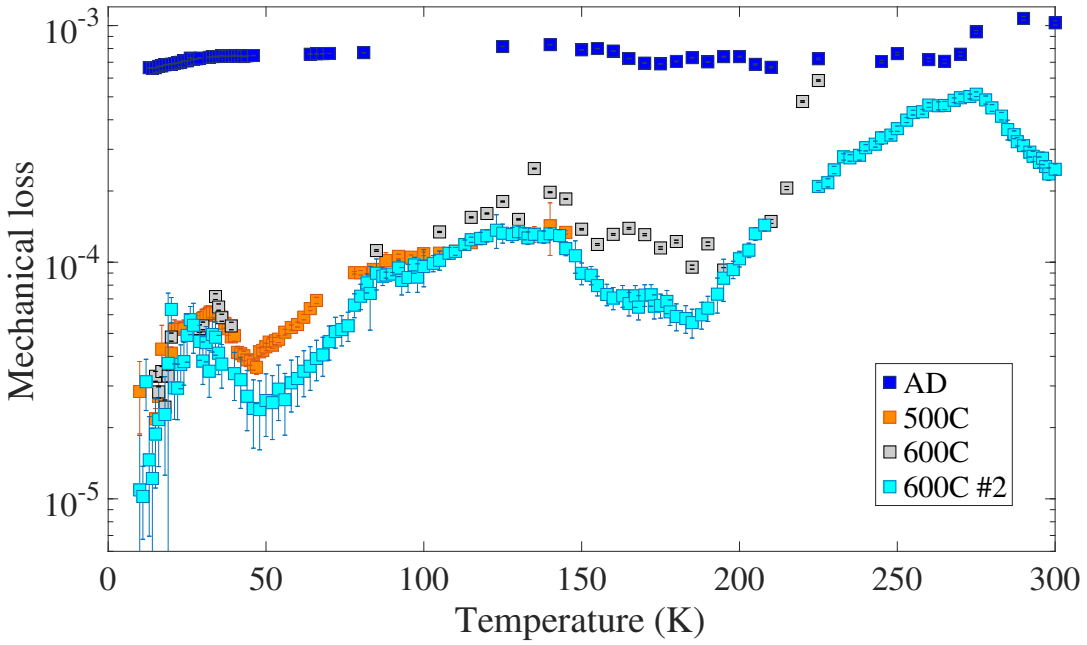

Fig. 6.7 IBS 68% Ti:Ta_2O_5 coating loss for all heat treatments as calculated from bending mode 4. The loss as-deposited and 600 °C sample 1 is part of ongoing research by P. Murray [359].

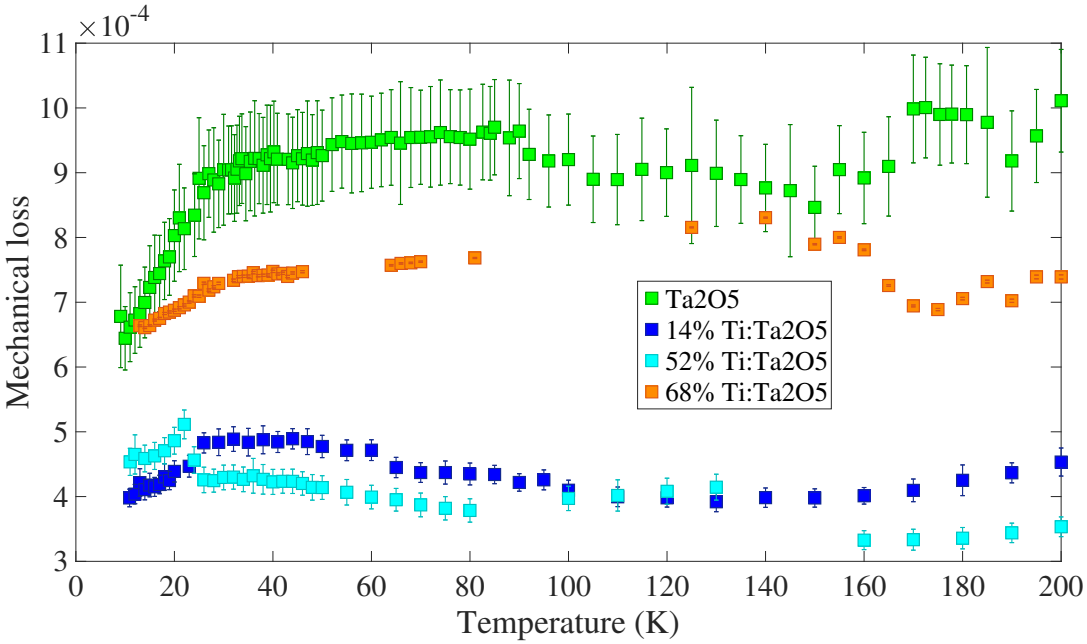

Fig. 6.8 Mechanical loss as-deposited for 0%, 14%, 52%, and 68% Ti:Ta_2O_5. All loss is calculated from bending mode 4 of the coated samples. Data for the pure Ta_2O_5 is from [256]; the data for 14% and 52% Ti:Ta_2O_5 is from [229, 280]. All losses are calculated from measurements of cantilever bending mode $n = 4$.

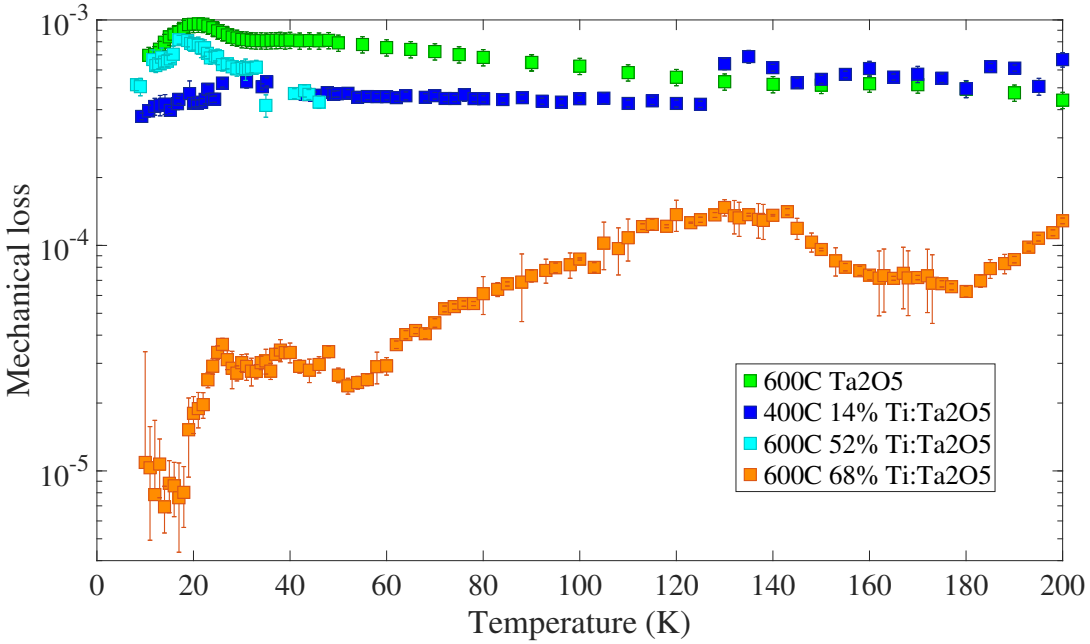

Fig. 6.9 Loss after heat treatment at 600 °C for 0%, 14%(400 °C), 52%, and 68% Ti:Ta_2O_5. Data for the 600 °C pure Ta_2O_5 is from [256]. The 400 °C 14% Ti:Ta_2O_5 and 600 °C 52% Ti:Ta_2O_5 data is from [229]. All losses are calculated from measurements of cantilever bending mode $n = 4$.

Figure 6.8 shows the as-deposited coating loss of 68% Ti:Ta_2O_5 compared to 14% and 52% as well as pure tantalum pentoxide. The lower doping percentages significantly reduce the tantala loss across all temperatures, but the 68% titania doping returns the loss to a level much closer to the pure tantala. However, the opposite is true with heat treatment of the coating. Figure 6.9 shows these same coatings heat treated at 600 °C*, where the 68% titania doped tantala exhibits loss an order of magnitude lower than the other doping percentages and pure tantala.

The reason behind the large drop in loss with heat-treated 68% Ti:Ta_2O_5 is unknown, but it is worth noting that EELS measurements showed evidence that the 68% Ti:Ta_2O_5 coating is not homogeneous; it appears to have distinct layers of varying titania doping percentages[360, 361]. The stated value of 68% titania is an averaging of the layers and further investigation is required in order to conclude that the higher titania doping percentage is worth replacing the 25% doping percentage used in the current generation of mirror coatings. It should also be noted that, while displaying low mechanical loss, this coating has visual evidence of crystallisation. Initial optical measurements show evidence of a more singular crystalline structure rather than a polycrystalline formation [362]. Investigations of the loss after heat treatments

*No data is available for the 600 °C14% Ti:Ta_2O_5, so the 400 °C heat treatment is shown instead.

below 500 °C would be valuable in order to see the progression between the high loss as-deposited and the large reduction with 500 °C and 600 °C heat treatments, and further measurements regarding the para-crystallinity of the structure are of interest for marrying the loss trends with coating structure.

6.2.3 IBS titanium dioxide

Titania has long been known as a high refractive index material (2.5 [363, 364]) with low mechanical loss over a wide temperature range [365]. It displays loss lower than that of pure Ta_2O_5, which, combined with compatible material properties, was the motivation for choosing TiO_2 as the dopant material to reduce the loss of tantalum pentoxide [165]. Titania could not fully replace the Ta_2O_5 because ion-beam sputtered TiO_2 displays polycrystalline structure formation after heat treatment at temperatures above 200 °C [353, 366]. This results in a significant increase in optical scatter and mechanical loss and has, to this point, eliminated titania as a high index coating layer in the multilayer detector coatings. There is evidence that doping pure titania with a more stable glass former, such as SiO_2, retards these crystallisation effects seen at low heat treatment temperatures, but with a decrease in refractive index [363, 367]. One possible solution to retain the low loss of titania films in a multilayer coating without reducing the refractive index is to use much thinner (∼20 nm) 'nanolayers', which lowers the crystallisation temperature of TiO_2 compared to thicker coatings [368]. This alternate coating structure replaces the high index layer with a collection of nanolayers of titania and silica. The refractive index of this composite is still high enough to be considered a high index coating, and the layered sub-structure inhibits crystallisation within the TiO_2. It is therefore of interest to measure the temperature dependent mechanical loss of IBS TiO_2 after heat treatment temperatures near, and above, 200 °C in order to investigate the effect of shrinking coating thickness to the nanometre scale on polycrystalline structure formation.

Figure 6.10 shows the coating loss of 500 nm of 150 °C heat-treated IBS TiO_2 calculated from bending mode decay of a 70.1 µm thick silicon cantilever. Loss is calculated from all measured bending modes of the coated sample and can be seen to be broadly frequency dependent, with about a 20% difference between the loss of the 3rd bending mode and the 11th. Over the short measurement temperature range the loss exhibits relatively little change, with a slight trough at about 20 K being the only defining feature. Figure 6.11 shows the loss after heat treatment at 300 °C, which produces a significant reduction in loss and a markedly different trend with respect to measurement temperature. The loss peak at about 120 K appears in all measured

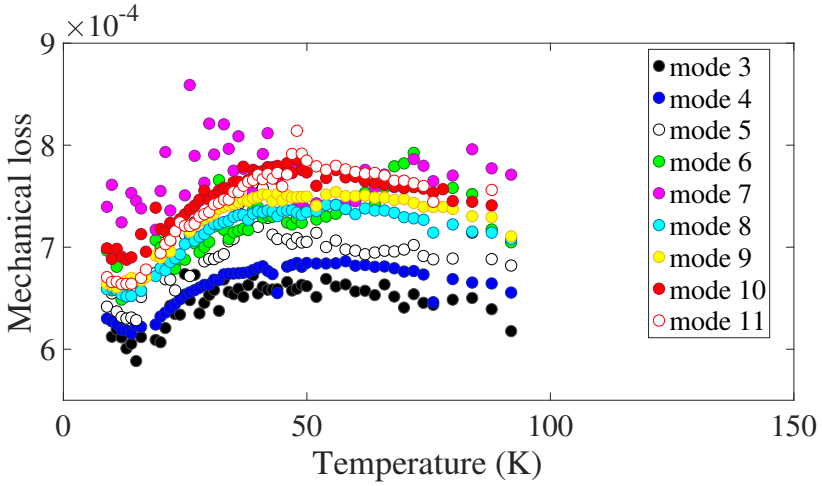

Fig. 6.10 Coating loss as calculated from all measured modes of the 150 °C heat-treated TiO_2 sample.

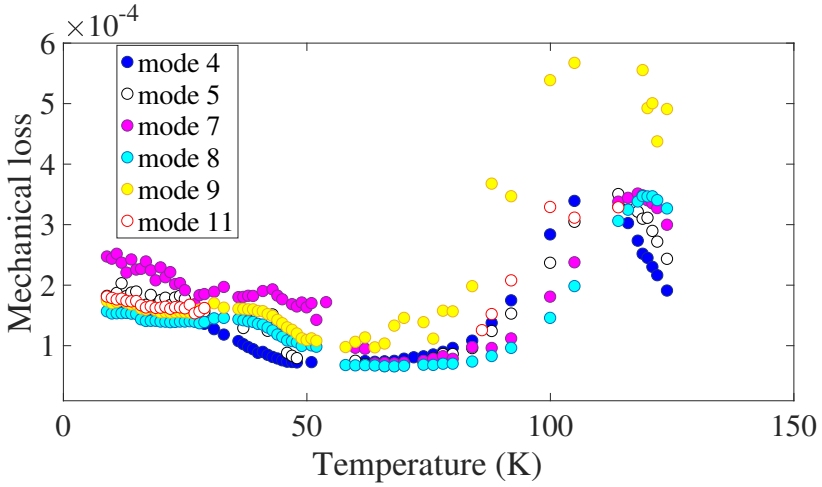

Fig. 6.11 Loss of 300 °C heat-treated IBS TiO_2 as calculated from all bending modes of the coated sample.

modes of the heat-treated sample, but there was only one clamp measured so it may be an artefact of the temperature cycle. This peak is thought to be spurious in part due to its absence in previous measurements, albeit of a much greater thickness of titania [365]. A second measurement of this heat treatment would be valuable to determine whether the peak is a structural feature of the 300 °C heat treatment.

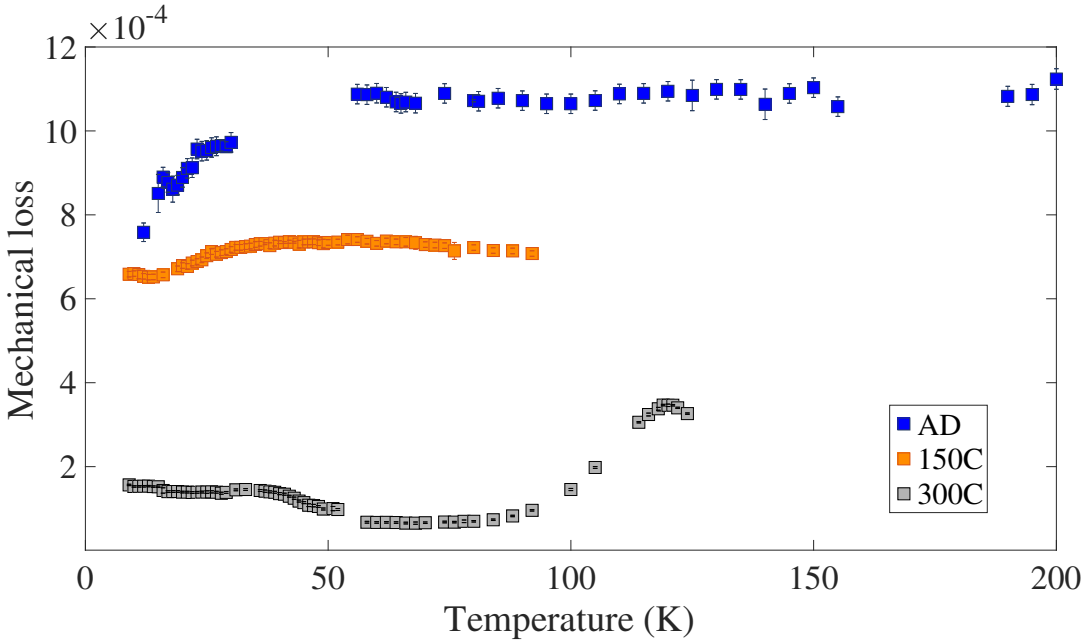

Fig. 6.12 Mechanical loss of TiO_2 loss as-deposited and heat treated at 150 °C and 300 °C. The AD TiO_2 data is from [359] and all loss is calculated from bending mode 8 of the coated samples.

Figure 6.12 shows a comparison of loss from the 150 °C and 300 °C heat treatments, with the loss of the coating as deposited included for reference. The continued heat treatment of the titania coating can be seen to significantly reduce the mechanical loss across all measurement temperatures. This is unexpected due to evidence in the literature of polycrystalline structure formation in TiO_2 after heat treatment at temperatures as low as 200 °C and the narrow low-temperature peaks and increased loss* in tantalum pentoxide as a result of crystallisation. Annealing pure titania at 300 °C was expected to induce loss effects consistent with the onset of crystallisation, but the loss instead reduced in magnitude and displayed no signs of forming a peak in the 20 to 40 K range.

Figure 6.13 shows the 600 °C heat-treated 68% Ti:Ta_2O_5 for comparison, where both coatings would be expected to show loss signs of polycrystalline structure formation. Neither coating exhibit such effects and, in fact, the 68% titania doped sample

*See figure 6.19 for the loss effects from heat-induced crystallisation in tantalum pentoxide.

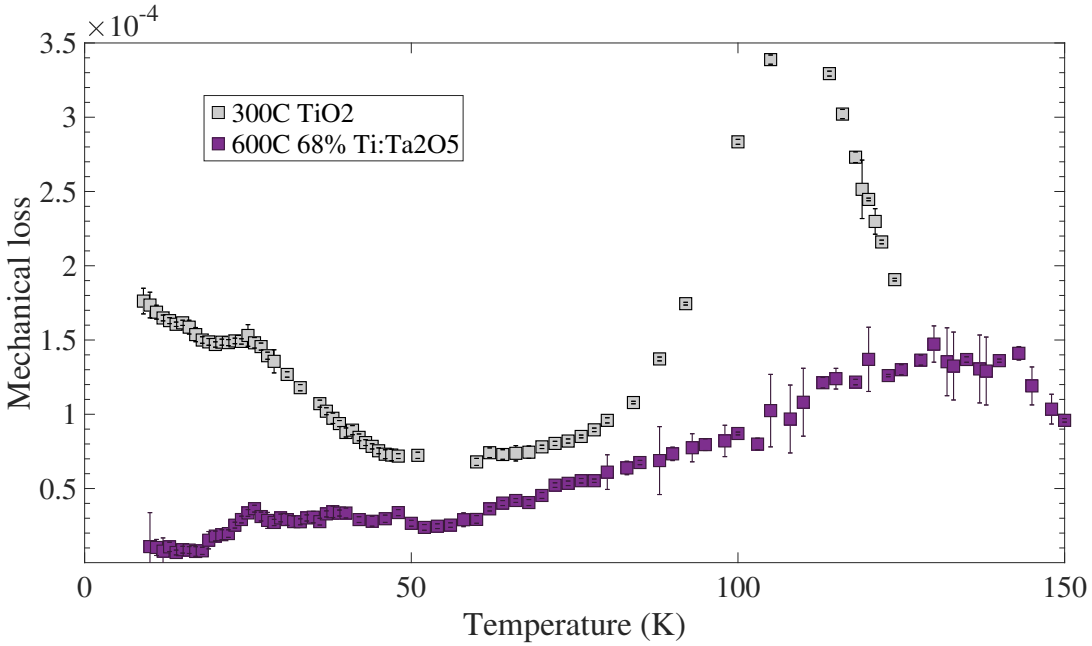

Fig. 6.13 Loss of 300 °C heat-treated TiO_2 compared to 600 °C 68% Ti:Ta_2O_5, as calculated from bending mode 8 of the cantilever samples.

has lower loss than the pure titania at all measurement temperatures. It is therefore of further interest to continue measuring the loss of IBS titania with heat treatment temperatures greater than 300 °C. Furthermore, there is evidence that IBS creates oxygen deficient titania coatings that tend towards TiO_2 with heat treatment [369]. This could be a possible explanation for the continued reduction in loss with heat treatment seen in pure titania, as well as the massive reduction in loss seen with the 68% Ti:Ta_2O_5. Measuring the stoichiometry of the titania coatings as-deposited and after heat treatments would serve to test this hypothesis.

6.2.4 34.5% zirconia-doped tantalum pentoxide

The significant reduction in tantalum pentoxide loss with titania doping led to structural investigations of TiO_2 doped compared to un-doped Ta_2O_5 in order to better understand the origins of coating mechanical loss. It was found that titania doping changed the atomic structure at the nearest-neighbour scale, which was thought to affect macroscopic processes such as mechanical loss through increased bond homogeneity and altered bond angle distribution [370]. Figure 6.14 shows an example of the short range (< 0.5 nm) order atomic structure of amorphous tantala, which contains ring structures that occur in its crystalline form. The vibrational modes of these tantalum-oxygen ring structures gives insight into their flexibility, which increases when doped

with titanium. Models doped with zirconium instead of titanium saw a further increase in flexibility, so zirconia-doped tantala was chosen as a promising new coating based on the hypothesis that the higher atomic flexibility of titania doped tantala could be the origin of its reduced mechanical loss [371, 372].

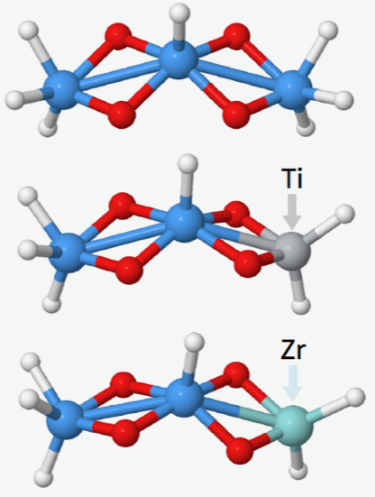

Fig. 6.14 Atomic models of ring structures [360] comprised of tanala (blue) and oxygen (red). The top model is un-doped, and the middle and bottom are doped with titanium and zirconium, respectively. Hydrogen (white) is added to keep the model charge zero, a requirement for vibrational analysis of these structures.

Doping Ta_2O_5 with concentrations of ZrO_2 between roughly 30% and 60% has also been shown to increase the temperature at which tantala coatings can be heated prior to crystallisation, with the amorphous-crystalline transition temperature increasing from approximately 600 °C to 900 °C [373]. As shown in figure 4.29, the loss of amorphous silica at room temperature improves with heat treatments up to 950 °C. Titania doping seems to have minimal effect on the crystallisation temperature of Ta_2O_5, limiting the heat treatment of a multilayer stack to below 600 °C. If the mechanical loss of zirconia-doped tantala is below that of Ti:Ta_2O_5 then it would provide the opportunity for high temperature heat treatment of a SiO_2 and Zr:Ta_2O_5 coating stack, which would lower the loss of both coating layers compared to a current silica and titania-doped tantala coating stack design. Lower loss compared to Ti:Ta_2O_5 would also provide evidence for the link between increased bond flexibility and mechanical loss.

A 162 ± 1 µm thick, welded silica cantilever was coated with 590 ± 10 nm of 34.5% Zr:Ta_2O_5 in order to measures the room temperature loss*. The results are shown in figure 6.15, which contains calculated loss of the coating as deposited, as well as after heat treatment at 300 °C, 400 °C, 500 °C, and 600 °C. The heat treatments

*The Young's modulus of the coating was found through nanoindentation to be 130 ± 2 GPa [374]

resulted in lower loss compared to the coating as-deposited, but there is little in terms of consistent loss trends. The loss of the 400 °C, 500 °C, and 600 °C samples are equal within measurement uncertainties for modes 1, 2, and 4, but are not equal for modes 3 and 5. Modes 6 and 7 were measured as well, but the loss of the coated sample was less than the measured loss of the uncoated cantilever for most heat treatments. Even for the modes presented in figure 6.15, the control data was within 50% of the measured coating data for heat treatments above 300 °C. The room temperature loss values are, therefore, taken to be upper estimates of the coating loss and the apparent stop in improvement after 400 °C attributed to the elevated loss of the cantilever rather than a trait of the coating. One conclusion from this upper estimate loss, and the plateaued improvement with heat treatment, is that crystallisation of the coating at 600 °C is unlikely due to the consistent low loss of this sample. It is also clear that heat treatment reduces the loss, which, after 400 °C, is equivalent to the accepted room temperature values of 25% Ti:Ta_2O_5 (2.0-2.4 $\times 10^{-4}$) [16, 40, 355].

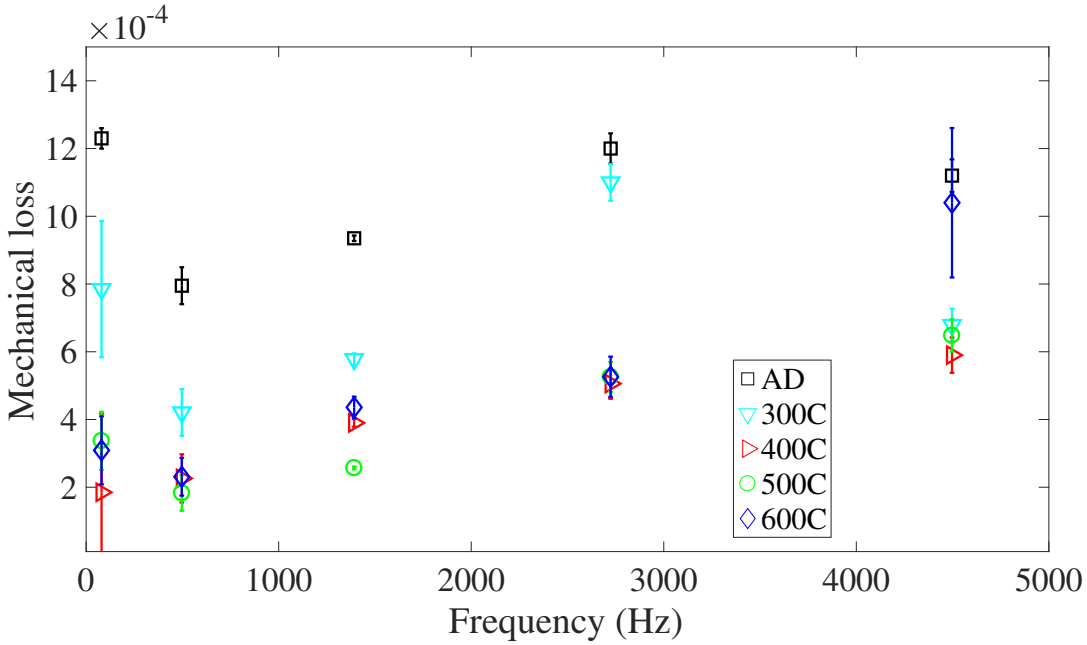

Fig. 6.15 Room temperature coating mechanical loss of 590 nm 34.5% Zr:Ta_2O_5, as measured on a welded silica cantilever. Loss is calculated from silica cantilever bending modes 1-5.

Silicon cantilevers* were coated at the same time as the silica cantilever in order to measure the loss at cryogenic temperatures. Figure 6.16 shows the coating loss calculated from all measured modes of the zirconia doped tantala sample, as-deposited. The loss increases with measurement frequency but is broadly similar in shape for all

*All measured cantilevers were ∼70 µm thick.

modes. Figure 6.17 shows the coating loss after heat treatment at 600 °C. There is a significant increase in loss compared to the annealed sample, as well as the formation of a sharp peak in loss at ∼25 K. The same frequency dependence is apparent for measurement temperature above the loss peak, but the coating loss is indistinguishable between modes at temperature below ∼25 K. This same trend remains after an 800 °C heat treatment, as shown in figure 6.18. The 800 °C heat treatment increased the magnitude and narrowed the low temperature peak seen with the 600 °C. Loss at temperatures above the peak remained similar.

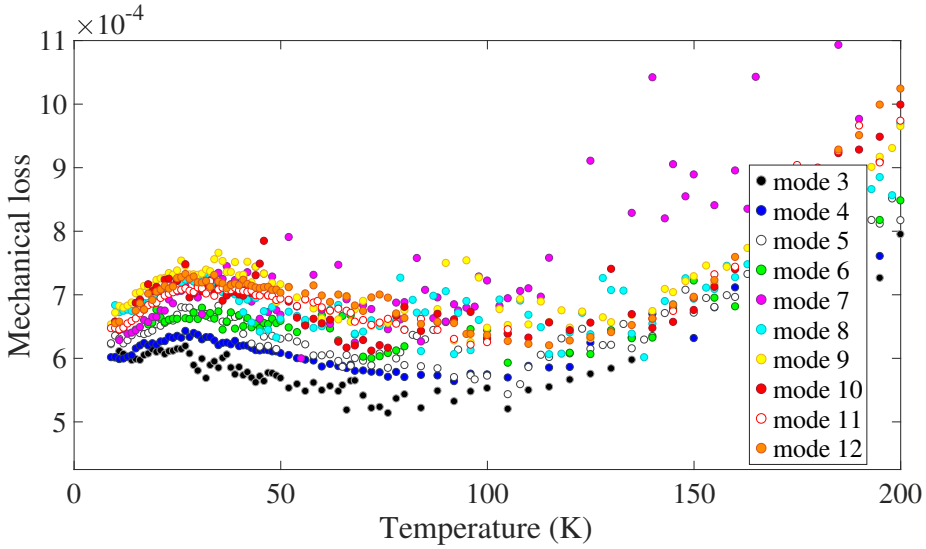

Fig. 6.16 Coating loss of 34.5% Zr:Ta_2O_5 as calculated from all measured modes of the sample as-deposited.

Figure 6.19 shows the loss of all zirconia doped tantala samples compared to the loss of equivalent heat treatments of pure Ta_2O_5. As shown in [256], the 800 °C heat treatment of pure Ta_2O_5 results in significant increase in loss at all temperatures and is associated with crystallisation of the coating. Doping with zirconium has clearly suppressed this effect and resulted in comparatively little change in loss with the high temperature anneal. Figure 6.20 shows the same loss comparison but zoomed in to omit the high loss of the 800 °C undoped Ta_2O_5.Here it can be seen that the zirconium doping results in reduced loss across all temperatures for the coatings as-deposited, but the 600 °C heat treatment results in very similar loss between the doped and undoped coatings. Noticeable, however, is the difference in peak shape between the 600 °C heat treatments: the pure Ta_2O_5 has a much sharper and a more well-defined peak. The sharp peak is thought to be indicative of a shift towards crystallinity within the coating, so the 600 °C heat treatment is beginning to crystallise the undoped Ta_2O_5 but not the Zr:Ta_2O_5. The 800 °C heat treatment produces a nearly identical sharp,

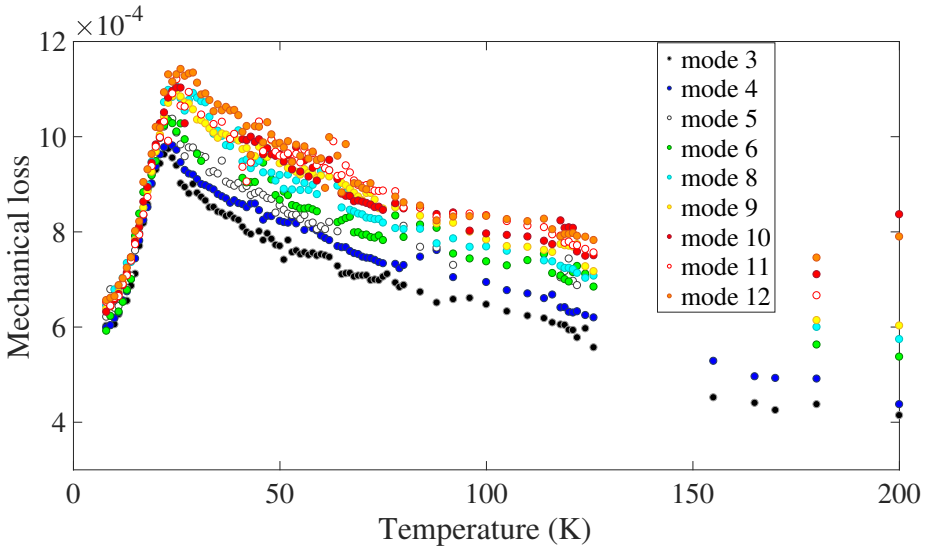

Fig. 6.17 Coating loss of 34.5% Zr:Ta_2O_5 as calculated from all measured modes of the sample after a 600 °C heat treatment.

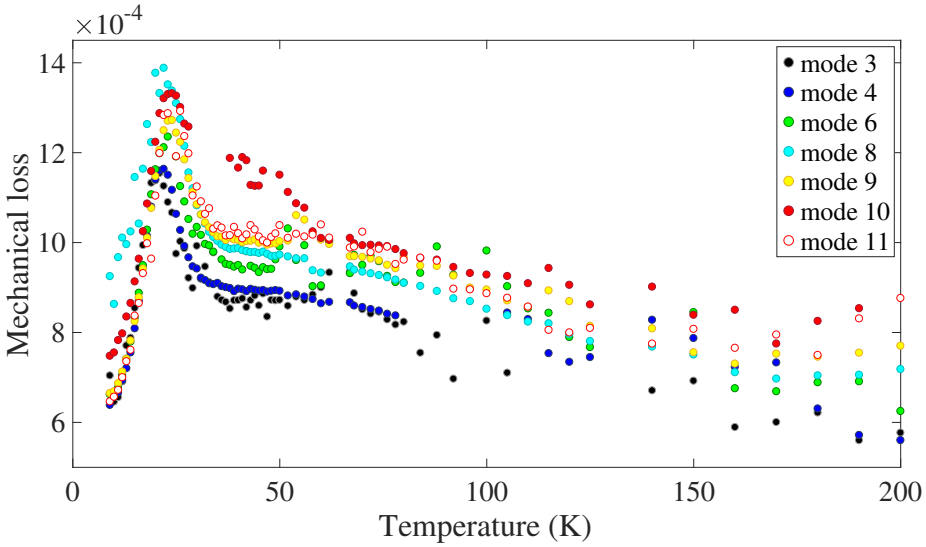

Fig. 6.18 Coating loss of 34.5% Zr:Ta_2O_5 as calculated from all measured modes of the sample after a 800 °C heat treatment.

defined peak at ∼25 K in the Zr:Ta_2O_5 as seen in the 600 °C annealed Ta_2O_5, leading to the conclusion that the doped coating is beginning to crystallise after 800 °C but has resisted paracrystallinity prior to this heat treatment.

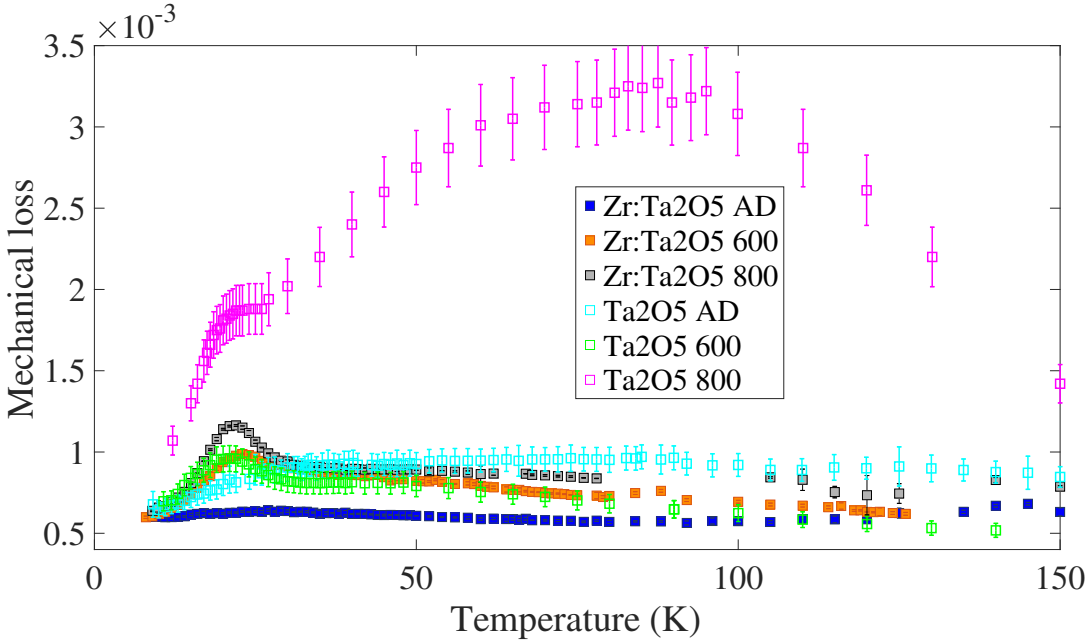

Fig. 6.19 Loss of 34.5% Zr:Ta_2O_5 compared to that of undoped Ta_2O_5 for the coatings as-deposited and heat treated at 600 °C and 800 °C. Loss data for the pure Ta_2O_5 is from [256, 359], and all loss is calculated from bending mode 4 (∼2.6 kHz).

The primary benefit of an increased crystallisation temperature is the ability to anneal multilayer coatings to a higher temperature. Thin film coatings usually tend towards lower room temperature loss with increased heat treatment up to the point of crystallisation. It is clear from both the low temperature and room temperature loss behaviour that doping Ta_2O_5 with 34.5% zirconium would allow for higher heat treatment temperatures and, therefore, possible improvement to the thermal noise performance of the current, SiO_2 and 25% Ti:Ta_2O_5 coating stack. Further studies of the room temperature loss with respect to heat treatment are of high interest to confirm the conclusions drawn from the low temperature loss behaviour of the Zr:Ta_2O_5. Figure 6.21 shows the loss compared to titania doped tantala, where it can be seen that the Zr:Ta_2O_5 would provide no benefit as a replacement high index layer for cryogenic detector mirror coatings. Further low temperature measurements are, therefore, not as valuable as a more in-depth look into possible benefits of using the coating in a room temperature coating stack able to be heat treated above the current 500 °C anneal and take advantage of reduced loss in both the high and low index layers.

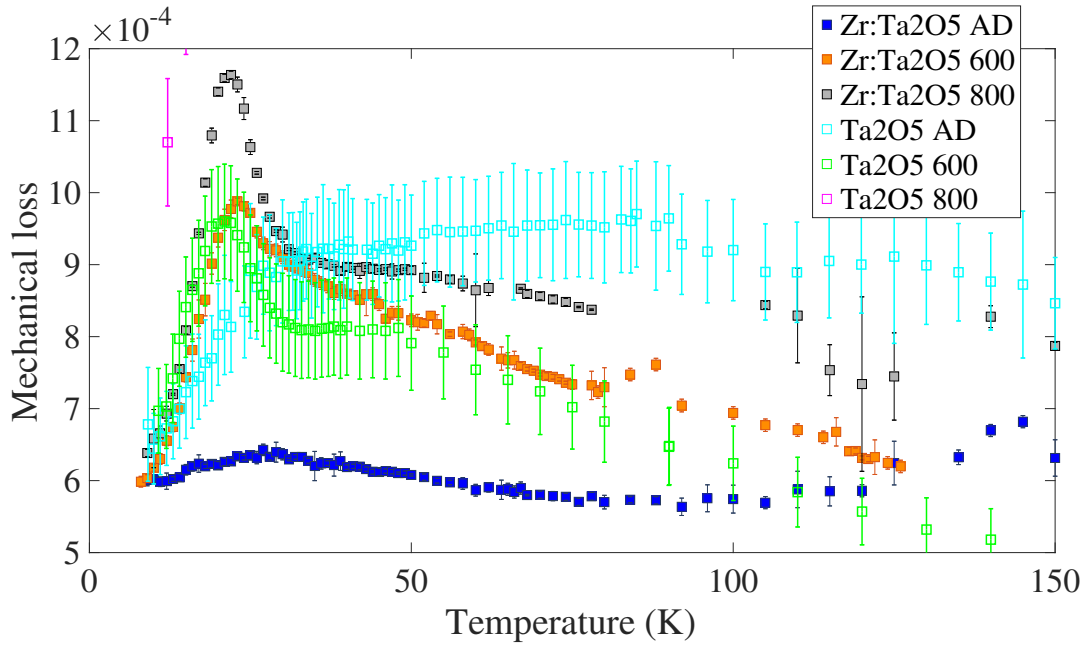

Fig. 6.20 Rescaled version of figure 6.19 shown to better observe the differences in loss shape and magnitude otherwise obscured by the 800 °C heat-treated Ta_2O_5.

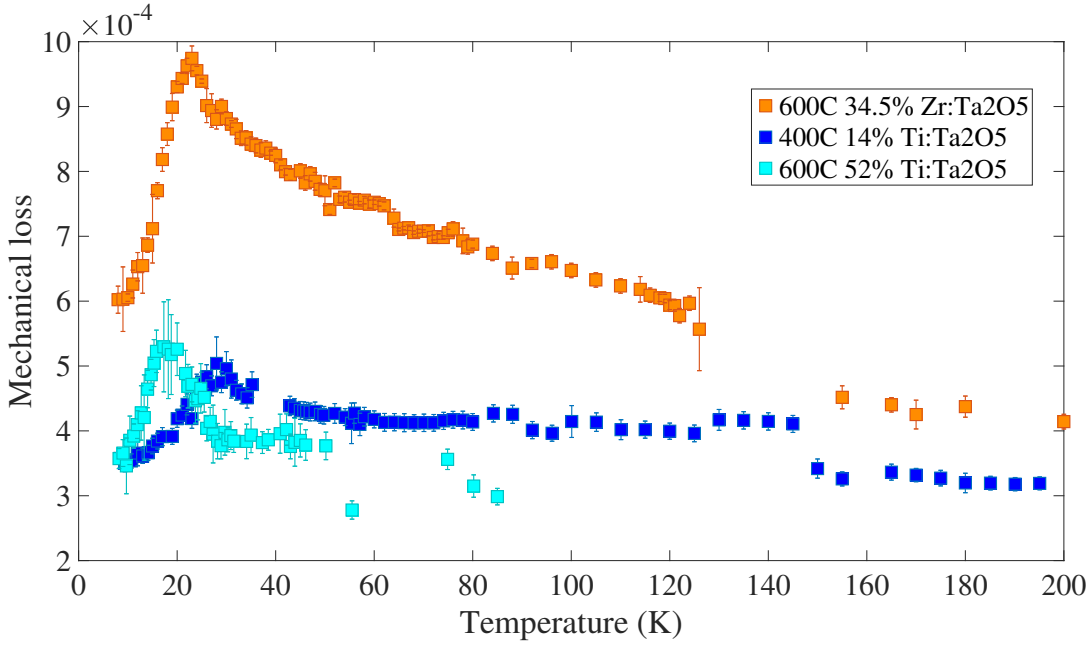

Fig. 6.21 Loss of 600 °C heat-treated 34.5% Zr:Ta_2O_5 compared to 400 °C 14% and 600 °C 52% Ti:Ta_2O_5. All loss was calculated from the fourth bending mode of the respective cantilever samples.

6.3 Alternative deposition methods

While IBS coatings are the current standard for low loss, low scatter, and low absorption mirror coatings, it is of interest to investigate different coating techniques to better understand the connection between structural differences within coatings of the same material and any resulting changes in optical and mechanical properties. This section contains temperature dependent mechanical loss results for high index coating materials deposited via direct current magnetron sputtering (DC magnetron) and reactive low-voltage ion-plating (RLVIP).

6.3.1 DC magnetron sputtered tantalum pentoxide

As discussed in section 3.2.1.2, DC magnetron sputtering differs from IBS in that the sputtering ions are created by a glow discharge plasma encompassing both the target and substrate, as opposed to IBS where the ablating ions are introduced by an ion gun aimed only at the sputtering target. DC magnetron sputtering produces coatings with less packing density than IBS, but with higher density than evaporative deposition methods [247, 250]. DC magnetron is cost-effective and comparatively simple to implement, and the creation of an ablating plasma directly on the target surface eliminates the potential for contamination present with most IBS systems. Standard IBS ion sources send the ions through an extraction grid, which erodes over time and must be replaced, leading to the potential introduction of sputtered screen molecules [322]. Comparing the loss characteristics of this deposition technique to the standard, IBS tantala coatings could possible further the understanding of the structural origins of coating loss in Ta_2O_5.

A 63.7 ± 0.1 µm thick silicon cantilever was coated with 5.22 ± 0.20 µm of DC magnetron sputtered Ta_2O_5 and measured following the procedures discussed in section 3.3.2. Tantalum pentoxide was chosen due to both the extensive characterisation of IBS Ta_2O_5 and the continued investigation of Ta_2O_5-based coatings as high index multilayer coatings. Figure 6.22 shows the loss of the as-deposited coating, which can be seen to exhibit the low temperature loss peak characteristic of IBS Ta_2O_5 coatings. The peak is centred around $\sim$45 K and is present in all measured modes of the sample, and the loss broadly increases with measurement frequency.

The substrate reaches temperatures of $\sim$90-100 °C in both IBS and DC magnetron sputtering, so a direct comparison of the coatings as-deposited is shown in figure 6.23. The measurement uncertainty for the DC magnetron coating is extremely low (<1%) across all measurement temperatures, but a 10% systematic uncertainty stemming

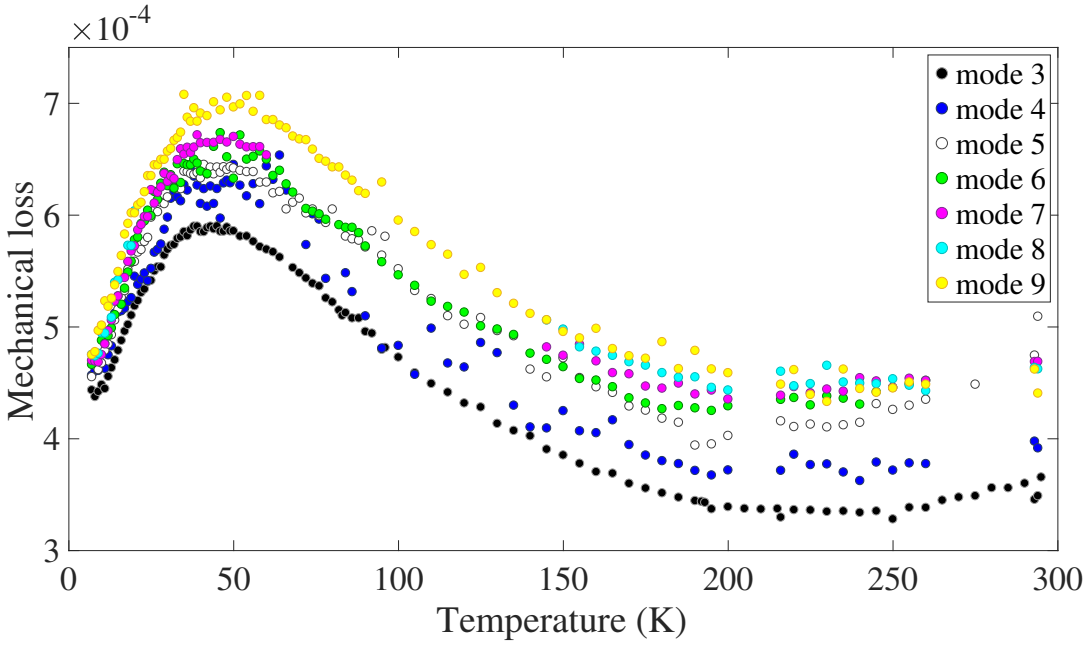

Fig. 6.22 Coating loss of DC magnetron sputtered Ta_2O_5, as calculated from all measured bending modes.

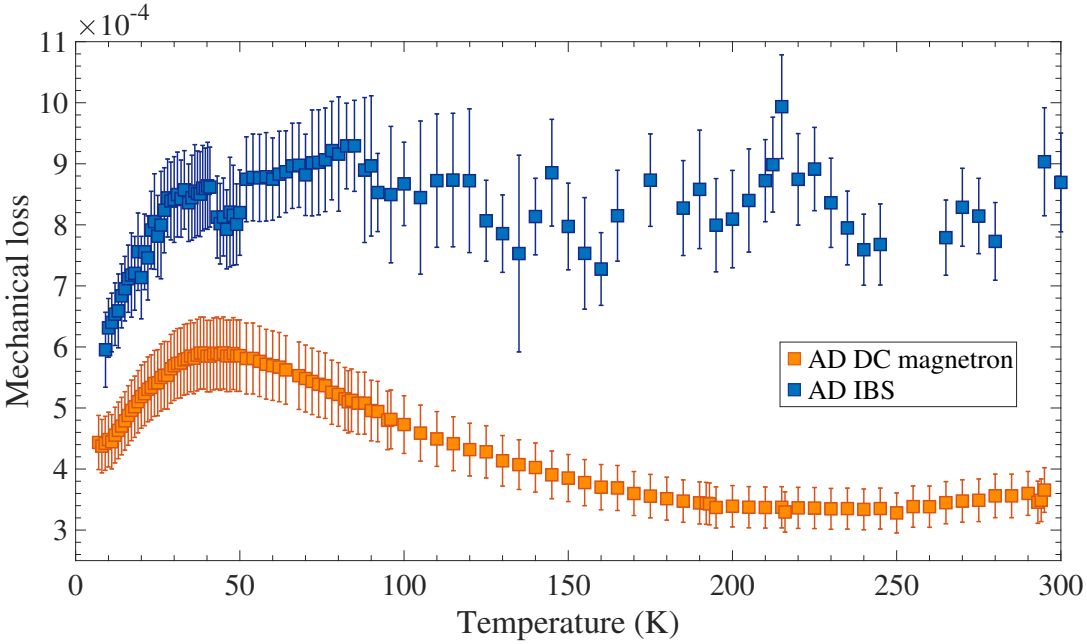

Fig. 6.23 Loss of DC magnetron Ta_2O_5 compared to that of IBS Ta_2O_5 (from [256]). Both displayed coatings are as-deposited, and loss was calculated from the third bending mode of each coated silicon sample.

from unknown Young's modulus has been added to the loss for figure 6.23 (140 GPa was used as the modulus for loss calculations). Even accounting for the large range of possible Young's moduli, the DC magnetron Ta_2O_5 exhibits lower mechanical loss across all measured temperatures, and the low temperature loss peak is more clearly defined than the peak in IBS Ta_2O_5. Interestingly, the loss magnitude and peak shape of the DC magnetron Ta_2O_5 is much closer to that of the IBS Ta_2O_5 heat treated to 300 °C. This comparison can be seen in figure 6.27 in section 6.3.3. The absorption, however, was found to be about 85 ppm, which is far greater than that of IBS Ta_2O_5 and high enough to outweigh the mechanical benefits of the coating [375].

6.3.2 RLVIP amorphous silicon

Ion-beam sputtered amorphous silicon (a-Si) is a candidate as a replacement high index coating layer in future, cryogenic detectors due to its extremely low mechanical loss [40, 376]. Amorphous silicon has already been shown to exhibit losses below 10^{-4} with heat treatment up to 450 °C over a wide range of measurement temperatures [259], which is well below that of the current high index layer (25% Ti:Ta_2O_5) dominating the coating thermal noise of the room temperature detector mirror coating. However, the absorption requirements for detector coatings are very strict: for aLIGO it is 0.5 ppm [165], the Voyager cryogenic upgrade to aLIGO is 1-2 ppm [376], and the ET design study has a requirement of less than 5 ppm [40]. These stringent limits are in place because coating absorption results in thermal distortion and lensing of the test-mass mirrors, and high coating absorption would inhibit cooling and temperature stability of the mirrors for cryogenic detectors. Increasing the laser wavelength from 1064 to 1550 nm reduces the absorption in amorphous silicon, but it is still at a level too great for use as a high index bilayer in detector coatings. Recent measurements of RLVIP a-Si show a significant reduction in absorption compared to other amorphous silicon coatings [325] that, while still prohibitively high, puts RLVIP a-Si in a promising position to replace IBS as a potential upgrade material in future coating stacks. It is therefore important to characterise the loss in order to make accurate thermal noise estimations. Furthermore, if heat treatment of the RLVIP SiO_2*, is found to decrease its loss and produce a viable replacement for IBS silica, then confirming low loss for RLVIP silicon will allow for all layers to be produced via the same sputtering technique, thereby eliminating significant engineering issues.

*The loss of RLVIP SiO_2 as deposited was shown in sections 4.5 and 4.6 to be below that of IBS SiO_2 at the low temperature loss peak, but greater than IBS SiO_2 at temperatures above ∼60 K. Further measurements are required to directly compare the coatings after a 600 °C heat treatment.

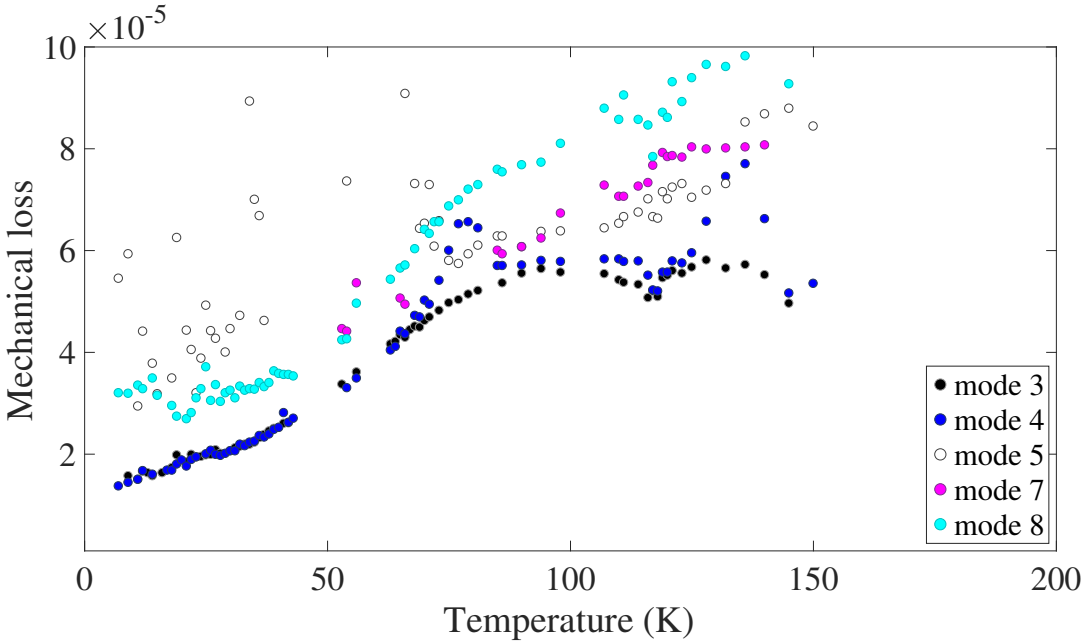

Fig. 6.24 Coating loss of as-deposited RLVIP a-Si calculated from cantilever bending modes 3-5, 7, and 8. All calculations assumed zero loss in the substrate, so the shown values represent an upper limit on coating loss.

Coating loss was calculated from measurements of a 67.0 ± 0.2 µm thick silicon cantilever coated with 1.00 ± 0.01 µm RLVIP a-Si. No thermal oxide was grown on the cantilevers prior to coating in anticipation of coating loss below that of the low temperature peak in loss created by thermally grown SiO_2. No control samples were used in the loss calculations; there were no measurements of un-oxidised cantilevers from the same wafer with which to subtract the loss of the substrate. Figure 6.24 shows the coating loss as calculated assuming zero substrate mechanical loss and a coating Young's modulus of 147 GPa*. The reported loss values are, therefore, an upper limit on the actual coating loss, which is likely to be much lower at temperatures below 50 K where the substrate loss is expected to be within 50% of the measured loss of the coated sample. Three of the measured modes (3, 4, and 8) shown in figure 6.24 agree well with each other, with the other two modes (5 and 7) displaying consistent loss above ∼75 K but scattered or no data at lower temperatures. The reason behind this low temperature scatter is unknown, but it is also evident in measurements of IBS amorphous silicon [259]. Even as an upper limit, the coating loss seen in figure 6.24 is

*This is the Young's modulus of IBS aSi as found through nanoindentation [280].

an order of magnitude lower than any of the doped or pure tantala coatings presented in this chapter at temperatures below 100 K*.

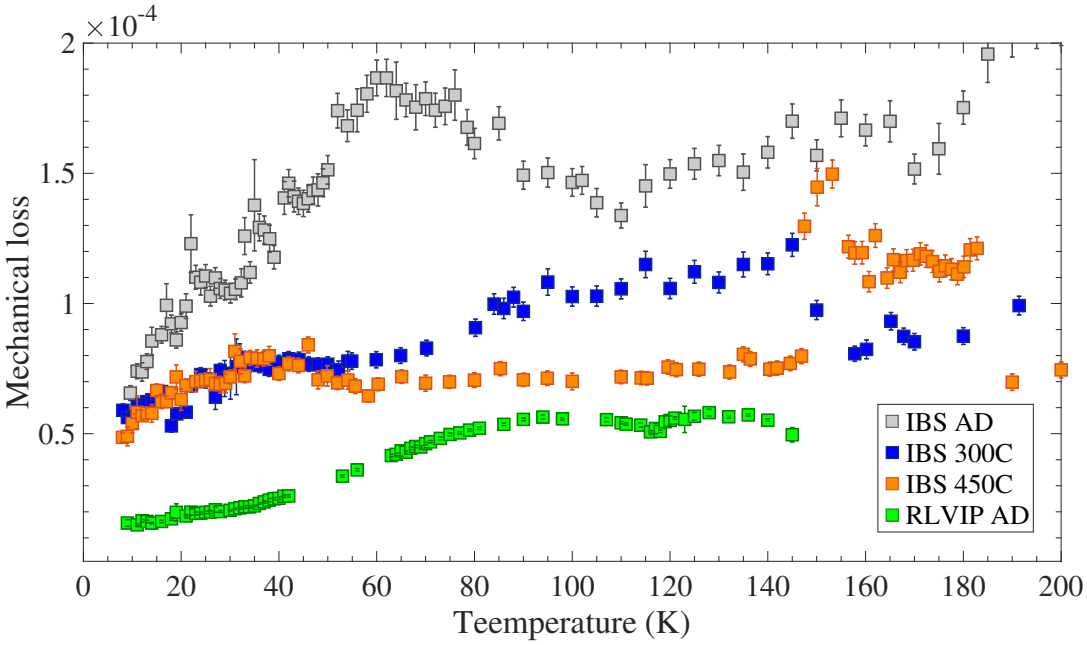

Fig. 6.25 Loss of as-deposited RLVIP a-Si compared to AD and 300 °C and 450 °C heat treated IBS amorphous silicon. All coating loss is calculated assuming zero substrate loss, and the IBS a-Si loss is from [259].

Figure 6.25 shows the loss compared to that of multiple heat treatments of IBS a-Si. With a deposition temperature of 250 °C, the RLVIP a-Si might best be compared to the 300 °C heat treated IBS silicon, but the RLVIP silicon exhibits significantly lower loss than all of the IBS heat treatments. All of the coating loss is calculated assuming a zero substrate mechanical loss, which means the loss shown in figure 6.25 represents the upper limit, and all the curves are likely to shift towards lower loss when the substrate is taken into account. However, for the lowest IBS loss (450 °C heat treatment) to reach the same loss as the RLVIP upper limit requires a substrate with loss on the order of 1-3 $\times$ 10^{-5} at temperatures below 150 K. This is an order of magnitude higher than the loss associated with bare silicon cantilevers, even with some ($\sim$20nm) of thermal oxide. It is therefore possible to conclude that RLVIP produces amorphous silicon with lower loss than IBS. This decrease in loss could occur due to a reduction in two-level systems accompanying the increased deposition temperature of RLVIP. As discussed in section 6.2.1, TLS in e-beam sputtered amorphous silicon have been shown to decrease with increased deposition temperatures [245].

*No peak in loss was seen in this temperature region, which, in addition to the IBS TiO_2 and Al_2O_3, eliminates the possibility of low temperature loss peaks being an artefact of loss measurements using silicon cantilevers.

The primary result of these loss measurements is confirmation of low loss in RLVIP deposited amorphous silicon, which, with the loss improvement seen in RLVIP SiO_2 over IBS, would warrant a switch in deposition method for future detector coatings from IBS to RLVIP. The absorption of RLVIP a-Si also provides an advantage over IBS; whereas IBS a-Si exhibits a significant increase in absorption at heat treatments above 450 °C, RLVIP a-Si remains at an absorption minimum with further heat treatment [377]. However, as will be discussed in Chapter 7, the high absorption of silicon coatings would require a multi-material coating stack, where the majority of the laser power is reflected in the first few layers of low absorption coating material bilayers on top of an a-Si bilayer stack. It is therefore necessary to understand the loss of RLVIP Ta_2O_5 as a possible high index material for the top bilayers of an RLVIP multi-material coating stack.

6.3.3 RLVIP tantalum pentoxide

Similar to the motivation for investigating the low temperature loss behaviour of DC magnetron Ta_2O_5, measuring RLVIP tantalum pentoxide gives further comparison of loss from the same coating material deposited in a different manner. The elevated deposition temperature (250 °C) inherent to this ion-plating deposition method is also of interest in relation to the high temperature IBS Ta_2O_5 coatings discussed in section 6.2.1. These comparisons provide both practical juxtaposition of losses for use in coating stack estimation and an increased possibility of finding correlations between mechanical loss and the structural formation of the different coatings.

The loss of RLVIP Ta_2O_5 at low temperatures is of particular interest given the low loss exhibited by RLVIP SiO_2*. While using multiple deposition methods within the same coating stack could be possible, utilising the same deposition technique for all coating layers is significantly less challenging and a more feasible option for altering the only coating chamber currently large enough to coat the test mass mirrors. If further heat treatment of the RLVIP SiO_2 results in even lower loss then it could be a viable replacement for IBS SiO_2 and knowledge of RLVIP Ta_2O_5 coating loss will be crucial for evaluating the thermal noise contribution from such a coating stack.

Figure 6.26 shows the coating loss as calculated from all measured bending modes of a coated (500 ± 10 nm) silicon cantilever sample. The low temperature loss peak characteristic of thin film tantala can be seen in all measured modes centred around ~ 50 K. The higher frequency modes (>4 kHz) exhibit a second peak above 150 K, but it is assumed to be a result of a clamp resonance due to the inconsistent shape

*See section 4.5.

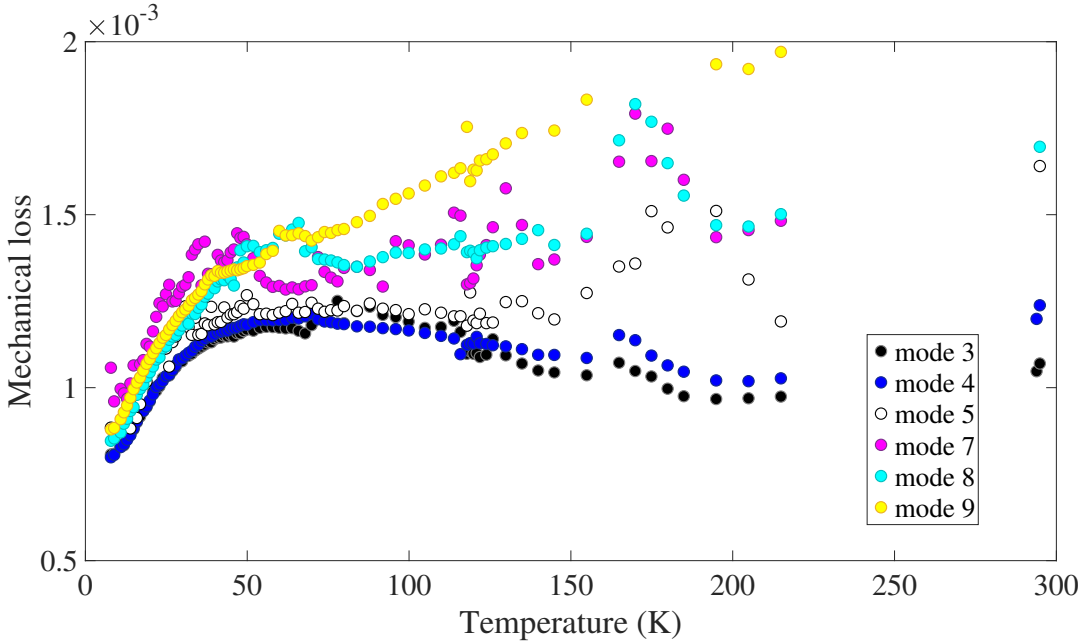

Fig. 6.26 RLVIP Ta_2O_5 coating loss calculated from all measured bending modes of the coated sample as-deposited.

and peak temperature between modes. Only one temperature cycle was measured for the sample, so this higher temperature peak would be expected to vanish with further measurements.

Figure 6.27 shows the loss in relation to other tantalum pentoxide coatings, where it can be seen to be greater in magnitude at all temperatures compared to all deposition methods except for atomic layer deposition (ALD)*. It should be noted that the ALD deposition temperatures can reach temperatures up to 350 °C [378], so it represents another iteration of elevated temperature deposition Ta_2O_5. A 300 °C heat treatment of the IBS tantala is included in figure 6.27 to further highlight that post-deposition annealing produces changes in loss different to those seen in similar temperature elevated deposition methods. Of note is the clear difference in temperature of the loss peaks seen in all the coatings. All of the losses are calculated from bending mode 3 (∼1.3 kHz), with the cantilever thicknesses being within 5 µm of each other. This, combined with similar coating thicknesses for all samples except DC magnetron, means that changes in peak temperature greater than about 0.5 K are a result of structural differences rather than differences in sample geometry. Further work to calculate the activation energies and barrier height distributions of each coating deposition method

*Atomic layer deposition is a chemical vapour deposition process where a thin film coating is grown one atomic layer at a time through alternating injections of reactive and inert gases into the deposition chamber. For more information see [378].

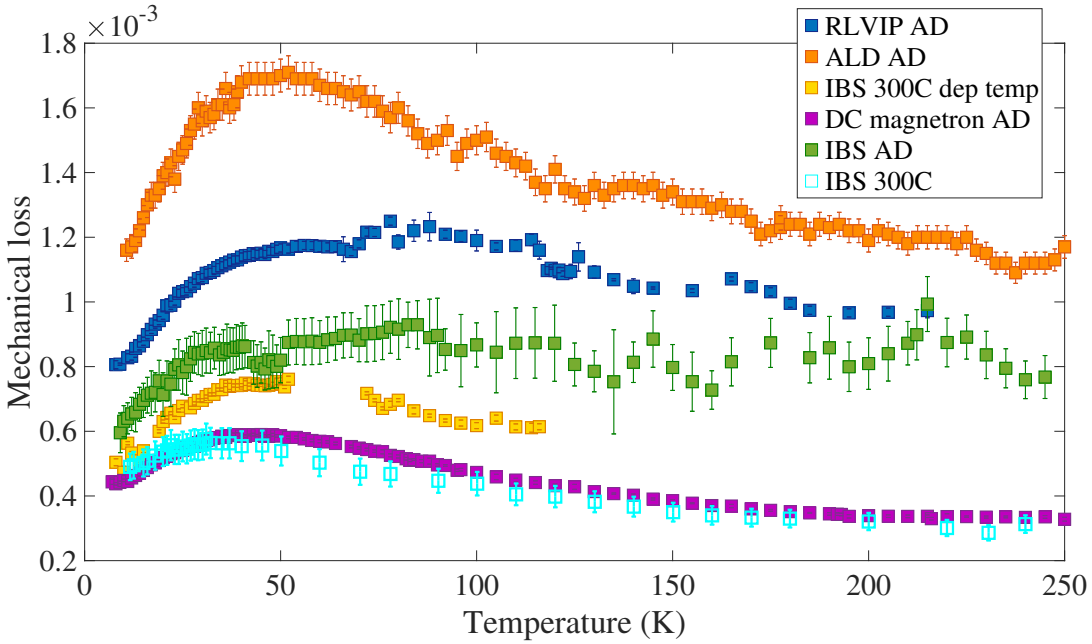

Fig. 6.27 Mechanical loss of Ta_2O_5 coatings formed through different deposition techniques. Loss results for the ALD coating are from [229], the AD IBS from [359], and 300 °C heat-treated IBS from [256]. The 300 °C deposition temperature IBS coating was also heat treated at 300 °C post-deposition.

is of high interest for a more in-depth comparison of the structural differences between deposition methods for Ta_2O_5 films.

With regards to RLVIP as a replacement deposition method for IBS, the increased magnitude of loss for RLVIP Ta_2O_5 would outweigh the benefits seen in the low index silica layers. Heat treatment has been shown to reduce the loss of elevated temperature IBS tantala coatings, but the coating as-deposited displays greater than twice the magnitude in loss across measurement temperatures; a disparity unlikely eliminated through annealing. This difference in loss also provides further evidence that elevated temperature deposition does not produce an ideal glass* or more relaxed formation of Ta_2O_5 films, where figure 6.27 shows all of the high temperature deposition methods to have higher loss than the comparable, 'low temperature' IBS Ta_2O_5.

6.4 Conclusions

A decade of research into high index materials since the upgrade to titania-doped tantala has produced no thermal noise improvements significant enough to warrant its

*The premise of which centres on extra surface mobility during deposition from the greater thermal energy and is discussed in section 6.2.1.

replacement. Low temperature mechanical loss measurements of high index materials are crucial for finding mirror coating stacks with reduced thermal noise for future, cryogenic gravitational wave detectors, but they also reveal structural characteristics of the coatings that could lead to more informed choices regarding research into these high index coating materials. This chapter has presented the temperature dependent loss of new, novel coating materials as well as variations of tantalum pentoxide, a well-characterised material from which the changes in loss behaviour with heat treatment and deposition method hopefully leads to better understanding of the origins of mechanical loss in thin films.

High deposition temperature IBS Ta_2O_5 was found to fall short of the hypothesised, ultra-stable glass formation, with loss in the same range as the standard deposition temperatures. Further research into the progression of the loss curve with heat treatment progression would allow for a more rigorous comparison, but measurements of the coating at room temperature have failed to produce the expected reduction in loss. One interesting result is the similarity in loss shape for the 300 °C deposition temperature and heat treatment compared to the 500 °C heat-treated standard deposition tantala, which suggests that thermal energy does play a different role in rearranging the structure of the coating depending on when it's applied. In other words, 300 °C deposition temperature is not the same as 300 °C heat treatment in terms of altering a coating's mechanical properties.

Samples of tantala doped with 68% titania were found to have potential issues due to coating inhomogeneity, but the coating loss after heat treatment was found to be over an order of magnitude lower than all other measured doping percentages at temperatures below 200 K. This result gives both an interesting look into the non-linearity of doping effects on coating mechanical loss and a potential upgrade to the 25% Ti:Ta_2O_5. Further investigation into the loss at heat treatments below 500 °C would be valuable for finding the temperature at which the sharp decrease in loss occurs. Continued analysis of the EELS data for this coating is also crucial for determining whether the titania doping percentage should be increased for future mirror coatings. Given the issues with scatter for TiO_2 coatings, measuring the optical qualities of this coating is also an important next step. The loss of pure titania was also investigated and shown to decrease across all temperatures with heat treatment at 150 and 300 °C. This is surprising given previous evidence of crystallisation after 200 °C, but further heat treatment to 500 °C would be valuable to see if the low loss of the 68% Ta_2O_5 could be mirrored by a drop in loss for pure titania. This low loss of annealed TiO_2 is a positive result for the future of nanolayer coatings, but the optical qualities may still preclude titania from use as a high index layer.

Doping tantalum pentoxide with 34.5% zirconium successfully raises the resistance of the coating to crystallisation, with an 800 °C heat treatment producing extreme increases in low temperature loss indicative of crystallinity in pure Ta_2O_5 but only the sharp loss peak associated with pre-crystalline tantala in the Zr:Ta_2O_5. While the loss at low temperature is too high to be a valuable replacement layer for cryogenic detector mirrors, this resistance to crystallisation could be a valuable characteristic for future room temperature detector upgrades; particularly since the room temperature loss for heat treatments from 400 °C to 600 °C is shown to be at least as low as titania doped tantala. Further investigation into the coating loss at room temperature is of high importance.

Amorphous silicon has already been shown to have loss at cryogenic temperatures well below any other high index material. However, the low index silica layers limit the benefit gained from the potential use of a-Si as the high index material*. RLVIP silicon exhibits lower loss than the already exceptional IBS a-Si, and, given the lower loss of RLVIP compared to IBS SiO_2, would allow for the same deposition method to be used for the entire coating stack. Both IBS and RLVIP a-Si have absorption too high to use as a high index material, but the RLVIP coating has been shown to reach minimum absorption after a 450 °C heat treatment and remain at this level with continued annealing [377]; IBS a-Si absorption worsens at these higher temperatures. RLVIP may, therefore, be useful as a coating technique for optimising the annealing of the silica without damaging the absorption of the silicon layers. Future work includes measuring the temperature dependent loss of RLVIP a-Si after heat treatment to investigate the difference in loss behaviour compared to heat-treated IBS a-Si.

DC magnetron and RLVIP tantala coatings were investigated for comparison to the ALD, IBS, and elevated temperature IBS already characterised. DC magnetron Ta_2O_5 is sputtered at about the same temperature as standard IBS, but it exhibited about 50% lower loss as-deposited. It also produced a significantly more defined low temperature loss peak. RLVIP tantala was shown to have much higher loss than any other tantala deposition method besides ALD, but changes with heat treatment would be interesting to try and correlate with any future structural investigations. Analysis of the activation energies and barrier height distributions for these different deposition techniques and heat treatments would be valuable for finding any possible correlation between film formation parameters or coating structure and mechanical loss.

High index sputtered coating materials are a primary source of thermal noise in the current detectors, so the more knowledge of loss characteristics the greater the chance

*This can be seen in figures 7.2 and 7.3, where replacing silica with the lower loss alumina allows the gains from amorphous silicon to be realised and results in much lower coating Brownian noise.

of more informed decisions regarding future research plans on the subject. An immediate benefit of the loss characterisation is the ability to give accurate estimation of the coating Brownian noise from a proposed stack of materials with known mechanical loss.

Chapter 7

Thermal noise implications of dual-material and multi-material coating combinations

7.1 Introduction

Coating thermal noise is a current limiting factor in the detection sensitivity of interferometric gravitational wave detectors. A push towards detector operation at cryogenic temperatures, e.g. 10, 20, or 123 K, provides a theoretically linear decrease in thermal noise power spectral density if all material properties remain constant. Properties such as Young's modulus or Poisson ratio change by a small enough degree so as to be insignificant in relation to the temperature change, but, as shown in Chapters 4 through 6, the mechanical loss of most coating materials changes with respect to temperature; coating stacks with minimal thermal noise at room temperature, such as the current advanced detector multilayer coating, would be prohibitively noisy when used at cryogenic temperatures. Characterising the change in mechanical loss over a wide range of temperatures for possible coating materials allows prediction of the thermal noise contribution at any potential operation temperature, for any possible combination of high and low index material.

The frequency dependent power spectral density of a coating stack's Brownian thermal noise is calculated from equation 7.1. The square root of this noise is the amplitude spectral density, which represents the magnitude of physical displacement noise from thermally-induced motion in the mirror coatings. This chapter presents comparative estimates of the coating Brownian noise at reduced operation temperature from a number of high and low index coating combinations based on the results

presented in previous chapters. Current design study estimations are updated to include the more accurate amorphous silica loss, and new coating stacks will be presented and compared to assess their potential as coating stack replacements for future, cryogenic test mass mirrors. A novel technique of utilising more than two materials in the same coating stack is also discussed [326, 332], with current estimates being upgraded and possible new multi-material stacks proposed.

7.2 Thermal noise parameters

As discussed in section 2.3, the power spectral density of the thermal noise, $S_x^{\text{total}}(f)$, of a multilayer coating is calculated using (equation 2.24) [164]:

$$S_x^{\text{total}}(f) = \frac{2k_{\text{B}}T(1-\nu^2)}{\pi^{3/2} f w_r Y}\phi_{\text{effective}} \,, \tag{7.1}$$

where k_{B} is the Boltzmann constant, T is temperature, f is frequency, w_r is the radius of the Gaussian laser beam, and Y and ν are the Young's modulus and Poisson's ratio, respectively, of the substrate. The loss term $\phi_{\text{effective}}$ is the effective mechanical loss angle of the coated test mass mirror and is given by equation 2.25. The parallel and perpendicular material properties (contained within equation 2.25) of dual material coating stacks are defined by equations 2.26 through 2.30. Section 7.4 will discuss coating stacks with three coating materials, in which case an extra term was added to each of these equations.

All mechanical loss values used for thermal noise estimation are contained within tables 7.1 and 7.2. Table 7.1 gives the coating loss at 10, 20, and 123 K for all low refractive index coating materials presented in previous chapters, as well as for the bulk form of materials used as test mass substrates[*]. These temperatures were chosen based on estimated operating temperatures for ET, KAGRA, and LIGO Voyager[†]. Table 7.2 gives the coating loss for high refractive index materials presented in Chapter 6, as well as from other, previously characterised coating materials of interest.

Table 7.3 shows the material properties used in conjunction with the mechanical loss to calculate coating Brownian noise. The Young's modulus, refractive index (n), and Poisson's ration are assumed to remain unchanged with both measurement temperature and heat treatment for the purpose of thermal noise calculations. These have not been characterised for many of the coating materials, specific doping per-

[*]Fused silica is not used in any thermal noise estimates for cooled detector mirrors due to its extremely high loss at cryogenic temperatures.

[†]See 1.6.5 for a discussion of these detectors.

centages, or deposition techniques, so values have been assumed based on those from similar coating materials. It should also be noted that Thermo-optic noise has not been included due to a lack of accurate values for temperature dependent thermal properties of most coatings. The cancellation of thermo-optic noise discussed in section 2.4.3 is therefore not guaranteed to occur for the presented coatings, as it depends on the opposite direction of thermal expansion between the materials.

The radius of the Gaussian interferometer laser beam incident of the mirrors differs between next generation detector designs, so the aLIGO end test mass beam radius of 6.2 cm was used for all calculations to provide direct comparison between coating designs. Furthermore, all calculations of thermal noise in this chapter assume a silicon test mass substrate. Sapphire test masses are installed in KAGRA, but crystalline silicon is the current proposed material for use in both ET and the LIGO upgrades. Thermal noise values for a given coating can be roughly* expected to decrease when applied to a sapphire substrate because of sapphire's elevated Young's modulus.

7.2.1 Coating stack reflectivity

The final parameter required for thermal noise calculation is the coating thickness, which is dependent on the refractive indices of the coating layer materials. The thickness, t, of a coating layer with refractive index n is related to the optical thickness, δ, by: $t = \delta/n$. The optical thickness of a coating layer in highly reflective mirror coatings is a quarter of the laser light wavelength. Current detectors use 1064 nm wavelength light, but future detector designs include a shift to operation at a wavelength of 1550 nm or longer laser light because of crystalline silicon's elevated absorption at 1064 nm [40, 181, 182]. The thickness of coating layers used for thermal noise estimations at cryogenic operation temperatures is therefore given (in nanometres) by:

$$t = \frac{1550}{4n} \,. \tag{7.2}$$

The reflectivity, R, of a coating comprised of an even number, $2N$, of these $\lambda/4$ high and low index coating layers is given by [389]:

$$R_{2N} = \left(\frac{n_s y - n_m}{n_s y + n_m} \right)^2 \,, \tag{7.3}$$

*In some cases an extra coating layer is required for a sapphire substrate compared to silicon in order to properly alternate refractive indices. In rare cases the loss and added thickness of this extra layer can negate the thermal noise benefits of sapphire.

Table 7.1 Mechanical loss of low refractive index coatings characterised in previous chapters, as well as bulk substrate materials. Samples with no post-deposition heat treatment are labelled as-deposited (AD). All coatings are deposited via IBS unless labelled otherwise. The listed alumina loss is from the 500 nm thick coating, as this is closer to layer thicknesses used in multilayer coatings (compared to 2 µm).

Coating	Heat treatment (°C)	Mechanical loss angle, $\phi \times 10^{-4}$		
		10 K	20 K	123 K
SiO_2	AD	8.8	9.8	11.4
	300	10.4	11.3	7.4
	450	8.5	9.2	4.1
	600	5.3	6.3	0.3
	800	5.9	7.2	0.2
	950	6.8	9.8	0.3
RLVIP SiO_2	AD	4.3	4.5	1.1
Al_2O_3	AD	4.1	4.0	7.1
	300	3.8	3.7	5.5
	400	3.8	3.8	5.5
	600	3.6	3.6	5.0
	800	3.7	3.6	5.4
SiO_2	Bulk [302]	7.1	10	8.2
Al_2O_3	Bulk [379]	0.00005	0.000067	0.00067
c-Si	Bulk [380]	0.00005	0.00004	0.0001

Table 7.2 Mechanical loss of high refractive index coatings characterised in Chapter 6, as well as other coating materials of interest. Samples with no post-deposition heat treatment are labelled as-deposited (AD). All coatings are deposited via IBS unless labelled otherwise.

Coating	Heat treatment (°C)	Mechanical loss angle, $\phi \times 10^{-4}$		
		10 K	20 K	123 K
Ta_2O_5	AD [359]	6.3	7.4	8.75
	300 [256]	4.9	5.4	4.0
	500 [359]	4.5	5.4	5.25
	600 [256]	7.6	10.2	4.86
	800 [256]	11.1	17.5	28.4
14% Ti:Ta_2O_5	AD [280]	3.9	4.25	3.7
	400 [229]	3.5	4.2	4.0
52% Ti:Ta_2O_5	AD [280]	4.2	4.3	3.4
	600 [229]	3.85	5.26	3.5
68% Ti:Ta_2O_5	AD [359]	6.5	6.88	7.8
	500 [359]	0.14	0.32	1.1
	600	0.11	0.34	1.29
TiO_2	AD [359]	6.0	7.5	9.5
	150	6.0	6.15	6.5
	300	1.75	1.47	2.45
34.5% Zr:Ta_2O_5	AD	6.0	6.1	5.66
	600	6.05	9.3	5.9
	800	6.46	11.4	7.34
RLVIP Ta_2O_5	AD	8.1	9.6	10.9
DCM Ta_2O_5	AD	4.5	5.2	4.3
HT dep Ta_2O_5	300	4.7	6.3	6.1
a-Si	AD [259]	0.74	0.93	1.50
	300 [259]	0.57	0.7	1.1
	450 [259]	0.54	0.68	0.75
RLVIP a-Si	AD	0.15	0.18	0.55

Table 7.3 Refractive index (n), Young's modulus (Y), and Poisson's ratio (ν) for materials listed in tables 7.1 and 7.2. Refractive indices are with respect to 1550 nm wavelength laser light. Values without citations are assumptions, and all properties are assumed to remain unchanged with respect to temperature.

Coating	n	Y (GPa)	ν
SiO_2	1.45[326]	72[296]	0.17[296]
RLVIP SiO_2	1.45	72	0.17
Al_2O_3	1.62[381]	200	0.24
Ta_2O_5	2.2[326]	140 [382]	0.23[40]
14% Ti:Ta_2O_5	2.2	140	0.23
52% Ti:Ta_2O_5	2.2	140	0.23
68% Ti:Ta_2O_5	2.2	140	0.23
TiO_2	2.43 [381]	151 [358]	0.27[358]
34.5% Zr:Ta_2O_5	2.25 [383]	130[374]	0.23
RLVIP Ta_2O_5	2.2	140	0.23
DCM Ta_2O_5	2.2	140	0.23
HT dep Ta_2O_5	2.2	140	0.23
a-Si	3.5[326]	147[280]	0.22 [384]
RLVIP a-Si	3.5	147	0.22
Bulk Al_2O_3	1.746[385]	400 [386]	0.24[40]
Bulk SiO_2	1.444[387, 388]	72 [386]	0.17 [386]
Bulk c-Si	3.453[40]	166 [276]	0.22[40]

where n_s is the refractive index of the substrate, n_m is the refractive index of the medium through which the laser beam travels en route to the first coating layer, and $y = (n_H/n_L)^{2N}$, where n_H and n_L are the refractive indices of the high and low index coating materials, respectively. The reflectivity of a coating stack with an odd number of layers, $2N+1$, is given instead by [389]:

$$R_{2N+1} = \left(\frac{n_H^2 y - n_m n_s}{n_H^2 y + n_m n_s} \right)^2 . \tag{7.4}$$

Thermal noise is proportional to the coating thickness, so it is valuable to create coating stacks with as few layers as possible. It is clear from equations 7.3 and 7.4 that more coating layers or a larger difference in refractive index between the coating materials increases the stack reflectivity. The coating thickness and thermal noise can therefore be reduced by using coating materials with a large difference in refractive indices. This also means, for example, that a potential replacement high index coating material with improved mechanical loss may not provide a thermal noise benefit if its refractive index is lower than 25% Ti:Ta_2O_5, thus requiring more layers to achieve the same reflectivity.

The designs for aLIGO and Advanced Virgo end test mass (ETM) mirrors* required reflectivity of 99.9995%, or 5 ppm transmission ($T = 1 - R$) [16, 167]. This is also the requirement for the ETM within the proposed Einstein Telescope (ET) [40], so all of the coatings presented in this chapter are constructed such that the maximum transmission is 5 ppm.

The reflectivity of multi-material coatings, which will be discussed in section 7.4, were calculated using *TFCalc* software made for designing and manufacturing optical thin-film coatings [390]. These coating stacks are also constructed such that the total reflectivity is 99.9995%.

7.3 Dual-material coatings

As discussed in section 7.2.1, highly reflective mirror coatings are comprised of $\lambda/4$ thick coating layers alternating between high and low refractive index materials. Each pair of high and low index coatings is known as a bilayer, a number of which are

*The ETM are at the end of the detector arms, as opposed to the input test masses (ITM), which are the mirrors through which light is injected into the Fabry-Perot cavities formed between the ITM and ETM in each arm. The ITM therefore require higher coatings transmission so that laser light can enter and exit the cavity arms, meaning the ETM will have a greater coating thickness to achieve a higher reflectivity.

stacked to provide the required reflectivity. The Brownian thermal noise of a coating stack increases with each bilayer, so reducing coating thickness without sacrificing reflectivity is one path towards an improved coating design. A coating material found to have exceedingly low mechanical loss–or excellent agreement with the substrate's Young's modulus–may fail to reduce the thermal noise contribution from the stack if it requires too many added bilayers to reach the required reflectivity. The current standard by which a potential multilayer, dual-material coating stack will be compared is the aLIGO/Advanced Virgo* IBS SiO_2 - 25% Ti:Ta_2O_5 coating stack.

Thirty-eight total coating layers of SiO_2 and 25% Ti:Ta_2O_5 are required to achieve the required design reflectivity of 99.9995% at $\lambda = 1064\,\text{nm}$ for a fused silica substrate. The coating stack is comprised of 18 bilayers plus a $\lambda/2$ thick SiO_2 cap layer and an extra $\lambda/4$ 25% Ti:Ta_2O_5 layer between the substrate and bilayers to maintain alternating refractive indices with the silica substrate, resulting in a total thickness of $\sim$6 µm. It should be noted that the actual thickness of the coating layers used for aLIGO are slightly larger (0.27λ) for the low n silica layers and slightly smaller (0.23λ) for the high n 25% Ti:Ta_2O_5 layers† [16]. This both reduces coating thermal noise and increases reflectivity at 532 nm, which is the wavelength of the laser used to lock the interferometer.

Using the same coating materials at cryogenic temperatures requires a slight redesign due to the increased operating wavelength and a crystalline silicon substrate rather than fused silica. The increased refractive index of tantala at $\lambda = 1550\,\text{nm}$ (2.2 rather than 2.065 [16, 326]) results in fewer bilayers required to achieve the same reflectivity, but the longer wavelength means there is still a net increase in coating thickness. The total thickness of the coating is 7.185 µm, of which 4.543 µm is silica and 2.642 µm is titania doped tantalum pentoxide; this corresponds to 15 bilayers plus a $\lambda/2$ silica cap layer.

Figure 7.1 shows the estimation of coating Brownian noise at 10, 20, and 123 K for this coating design based on the mechanical loss and elastic property values given in section 7.2. The actual aLIGO coating is heat-treated for ten hours at 500 °C [229], but there is no available data for the individual coating layers at these temperatures. Both sets of estimations in figure 7.1 use the 400 °C 14% Ti:Ta_2O_5 loss as an approximation for the 25% titania doped tantala. It is expected that a 600 °C heat treatment would increase the loss at 20 K based on low temperature loss peak trends seen with

*Both detectors utilise the same mirror coating stack, but from here forward this stack will be described as the 'aLIGO' coating for the sake of brevity.

†This optimisation was not performed for any of the coating designs shown in this chapter in order to provide direct comparison between all the coatings based on a standard model.

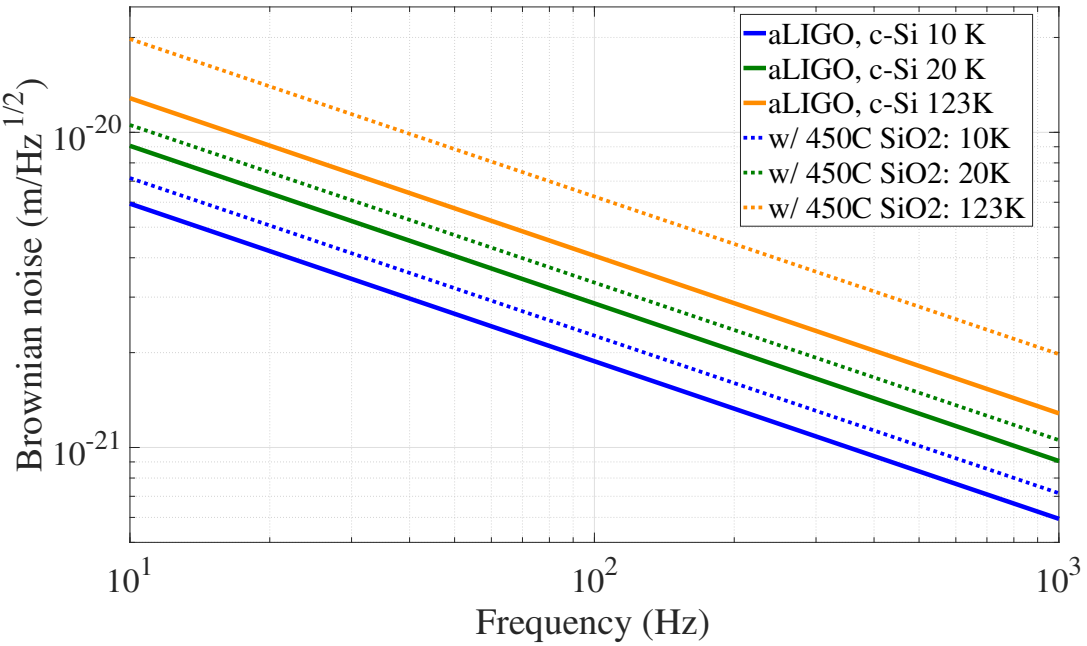

Fig. 7.1 Brownian thermal noise of aLIGO and Advanced Virgo coating at 10, 20, and 123 K. The estimated thermal noise of the same coating, but using the mechanical loss of IBS silica after a 450 °C heat-treatment (rather than 600 °C) is shown to both highlight the significance of loss on thermal noise and give an upper range of noise based on the coating stack heat-treatment of 500 °C.

pure Ta_2O_5 and 52% Ti:Ta_2O_5, thus slightly underestimating the 20 K thermal noise contribution of the tantala layer in figure 7.1. Similar changes are not expected at 10 or 123 K, where loss differences are less pronounced between these heat treatment temperatures.

The solid lines in 7.1 are calculated with the loss of SiO_2 heat-treated at 600 °C and the dashed lines with the loss of silica after a 450 °C heat treatment. The dashed lines are given as a reference to show a pessimistic estimation of the aLIGO coating noise at low temperatures, illustrating the effect of increased loss on coating thermal noise and showing silica's limitations as a coating material. The solid lines (600 °C SiO_2) are used as the aLIGO comparison for the rest of this chapter to provide an estimation at the low end of the uncertainty with which to compare alternative coating stacks. Justification for replacing the current coating stack requires a significant reduction in estimated thermal noise because of the difficulties and costs associated with altering the current, proven coating chamber [391]. An optimistic baseline thermal noise is therefore used so that any potential improvements shown in sections 7.3.1 and 7.4.1 will hold greater weight.

It should be noted that the loss of the aLIGO coating stack was measured at low temperature and found to have mechanical loss at 10, 20, and 123 K of about 7.5×10^{-4}, 8.8×10^{-4}, and 4.0×10^{-4}, respectively [229, 231]. The estimated thermal noise from these measurements was not used for comparison because this coating was designed for reflecting 1064 nm laser light, with optimised layer thicknesses deviating from $\lambda/4$. All of the coating stack designs presented in the following sections are constructed with exactly $\lambda/4$ thick coating layers stacked to reflect 1550 nm wavelength light and, as such, are compared to the estimated noise shown in figure 7.1.

7.3.1 Dual-material coating stack alternatives

As discussed in sections 7.2 and 7.2.1, a coating stack design's thermal noise is dependent on a combination of the relative mechanical losses, refractive indices, and elastic properties. Coating materials that have low mechanical loss may fail to provide thermal noise benefits because of a need to increase the number of bilayers to achieve 5 ppm transmission. Table 7.4 shows the thicknesses required to reach this reflectivity. The refractive indices of all coating materials are assumed to remain the same with heat treatment, and the refractive index of the titania doped tantala is also assumed to remain constant with increased doping percentages*. RLVIP coating materials are assumed to have the same refractive index as their IBS counterparts, so the thickness of an RLVIP coating stack is the same thickness as an IBS stack of the same materials. Table 7.4 gives the coating stack design for all of the thermal noise estimates in figures 7.2, 7.3, and 7.4.

Table 7.5 gives the heat-treatments used for each material within the coating stack designs (the losses for each material at the given heat treatments can be found in tables 7.1 and 7.2). A heat treatment temperature of 600 °C was chosen when possible, which is the ideal heat treatment of IBS SiO_2 for low temperature mechanical loss. The absorption of IBS amorphous silicon improves for heat treatments up to 450 °C, after which the absorption worsens [392], so a heat-treatment temperature of 450 °C was used for multilayers containing IBS aSi. A 300 °C anneal is used for coating stacks containingTiO_2, corresponding to minimum measured loss (shown in section 6.2.3). However, this is above the literature crystallisation temperature [353, 366], and checks on the crystallinity and optical scattering from such coatings would be required.

Two versions of the RLVIP SiO_2 and aSi are given in table 7.5; there is only measured loss data for the coatings as-deposited, but a second, theoretical coating

*This could result in the noise being overstated for the 68% Ti:Ta_2O_5 because it may need fewer bilayers than stated in table 7.4 if the refractive index is closer to that of titania than tantala.

Table 7.4 Coating thicknesses required to reach reflectivity requirement of 99.9995%. Refractive indices used for the thickness calculations can be found in table 7.3. The same thicknesses were used for all titania doping percentages, and RLVIP coatings were constructed with the same thicknesses as the IBS SiO_2 - aSi coating. All coatings have a $\lambda/2$ thick cap layer of the low index coating material.

Coating (low n - high n)	Bilayers	Thickness, μm		
		low n	high n	total
Al_2O_3 - Ta_2O_5	21	5.502	3.699	9.201
Al_2O_3 - aSi	8	2.392	0.886	3.278
Al_2O_3 - TiO2	16	4.306	2.551	6.857
SiO_2 - Ta_2O_5	15	4.543	2.642	7.185
SiO_2 - aSi	7	2.405	0.775	3.180
SiO_2 - TiO_2	12	3.741	1.914	5.655

Table 7.5 Summary of the coating heat treatments used for Brownian thermal noise estimation. Coatings are deposited via IBS unless otherwise stated. As-deposited coatings are listed as 'AD'. The idealised RLVIP coating uses theoretical losses for noise calculations; the temperatures given for the (HT) version of the coating match those assumed during speculation. The mechanical losses of all listed coatings/heat-treatments can be found in tables 7.1 and 7.2.

Coating	HT temp (°C)	Coating	HT temp (°C)
Al_2O_3 - aSi	400 - 450	SiO_2 - aSi	450 - 450
Al_2O_3 - TiO2	300 - 300	SiO_2 - TiO_2	300 - 300
Al_2O_3 - 14% Ti:Ta_2O_5	600 - 400	SiO_2 - 14% Ti:Ta_2O_5	600 - 400
Al_2O_3 - 68% Ti:Ta_2O_5	600 - 600	SiO_2 - 68% Ti:Ta_2O_5	600 - 600
RLVIP: SiO_2 - aSi	AD - AD	HT RLVIP: SiO_2 - aSi	600 - 600

stack is proposed based on potential changes in loss with heat-treatment, motivated by changes observed with heat treatment in IBS SiO_2. This coating stack is the same thickness as the as-deposited RLVIP multilayer coating, but the mechanical loss of the silica layers is assumed to have reduced by ∼30%, the same amount of loss reduction seen in IBS SiO_2 between heat-treatment at 450 °C and 600 °C. This heat treatment temperature would not be possible with IBS aSi because of the increased absorption [392], but a significant advantage of the RLVIP aSi over IBS aSi is that the coating's absorption remains at a minimum value after heat-treatment at temperatures above 450 °C [377]. This would allow for a heat treatment of 600 °C for coatings with RLVIP aSi, and, therefore, a potential reduction in Brownian noise through the loss decrease following a 'heat-treatment' of the RLVIP SiO_2. This, of course, assumes that the RLVIP aSi loss has negligible change in mechanical loss with heat-treatment and is taken as an ideal outcome of the continued investigation into this new coating deposition method*.

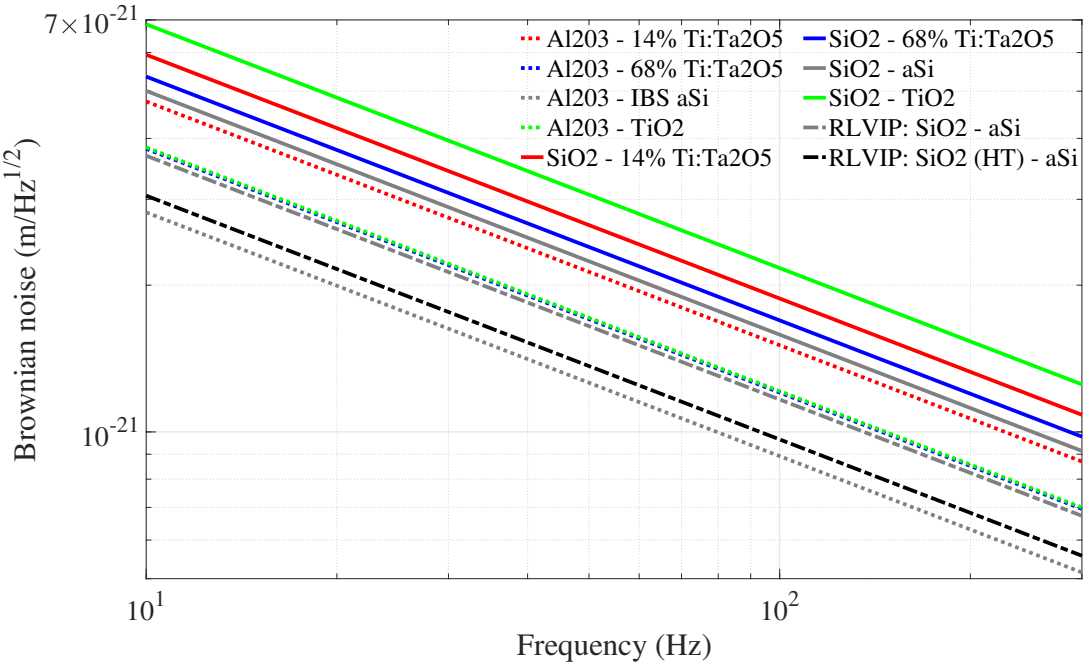

Fig. 7.2 Brownian coating noise estimates of ten dual-material, multilayer coating stacks for a gravitational wave detector operating at 10 K. The solid red line corresponds to the noise estimate of the aLIGO and Advanced Virgo coating stack and is used for evaluating the relative change in noise of the other coating stacks. It should be noted that the noise of Al_2O_3 - TiO_2 is effectively identical to that of the Al_2O_3 - 68% $Ti:Ta_2O_5$, so the lines are overlapping and difficult to distinguish.

*For more information on the losses of RLVIP SiO_2 and aSi see sections 4.5 and 6.3.2, respectively

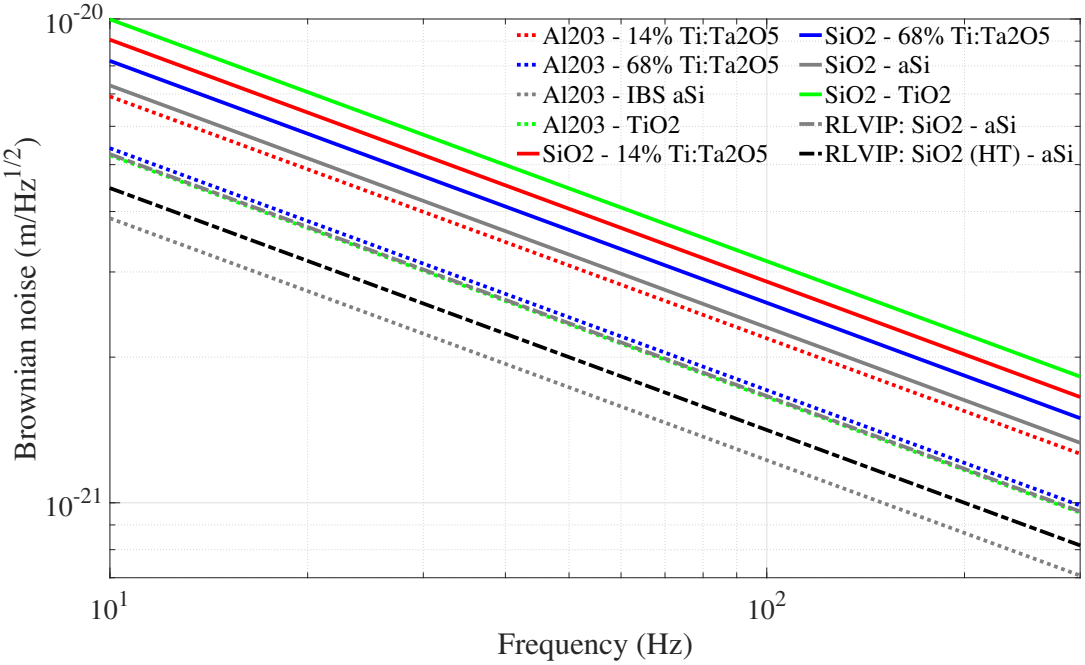

Fig. 7.3 Brownian coating noise estimates of ten dual-material, multilayer coating stacks for a gravitational wave detector operating at 20 K. The solid red line corresponds to the noise estimate of the aLIGO and Advanced Virgo coating stack and is used for evaluating the relative change in noise of the other coating stacks.

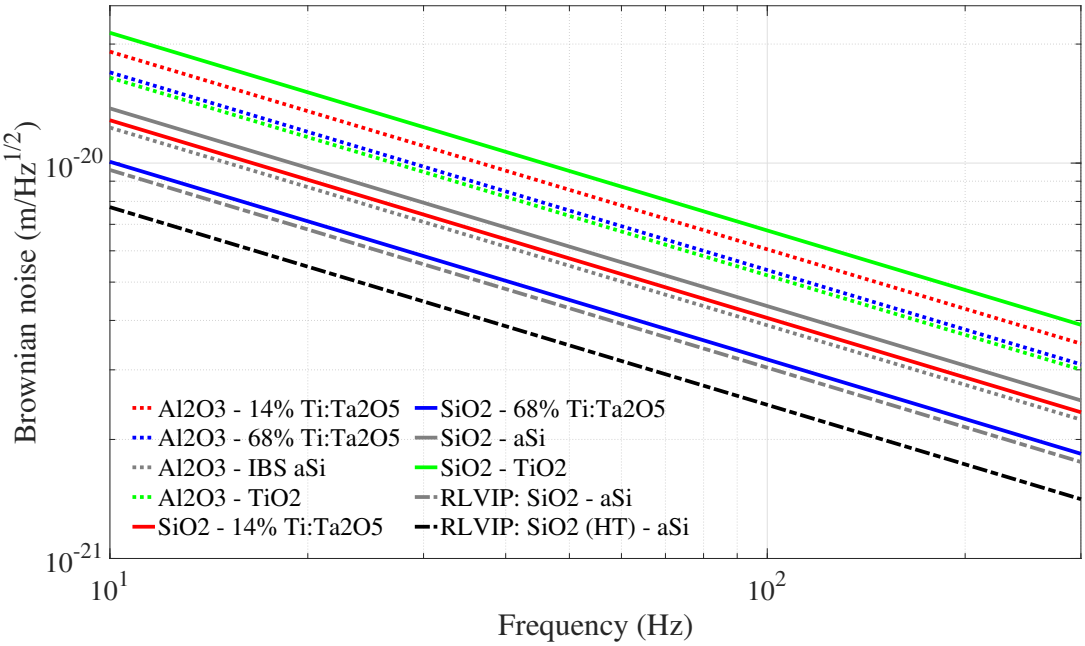

Fig. 7.4 Brownian coating noise estimates of ten dual-material, multilayer coating stacks for a gravitational wave detector operating at 123 K. The solid red line corresponds to the noise estimate of the aLIGO and Advanced Virgo coating stack and is used for evaluating the relative change in noise of the other coating stacks.

Table 7.6 Relative change in thermal noise of multilayer coatings compared to aLIGO coatings at 100 Hz. For example, a value of 0.10 would mean the coating displays 10% of the noise exhibited by the aLIGO coating. Smaller values, therefore, represent greater thermal noise improvement and values greater than 1 correspond to an increase in thermal noise. The aLIGO/Advanced Virgo coating exhibits noise at 100 Hz of about 1.9×10^{-21}, 2.9×10^{-21}, and 4.1×10^{-21} at 10, 20, and 123 K, respectively. Coatings are IBS unless specified otherwise.

Coating (low n - high n)	Thermal noise relative to aLIGO at 100 Hz		
	10 K	20 K	123 K
Al_2O_3 - aSi	0.47	0.42	0.96
Al_2O_3 - TiO2	0.64	0.58	1.28
Al_2O_3 - 14% Ti:Ta_2O_5	0.80	0.76	1.49
Al_2O_3 - 68% Ti:Ta_2O_5	0.64	0.60	1.32
SiO_2 - aSi	0.85	0.80	1.07
SiO_2 - TiO_2	1.15	1.10	1.67
SiO_2 - 14% Ti:Ta_2O_5	–	–	–
SiO_2 - 68% Ti:Ta_2O_5	0.90	0.91	0.79
RLVIP: SiO_2 - aSi	0.62	0.57	0.75
HT RLVIP: SiO_2 - aSi	0.52	0.49	0.60

Figures 7.2, 7.3, and 7.4 show estimated Brownian noise at operating temperatures of 10, 20, and 123 K, respectively, for the ten dual-material coating stacks given in table 7.5. Alumina-based multilayer coatings are represented by dotted lines, silica-based coatings by solid lines, and the RLVIP coating stacks by dot-dashed lines. The colour of each line corresponds to the high index material: green represents TiO_2, red 14% Ti:Ta_2O_5, blue 68% Ti:Ta_2O_5, and grey aSi (except the speculative RLVIP, which is black). The solid red line (labelled SiO_2 - 14% Ti:Ta_2O_5) is the aLIGO coating stack also shown in figure 7.1 and provides the primary comparison from which to judge the merits of a given multilayer coating. Table 7.6 gives the difference in Brownian noise at 100 Hz between all the coating combinations and the aLIGO for all three operating temperatures.

One clear result from these comparisons is the high potential of alumina as a replacement low index coating material. Even with the coating thickness increase accompanying a slightly higher refractive index than silica, alumina multilayer coatings exhibit significant improvement over the silica-based coatings at 10 and 20 K. This is due to the lack of a low temperature loss peak in IBS alumina and its Young's modulus providing a better match than IBS silica for the crystalline silicon substrate. Alumina's relatively high loss at 123 K, however, prohibits any gains to Brownian thermal noise

at this operation temperature. This is a trend with most of the alternate coating stacks; while eight out of nine possible coatings improved on the aLIGO Brownian thermal noise at 10 K, only four provided lower noise at 123 K. Unfortunately, most of the coatings with the lowest Brownian noise cannot currently be considered as viable alternatives to the SiO_2 - Ti:Ta_2O_5 multilayer due to issues with optical properties. As mentioned in section 6.2.2, the 68% Ti:Ta_2O_5 coating showed visible signs of crystallinity (even though there were no signs in the loss data), which may lead to significant issues with scatter; any heat-treated coatings containing TiO_2 could have a similar issue.

The RLVIP coatings, both real and speculative, provided the greatest reduction across all temperatures, with the Al_2O_3 - aSi multilayer displaying similarly low noise compared to the aLIGO coating. However, the optical requirements for detector coatings are stringent, with the multilayer coating on the aLIGO and Advanced Virgo ETM exhibiting absorption in the range of 0.2-0.5 ppm [16, 167]. With ion-plated SiO_2 - aSi multilayer coatings exhibiting absorption on the order of 1000 ppm [325], using dual-material multilayer coatings with low loss silicon is not currently feasible from an optical standpoint.

It should be noted, however, that significant steps in reducing the absorption of amorphous silicon through heat-treatment and novel deposition techniques have been achieved [393]. The absorption is also known to decrease at both low temperatures [392] and longer wavelengths (2 µm) [394], so the realisation of optically-suitable aSi coatings maybe possible in the near future. Another solution to gaining the loss benefits of aSi could be the use of 'multi-material' coatings rather than alternating stacks of just two materials.

7.4 Multimaterial coatings

A proposed solution for utilising low loss materials with high absorption, e.g. silicon, is to construct coating stacks with more than just two materials, where the vast majority of light is reflected within front bilayers of low absorption and only a small fraction is transmitted to a back set of bilayers containing the high absorption silicon [326, 332]. So-called 'multi-material' coatings could effectively reduce both the overall coating thickness and the amount of lossy high index materials used to reach 99.9995% reflectivity for the ETM mirrors. Figure 7.5 shows the design of a multi-material coating stack, which is comprised of a $\lambda/2$ SiO_2 cap layer, seven bilayers of $\lambda/4$ thick SiO_2 - Ti:Ta_2O_5, and four bilayers of $\lambda/4$ thick SiO_2 - aSi. The total coating thickness

is 5.150 µm, of which 3.474 µm is SiO_2, 1.233 µm is Ti:Ta_2O_5, and 0.443 µm is aSi. Figure 7.5 also shows the normalised electric field intensity (EFI) of a 1550 nm laser beam incident on the face of the coating, where it can be seen that only 0.34% of the laser light is transmitted to the highly absorptive amorphous silicon bilayers. The total optical absorption of a similar coating was predicted to be ∼5 ppm, but with the potential to reduce this number to about 1 ppm [326].

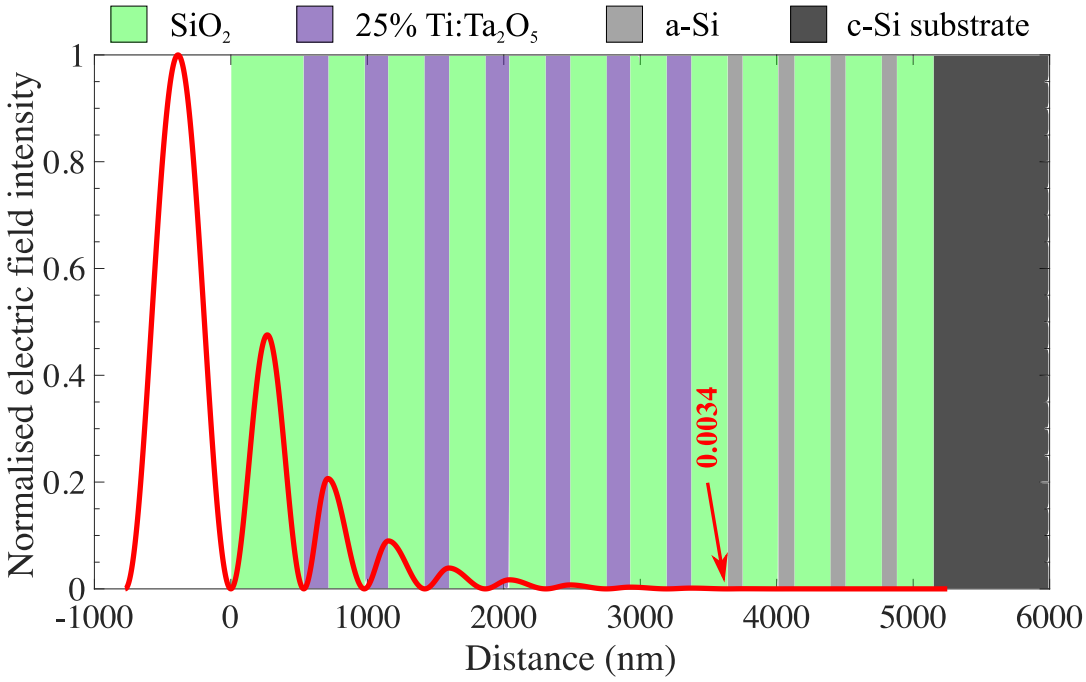

Fig. 7.5 Normalised electric field intensity through the thickness of a multi-material coating. A distance of zero corresponds to the front face of the coating. Width of the coloured areas are to scale and show all layers of the 99.9995% reflective, 5.150 µm thick coating stack.

The initial thermal noise estimates for the multi-material coating stack show a ∼25% reduction in Brownian thermal noise at potential cryogenic operating temperatures, but these calculations were performed assuming loss from 600 °C heat-treated silica [326]. The absorption of IBS amorphous silicon decreases with heat treatment up to 450 °C, after which it increases with continued heat treatment [377]. The coating stack would, therefore, require post-deposition heat treatment at 450 °C to minimise the absorption of the aSi layers, and the coating Brownian noise estimate needs updating to reflect the comparatively high loss of 450 °C heat-treated silica.

Figure 7.6 shows the coating Brownian thermal noise at 10, 20, and 123 K with updated silica loss (blue) and, for comparison, the noise if the loss of silica after

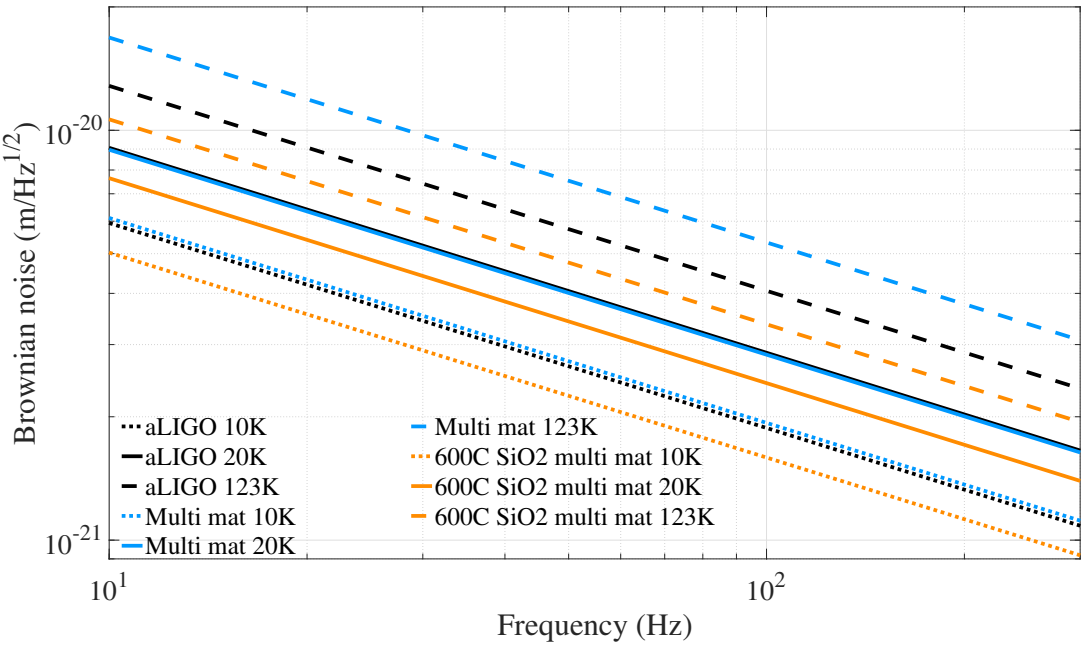

Fig. 7.6 Updated thermal noise estimation of multi-material coating design (based on losses following heat-treatment at 450 °C) compared to the aLIGO multilayer coating. The estimated noise of the same stack calculated with the loss of silica after heat-treatment at 600 °C is shown for comparison to emphasise the influence of annealing on coating Brownian noise, as well as to highlight the importance of extensive coating loss characterisation for accurate noise estimation. It should be noted that the black and blue solid lines representing noise at 20 K for the aLIGO and multi-material coating, respectively, overlap and may be difficult to distinguish.

a 600 °C heat-treatment were used instead*. The elevated loss of silica with the lower temperature anneal causes the thermal noise to increase significantly at all three operating temperatures, and the multi-material design is now slightly worse than the aLIGO coating at 10 K and much worse at 123 K. The noise performance is nearly identical to the aLIGO coating at 20 K, likely due to the dominance of the Ti:Ta_2O_5 loss peak at this temperature. The next section will investigate replacing layers in the multi-material design in an attempt to provide the thermal noise improvement originally estimated from the IBS silica - tantala - silica - silicon multi-material coating.

7.4.1 Multimaterial coating stack alternatives

The multi-material coatings considered here were designed in the same manner as the original IBS multilateral coating discussed in section 7.4. Bilayers of low absorption high and low index coating materials are stacked until at least 99.6495% reflectivity is achieved, at which point the light power is low enough for the absorption of aSi to be tolerable. Bilayers comprised of the same low index material paired with the low loss amorphous silicon are then added to reach the target reflectivity of at least 99.9995%.

The first proposed design is identical to the original stack, but with all of the materials deposited via RLVIP rather than IBS. The primary issue with the original design was the unfortunate, high loss of silica when heat treated at the temperature required to maintain somewhat reasonable absorption in the silicon layers. RLVIP silica as deposited has significantly lower loss at low temperatures than any heat treatment of IBS silica, thus providing a possible thermal noise improvement. Figure 7.7 shows the estimated Brownian noise of this coating stack, where it can be seen to provide about a 15-20% reduction in thermal noise at 10 and 20 K compared to the aLIGO coating but a ∼15% increase at 123 K. The noise of the coating stack at the lower temperatures is dominated by the high mechanical loss of the tantala layers, which, as shown in section 6.3.3, is significantly higher than even un-doped IBS Ta_2O_5 and prohibits the lower losses of the silica and silicon from providing a larger decrease in noise. The loss of RLVIP silica at 123 K is higher than that of IBS, hence the multi-material's poor performance at this temperature.

Figure 7.7 includes another RLVIP multi-material coating. Labelled 'ideal', this has the same thickness and design as the other RLVIP coating but is given as a speculative ideal RLVIP coating stack. The same '600 °C heat-treatment' silica loss

*The same 14% Ti:Ta_2O_5 coating loss used to approximate the 25% doped tantala in the aLIGO coating is used for these estimates. It should be noted that pure tantalum pentoxide is used for noise estimates in [326].

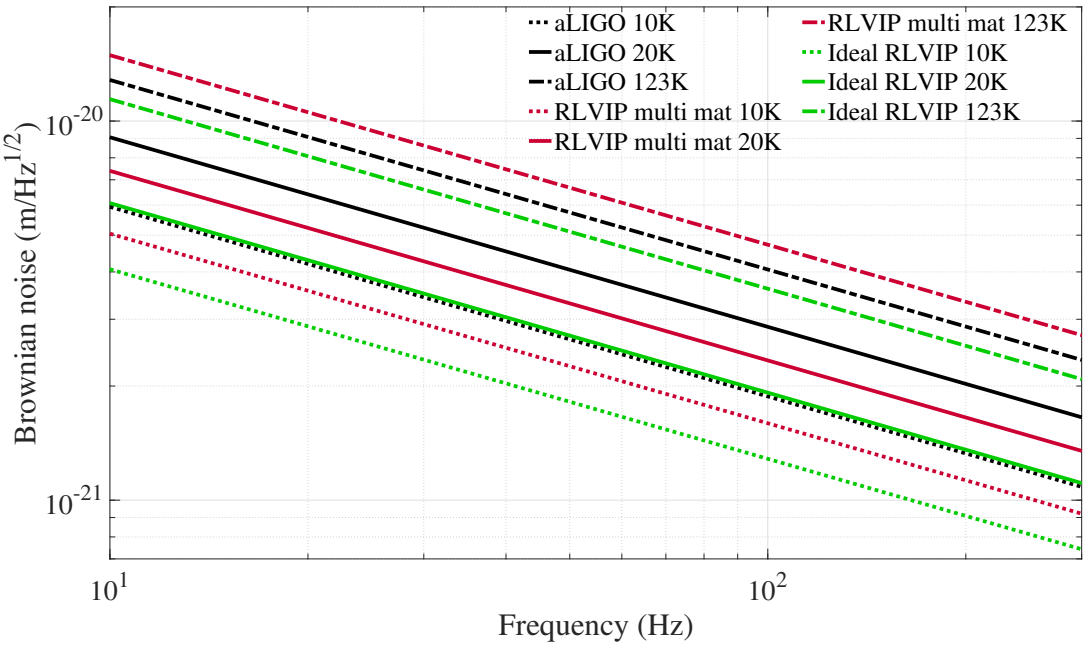

Fig. 7.7 Estimated Brownian thermal noise of an all RLVIP multi-material coating design compared to the aLIGO multilayer coating. An idealised coating with potential future loss reductions is shown as well.

reduction and silicon absorption plateau discussed in section 7.3.1 is applied here, as well as the assumption that the aSi loss will remain at a similar, low level with this heat-treatment temperature. In this multi-material case, the tantala loss would negate any benefit of even lower silica loss, so the idealised case assumes a 40% reduction in RLVIP tantala loss consistent with that seen in IBS tantala with titania doping*. This ideal RLVIP coating doubles the thermal noise reductions seen at 10 and 20 K with the as-deposited RLVIP multi-material coating, and it provides a ∼10% decrease in Brownian noise at 123 K compared to the aLIGO coating rather than the net increase displayed with the un-annealed, pure tantala RLVIP multi-material.

This speculative coating provides significant thermal noise improvement across all operation temperatures, but the largest relative reduction in coating Brownian noise can be seen in figure 7.9 at 20 K. Figure 7.9 shows the noise of an alumina-based multi-material coating design, the specifics of which are given in figure 7.8. Due to the higher index of alumina compared to silica, this coating requires an additional three bilayers in front of the silicon bilayers to achieve the 99.6495% reflectivity required in the front stack. Even with the added 900 nm of total thickness, this coating provides about a 30% reduction in coating Brownian noise at 10 K and ∼40% at 20 K. The elevated mechanical loss of alumina at 123 K results in this coating

*An example of this loss reduction can be seen in figure 6.8.

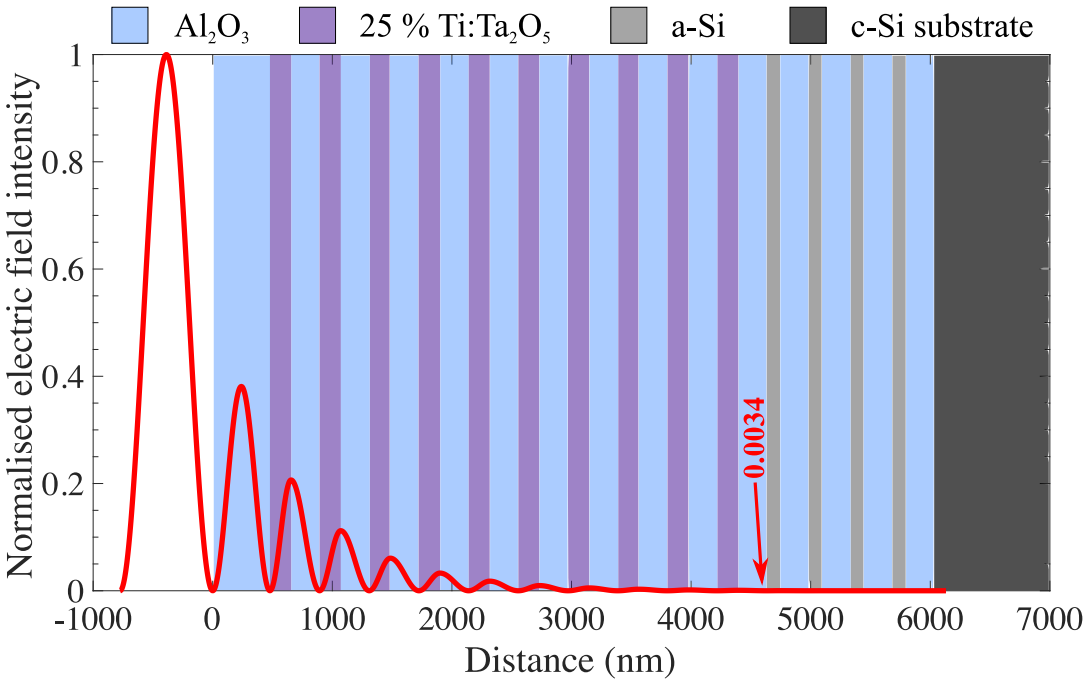

Fig. 7.8 Normalised electric field intensity through the thickness of an Al_2O_3-based, IBS multi-material coating. A distance of zero corresponds to the front face of the coating. Width of the coloured areas are to scale and show all layers of the 99.9995% reflective, 6.031 µm thick coating stack, of which 3.827 µm is Al_2O_3, 1.761 µm is $Ti:Ta_2O_5$, and 0.443 µm is aSi.

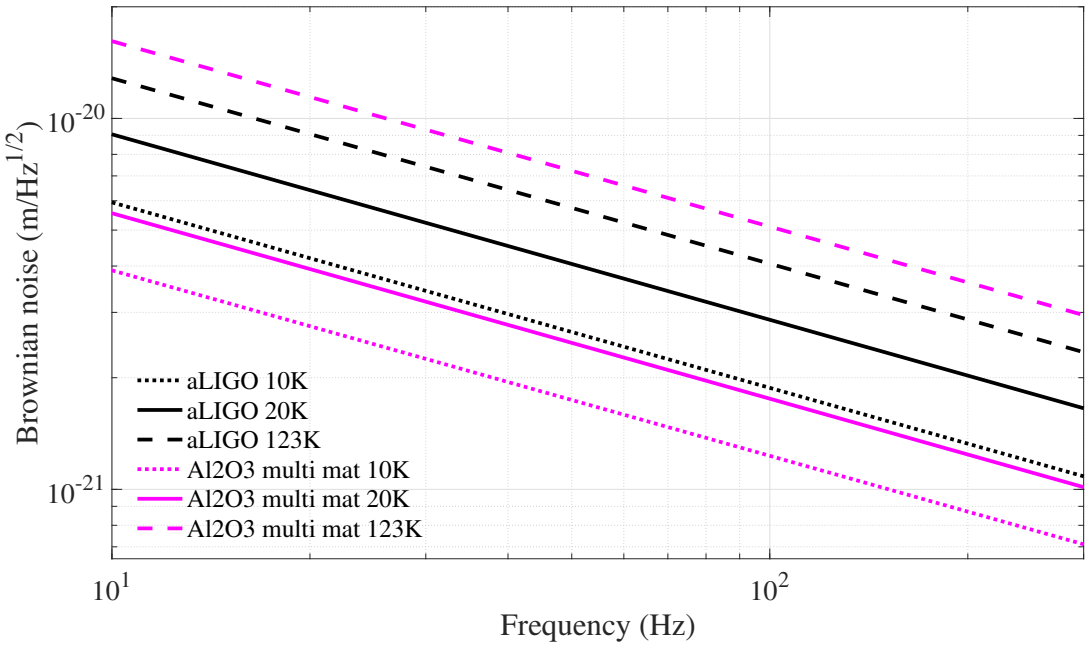

Fig. 7.9 Estimated Brownian thermal noise of an IBS Al_2O_3-based multi-material coating stack compared to the aLIGO multilayer coating. The losses correspond to heat treatments of 400 °C for the alumina, 400 °C for the titania-doped tanatala, and 450 °C for the amorphous silicon.

Table 7.7 Relative change in thermal noise of multi-material coatings compared to aLIGO coatings at 100 Hz. For example, a value of 0.10 would mean the coating displays 10% of the noise exhibited by the aLIGO coating. Smaller values, therefore, represent greater thermal noise improvement and values greater than 1 correspond to an increase in thermal noise. The aLIGO/Advanced Virgo coating exhibits noise at 100 Hz of 1.9×10^{-21}, 2.9×10^{-21}, and 4.1×10^{-21} at 10, 20, and 123 K, respectively. Coatings are IBS unless specified otherwise

Coating (low n - high n - high n)	Thermal noise relative to aLIGO at 100 Hz		
	10 K	20 K	123 K
SiO_2 - 14% Ti:Ta_2O_5 - aSi	1.03	0.99	1.31
Al_2O_3 - 14% Ti:Ta_2O_5 - aSi	0.65	0.61	1.26
RLVIP: SiO_2 - Ta_2O_5 - aSi	0.85	0.82	1.16
RLVIP: SiO_2 - Ta_2O_5 - aSi (idealised)	0.69	0.67	0.89

being unsuitable for a detector run at that temperature, but the thermal noise benefits of this alumina-based multimaterial design are significant for the lower operating temperatures. It should be noted that while the absorption of Al_2O_3 is unknown at 1550 nm, preliminary measurements at 1064 nm show absorption on par with tantalum pentoxide [395]. Table 7.7 gives a summary of the noise relative to aLIGO for all of the multi-material coatings, where the theoretical RLVIP coating shows promise for all operating temperatures, but the alumina-based stack shows better thermal noise improvement and is made without any assumptions regarding heat treatment or mechanical loss.

7.5 Conclusion

The SiO_2 - 25% Ti:Ta_2O_5 multilayer coating in use within aLIGO and Advanced Virgo will soon be the primary limiting noise source in the most sensitive frequency band of ground-based interferometric gravitational wave detectors, and the switch to cryogenic operation temperatures for next-generation detectors provides an even greater need to improve the thermal noise performance of the highly reflective test-mass coatings. Thermal noise estimates of a number of dual material multilayer coatings produce no clear replacement for the high index, 25% titania-doped tantala layer, as any significant gains in noise performance, such as the reduction seen with amorphous silicon and 68% Ti:Ta_2O_5, are accompanied by potentially prohibitive optical performance, namely absorption and scatter.

A multi-material coating design has been proposed as a way to glean the loss benefits from high absorption materials. The initially proposed design of IBS silica - tantala - silica - silicon used silica loss values obtained following 600 °C heat-treatment (the only data available at the time of the publication), when the coating would ideally be heat-treated at 450 °C to minimise the absorption of the aSi layers. The work in this thesis has been used to update the thermal noise performance for this design using loss measurements of silica heat-treated at 450 °C. The loss of silica was significantly higher than expected at this heat-treatment, and was found to negate the benefits of including aSi in the coating.

Al_2O_3 shows significant promise as a potential replacement for silica as the low index coating layer in both two-material and multi-material mirror coatings for detectors operating at 10 or 20 K. Keeping the same titania-doped tantala layers but replacing silica with alumina results in a 20% and 24% reduction in thermal noise at these operating temperatures, respectively, for a multilayer dual-material coating. A potential 35% and 39% reduction in noise (compared to the aLIGO stack) could be achieved by replacing the lossy silica layers in a 450 °C heat-treated multi-material stack with alumina. Initial optical investigations of alumina are promising, but further research into absorption and scatter is crucial. It should be noted that the absorption of aSi is currently being reduced, which would result in greater transmission tolerance from the front, lossy bilayers of a multi-material stack and increase significantly the thermal noise gains from a multi-material design. Alumina multi-material coatings would see an even greater decrease in noise than silica-based designs because they are limited by the high loss tantala coating layers, the number of which would be reduced in this case.

Replacing IBS with RLVIP deposition in both two-material and multi-material coating designs is also shown to be a promising option for reducing coating thermal noise. While RLVIP aSi suffers from the same high absorption as IBS, the ability of the coating to maintain minimum absorption after heat treatment at temperatures above 450 °C gives it a significant advantage over amorphous silicon deposited by IBS. RLVIP Ta_2O_2 currently limits the noise improvements in multi-material applications, but speculative reduction in losses in the silica and tantala layers through heat treatment and titania doping, respectively, produces the best coating in terms of reducing coating thermal noise at all three potential cryogenic operating temperatures. This 'ideal' coating produces 31%, 33%, and 11% reductions to coating Brownian noise compared to the aLIGO stack at 10, 20, and 123 K. Similar to the proposed alumina multi-material design, this all RLVIP multi-material coating would see significant, further reduction in thermal noise contribution if the absorption of aSi was reduced and

multiple bilayers of the tantala-based front stack were then removed. Further work is required to accurately characterise the loss of these coatings after heat treatment, as well as to investigate the potential of RVIP titania-doped tantala.

It should be noted that many other material combinations are possible as alternative dual or multi-material coating stacks, with materials such as silicon nitride showing very low cryogenic mechanical loss and reasonable absorption [396, 397]. Here, analysis has been restricted to materials studied in this thesis, but it should be noted that these presented materials may find even greater application when used in conjunction with other promising coatings which are under development.

Chapter 8

Conclusions

The first direct detection of gravitational waves occurred in September of 2015, when a signal (denoted GW150914) from a binary black hole merger was observed by the aLIGO detectors. Five other confirmed gravitational wave signals have been detected since then, ushering in a new era of gravitational wave astronomy. These detections occurred because of decades of research into improving the sensitivity limits of ground-based, interferometric gravitational wave detectors, two of which (aLIGO and Advanced Virgo) are successfully operating close to design sensitivity as second generation detectors having been upgraded to lower the noise from a number of sources limiting detection range. It is expected that further increases to detector sensitivity would provide not only more frequent measurements of black hole and binary star inspiral/mergers but also possible measurement of other, new sources, e.g. supernovae or stochastic background gravitational waves.

The current limiting noise sources within the detectors' most sensitive frequency band are quantum noise and coating thermal noise. Advances in quantum noise mitigation techniques, i.e squeezing, mean that Brownian noise from thermal energy within the highly reflective multilayer test mass mirror coatings will be the primary limiting noise source for current and future generations of gravitational wave detectors at their most sensitive frequencies ($\sim$100 Hz). Reducing the coating thermal noise is, therefore, required in order to continue improving the detection range. Proposed third generation detectors such as ET or LIGO Voyager are designed to operate at cryogenic temperatures* in order to decrease the available thermal energy. However, coating thermal noise is also dependent on the mechanical loss of the coating materials, so lowering coating mechanical loss is required for improving detector sensitivity and gaining the thermal noise benefits of cryogenic operating temperatures. Measuring the

*As is the current Japanese detector, KAGRA

mechanical loss of a number of coating materials across a wide range of temperatures is, therefore, a crucial step in improving coating thermal noise, as is furthering our understanding of the connection between mechanical loss and coating structure, which leads to more informed decisions regarding which coatings to research in future experiments with the goal of finding ideal coatings for reduced thermal noise.

The loss of IBS silica was measured as-deposited and after heat treatments of 300 °C, 450 °C, 600 °C, 800 °C, and 950 °C. The loss transitioned from a wide, poorly defined peak centred at ∼85 K to a narrow, well-defined loss peak centred at ∼33 K; the minimum loss across all measured temperatures was observed after a 600 °C heat treatment. This contrasts the trend of silica loss at room temperature, which displays a minimum loss after a 950 °C heat treatment, but fits within overall trend of IBS SiO_2 loss tending towards bulk silica loss with continued annealing. No trend was observed in the activation energy associated with the low-temperature loss peak in the coating with heat treatment; all heat treatments agreed within uncertainty to a value of about 50 meV, which agrees with the literature values for fused silica but not with previous measurements of IBS silica. The stress was found to decrease with continued heat treatment, with the stress in a previous IBS silica coating matching the equivalent heat treatment from this study and the stress within RLVIP silica agreeing with the trend if taken to be heat-treated at its deposition temperature of 250 °C. The loss of RLVIP silica was measured and found to have lower loss than any IBS heat treatment at temperatures below 40 K, with an activation energy of 46.6 ± 5.8 meV (well within agreement with IBS). It is possible that the elevated deposition temperature of RLVIP is the cause of this reduced loss, with the as-deposited RLVIP silica displaying a similar barrier height distribution to 450 °C heat-treated IBS SiO_2 but with fewer barriers at all potential energies, i.e. fewer two-level systems.

The presented loss characterisation of IBS and RLVIP SiO_2 gives a more thorough understanding of the link between room and low temperature coating loss with respect to thermally-induced structural changes, and it may provide a significant improvement to computational modelling of amorphous coatings. Further investigation into the changes in loss with heat treatment of RLVIP are valuable for evaluating its use as a lower loss replacement to IBS for low temperatures, as well as for observing its change in structure compared to IBS SiO_2. Measurement of IBS SiO_2 deposited at an elevated temperature is also an important future experiment to test the hypothesis that RLVIP SiO_2 displays low loss due to an elevated deposition temperature.

Alumina was investigated as a potential low index replacement material, with 505 nm and 2.02 µm thick coatings measured as-deposited and after heat treatment at 300 °C, 400 °C, 600 °C, and 800 °C. Both thicknesses experienced a reduction in

loss above 60 K after the 300 °C anneal and then comparatively little change after all further heat treatments. The loss remained consistent below ∼50 K for all heat treatments of both coating thicknesses. The change stress with heat treatment was roughly consistent between the two thicknesses, with the 2.02 µm coating going from 461 ± 35 GPa of compressive stress to 147 ± 10 GPa of tensile, and the 505 nm coating changing from 504 ± 35 GPa compressive to 210 ± 13 GPa tensile. The large change in stress with heat treatment with seemingly little to no effect on the loss contrasts with the correlation observed with amorphous silica. An increasing difference in loss between the two coating thicknesses with heat treatment was observed and attributed, potentially, to a thickness-dependent changing of Young's modulus with annealing temperature. Measuring the Young's modulus of the IBS alumina samples is a crucial follow up experiment to both test this thickness dependence hypothesis and eliminate the systematic uncertainty in mechanical loss from an assumed, constant value of 200 GPa. The loss of alumina makes it very promising for use as a low index material in multilayer coatings; after heat treatment at 600 °C alumina has a loss of 3.6×10^{-4}, roughly 60% lower than IBS silica.

A number of high refractive index coating materials were investigated. Undoped IBS tantala deposited at an elevated temperature (300 °C) and then heat treated at 300 °C was found to exhibit higher loss above 20 K than tantala deposited at the standard temperature (∼100 °C) and then heat treated at 300 °C. This measurement was motivated by the hypothesis that elevated deposition temperatures are more effective at reaching a so-called 'ideal glass' state with significantly reduced two-level systems, but, unlike the RLVIP SiO_2 results, the elevated temperature IBS Ta_2O_5 did not exhibit lower mechanical loss. The low temperature peak, however, was found to closely match the shape of the peak from 'standard' IBS Ta_2O_5 heat treated to 500 °C. This could be further evidence that thermal energy applied during deposition alters coating structure in a different manner to the same magnitude of thermal energy applied post-deposition, even when not trended towards an ideal glass state.

DC magnetron Ta_2O_5 was measured as-deposited and found to have lower loss than that of IBS tantala but with a prohibitively high absorption of 85 ppm. The loss of RLVIP tantala was characterised and found to have loss about 50% greater than as-deposited IBS tantala and almost 200% greater than IBS tantala heat treated at 300 °C. The changes in RLVIP Ta_2O_5 loss with heat treatment is still of interest with regards to its use in an all RLVIP multi-material coating, so further measurements should be performed. Measuring coating stress and calculating the activation energies of the low temperature peaks from tantala deposited by all the different coating techniques is a

valuable next step in searching for correlation between coating structure, mechanical loss, and deposition parameters.

Increasing the titania doping percentage to 68% was found to potentially reduce coating loss by over an order of magnitude at temperatures below 200 K after heat treatment at 600 °C. This confirms previous research of the material and provides an interesting example of non-linear change in loss with doping percentage. There is uncertainty surrounding the homogeneity and optical properties of this coating, so further work is required to evaluate its validity as a potential low loss, high index coating material. The loss of pure TiO_2 was also measured and found to decrease across all measured temperatures with heat treatment at 150 °C and 300 °C. This is surprising in light of titania previously showing evidence of crystallisation after 200 °C. Optical measurements of these samples would be valuable, since the measured low loss is a promising result for the use of titania as a material in nanolayer coatings.

Measurements of 34.5% zirconia-doped tantala after heat treatment at 600 °C and 800 °C were motivated by evidence of zirconia increasing tantala's crystallisation temperature (crystallised by 800 °C anneal), as well as by atomic structural modelling results suggesting zirconia increases bond flexibility to an even greater degree than titania. The loss at low temperatures was found to be greater than titania-doped tantala, but the coating did show evidence of an increased crystallisation temperature, with an 800 °C heat treatment creating similar low temperature loss peak formation as seen with a 600 °C heat treatment of pure tantala. The primary interest of this coating, however, is as a potential room temperature coating layer. The loss at room temperature was found to decrease with heat treatments up to 600 °C and reach $\sim 2 \times 10^{-4}$, which is comparable to the loss of titania doped tantala. A lossy substrate prohibited measurement of further decreases, so continued measurements of this coating on a different substrate are important to determine if zirconia could be a preferred dopant for future upgrades.

The loss of RLVIP amorphous silicon was measured and found to be roughly half that of any heat treatment of IBS aSi. Amorphous silicon coatings currently have prohibitively high absorption, but resent results show potential for decreasing the absorption of silicon coatings. RLVIP aSi reaches a minimum absorption after heat treatment at 450 °C and, unlike IBS aSi, maintains this value with continued heat treatment. Given the significant decrease in the low temperature loss of silica with heat treatment at 600 °C (and the promising loss results from the as-deposited RLVIP SiO_2), this ability to reach greater annealing temperatures without sacrificing optical quality makes RLVIP a very promising coating material for use in cryogenic detectors.

The losses from all of the measured coating materials and heat treatments were then used to estimate the coating Brownian noise of a number of multilayer coating combinations, which were compared to the aLIGO and Advanced VIRGO coating stack. The most promising new dual material coating design was found to be alternating layers of IBS Al_2O_3 and IBS 14% Ti:Ta_2O_5 (as a substitute for 25% for the purpose of estimation). This coating resulted in a 20% reduction in coating Brownian noise at 10 K and a 24% reduction at 20 K, but it would increase the noise at 123 K. In a theoretical case where the loss of RLVIP silica were to reduce at low temperatures with heat treatment to a similar degree as IBS silica and the absorption of RLVIP silicon improved, then the best dual material coating would be RLVIP SiO_2 - RLVIP aSi, with 48%, 51%, and 40% improvement to coating Brownian noise at 10 K, 20 K, and 123 K, respectively.

Multi-material coating stacks have been discussed as an alternative to the two material multilayer that allows the use of high absorption materials like aSi by reflecting over 99% of the incident laser light with top bilayers of low absorption materials. The initial proposed multi-material design was updated based on the mechanical loss characterisation of IBS SiO_2 after heat treatment at 450 °C (the ideal heat treatment for minimising aSi is 450 °C), which produces much higher loss than expected across all temperatures, and, therefore, increases significantly the estimated thermal noise of the coating design. This result emphasises the importance of systematic loss characterisation of coating materials for accurate coating thermal noise estimation. Furthermore, the same elevated 450 °C SiO_2 loss results could explain the disparity between the predicted and measured mechanical loss of the advanced detector coating stack, which previously used SiO_2 loss from a 600 °C heat treatment to estimate the total coating stack loss after heat treatment at $\sim$500 °C.

Alternative multi-material designs were proposed in light of the increase in estimated noise from elevated SiO_2 loss. RLVIP coatings are the most promising option for improving thermal noise at 123 K, with an idealised, all RLVIP multi-material coating stack providing an 11% reduction in noise compared to the advanced detector multilayer coating stack. With continued reduction of aSi absorption expected, this coating design will see significant, further coating Brownian noise improvement based on the reduction of Ta_2O_5 layers. Alumina showed the greatest promise for improving the thermal noise of mirror coatings at 10 K or 20 K. A multi-material coating comprised of Al_2O_3 and 14% Ti:Ta_2O_5 bilayers on top of Al_2O_3 and aSi (all IBS) reduced thermal noise at 10 K and 20 K by 35% and 39%, respectively. This is a realistic and practical coating design able to immediately and significantly reduce coating Brownian noise at the lowest proposed detector operating temperatures.

Lowering the mechanical loss of coating materials in interferometric gravitational wave detectors is crucial for realising the design sensitivity of the current, advanced detectors, their upgrades, and proposed future detectors. Any improvements to coating thermal noise is linked to increased detector range and more gravitational wave detections. The coating characterisation within this thesis significantly improves the ability to estimate thermal noise of future coating designs and contributes towards our understanding of the link between a coating's structure and its mechanical loss, a crucial connection for finding the ideal coatings for future interferometric gravitational wave detectors.

Appendix A

Hydroxide-catalysis bonded silicon cantilevers

A.1 Introduction

Chemically etched silicon cantilevers are the current standard for measuring coating mechanical loss at reduced temperatures. As discussed in Chapter 3, these cantilevers have low enough internal friction for accurate calculation of loss within a thin-film coating applied to the surface. Separating the energy dissipated within the coating from energy dissipated within the cantilever is a necessary step in this calculation and it relies on the assumption of a uniform thickness across the length of the cantilever blade.

An optical profiler* created for measuring mirror suspension fibres was used to check the thickness consistency along the 35 mm length of fifteen cantilever blades etched from different wafers. Table A.1 shows the results, where maximum and minimum thicknesses tended to give the thickness at the base or tip and middle, respectively, and a cantilever with a large thickness deviation represent a more pronounce 'D' shape. It should be noted that all of the cantilevers were produced under the same etching specifications. Every cantilever has at least a 15 µm difference between the maximum and minimum thickness, with one (PC68) having a middle portion twice as thick as either end. This observed deviation in cantilever thickness introduces uncertainty into the frequency-based thickness calculations used for coating loss, where the calculation

*The optical profiler consists of a camera and LED backlight mounted on either side of a sample holder. The camera takes video of the shadow created by an object between it and the LED, and both move vertically to track the full length of the sample. The size of the shadow determines sample thickness, with the focus calibrated prior to measurement using objects of known thickness to ensure accurate shadow measurement. For more information see [398].

Table A.1 Thickness measurements of bare silicon cantilevers as found using an optical profiler. The standard deviation from the mean thickness is reported to quantify the consistency of a cantilever's thickness across its length. The maximum and minimum values show the severity of curvature on the etched face of the cantilever, where the minimum for all samples is at either the base or the tip and the maximum is close to the middle.

Cantilever origin wafer	Average thickness (μm)	Standard deviation (μm)	Minimum thickness (μm)	Maximum thickness (μm)
B 1	49	6	38	55
PC 18	56	4	38	61
PC 53	56	6	46	61
PC 24	57	6	43	62
PC 58	58	5	41	66
N 20	62	6	43	70
TBM 9	63	5	48	70
PC 21	63	9	48	70
PC 51	74	13	53	79
PC 30	75	8	49	79
PC 46	76	11	48	84
PC 72	79	15	51	87
PC 07	80	5	66	86
PC 10	80	15	54	83
PC 68	86	13	50	100

derived for thickness calculation assumes a perfectly rectangular beam. Furthermore, this could possibly induce differential curvature across the face when the cantilever is under stress, which would affect the measurement of coating stress discussed in section 3.4. It is therefore of interest to investigate alternative methods of constructing silicon cantilevers that would result in significantly less thickness deviation from base to tip.

A method is proposed to create silicon blade cantilevers with silica clamping blocks utilising hydroxide-catalysis bonding (HCB), which is a proven joining technique used in current detectors to attach silica 'ears' on the test masses (onto which the suspension fibres are then welded to create monolithic suspensions) [16]. It combines the precision and cleanliness of optical contacting with the strength and reliability of methods requiring external bonding materials. The loss of the HCB cantilevers is measured and then compared to that of their chemically etched counterparts.

A.2 Procedure

Hydroxide-catalysis bonding is a room temperature joining method that chemically bonds two flat silica (or alumina) surfaces using a hydroxide and silicate solution [399]. To create the bonds, two silica surfaces are thoroughly cleaned and pressed together with the hydroxide solution in between. The water and OH^- in the solution catalyse hydration and subsequent dehydration of both surfaces, which results in structural linking of the Si and O molecules of both surfaces [400]. Some residual hydrogen remains within the bond, but there is comparatively little contamination compared to other bonding methods [399]. The cantilevers created through HCB are similar in construction to the laser welded silica cantilevers discussed in section 3.2.2.1, but with silicon blades and no melting of the clamping block or cantilever blade.

Eight cantilever blades were made by scoring a 50 µm crystalline silicon wafer using a diamond scribe and splitting it into blades measuring roughly 5 mm by 40 mm. These blades were cleaned and baked at 1000 °C for fifteen minutes to grow about 20 nm of thermal oxide, which creates the silica surface necessary for HCB. The blades were then cleared of surface contaminants through ozone cleaning. The same silica clamping blocks used for laser welded cantilevers were prepared for bonding by scrubbing with cerium oxide and bicarbonate of soda before wiping with methanol. Roughly 5 mm of the cantilever blade was placed on the top face of the silica clamping block, with 0.3 µl of bonding solution between the surfaces. The free end of the cantilever blades rested on silica slides of equal thickness to the clamping block to ensure a level bond. Cantilevers containing visible bubbles in the bond were separated, cleaned, and put back together with another dose of the bonding solution. Any excess solution was wiped off the cantilevers with methanol and all were allowed to cure for a month before handling.

A.3 Mechanical loss

The bonded samples were clamped and their mechanical loss measured following the procedure discussed in Chapter 3. Four cantilevers were chosen for loss measurements based on the visible clarity of their bonds. Thermoelastic loss should be the dominant source of energy dissipation within silicon at 295 K, so measuring room temperature mechanical loss of the bonded cantilevers is a first check as to whether the bonds introduce excess dissipation. Figure A.1 shows the room temperature loss of these cantilevers compared to an etched cantilever of identical thickness. All cantilevers are 50 µm thick, so the expected level of thermoelastic loss should be the same and

is shown as a black line in figure A.1. Cantilevers 2, 5, and 8 show consistent loss at frequencies below 7 kHz, but diverge at the higher frequency modes. Only cantilever 2 displays loss consistent with thermoelastic limited damping at higher frequencies. The room temperature loss for cantilever 1 is identical to that of number two at ∼1 kHz (third bending mode), and is therefore hidden in figure A.1 but visible in figure A.2, which is scaled such that only the first three measured modes (3-5) are shown. It is clear from both figures that all of the bonded cantilevers have higher loss than the etched cantilever used for comparison, which, apart from modes 6 and 7, displays loss barely above the expected thermoelastic dissipation. The elevated loss at room temperature relative to expected thermoelastic loss is evidence of excess energy dissipation within the bond, or, possibly, insufficient energy isolation between the cantilever blade and clamping block. The reason behind the inconsistent loss above ∼7 kHz is unknown.

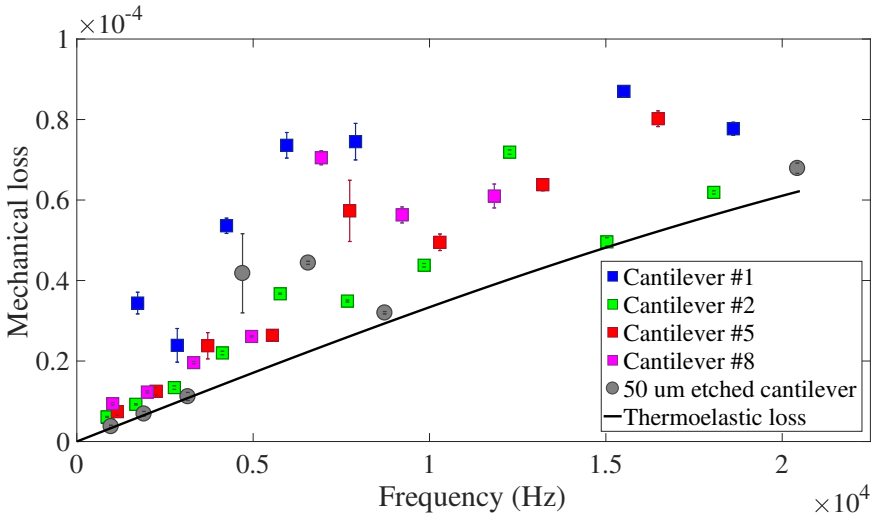

Fig. A.1 Loss versus bending mode frequency for all measured bonded cantilevers compared to a traditional, etched cantilever of nearly identical thickness. Energy dissipation within crystalline silicon at room temperature is expected to be dominated by thermoelastic loss, the expected magnitude of which is shown as a black line.

Measuring the room temperature loss is an interesting first check of the bonded cantilevers, but the motivation for their construction was as a more cost and time effective replacement to the etched silicon cantilevers as a substrate for low temperature coating loss measurements. Figure A.3 shows the loss of bonded cantilever number 8, as measured at bending modes 3-6 and 9*. Similar to the room temperature loss, the magnitude of low temperature loss is consistent between modes 3, 4, and 5, but is significantly increased for the higher frequency modes. Bending mode 9 (11.8 kHz)

*Modes 7 and 8 produced incoherent loss results and are therefore not shown.

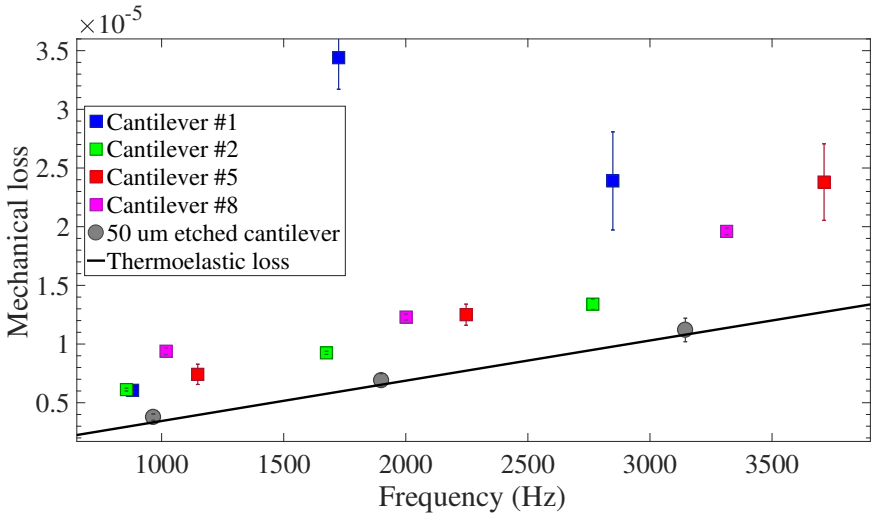

Fig. A.2 Loss versus bending mode frequency for modes 3, 4, and 5 of the bonded cantilevers compared to a traditional, etched cantilever of nearly identical thickness and expected thermoelastic loss. This is a identical data to figure A.1 but scaled to only show three modes for clarity.

exhibits loss about five times greater than that of the lower modes at 30 K, which is where a peak in loss is seen in all modes.

A loss peak at this temperature is expected based on the 30-40 nm of total thermal oxide on the bonded cantilever blades, but it is significantly more pronounced than would be expected for this oxide thickness. Figure A.4 shows the loss from mode 4 of the bonded sample compared to a 50 µm thick etched cantilever with nearly identical thermal oxide thickness. It includes a dashed line representing the loss of a different etched cantilever with 181 nm of thermally grown SiO_2*, which provides a closer match to the bonded sample in terms of loss peak magnitude and shape than the etched cantilever with ∼40 nm of thermal oxide growth.

There is no material difference between the wafers used for the cantilever etching process and the wafer from which the bonded cantilever blades were cut, so the significant loss disparity between the bonded and etched cantilevers must be a result of the bond layer or clamping block. The thickness of a HCB layer is thought to be between 30 and 100 nm thick [401] for precision application. The 300 nl of bonding solution used was an estimated volume to ensure full coverage of the ∼25 mm^2 bonding area. Every bonded cantilever had bonding excess hydroxide solution outwith the bonding area, implicating more was used than in the precision applications of which the bond layer thicknesses have been previously measured. It is therefore reasonable to assume that there may be more than 100 nm of silicate structure, i.e.

*This loss curve is also shown in relation to other thermal oxide thicknesses in figure 4.3.

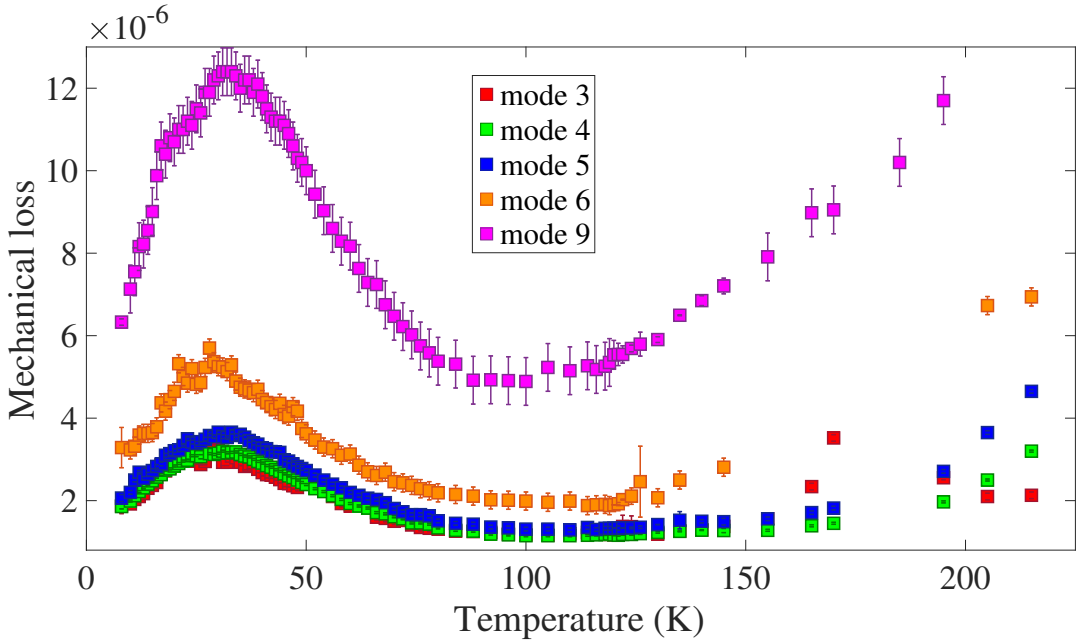

Fig. A.3 Mechanical loss of an uncoated, hydroxide-catalysis bonded silicon cantilever (#8). The loss is from bending modes 3 (1.02 kHz), 4 (2.00 kHz), 5 (3.31 kHz), 6 (4.96 kHz), and 9 (11.8 kHz).

bond layer, between the cantilever blade and clamping block. The loss peak of the bonded cantilever shown in figure A.4 appears to mimic a cantilever with ∼170nm of thermal oxide, so it is conceivable that the extra 130 nm of oxide peak displayed by the bonded cantilever could be from a thick silicate bond layer. This, of course, assumes that the bond layer loss is roughly equivalent to the loss of thermally grown SiO_2.

This bond layer, thermal oxide equivalency argument fails to explain the elevated loss above 75 K, where it can be seen from figure A.4 that the bonded cantilever exhibits significantly higher loss from the oxide peak through into temperatures dominated by thermoelastic loss. The oxide cannot account for this region, since the 181 nm thick thermal oxide loss curve displays a higher peak loss than the bonded cantilever but exhibits nearly one third of the loss between 100 and 150 K. A possible source of this extra dissipation could be energy transfer between the cantilever blade and the bulk silica clamping block. The minimum thicknesses given in table A.1 for the etched cantilevers, while unfortunate in terms of thickness uniformity, provides excellent energy isolation. The thickness at the cantilever-base connection is at least 10 nm thinner than the average thickness across the blade, with some cantilevers exhibiting a difference as high as 36 nm. The bonded cantilevers have no such sharp distinction between the blade and clamping block; about 12.5% of the total surface area of the cantilever blade is bonded to the silica clamping block, which is expected to have

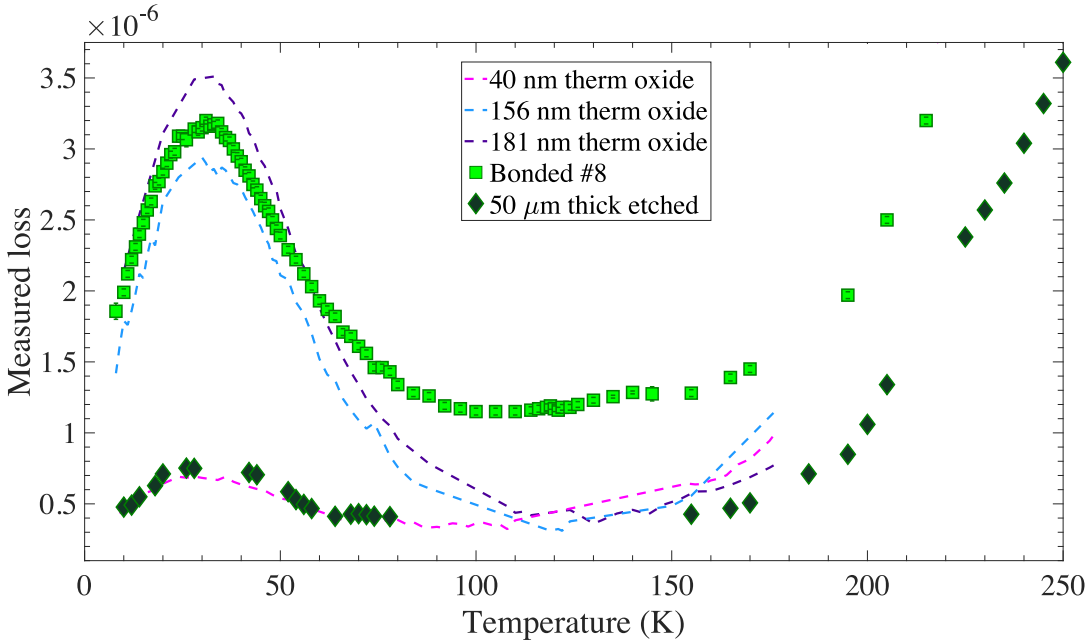

Fig. A.4 Loss calculated from mode 4 of bonded cantilever number 8 compared to an etched cantilever of the same thickness. Both cantilevers have the same thermal oxide thickness of about 40 nm, but the loss of other etched cantilevers with oxide thicknesses of 156 and 181 nm are shown as comparison due to the bonded cantilever's elevated loss peak.

loss on the order of 1×10^{-4} from 100 to 200 K. It is therefore hypothesised that the elevated bonded cantilever loss in this temperature region is a result of excess energy transfer between the cantilever blade and clamping block.

A.4 Conclusion

A silicon cantilever constructed through hydroxide-catalysis bonding of a blade cut from a wafer of uniform thickness to a fused silica clamping block is proposed as a possible alternative to the chemically etched silicon cantilevers currently used for low temperature loss characterisation of thin-film coatings. The possible advantages to these bonded cantilevers include a markedly improved thickness consistency along the length of the blade, thickness uniformity from cantilever to cantilever, and a significant reduction in the time and monetary cost of manufacturing. In order to be a viable replacement, HCB cantilevers need to exhibit mechanical loss of the same magnitude of the current, etched cantilevers.

The loss of four bonded cantilevers was measured at room temperature, where the dissipation should be thermoelastic limited. All of the samples exhibited greater loss

than expected given the thermoelastic approximation. One sample was measured from 10 to 295 K and found to have consistently elevated loss in the thermoelastic region, a pronounced loss peak at 30 nm much greater in magnitude than expected given the thickness of thermal oxide on the cantilever, and loss about three times greater than an etched cantilever in between the loss peak and the thermoelastic region ($\sim$100 to 200 K). Bonded cantilevers are, therefore, shown to not yet be a viable option for replacing the chemically etched cantilevers used throughout this thesis.

Further study is required to confirm the hypothesis that a large bond area is the cause of elevated loss in the mid-temperature range. Reducing the portion of the cantilever bonded to the clamping block by as much as 4 mm is possible and would produce interesting results. Furthermore, a more precise calculation for the required volume of hydroxide solution could produce a thinner bond layer and may reduce the loss peak. It is also unknown why there is such marked change in loss with respect to frequency for bending modes greater $\sim$7 kHz. Discovering the cause of this effect would lead to better understanding of frequency dependent loss in etched cantilevers, as well as resonators of other shapes.

Bibliography

[1] A. Einstein, "Die Grundlage der allgemein Relativitatstheorie", Annalen der Physik **49**, 769 (1916).

[2] B. P. Abbott et al., "Observation of Gravitational Waves from a Binary Black Hole Merger", Physical Review Letters **116**, 61102 (2016).

[3] B. F. Schutz, "Gravitational-wave sources", Classical and Quantum Gravity **13**, A219–A238 (1996).

[4] A. A. Penzias and R. W. Wilson, "A measurement of excess antenna temperature at 4080 Mc/s", The Astrophysical Journal **142**, 419–421 (1965).

[5] R. H. Dicke, P. J. E. Peebles, P. G. Roll, and D. T. Wilkinson, "Cosmic blackbody radiation", The Astrophysical Journal **142**, 414–419 (1965).

[6] B. P. Abbott et al., "The Rate of Binary Black Hole Mergers Inferred From Advanced Ligo Observations Surrounding GW150914", The Astrophysical Journal **833**, L1 (2016).

[7] B. P. Abbott et al., "The basic physics of the binary black hole merger", Annalen der Physik **529**, 1600209 (2017).

[8] R. A. Hulse and J. H. Taylor, "Discovery of a Pulsar in a Binary System", The Astrophysical Journal **195**, L51–L53 (1975).

[9] J. M. Weisberg and J. H. Taylor, "Relativistic Binary Pulsar B1913+16: Thirty Years of Observations and Analysis", ASP Conference Series **328**, 25–31 (2005).

[10] B. P. Abbott et al., "GW151226: Observation of Gravitational Waves from a 22-Solar-Mass Binary Black Hole Coalescence", Physical Review Letters **116**, 241103 (2016).

[11] B. P. Abbott et al., "GW170104: Observation of a 50-Solar-Mass Binary Black Hole Coalescence at Redshift 0.2", Physical Review Letters **118**, 1–17 (2017).

[12] B. P. Abbott et al., "GW170608: Observation of a 19-solar-mass Binary Black Hole Coalescence", The Astrophysical Journal Letters **851**, L35 (2017).

[13] B. P. Abbott et al., "GW170817: Observation of Gravitational Waves from a Binary Neutron Star Inspiral", Physical Review Letters **119**, 161101 (2017).

[14] B. P. Abbott et al., "GW170814: A Three-Detector Observation of Gravitational Waves from a Binary Black Hole Coalescence", Physical Review Letters **119**, 141101 (2017).

[15] J. Weber, "Detection and generation of gravitational waves", Physical Review **117**, 306–313 (1960).

[16] J. Aasi et al., "Advanced LIGO", Classical and Quantum Gravity **32**, 074001 (2015).

[17] F. Acernese et. al., "The Advanced Virgo detector", Journal of Physics: Conference Series **610**, 012014 (2015).

[18] K. Somiya and the KAGRA Collaboration, "Detector configuration of KAGRA–the Japanese cryogenic gravitational-wave detector", Classical and Quantum Gravity **29**, 124007 (2012).

[19] R. P. Feynman, F. B. Morinigo, and W. G. Wagner, *Feynman Lectures on Gravitation*, edited by B. Hatfield (Addison-Wesley, Wokingham, 1995).

[20] B. Sathyaprakash and B. F. Schutz, "Physics , Astrophysics and Cosmology with Gravitational Waves", Living Reviews in Relativity **12** (2009).

[21] P. R. Saulson, *Fundamentals of Interferometric Gravitational Wave Detectors* (World Scientific, 1994).

[22] R. B. Larson, "The Collapse of a Rotating Cloud", Monthly Notices of the Royal Astronomical Society **156**, 437–458 (1972).

[23] R. H. Durison, M. F. Sterzik, and B. K. Pickett, "A two-step initial mass function: Consequences of clustered star formation for binary properties", Astronomy and Astrophysics **371**, 952–962 (2001).

[24] B. F. Schutz, "Determining the Hubble constant from gravitational wave observations", Nature **323**, 310–311 (1986).

[25] B. Giacomazzo et al., "Compact Binary Progenitors of Short Gamma-Ray Bursts", The Astrophysical Journal Letters **762**, L18 (2013).

[26] LIGO Scientific Collaboration, Virgo Collaboration, F. G.-R. B. Monitor, and INTEGRAL, "Gravitational Waves and Gamma-rays from a Binary Neutron Star Merger: GW170817 and GRB 170817A", The Astrophysical Journal Letters **848**, L13 (2017).

[27] *The LSC-Virgo White Paper on Gravitational Wave Searches and Astrophysics Executive Summary (2014-2015 edition)*, LIGO technical document: LIGO-T1400054-v7 (2014).

[28] C. M. Will, "Verification of general relativity: strong fields and gravitational waves", in *The century of space science*, edited by J. A. Bleeker, J. Geiss, and M. Huber (Springer Netherlands, 2001) Chap. 16, pp. 353–372.

[29] B. P. Abbott et al., "A gravitational-wave standard siren measurement of the Hubble constant", Nature **551**, 85–98 (2017).

[30] C. L. Fryer, D. E. Holz, and S. A. Hughes, "Gravitational wave emission from core collapse of massive stars", The Astrophysical Journal **565**, 430–446 (2002).

[31] C. L. Fryer, "Gravitational waves from stellar encounters", AIP Conference Proceedings **575**, 209 (2001).

[32] B. P. Abbott et al., "All-sky search for short gravitational-wave bursts in the first Advanced LIGO run", Physical Review D **95**, 042003 (2017).

[33] B. P. Abbott et al., "Observing gravitational-wave transient GW150914 with minimal assumptions", Physical Review D **93**, 122004 (2016).

[34] Y. B. Zel'dovich and A. G. Polnarev, "Radiation of gravitational waves by a cluster of superdense stars", Soviet Astronomy **18**, 17–23 (1974).

[35] V. B. Braginsky and K. S. Thorne, "Gravitational-wave bursts with memory and experimental prospects", Nature **327**, 123–125 (1987).

[36] D. Christodoulou, "Nonlinear nature of gravitation and gravitational-wave experiments", Physical Review Letters **67**, 1486–1489 (1991).

[37] P. D. Lasky et al., "Detecting Gravitational-Wave Memory with LIGO: Implications of GW150914", Physical Review Letters **117**, 061102 (2016).

[38] L. O. McNeill, E. Thrane, and P. D. Lasky, "Gravitational Waves From Orphan Memory", Physical Review Letters **118**, 181103 (2017).

[39] M. Favata, "The gravitational-wave memory effect", Classical and Quantum Gravity **27**, 084036 (2010).

[40] M. Abernathy et al., *Einstein gravitational wave Telescope conceptual design study*, ET technical document: ET-0106C-10 (2011).

[41] B. P. Abbott et al., "First Search for Gravitational Waves from Known Pulsars with Advanced LIGO", The Astrophysical Journal **839**, 12 (2017).

[42] C. Van Den Broeck, "The gravitational wave spectrum of non-axisymmetric, freely precessing neutron stars", Classical and Quantum Gravity **22**, 1825–1839 (2005).

[43] B. J. Owen and L. Lindblom, "Gravitational radiation from the r -mode instability", Classical and Quantum Gravity **19**, 1247–1253 (2002).

[44] G. Ushomirsky, "R-modes in Accreting and Young Neutron Stars", in *Astrophysical sources for ground-based gravitational wave detectors: Philadelphia, Pennsylvania, 30 october - 1 november 2000*, edited by J. M. Centrella (American Institute of Physics, Melville, NY, 2001), pp. 284–295.

[45] S. Chandrasekhar, "Solutions of two problems in the theory of graviational radiation", Physical Review Letter **24**, 611–615 (1970).

[46] C. Cutler, "Gravitational waves from neutron stars with large toroidal B fields", Physical Review D **66**, 084025 (2002).

[47] M. Pitkin, *Continuous waves from rotating neutron stars*, LIGO technical document: LIGO-G1500603, Talk, DAWN Workshop, May 2015.

[48] J. Aasi et al., "Gravitational Waves From Known Pulsars: Results From the Initial Detector Era", The Astrophysical Journal **785**, 119 (2014).

[49] P. F. Michelson, "On detecting stochastic background gravitational radiation with terrestrial detectors", Monthly Notices of the Royal Astronomical Society **227**, 933–941 (1987).

[50] N. Christensen, "Measuring the stochastic gravitational-radiation background with laser-interferometric antennas", Physical Review D **46**, 5250–66 (1992).

[51] E. E. Flanagan, "Sensitivity of the Laser Interferometer Gravitational Wave Observatory to a stochastic background, and its dependence on the detector orientations", Physical Review D **48**, 2389–2407 (1993).

[52] B. Abbott et al., "Searching for a Stochastic Background of Gravitational Waves with the Laser Interferometer Gravitational-Wave Observatory", The Astrophysical Journal **659**, 918–930 (2007).

[53] X.-J. Zhu et al., "Stochastic Gravitational Wave Background From Coalescing Binary Black Holes", The Astrophysical Journal **739**, 86 (2011).

[54] X. Siemens, V. Mandic, and J. Creighton, "Gravitational-wave stochastic background from cosmic strings", Physical Review Letters **98**, 111101 (2007).

[55] P. D. Lasky, M. F. Bennett, and A. Melatos, "Stochastic gravitational wave background from hydrodynamic turbulence in differentially rotating neutron stars", Physical Review D **87**, 063004 (2013).

[56] A. Kosowsky, A. Mack, and T. Kahniashvili, "Stochastic gravitational radiation from phase transitions", AIP Conference Proceedings **575**, 191 (2001).

[57] X. J. Zhu, E. Howell, and D. Blair, "Observational upper limits on the gravitational wave production of core collapse supernovae", Monthly Notices of the Royal Astronomical Society: Letters **409**, L132–6 (2010).

[58] B. P. Abbott et al., "LIGO: the Laser Interferometer Gravitational-Wave Observatory", Reports on Progress in Physics **72**, 076901 (2009).

[59] B. Allen, "The stochastic gravity-wave background: sources and detection", in *Relativistic gravitation and gravitational radiation* (Cambridge University Press, 1997), pp. 373–417.

[60] B. P. Abbott et al., "Upper Limits on the Stochastic Gravitational-Wave Background from Advanced LIGO's First Observing Run", Physical Review Letters **118**, 121101 (2017).

[61] B. P. Abbott et al., "Directional limits on persistent gravitational waves from Advanced LIGO's first observing run", Physical Review Letters **118**, 121102 (2017).

[62] J. Weber, "Evidence for Discovery of Gravitational Radiation", Physical Review Letters **22**, 1320–1324 (1969).

[63] J. Weber, "Anisotropy and polarization in the gravitational-radiation experiments", Physical Review Letters **25**, 180–184 (1970).

[64] R. L. Forward et al., "Upper Limit for Interstellar Millicycle Gravitational Radiation", Nature **189**, 473 (1961).

[65] *The Gravitational Wave International Committee Roadmap: The future of gravitational wave astronomy*, GWIC subcommittee report (2010), pp. 1–116.

[66] R. W. P. Drever, J. Hough, R. Bland, and G. W. Lessnoff, "Search for Short Bursts of Gravitational Radiation", Nature **246**, 340–344 (1973).

[67] O. D. Aguiar, "Past, present and future of the Resonant-Mass gravitational wave detectors", Research in Astronomy and Astrophysics **11**, 1–42 (2011).

[68] A. Vinante et al., "Thermal noise in a high Q ultracryogenic resonator", Review of Scientific Instruments **76**, 074501 (2005).

[69] P. Astone, "Resonant mass detectors: present status", Classical and Quantum Gravity **19**, 1227 (2002).

[70] S. E. Whitcomb, "Ground-based gravitational-wave detection: now and future", Classical and Quantum Gravity **25**, 114013 (2008).

[71] P. Astone et al., "EXPLORER and NAUTILUS gravitational wave detectors: a status report", Classical and Quantum Gravity **25**, 114048 (2008).

[72] *Status of the AURIGA detector as May 2009*, http://www.auriga.lnl.infn.it/auriga/status/status_may09.html, 2009.

[73] W. Johnson, *A voice from the grave: lessons learned from ALLEGRO 1970-2007 R.I.P*, LIGO technical document: LIGO-G0900637-v1, Talk, GWADW Meeting, 2009.

[74] *EXPLORER's life comes to a fruitful end*, http://cerncourier.com/cws/ article/cern/48606, 2012.

[75] C. F. Da Silva Costa and O. D. Aguiar, "Spherical gravitational wave detectors: MiniGRAIL and Mario Schenberg", in Proceedings of the 7th International Conference on Gravitation and Cosmology (ICGC2011), Vol. 484 (2014), p. 012012.

[76] A. Saha and S. Gangopadhyay, "Resonant detectors of gravitational wave as a possible probe of the noncommutative structure of space", Classical and Quantum Gravity **33**, 205006 (2016).

[77] M. E. Gertsenshtein and V. I. Pustovoit, "On the detection of low frequency gravitational waves", Journal of Experimental and Theoretical Physics (U.S.S.R.) **43**, 605–607 (1962).

[78] R. Weiss, *Quarterly Progress Report: Electromagnetically Coupled Broadband Gravitational Antenna*, LIGO technical document: LIGO-P720002-v1, 1972.

[79] F. A. E. Pirani, "On the physical significance of the Riemann tensor", Acta Physica Polonica **15**, 389–405 (1956).

[80] G. E. Moss, L. R. Miller, and R. L. Forward, "Photon-Noise-Limited Laser Transducer for Gravitational Antenna", Applied Optics **10**, 2495–2498 (1971).

[81] R. L. Forward, "Wideband laser-interferometer graviational-radiation experiment", Physical Review D **17**, 379–390 (1978).

[82] H. Billing et al., "An argon laser interferometer for the detection of gravitational radiation", Journal of Physics E: Scientific Instruments **12**, 1043–1050 (1979).

[83] D. Shoemaker et al., "Noise behavior of the Garching 30-meter prototype gravitational-wave detector", Physical Review D **38**, 423–432 (1988).

[84] R. W. P. Drever, J. R. Pugh, W. A. Edelstein, and H. Ward, "Gravitational Wave Detectors", Proceedings of the Royal Society of London A **368**, 11–18 (1979).

[85] H. Ward et al., "Laser Interferometric Sensing Techniques for Very Small Displacements With Applications to Gravitational Radiation Detectors", IEEE Transactions on Instrumentation and Measurement **34**, 261 (1985).

[86] A. Abramovici et al., "Improved sensitivity in a gravitational wave interferometer and implications for LIGO", Physics Letters A **218**, 157–163 (1996).

[87] J. Hough, S. Rowan, and B. S. Sathyaprakash, "The search for gravitational waves", Journal of Physics B **38**, S497–S519 (2005).

[88] K. Kawabe et al., "Demonstration of a recombined Fabry-Perot-Michelson interferometer with suspended mirrors", Applied Physics B **62**, 135–138 (1996).

[89] P. Fritschel et al., "High Power Interferometric Phase Measurement Limited by Quantum Noise and Application to Detection of Gravitational Waves", Physical Review Letters **80**, 3181–3184 (1998).

[90] W. Heisenberg, "Über den anschaulichen Inhalt der quantentheoretischen Kinematik und Mechanik", Zeitschrift für Physik **43**, 172–198 (1927).

[91] W. A. Edelstein, J. Hough, J. R. Pugh, and W. Martin, "Limits to the measurement of displacement in an interferometric gravitational radiation detector", Journal of Physics E: Scientific Instruments **11**, 710–712 (1978).

[92] M. Pitkin, S. Reid, S. Rowan, and J. Hough, "Gravitational Wave Detection by Interferometry (Ground and Space)", Living Reviews in Relativity **14** (2011).

[93] R. Loudon, "Quantum limit on the michelson interferometer used for gravitational-wave detection", Physical Review Letters **47**, 815 (1981).

[94] C. M. Caves, "Quantum-mechanical noise in an interferometer", Physical Review D **23**, 1693 (1981).

[95] C. M. Caves, "Quantum-Mechanical Radiation-Pressure Fluctuations in an Interferometer", Physical Review Letters **45**, 75 (1980).

[96] V. B. Braginsky and F. Y. Khalily, "Nonlinear meter for the gravitational wave antenna", Physics Letters A **218**, 167–174 (1996).

[97] V. B. Braginsky, M. L. Gorodetsky, F. Y. Khalili, and K. S. Thorne, "Dual-resonator speed meter for a free test mass", Physical Review D **61**, 044002 (2000).

[98] V. B. Braginsky and F. J. Khalili, "Gravitational wave antenna with QND speed meter", Physics Letters A **147**, 251–256 (1990).

[99] C. Gräf et al., "Design of a speed meter interferometer proof-of-principle experiment", Classical and Quantum Gravity **31**, 215009 (2014).

[100] S. H. Huttner et al., "Candidates for a possible third-generation gravitational wave detector: comparison of ring-Sagnac and sloshing-Sagnac speedmeter interferometers", Classical and Quantum Gravity **34**, 024001 (2017).

[101] E. Knyazev, S. Danilishin, S. Hild, and F. Y. Khalili, "Speedmeter scheme for gravitational-wave detectors based on EPR quantum entanglement", Physics Letters A, Advance Online Publication (2017).

[102] S. L. Danilishin et al., *A new type of quantum speed meter interferometer: How measuring speed can help to observe black holes*, LIGO technical document:LIGO-P1700008, 2017.

[103] T. Suzuki and H. Hirakawa, "Local Field and Gravitational Radiation Experiments", Journal of the Physical Society of Japan **48**, 685 (1980).

[104] P. R. Saulson, "Terrestrial gravitational noise on a gravitational wave antenna", Physical Review D **30**, 732–736 (1984).

[105] S. Hughes and K. Thorne, "Seismic gravity-gradient noise in interferometric gravitational-wave detectors", Physical Review D **58**, 122002 (1998).

[106] M. G. Beker et al., "Improving the sensitivity of future GW observatories in the 1-10 Hz band: Newtonian and seismic noise", General Relativity and Gravitation **43**, 623–656 (2011).

[107] M. Beccaria et al., "Relevance of Newtonian seismic noise for the VIRGO interferometer sensitivity", Classical and Quantum Gravity **15**, 3339–3362 (1998).

[108] T. Creighton, "Tumbleweeds and airborne gravitational noise sources for LIGO", Classical and Quantum Gravity **25**, 125011 (2008).

[109] M. Musha, "Japanese space gravitational wave antenna DECIGO and DPF", in ICSO 2014 - International Conference on Space Optics, October (2014).

[110] K. Danzmann et al., *LISA Laser Interferometer Space Antenna*, ESA L3 Proposal (2017).

[111] S. Hild et al., "Sensitivity studies for third-generation gravitational wave observatories", Classical and Quantum Gravity **28**, 094013 (2011).

[112] M. Bader, A. Bertolini, J. van den Brand, and J. V. Heijningen, *Newtonian Noise : Survey of low seismic noise environments , and sub-ng instrumentation*, 4th ELiTES General Meeting, Talk, Tokyo, 2015.

[113] S. Custodio et al., "Ambient Noise Recorded by a Dense Broadband Seismic Deployment in Western Iberia", Bulletin of the Seismological Society of America **104**, 2985–3007 (2014).

[114] E. J. Daw et al., "Long-term study of the seismic environment at LIGO", Classical and Quantum Gravity **21**, 2255 (2004).

[115] S. Rowan and J. Hough, "Gravitational Wave Detection by Interferometry (Ground and Space)", Living Reviews in Relativity **3**, 3 (2000).

[116] M. Plissi et al., "GEO 600 triple pendulum suspension system: Seismic isolation and control", Review of Scientific Instruments **71**, 2539 (2000).

[117] S. Braccini et al., "Measurement of the seismic attenuation performance of the VIRGO Superattenuator", Astroparticle Physics **23**, 557–565 (2005).

[118] G. Losurdo et al., "Inertial control of the mirror suspensions of the VIRGO interferometer for gravitational wave detection", Review of Scientific Instruments **72**, 3653–3661 (2001).

[119] F. Matichard et al., "Seismic isolation of Advanced LIGO: Review of strategy, instrumentation and performance", Classical and Quantum Gravity **32**, 185003 (2015).

[120] A. Nowick and B. Berry, *Anelastic Relaxation in Crystalline Solids* (Academic Press, New York, 1972).

[121] A. Ageev et al., "Very high quality factor measured in annealed fused silica", Classical and Quantum Gravity **21**, 3887–3892 (2004).

[122] S. Rowan et al., "Q factor measurements on prototype fused quartz pendulum suspensions for use in gravitational wave detectors", Physics Letters A **233**, 303–308 (1997).

[123] G. Cagnoli et al., "Very high Q measurements on a fused silica monolithic pendulum for use in enhanced gravity wave detectors", Physical Review Letters **85**, 2442 (2000).

[124] A. Abramovici et al., "LIGO: The Laser Interferometer Gravitational-Wave Observatory", Science **256**, 325–333 (1992).

[125] G. Cagnoli and P. Willems, "Effects of nonlinear thermoelastic damping in highly stressed fibers", Physical Review B **65**, 174111 (2002).

[126] C. Bell et al., "Experimental results for nulling the effective thermal expansion coefficient of fused silica fibres under a static stress", Classical and Quantum Gravity **31**, 065010 (2014).

[127] B. Willke et al., "The GEO 600 gravitational wave detector", Classical and Quantum Gravity **19**, 1377 (2002).

[128] D. R. Herriott and H. J. Schulte, "Folded Optical Delay Lines", Applied Optics **4**, 883–889 (1965).

[129] D. V. Martynov et al., "Sensitivity of the Advanced LIGO detectors at the beginning of gravitational wave astronomy", Physical Review D **93**, 112004 (2016).

[130] A. Perot and C. Fabry, "On the Application of Interference Phenomena to the Solution of Various Problems of Spectroscopy and Metrology", The Astrophysical Journal **9**, 87 (1899).

[131] J. Levine and J. L. Hall, "Design and operation of a methane absorption stabilized laser strainmeter", Journal of Geophysical Research **77**, 2595–2609 (1972).

[132] M. Evans et al., "Observation of Parametric Instability in Advanced LIGO", Physical Review Letters **114**, 161102 (2015).

[133] V. B. Braginsky, S. E. Strigin, and S. P. Vyatchanin, "Parametric oscillatory instability in Fabry–Perot interferometer", Physics Letters A **287**, 331–338 (2001).

[134] R. W. P. Drever et al., "Gravitational wave detectors using laser-interferometers and optical cavities: Ideas, principles, and prospects", in *Quantum optics, experimental gravity, and measurement theory*, edited by P. Meystre and M. O. Scully (Springer, Series NATO Advanced Science Institutes, 1983), pp. 503–514.

[135] B. J. Meers, "Recycling in laser-interferometric gravitational-wave detectors", Physical Review D **38**, 2317–2326 (1988).

[136] K. A. Strain and B. J. Meers, "Experimental demonstration of dual recycling for interferometric gravitational-wave detectors", Physical Review Letters **66**, 1391–1394 (1991).

[137] G. Heinzel et al., "Experimental Demonstration of a Suspended Dual Recycling Interferometer for Gravitational Wave Detection", Physical Review Letters **81**, 5493–5496 (1998).

[138] S. Hild et al., "Demonstration and comparison of tuned and detuned signal recycling in a large-scale gravitational wave detector", Classical and Quantum Gravity **24**, 1513–1523 (2007).

[139] D. F. Walls, "Squeezed states of light", Nature **306**, 141–146 (1983).

[140] M. Mehmet et al., "Observation of squeezed states with strong photon-number oscillations", Physical Review A **81**, 013814 (2010).

[141] A. F. Pace, M. J. Collett, and D. F. Walls, "Quantum limits in interferometric detection of gravitational radiation", Physical Review A **47**, 3173 (1993).

[142] G. Breitenbach, S. Schiller, and J. Mlynek, "Measurement of the quantum states of squeezed light", Nature **387**, 471 (1997).

[143] K. McKenzie et al., "Experimental Demonstration of a Squeezing-Enhanced Power-Recycled Michelson Interferometer for Gravitational Wave Detection", Physical Review Letters **88**, 231102 (2002).

[144] H. J. Kimble et al., "Conversion of conventional gravitational-wave interferometers into quantum nondemolition interferometers by modifying their input and/or output optics", Physical Review D **65**, 022002 (2001).

[145] R. Schnabel, "Squeezed states of light and their applications in laser interferometers", Physics Reports **684**, 1–52 (2017).

[146] H. Vahlbruch et al., "The GEO 600 squeezed light source", Classical and Quantum Gravity **27**, 084027 (2010).

[147] H. Grote et al., "First long-term application of squeezed states of light in a gravitational-wave observatory", Physical Review Letters **110**, 181101 (2013).

[148] J. Veitch et al., "Estimating parameters of coalescing compact binaries with proposed advanced detector networks", Physical Review D **85**, 104045 (2012).

[149] M. Evans, R. Sturani, and S. Vitale, *Unofficial sensitivity curves (ASD) for aLIGO, Kagra, Virgo, Voyager, Cosmic Explorer, and ET*, LIGO technical document: LIGO–T1500293–v8, 2016.

[150] J. Smith, *GEO600 Sensitivity Curves*, http://www.geo600.uni-hannover.de/geocurves/, 2006.

[151] ICRR GW Group, *KAGRA official sensitivity limit*, http://gwcenter.icrr.u-tokyo.ac.jp/en/researcher/parameter, 2010.

[152] H. Lück et al., "Thermal correction of the radii of curvature of mirrors for GEO 600", Classical and Quantum Gravity **21**, S985–S989 (2004).

[153] H. Lück et al., "The upgrade of GEO 600", Journal of Physics: Conference Series **228**, 012012 (2010).

[154] H. Grote, "The GEO 600 status", Classical and Quantum Gravity **27**, 084003 (2010).

[155] J. Lough, *Beyond GEO HF: the wrap up*, GEO meeting, Talk, Mallorca, 2016.

[156] J. R. Smith and F. T. L. S. Collaboration, "The path to the enhanced and advanced LIGO gravitational-wave detectors", Classical and Quantum Gravity **26**, 114013 (2009).

[157] https://www.ligo.caltech.edu/WA/images, 2017.

[158] S. D. Penn et al., "Mechanical Loss in Tantala/Silica Dielectric Mirror Coatings", Classical and Quantum Gravity **20**, 2917–2928 (2003).

[159] R. Adhikari, P. Fritschel, and S. Waldman, *Technical Note: Enhanced LIGO*, LIGO technical document: LIGO–T060156–01–I, 2006.

[160] T. T. Fricke et al., "DC readout experiment in Enhanced LIGO", Classical and Quantum Gravity **29**, 065005 (2012).

[161] G. M. Harry et al., "Thermal noise in interferometric gravitational wave detectors due to dielectric optical coatings", Classical and Quantum Gravity **19**, 897–917 (2002).

[162] D. R. M. Crooks et al., "Experimental measurements of coating mechanical loss factors", Classical and Quantum Gravity **21**, S1059–S1065 (2004).

[163] D. R. M. Crooks et al., "Experimental measurements of mechanical dissipation associated with dielectric coatings formed using SiO_2, Ta_2O_5 and Al_2O_3", Classical and Quantum Gravity **23**, 4953–4965 (2006).

[164] G. M. Harry et al., "Thermal noise from optical coatings in gravitational wave detectors", Applied Optics **45**, 1569–1574 (2006).

[165] G. M. Harry et al., "Titania-doped tantala/silica coatings for gravitational-wave detection", Classical and Quantum Gravity **24**, 405–415 (2007).

[166] F. Acernese et al., "Results of the Virgo Central Interferometer Commissioning", Classical and Quantum Gravity **21**, S395 (2004).

[167] The Virgo Collaboration, *Advanced Virgo Technical Design Report*, VIRGO Technical Document: VIR–0128A–12, 2012.

[168] R. Gouaty, *Status of the Advanced Virgo gravitational wave detector*, 50th Rencontres de Moriond-Gravitation, Talk, Aosta Valley, Italy, 2015.

[169] M. Razzano, *A very exciting LIGO-Virgo observing run draws to a close on the 25th of August*, Virgo Press Release, public.virgo-gw.eu/exciting-ligo-virgo-observing-run-draws-close-25th-august/, 2017.

[170] K. Kuroda et al., "Japanese large-scale interferometers", Classical and Quantum Gravity **19**, 1237–1245 (2002).

[171] K. Arai et al., "Status of Japanese gravitational wave detectors", Classical and Quantum Gravity **26**, 204020 (2009).

[172] K. Yamamoto et al., "Current status of the CLIO project", Journal of Physics: Conference Series **122**, 012002 (2008).

[173] T. Uchiyama et al., "Reduction of thermal fluctuations in a cryogenic laser interferometric gravitational wave detector", Physical Review Letters **108**, 141101 (2012).

[174] K. Yamamoto and the KAGRA Collaboration, *Current Status of KAGRA*, LIGO technical document: LIGO G1601857-v2, Talk, LVC Meeting: Glasgow, 2016.

[175] M. Nakano, *Status of KAGRA*, LIGO technical document: LIGO–G1600748, Talk, LVC Meeting: Pasadena, 2016.

[176] S. Finn et al., *Report of the Committee to Compare the Scientific Cases for Two Gravitational-wave Detector Networks : (AHLV) Australia , Hanford , Livingston , VIRGO ; and (HHLV) two detectors at Hanford , one at Livingston , and VIRGO*, LIGO technical document: T1000251-v1, 2010.

[177] B. Iyer et al., *LIGO-India: Proposal of the Consortium for Indian Initiative in Gravitational-wave Observations (IndIGO)*, LIGO technical document: M1100296-v2, 2011.

[178] *LIGO-India*, http://gw-indigo.org/tiki-index.php?page=LIGO-India, 2016.

[179] S. Priyadarashini, "Gravitational waves send ripples of joy for LIGO-India", Nature India online (2016).

[180] The LIGO Scientific Collaboration, *Instrument Science White Paper*, LIGO technical document: LIGO-T15TBI-v1 (2016).

[181] The LIGO Scientific Collaboration, *Instrument Science White Paper*, LIGO technical document: LIGO-T1600117-v4 (2016).

[182] R. X. Adhikari et al., *LIGO Voyager Upgrade: Design Concept*, LIGO technical document: LIGO–T1400226–v8, 2017.

[183] B. P. Abbott et al., "Exploring the sensitivity of next generation gravitational wave detectors", Classical and Quantum Gravity **34**, 044001 (2017).

[184] A. Freise and K. Strain, "Interferometer Techniques for Gravitational-Wave Detection", Living Reviews in Relativity **13** (2010).

[185] K. Danzmann et al., *LISA Unveiling a hidden Universe-Assessment study report*, tech. rep. (ESA/SRE, 2011).

[186] P. Amaro-Seoane et al., "Intermediate and Extreme Mass-Ratio Inspirals – Astrophysics, Science Applications and Detection using LISA", Classical and Quantum Gravity **24**, R113–R169 (2007).

[187] P. McNamara, S. Vitale, and K. Danzmann, "LISA Pathfinder", Classical and Quantum Gravity **25**, 114034 (2008).

[188] M. Armano et al., "Sub-Femto- g Free Fall for Space-Based Gravitational Wave Observatories: LISA Pathfinder Results", Physical Review Letters **116**, 231101 (2016).

[189] B. P. Abbott et al., "Binary Black Hole Mergers in the first Avanced LIGO Observing Run", Physical Review X **6**, 041015 (2016).

[190] B. P. Abbott et al., "Properties of the Binary Black Hole Merger GW150914", Physical Review Letters **116**, 241102 (2016).

[191] B. P. Abbott et al., "GW150914: First results from the search for binary black hole coalescence with Advanced LIGO", Physical Review D **93**, 1–21 (2016).

[192] C. Cutler and E. E. Flanagan, "Gravitational waves from merging compact binaries: How accurately can one extract the binary's parameters from the inspiral waveform?", Physical Review D **49**, 2658–2697 (1994).

[193] L. Blanchet et al., "Gravitational-radiation damping of compact binary systems to second post-Newtonian order", Physical Review Letters **74**, 3515–3518 (1995).

[194] B. P. Abbott et al., "Astrophysical Implications of the Binary Black Hole Merger GW150914", The Astrophysical Journal Letters **818**, L22 (2016).

[195] M. Fejer et al., "Thermoelastic dissipation in inhomogeneous media: loss measurements and displacement noise in coated test masses for interferometric gravitational wave detectors", Physical Review D **70**, 082003 (2004).

[196] M. Evans et al., "Thermo-optic noise in coated mirrors for high-precision optical measurements", Physical Review D **78**, 102003 (2008).

[197] R. Brown, "XXVII. A brief account of microscopical observations made in the months of June, July and August, 1827, on the particles contained in the pollen of plants; and on the general existence of active molecules in organic and inorganic bodies", The Philosophical Magazine **4**, 161–173 (1828).

[198] A. Einstein, "Über die von der molekularkinetischen Theorie der Wärme geforderte Bewegung von in ruhenden Flüssigkeiten suspendierten Teilchen", Annalen der Physik **322**, 549–560 (1905).

[199] J. B. Johnson, "Thermal agitation of electricity in conductors", Nature **119**, 50 (1927).

[200] J. B. Johnson, "Thermal agitation of electricity in conductors", Physical Review **32**, 97–109 (1928).

[201] H. Nyquist, "Thermal agitation of electric charge in conductors", Physical Review **32**, 110–113 (1928).

[202] H. B. Callen and T. A. Welton, "Irreversibility and generalized noise", Physical Review **83**, 34–40 (1951).

[203] R. F. Greene and H. B. Callen, "On the formalism of thermodynamic fluctuation theory", Physical Review **83**, 1231–1235 (1951).

[204] H. Callen and R. Greene, "On a Theorem of Irreversible Thermodynamics", Physical Review **86**, 702–710 (1952).

[205] P. Saulson, "Thermal noise in mechanical experiments", Physical Review D **42**, 2437–2445 (1990).

[206] V. B. Braginsky and A. B. Manukin, *Measurement of Weak Forces in Physics Experiments* (University of Chicago Press, Chicago, 1977).

[207] C. Zener, *Anelasticity of metals* (University of Chicago Press, 1948).

[208] O. L. Anderson and H. E. Bommel, "Ultrasonic Absorption in Fused Silica at Low Temperatures and High Frequencies", Journal of the American Ceramic Society **38**, 125–131 (1955).

[209] P. W. Anderson, B. I. Halperin, and C. M. Varma, "Anomalous low-temperature thermal properties of glasses and spin glasses", Philosophical Magazine **25**, 1–9 (1972).

[210] J. P. Trinastic et al., "Unified interatomic potential and energy barrier distributions for amorphous oxides.", The Journal of Chemical Physics **139**, 154506 (2013).

[211] C. R. Billman et al., "Origin of the second peak in the mechanical loss function of amorphous silica", Physical Review B - Condensed Matter and Materials Physics **95**, 24–27 (2017).

[212] C. Zener, "Internal Friction in Solids II. General Theory of Thermoelastic Internal Friction", Physical Review **53**, 90–99 (1938).

[213] C. Zener, "Internal Friction in Solids. I. Theory of Internal Friction in Reeds", Physical review **52**, 230–5 (1937).

[214] R. Lifshitz and M. Roukes, "Thermoelastic damping in micro- and nanomechanical systems", Physical Review B **61**, 5600–5609 (2000).

[215] A. Gillespie and F. Raab, "Thermally excited vibrations of the mirrors of laser interferometer gravitational-wave detectors", Physical Review D **52**, 577 (1995).

[216] K. Yamamoto, "Study of the thermal noise caused by inhomogeneously distributed loss", PhD thesis (University of Tokyo, 2000).

[217] E. Majorana and Y. Ogawa, "Mechanical thermal noise in coupled oscillators", Physics Letters A **233**, 162–168 (1997).

[218] Y. Levin, "Internal thermal noise in the LIGO test masses : a direct approach", Physical Review D **57**, 659 (1998).

[219] F. Bondu, P. Hello, and J.-Y. Vinet, "Thermal noise in mirros of interferometric gravitational wave antennas", Physics Letters A **246**, 227–236 (1998).

[220] Y. T. Liu and K. S. Thorne, "Thermoelastic noise and homogeneous thermal noise in finite sized gravitational-wave test masses", Physical Review D **62**, 122002 (2000).

[221] S. Rowan, J. Hough, and D. R. M. Crooks, "Thermal noise and material issues for gravitational wave detectors", Physics Letters A **347**, 25–32 (2005).

[222] G. Lovelace, "The dependence of test-mass thermal noises on beam shape in gravitational-wave interferometers", Classical and Quantum Gravity **24**, 4491–4512 (2007).

[223] N. Nakagawa, a. M. Gretarsson, E. K. Gustafson, and M. M. Fejer, "Thermal noise in half-infinite mirrors with nonuniform loss: A slab of excess loss in a half-infinite mirror", Physical Review D **65**, 102001 (2002).

[224] V. Braginsky and S. Vyatchanin, "Thermodynamical fluctuations in optical mirror coatings", Physics Letters A **312**, 244–255 (2003).

[225] V. B. Braginsky, M. L. Gorodetsky, and S. P. Vyatchanin, "Thermo-refractive noise in gravitational wave antennae", Physics Letters A **271**, 303–307 (2000).

[226] Y. Levin, "Fluctuation–dissipation theorem for thermo-refractive noise", Physics Letters A **372**, 1941–1944 (2008).

[227] M. L. Gorodetsky, "Thermal noises and noise compensation in high-reflection multilayer coating", Physics Letters A **372**, 6813–6822 (2008).

[228] H. J. Kimble, B. L. Lev, and J. Ye, "Optical interferometers with reduced sensitivity to thermal noise", Physical Review Letters **101**, 1–4 (2008).

[229] K. Craig, "Studies of the mechanical dissipation of thin films for mirrors in interferometric gravitational wave detectors", PhD thesis (University of Glasgow, 2015).

[230] K. Yamamoto et al., "Measurement of the mechanical loss of a cooled reflective coating for gravitational wave detection", Physical Review D **74**, 1–8 (2006).

[231] M. Granata et al., "Cryogenic measurements of mechanical loss of a high-reflectivity coating and estimation of thermal noise", Optics Letters **38**, 5268 (2013).

[232] J. Wu and C. C. Yu, "How stress can reduce dissipation in glasses", Physical Review B **84**, 174109 (2011).

[233] P. Willems, D. Ottaway, and P. Beyersdorf, "Absorption and thermal issues", in *Optical coatings and thermal noise in precision measurement*, edited by G. Harry, T. P. Bodiya, and R. DeSalvo (Cambridge University Press, 2012) Chap. 10, pp. 145–162.

[234] A. C. Lin et al., "Epitaxial growth of GaP / AlGaP mirrors on Si for low thermal noise optical coatings", Optical Materials Express **5**, 1890–1897 (2015).

[235] A. V. Cumming et al., "Measurement of the mechanical loss of prototype GaP / AlGaP crystalline coatings for future gravitational wave detectors", Classical and Quantum Gravity **32**, 035002 (2015).

[236] E. H. Parker, ed., *The Technology and Physics of Molecular Beam Epitaxy* (Plenum Press, 1985).

[237] M. A. Herman and H. Sitter, *Molecular Beam Epitaxy, Fundamentals and Current Status* (Springer Verlag, Berlin, 1989).

[238] J. Y. Tsao, *Materials Fundamentals of Molecular Beam Epitaxy* (Academic Press, London, 1993).

[239] S. Reid, *Private Communication*, 2017.

[240] Advanced Thin Films, *http://advancedthinfilms.com/Capabilities/IBS-Thin-film-Coatings*.

[241] N. A. Robertson, K. A. Strain, and J. Hough, "Measurements of losses in high reflectance mirrors coated for lambda = 514.5 nm", Optics Communications **69**, 345–348 (1989).

[242] S. Chao, "Coating Technology", in *Optical coatings and thermal noise in precision measurement*, edited by G. Harry, T. P. Bodiya, and R. De Salvo (Cambridge University Press, New York, 2012) Chap. 2, pp. 7–23.

[243] G. Parisi and F. Sciortino, "Structural glasses: Flying to the bottom", Nature Materials **12**, 94–95 (2013).

[244] S. Singh, M. D. Ediger, and J. de Pablo, "Ultrastable glasses from in silico vapour deposition", Nature materials **12**, 139–44 (2013).

[245] X. Liu et al., "Hydrogen-free amorphous silicon with no tunneling States.", Physical review letters **113**, 025503 (2014).

[246] M. Granata, *Coating R&D at LMA*, LIGO technical document: LIGO G1701598-v1, Talk, LVC Meeting: Geneva, 2017.

[247] P. Kelly and R. Arnell, "Magnetron sputtering: a review of recent developments and applications", Vacuum **56**, 159–172 (2000).

[248] Hauzer: Industrial Plasma Solutions, *https://www.hauzertechnocoating.com/en/plasma-coating/*.

[249] D. Christie, "Making Magnetron Sputtering Work: Reversing the Glow to Arc Transition", SVC Bulletin, 32–35 (2014).

[250] E. Alfonso, J. Olaya, and G. Cubillos, "Thin Film Growth Through Sputtering Technique and Its Applications", in *Crystallization - science and technology*, edited by M. R. B. Andreeta (InTech, 2012) Chap. 15, pp. 397–431.

[251] D. M. Mattox, *Handbook of Physical Vapor Deposition (PVD) Processing*, 2nd (Elsevier Inc, 2010).

[252] Tafelmaier: coating technology, *http://www.tafelmaier.de/index.php?lng=en*.

[253] B. S. Berry and W. C. Pritchet, "Vibrating Reed Internal Friction Apparatus for Films and Foils", IBM Journal of Research and Development **19**, 334–343 (1975).

[254] I. W. Martin et al., "Measurements of a low-temperature mechanical dissipation peak in a single layer of Ta_2O_5 doped with TiO_2", en, Classical and Quantum Gravity **25**, 055005 (2008).

[255] I. W. Martin et al., "Comparison of the temperature dependence of the mechanical dissipation in thin films of Ta_2O_5 and Ta_2O_5 doped with TiO_2", Classical and Quantum Gravity **26**, 155012 (2009).

[256] I. W. Martin et al., "Effect of heat treatment on mechanical dissipation in Ta_2O_5 coatings", Classical and Quantum Gravity **27**, 225020 (2010).

[257] M. R. Abernathy et al., "Cryogenic mechanical loss measurements of heat-treated hafnium dioxide", Classical and Quantum Gravity **28**, 195017 (2011).

[258] I. W. Martin et al., "Low temperature mechanical dissipation of an ion-beam sputtered silica film", Classical and Quantum Gravity **31**, 035019 (2014).

[259] P. G. Murray et al., "Ion-beam sputtered amorphous silicon films for cryogenic precision measurement systems", Physical Review D **92**, 062001 (2015).

[260] T. J. Quinn, C. C. Speake, R. S. Davis, and W. Tew, "Stress-dependant damping in Cu-BE torsion and flexure suspensions at stresses up to 1.1 GPa", Physics Letters A **197**, 197–208 (1995).

[261] Kelvin Nanotechnology, *https://www.kelvinnanotechnology.com/*.

[262] M. E. Fine, "Low-Temperature Internal Friction and Elasticity Effects in Vitreous Silica", Journal of Applied Physics **25**, 402 (1954).

[263] S. Reid et al., "Mechanical dissipation in silicon flexures", Physics Letters A **351**, 205–211 (2006).

[264] R. Nawrodt et al., "Investigation of mechanical losses of thin silicon flexures at low temperatures", Classical and Quantum Gravity **30**, 115008 (2013).

[265] SENTECH Instruments, *http://www.sentech.com/en/*.

[266] R. M. A. Azzam and N. M. Bashara, *Ellipsometry and polarized light* (North-Holland, Amsterdam, 1987).

[267] E. Garcia-Caurel, A. De Martino, J. P. Gaston, and L. Yan, "Application of spectroscopic ellipsometry and mueller ellipsometry to optical characterization", Applied Spectroscopy **67**, 1–21 (2013).

[268] W. Andrew, *Handbook of Ellipsometry* (William Andrew Publishing, New York, 2005).

[269] N. McLachlan, *Theory of Vibrations* (Dover, 1952).

[270] D. R. M. Crooks, "Mechanical loss and its significance in the test mass mirrors of gravitational wave detectors", PhD thesis (University of Glasgow, 2002).

[271] B. E. White Jr and R. O. Pohl, "Internal Friction of Subnanometer a-SiO2 Films", Physical Review Letters **75**, 4437–4439 (1995).

[272] A. Heptonstall, G. Cagnoli, J. Hough, and S. Rowan, "Characterisation of mechanical loss in synthetic fused silica ribbons", Physics Letters A **354**, 353–359 (2006).

[273] S. Grasso et al., "Electrostatic systems for fine control of mirror orientation in interferometric GW antennas", Physics Letters A **244**, 360–370 (1998).

[274] D. V. Koptsov, L. G. Prokhorov, and V. P. Mitrofanov, "Measurement of fluctuations of electrostatic force acting between a dielectric plate and an electrostatic drive", Review of Scientific Instruments **88**, 044701 (2017).

[275] Lakeshore silicon diode DT-670, *http://www.lakeshore.com/products/cryogenic-temperature-sensors/silicon-diodes/dt-670/pages/Specifications.aspx*.

[276] Y. S. Touloukian and C. Y. Ho, *Thermophysical Properties of Matter: The TPRC Data Series* (Plenum, New York, 1970).

[277] Lakeshore 340 cryogenic temperature controller, *http://www.lakeshore.com/ObsoleteAndResearchDocs/340_Manual.pdf*.

[278] R. Flaminio, *Development of the coatings for the Advanced LIGO and Advanced Virgo mirrors*, 10th Amaldi Conference on Gravitational Waves, Talk, Warsaw, 2013.

[279] M. F. Doerner and W. D. Nix, "Stresses and deformation processes in thin films on substrates", Critical Reviews in Solid State and Materials Sciences **14**, 225–268 (1988).

[280] M. R. Abernathy, "Mechanical properties of coating materials for use in the mirrors of interferometric gravitational wave detectors", PhD thesis (University of Glasgow, 2012).

[281] E. Klokholm and B. S. Berry, "Intrinsic Stress in Evaporated Metal Films", Journal of The Electrochemical Society **115**, 823–26 (1968).

[282] R. Hoffman, "The mechanical properties of thin condensed films", in *Physics of thin films* (Academic Press, 1966).

[283] G. G. Stoney, "The Tension of Metallic Films Deposited by Electrolysis", Proceedings of the Royal Society A: Mathematical, Physical and Engineering Sciences **82**, 172–175 (1909).

[284] P. Flinn, D. Gardner, and W. Nix, "Measurement and Interpretation of stress in aluminum-based metallization as a function of thermal history", IEEE Transactions on Electron Devices **34**, 689–699 (1987).

[285] S. Penn et al., *Recent Measurements of Mechanical Loss for aLIGO Coating Research Recent Coating Loss measurements*, LIGO technical document: LIGO-G1000356-v1, Talk, LVC Meeting: Pasadena, 2010.

[286] J. W. Marx and J. M. Sivertsen, "Temperature Dependence of the Elastic Moduli and Internal Friction of Silica and Glass", Journal of Applied Physics **24**, 81 (1953).

[287] H. J. McSkimin, "Measurement of elastic constants at low temperatures by means of ultrasonic waves-data for silicon and germanium single crystals, and for fused silica", Journal of Applied Physics **24**, 988 (1953).

[288] B. E. Deal and A. S. Grove, "General relationship for the thermal oxidation of silicon", Journal of Applied Physics **36**, 3770–3778 (1965).

[289] L. N. Lie, R. R. Razouk, and B. E. Deal, "High Pressure Oxidation of Silicon in Dry Oxygen", Journal of The Electrochemical Society **129**, 2828 (1982).

[290] C. Krzeminski et al., "Silicon dry oxidation kinetics at low temperature in the nanometric range: Modeling and experiment", Journal of Applied Physics **101**, 064908 (2007).

[291] G. Gerlach and K. Maser, "A Self-Consistent Model for Thermal Oxidation of Silicon at Low Oxide Thickness", Advances in Condensed Matter Physics **2016**, 1–13 (2016).

[292] C. Hollauer, "Modelling of Thermal Oxidation and Stress Effects", PhD thesis (TU Wien, 2007).

[293] J. D. Plummer, M. Deal, and P. D. Griffin, *Silicon VLSI Technology: Fundamentals, Practice, and Modeling* (Prentice Hall, 2000).

[294] S. Wolf and R. N. Tauber, *Silicon Processing for the VLSI Era: Process Technology, Volume 1*, 2nd (Lattice Press, 2000).

[295] M. Fletcher, *Private communication*, 2017.

[296] S. Musikant, *Optical Materials* (Marcel Dekker Inc., New York, 1985).

[297] R. W. Wynant and M. N. Ediger, *Electro-Optics Handbook* (McGraw-Hill, New York, 1994).

[298] C. H. Cho, "Characterization of Young's modulus of silicon versus temperature using a "beam deflection" method with a four-point bending fixture", Current Applied Physics **9**, 538–545 (2009).

[299] E. J. Boyd, L. Li, R. Blue, and D. Uttamchandani, "Measurement of the temperature coefficient of Young's modulus of single crystal silicon and 3C silicon carbide below 273 K using micro-cantilevers", Sensors and Actuators, A: Physical **198**, 75–80 (2013).

[300] R. Bruckner, "Properties and structure of vitreous silica. I", Journal of Non-Crystalline Solids **5**, 123–175 (1970).

[301] A. K. Raychaudhuri and S. Hunklinger, "Low frequency elastic properties of glasses at low temperatures-implications on the tunneling model", Zeitschrift für Physik B Condensed Matter **57**, 113–125 (1984).

[302] D. G. Cahill and J. E. Van Cleve, "Torsional oscillator for internal friction data at 100 kHz", Review of Scientific Instruments **60**, 2706–2710 (1989).

[303] K. S. Gilroy and W. a. Phillips, "An asymmetric double-well potential model for structural relaxation processes in amorphous materials", Philosophical Magazine Part B **43**, 735–746 (1981).

[304] W. A. Phillips, "Tunneling states in amorphous solids", Journal of Low Temperature Physics **7**, 351–360 (1972).

[305] R. O. Pohl, X. Liu, and E. Thompson, "Low-temperature thermal conductivity and acoustic attenuation in amorphous solids", Reviews of Modern Physics **74**, 991–1013 (2002).

[306] W. A. Phillips, "Two-level states in glasses", Reports on Progress in Physics **50** (1987).

[307] M. Callens-Raadschelders, R. De Batist, and R. Gevers, "Debye relaxation equations for a standard linear solid with high relaxation strength", Journal of Materials Science **12**, 251–263 (1977).

[308] M. S. Blanter, I. S. Golovin, H. Neuhauser, and H. R. Sinning, *Internal Friction in Metallic Materials* (Springer-Verlag, 2007).

[309] Origin, *http://www.originlab.com/*.

[310] G. Bartenev, V. Lomovskoi, and G. Sinitsyna, "Relaxation processes in silica glass", Inorganic Materials **32**, 671–682 (1996).

[311] L. Nuccio, S. Agnello, and R. Boscaino, "Annealing of radiation induced oxygen deficient point defects in amorphous silicon dioxide: evidence for a distribution of the reaction activation energies", Journal of physics. Condensed matter **20**, 385215 (2008).

[312] L. Berthier, P. Charbonneau, E. Flenner, and F. Zamponi, "Origin of Ultrastability in Vapor-Deposited Glasses", Physical Review Letters **119**, 188002 (2017).

[313] R. E. Strakna, "Investigation of Low-Temperature Ultrasonic Absorption in Fast-Neutron Irradiated SiO_2 Glass", Physical Review **123**, 2020–26 (1961).

[314] M. R. Vukcevich, "A new interpretation of the anomalous properties of vitreous silica", Journal of Non-Crystalline Solids **11**, 25–63 (1972).

[315] R. Hamdan, J. P. Trinastic, and H. P. Cheng, "Molecular dynamics study of the mechanical loss in amorphous pure and doped silica", Journal of Chemical Physics **141**, 054501 (2014).

[316] User:Polyamorph, *https://commons.wikimedia.org/wiki/File:Silica.svg*, Wikimedia Commons, 2008.

[317] K. Topp and D. G. Cahill, "Elastic properties of several amorphous solids and disordered crystals below 100 K", Zeitschrift für Physik B Condensed Matter **101**, 235–245 (1996).

[318] A. Polian, D. Vo-Thanh, and P. Richet, "Elastic properties of a-SiO_2 up to 2300 K from Brillouin scattering measurements", Europhysical Letters **57**, 375 (2002).

[319] A. Nittke et al., "Low temperature heat release, sound velocity and attenuation, specific heat and thermal conductivity in polymers", Journal of Low Temperature Physics **98**, 517 (1994).

[320] J. P. Trinastic, R. Hamdan, C. Billman, and H.-P. Cheng, "Molecular dynamics modelling of mechanical loss in amorphous tantala and titania-doped tantala", Physical Review B **93**, 014105 (2016).

[321] H. Windischmann, "Intrinsic Stress in Sputter-Deposited Thin Films", Critical Reviews in Solid State and Materials Sciences **17**, 547–596 (1992).

[322] S. Reid et al., *Elevated temperature ion-beam deposition of aSi and* Ta_2O_5, LIGO technical document: LIGO G1700471-v3, Talk, LVC Meeting: Pasadena, 2017.

[323] E. Gustafson, *Progress on Optical Coatings Research for A+*, LIGO technical document: LIGO G1701026-v17 (LIGO Laboratory, 2017).

[324] G. Vajente et al., *Update on coating research at Caltech*, LIGO technical document: LIGO G1700350-v1, Talk, LVC meeting: Pasadena, 2017.

[325] J. Steinlechner, A. Khalaidovski, and R. Schnabel, "Optical absorption measurement at 1550 nm on a highly-reflective Si/SiO_2 coating stack", Classical and Quantum Gravity **31**, 105005 (2014).

[326] J. Steinlechner et al., "Thermal noise reduction and absorption optimization via multimaterial coatings", Physical Review D **91**, 042001 (2015).

[327] I. W. Martin, "Studies of materials for use in future interferometric gravitational wave detectors", PhD thesis (University of Glasgow, 2009).

[328] R. Vacher, E. Courtens, and M. Foret, "Anharmonic versus relaxational sound damping in glasses. II. Vitreous silica", Physical Review B **72**, 214205 (2005).

[329] J. Reinisch and A. Heuer, "What is moving in silica at 1 K? A computer study of the low-temperature anomalies", Physical Review Letters **95**, 5–8 (2005).

[330] F. Travasso et al., "Low-frequency losses in silica glass at low temperature", Materials Science and Engineering A **521-522**, 268–271 (2009).

[331] J. E. Shelby, "Density of vitreous silica", Journal of Non-Crystalline Solids **349**, 331–336 (2004).

[332] W. Yam, S. Gras, and M. Evans, "Multimaterial coatings with reduced thermal noise", Physical Review D - Particles, Fields, Gravitation and Cosmology **91**, 1–6 (2015).

[333] R. H. French, H. Müllejans, and D. J. Jones, "Optical Properties of Aluminum Oxide: Determined from Vacuum Ultraviolet and Electron Energy-Loss Spectroscopies", Journal of the American Ceramic Society **57**, 2549–2557 (1998).

[334] R.-L. Chiu and P.-H. Chang, "Thickness dependence of refractive index for anodic aluminium oxide films", Journal of Materials Science Letters **16**, 174–178 (1997).

[335] P. Kumar, M. K. Wiedmann, C. H. Winter, and I. Avrutsky, "Optical properties of Al_2O_3 thin films grown by atomic layer deposition", Applied Optics **48**, 5407 (2009).

[336] G. T. Mearini and R. W. Hoffman, "Tensile properties of aluminum/alumina multi-layered thin films", Journal of Electronic Materials **22**, 623–629 (1993).

[337] P. Nayar et al., "Structural, optical and mechanical properties of amorphous and crystalline alumina thin films", Thin Solid Films **568**, 19–24 (2014).

[338] D. C. Miller et al., "Thermo-mechanical properties of alumina films created using the atomic layer deposition technique", Sensors and Actuators A: Physical **164**, 58–67 (2010).

[339] J. B. Wachtman and D. G. Lam, "Young's Modulus of Various Refractory Materials as a Function of Temperature", Journal of the American Ceramic Society **42**, 254–260 (1959).

[340] J. Musil et al., "Thermal stability of alumina thin films containing γ-Al_2O_3 phase prepared by reactive magnetron sputtering", Applied Surface Science **257**, 1058–1062 (2010).

[341] J. M. Schneider, W. D. Sproul, and A. Matthews, "Phase formation and mechanical properties of alumina coatings prepared at substrate temperatures less than 500 °C by ionized and conventional sputtering", Surface and Coatings Technology **94-95**, 179–183 (1997).

[342] K. Bobzin, E. Lugscheider, M. Maes, and C. Piñero, "Relation of hardness and oxygen flow of Al_2O_3 coatings deposited by reactive bipolar pulsed magnetron sputtering", Thin Solid Films **494**, 255–262 (2006).

[343] K. Koski, J. Hölsä, and P. Juliet, "Properties of aluminium oxide thin films deposited by reactive magnetron sputtering", Thin Solid Films **339**, 240–248 (1999).

[344] A. Schütze and D. T. Quinto, "Pulsed plasma-assisted PVD sputter-deposited alumina thin films", Surface and Coatings Technology **162**, 174–182 (2003).

[345] G. Balakrishnan et al., "Effect of substrate temperature on microstructure and optical properties of nanocrystalline alumina thin films", Ceramics International **39**, 9017–9023 (2013).

[346] N. Kim, R. Bassiri, M. M. Fejer, and J. F. Stebbins, "The structure of ion beam sputtered amorphous alumina films and effects of Zn doping: High-resolution 27Al NMR", Journal of Non-Crystalline Solids **405**, 1–6 (2014).

[347] Q. Y. Zhang et al., "Microstructure, morphology and their annealing behaviors of alumina films synthesized by ion beam assisted deposition", Nuclear Instruments and Methods in Physics Research, Section B: Beam Interactions with Materials and Atoms **206**, 357–361 (2003).

[348] I. N. Reddy et al., "Optical and Microstructural Characterisations of Pulsed RF Magnetron Sputtered Alumina Thin Film", Journal of Materials Science and Technology **29**, 929–936 (2013).

[349] V. Edlmayr, M. Moser, C. Walter, and C. Mitterer, "Thermal stability of sputtered Al_2O_3 coatings", Surface and Coatings Technology **204**, 1576–1581 (2010).

[350] A. I. Osman et al., "Effect of precursor on the performance of alumina for the dehydration of methanol to dimethyl ether", Applied Catalysis B: Environmental **127**, 307–315 (2012).

[351] A. Dey and A. K. Mukhopadhyay, *Nanoindentation of Brittle Solids* (CRC Press, 2014).

[352] A. V. Cumming, "Aspects of mirrors and suspensions for advanced gravitational wave detectors", PhD thesis (University of Glasgow, 2008).

[353] W.-H. Wang and S. Chao, "Annealing effect on ion-beam-sputtered titanium dioxide film", Optics Letters **23**, 1417–1419 (1998).

[354] S. V. Ushakov et al., "Crystallization in hafnia- and zirconia-based systems", Physica Status Solidi (B) Basic Research **241**, 2268–2278 (2004).

[355] R. Flaminio et al., "A study of coating mechanical and optical losses in view of reducing mirror thermal noise in gravitational wave detectors", Classical and Quantum Gravity **27** (2010) 10.1088/0264-9381/27/8/084030.

[356] F. Beauville et al., "Low-loss coatings for the Virgo large mirrors", in Proceedings of SPIE, Vol. 5205, Optical Systems Design (2003).

[357] S. G. Yoon et al., "Comparision of residual stress and optical properties in Ta_2O_5 thin films deposited by single and dual ion beam sputtering", Materials Science and Engineering B **118**, 234–237 (2005).

[358] L. Borgese et al., "Young modulus and Poisson ratio measurements of TiO 2 thin films deposited with Atomic Layer Deposition", Surface and Coatings Technology **206**, 2459–2463 (2012).

[359] P. G. Murray, *Private Communication*, 2017.

[360] R. Bassiri, *Private Communication*, 2017.

[361] H. N. B. Isa, *Private Communication*, 2017.

[362] M. Hart, *Private Communication*, 2016.

[363] S. Chao, W.-H. Wang, and C.-C. Lee, "Low-loss dielectric mirror with ion-beam-sputtered TiO_2–SiO_2 mixed films", Applied Optics **40**, 2177 (2001).

[364] C. Bundesmann et al., "Systematic investigation of the properties of TiO 2 films grown by reactive ion beam sputter deposition", Applied Surface Science **421**, 331–340 (2017).

[365] W. W. Scott and R. MacCrone, "Apparatus for Mechanical Loss Measurements in Low Loss Materials at Audio Frequencies and Low Temperatures", Review of Scientific Instruments **39**, 821 (1968).

[366] M. J. Colgan, B. Djurfors, D. G. Ivey, and M. J. Brett, "Effects of annealing on titanium dioxide structured films", Thin Solid Films **466**, 92–96 (2004).

[367] S. Chao, W.-H. Wang, M.-Y. Hsu, and L.-C. Wang, "Characteristics of ion-beam-sputtered high-refractive-index TiO_2-SiO_2 mixed films", Journal of the Optical Society of America **16**, 1477 (1999).

[368] H.-W. Pan et al., "Thickness-dependent crystallization on thermal anneal for titania/silica nm-layer composites deposited by ion beam sputter method", Optics Express **22**, 29847 (2014).

[369] J.-C. Hsu and C.-C. Lee, "Single- and dual-ion-beam sputter deposition of titanium oxide films", Applied Optics **37**, 1171 (1998).

[370] R. Bassiri et al., *Coating Atomic Structure Investigations*, LIGO technical document: LIGO G1300379, Talk, LVC Meeting: Bethesda, 2013.

[371] K. L. Evans, "Computational modelling of amorphous mirror coatings for use in advanced gravitational wave detectors", PhD thesis (University of Glasgow, 2012).

[372] K. Borisenko, *Private communication*, 2012.

[373] J.-Y. Tewg, Y. Kuo, and J. Lu, "Suppression of Crystallization of Tantalum Oxide Thin Film by Doping with Zirconium", Electrochemical and Solid-State Letters **8**, G27–G29 (2005).

[374] M. Abernathy, *Private Communication*, 2014.

[375] P. G. Murray et al., *Coating mechanical loss investigations*, LIGO technical document, Talk, LVC Meeting: Nice, 2014.

[376] R. Adhikari et al., *LIGO Voyager Upgrade Conceptual Design*, LIGO technical document: LIGO–T1400226–v7 (2016).

[377] J. Steinlechner, *Private Communication*, 2017.

[378] R. W. Johnson, A. Hultqvist, and S. F. Bent, "A brief review of atomic layer deposition: From fundamentals to applications", Materials Today **17**, 236–246 (2014).

[379] T. Uchiyama et al., "Mechanical quality factor of a cryogenic sapphire test mass for gravitational wave detectors", Physics Letters A **261**, 5–11 (1999).

[380] R. Nawrodt et al., "High mechanical Q-factor measurements on silicon bulk samples", Journal of Physics: Conference Series **122**, 012008 (2008).

[381] J. Kischkat et al., "Mid-infrared optical properties of thin films of aluminum oxide, titanium dioxide, silicon dioxide, aluminum nitride, and silicon nitride", Applied Optics **51**, 6789 (2012).

[382] P. Martin et al., "Mechanical and Optical Properties of The Films of Tantalum Oxide Deposited by Ion-Assisted Deposition", MRS Proceedings **308**, 583 (1993).

[383] K. Kukli et al., "Atomic layer deposition and properties of mixed Ta_2O_5 and ZrO_2 films", AIP Advances **7**, 025001 (2017).

[384] L. B. Freund and S. Suresh, *Thin Film Materials* (Cambridge University Press, 2003).

[385] I. H. Malitson, F. V. Murphy Jr., and W. S. Rodney, "Refractive Index of Synthetic Sapphire", Journal of the Optical Society of America **48**, 72–73 (1958).

[386] R. W. Waynant and M. Ediger, *Electro-Optics Handbook* (McGraw-Hill, New York, 1994).

[387] I. H. Malitson, "Interspecimen Comparison of the Refractive Index of Fused Silica", Journal of the Optical Society of America **55**, 1205 (1965).

[388] C. Z. Tan, "Determination of refractive index of silica glass for infrared wavelengths by IR spectroscopy", Journal of Non-Crystaline Solids **223**, 158–163 (1998).

[389] O. S. Heavens, *Thin Film Physics* (Methuen and Co, London, 1970).

[390] Software Pectra, Inc., *http://www.sspectra.com/*.

[391] G. Cagnoli, *Private Communication*, 2016.

[392] J. Steinlechner et al., "Optical absorption of ion-beam sputtered amorphous silicon coatings", Physical Review D **93**, 1–9 (2016).

[393] D. Vine et al., *Elevated temperature ion-beam deposition of aSi and* Ta_2O_5, LIGO technical document, Talk, GWADW meeting: Hamilton Island, 2017.

[394] I. W. Martin et al., *Development of silicon mirrors and coatings*, LIGO technical document: LIGO-G1700882-v1, GWADW meeting: Hamilton Island, 2017.

[395] A. S. Markosyan, *Private Communication*, 2017.

[396] J. Steinlechner et al., "Optical absorption of silicon nitride membranes at 1064 nm and at 1550 nm", Physical Review D **96**, 1–9 (2017).

[397] H.-W. Pan et al., "Silicon nitride films fabricated by a plasma-enhanced chemical vapor deposition method for coatings of the laser interferometer gravitational wave detector", Physical Review D **97**, 022004 (2018).

[398] A. Cumming, R. Jones, M. Barton, et al., "Apparatus for dimensional characterization of fused silica fibers for the suspensions of advanced gravitational wave detectors", Review of Scientific Instruments **82**, 044502 (2011).

[399] D.-H. Gwo, *Ultra precision and reliable bonding method*, US Patent 6,284,085 B1, 2001.

[400] R. K. Iler, *The Chemistry of Silica* (John Wiley and Sons, 1979).

[401] P. G. Murray, "Measurement of the mechanical loss of test mass materials for advanced gravitational wave detectors", Ph.D Thesis (University of Glasgow, 2008).